

PHASE CHANGE MATERIALS FOR THERMAL MANAGEMENT AND THERMAL ENERGY STORAGE APPLICATIONS

Ph.D. Thesis

By
ROHIT KOTHARI



**DEPARTMENT OF MECHANICAL ENGINEERING
INDIAN INSTITUTE OF TECHNOLOGY INDORE**

MAY 2021

PHASE CHANGE MATERIALS FOR THERMAL MANAGEMENT AND THERMAL ENERGY STORAGE APPLICATIONS

A THESIS

*Submitted in partial fulfillment of the
requirements for the award of the degree
of*
DOCTOR OF PHILOSOPHY

by
ROHIT KOTHARI



**DEPARTMENT OF MECHANICAL ENGINEERING
INDIAN INSTITUTE OF TECHNOLOGY INDORE**

MAY 2021



INDIAN INSTITUTE OF TECHNOLOGY INDORE

CANDIDATE'S DECLARATION

I hereby certify that the work which is being presented in the thesis entitled **PHASE CHANGE MATERIALS FOR THERMAL MANAGEMENT AND THERMAL ENERGY STORAGE APPLICATIONS** in the partial fulfillment of the requirements for the award of the degree of **DOCTOR OF PHILOSOPHY** and submitted in the **DEPARTMENT OF MECHANICAL ENGINEERING, Indian Institute of Technology Indore**, is an authentic record of my own work carried out during the time period from July 2016 to May 2021 under the supervision of **Dr. Santosh Kumar Sahu, Associate Professor, Indian Institute of Technology Indore** and **Dr. Shailesh Ishwarlal Kundalwal, Associate Professor, Indian Institute of Technology Indore**.

The matter presented in this thesis has not been submitted by me for the award of any other degree of this or any other institute.

(May 08, 2021)

**Signature of the student with date
(Rohit Kothari)**

This is to certify that the above statement made by the candidate is correct to the best of my/our knowledge.

May 08, 2021

Signature of Thesis Supervisor with date
(Dr. Santosh Kumar Sahu)

(DR. S. I. KUNDALWAL) 08.05.2021

Signature of Thesis Supervisor with date
(Dr. Shailesh Ishwarlal Kundalwal)

ROHIT KOTHARI has successfully given his/her Ph.D. Oral Examination held on **September 06, 2021**.

06.09.2021

Signature of Thesis Supervisor with date
(Dr. Santosh Kumar Sahu)

(DR. S. I. KUNDALWAL) 06.09.2021

Signature of Thesis Supervisor with date
(Dr. Shailesh Ishwarlal Kundalwal)

ACKNOWLEDGEMENTS

I would like to express my sincere gratitude to my supervisor, **Dr. Santosh Kumar Sahu**, Department of Mechanical Engineering, Indian Institute of Technology Indore, and **Dr. Shailesh Ishwarlal Kundalwal**, Department of Mechanical Engineering, Indian Institute of Technology Indore, for their valuable guidance, consistent effort and encouragement throughout my research work. I am very grateful to them for their support, motivation and enthusiasm provided to me during the course of this research. At many stages in the course of this research project, I benefited from their advice. Their careful editing contributed enormously to the production of this thesis.

My sincere thanks and respect to **Prof. Shripad T. Revankar**, Professor, Nuclear Engineering, Purdue University, USA for their valuable guidance, consistent effort and encouragement during my visit to USA. I have been fortunate to carry out a part of this research work under his supervision. I am very grateful to him for his support, motivation and enthusiasm provided to me during the course of this research.

I wish to express my gratitude to my Ph.D. progress committee members, **Dr. Shanmugam Dhinakaran**, Associate Professor, Department of Mechanical Engineering, Indian Institute of Technology Indore, **Dr. Swadesh Kumar Sahoo**, Associate Professor, Department of Mathematics, Indian Institute of Technology Indore, and **Dr. Anil Kumar Emadabathuni**, Department of Mechanical Engineering, Indian Institute of Technology Tirupati for providing various technical inputs and valuable suggestions, which has greatly helped in shaping this thesis. I am also thankful to Head, DPGC convener, all faculty members and staff of the Department of Mechanical Engineering for their timely help and support throughout.

My sincere acknowledgement and respect to **Prof. Neelesh Kumar Jain**, Director (Officiating), Indian Institute of Technology Indore for providing me the opportunity to explore my research capabilities at **Indian Institute of Technology Indore**. I am grateful to him for providing me financial support to present my research work in International conferences within and outside India.

I am thankful to the **Department of Science and Technology (DST)**, Ministry of Science and Technology, India for the financial supports provided during the tenure of my PhD under the award of **INSPIRE Fellowship [IF170534]**. I acknowledge the **Ministry of Education**

(MoE), India for providing support to pursue my research. Also, I want to thank **Science and Engineering Research Board (SERB)**, India and **Purdue University, USA** for the research and financial support provided under **Overseas Visiting Doctoral Fellowship (OVDF)**. The fellowship has provided an opportunity to carry out a part of doctoral research work at Purdue University, USA for one year.

I acknowledge the **Science and Engineering Research Board (SERB)**, New Delhi, India for the financial aid sanctioned to me under International Travel Support for presenting my research work in **ICNMM2018** held at **Dubrovnik, Croatia**. I am thankful to **American Society of Mechanical Engineering (ASME)**, USA, for the financial support to present my work in **POWER2019** at **Salt Lake City, UT, USA**, and **ICONE28-POWER2020** (Virtual Conference) at **USA**.

I am thankful to all the staff members of **Workshop, Advanced Manufacturing Processes Laboratory, Mechatronics and Instrumentation Laboratory** and **Sophisticated Instrument Centre (SIC)** for their extended effort during development of test facility, fabrication of test surfaces, and characterization at IIT Indore. Many thanks to **Mr. Arun Kumar Bhagwaniya**, Fluid Mechanics and Machinery Lab for his assistance for fabrication of test facility. I am thankful to all the members of **Central Library**, Indian Institute of Technology Indore for extended help during my Ph.D. work.

I am indebted to my seniors, lab mates and colleague researchers especially **Dr. Hari Mohan Kushwaha, Dr. Mayank Modak, Dr. Avadhesh K Sharma, Dr. Saurabh Yadav, Dr. Vishal Nirgude, Mr. Pushpanjay K Singh, Mr. Anuj Kumar, Dr. Dharmendra Panchariya, Mr. Vijay Choyal, Mr. Jay Joshi, Mr. Jayanta Sutradhar, Mr. Pawan Sharma, Mr. Akhalesh Sharma, Mr. Pradeep Singh, Mr. Vivek Saxena, Mr. Sreetam Das, Mr. Pawan Mahalkar, Mr. Deshraj Meena, Mr. Nitin Goyal, Mr. Sohan Sahoo, Mr. Vinay Shelke, Mr. Vaidya Dattaray Vilas, Mr. Vikrant Singh**, Dr. Kishor Shingare, Mr. Vijay K. Choyal, Mr. Subhash Nehwal, Mr. Ankit Rathi, Mr. Vraj Mundra, Ms. Priyanka Bhagoria, Mr. Rushikesh Vaidya, and Mr. Pawan Kumar Singh for their cooperation during the course of my research.

I would like to express my sincere respect to **my late grandmother** and **my parents** for their love, care, and support they have provided to me throughout my life. Special thanks to **my brother, my sisters-in-law, my uncle, my aunty and my cousins** for their support and

encouragements. I want to show my deepest love to my cute nieces **Nirvi** for bringing happiness in my life.

Finally, I am thankful to all who directly or indirectly contributed, helped and supported me. I always learned and believed that I want to sum up in one line.

“Everything happens for a reason, probably a good one”

Lastly, I want to sign off with a very popular mantra.

ॐ सर्वे भवन्तु सुखिनः
सर्वे सन्तु निरामयाः।
सर्वे भद्राणि पश्यन्तु मा कश्चिद्दुःखभाग्भवेत्।
ॐ शान्तिः शान्तिः शान्तिः॥

*May all sentient beings be at peace,
may no one suffer from illness,
May all see what is auspicious, may no one suffer.
Om peace, peace, peace.*

Rohit Kothari

***Dedicated to my family and friends
for their love, care and blessings***

ABSTRACT

Present dissertation reports the theoretical and experimental investigations pertaining to the heat transfer characteristics of phase change materials (PCMs) during melting/solidification. The objective of the present study is to analyze the thermal performance of PCM based systems for various applications including thermal management of electronic components and thermal energy storage systems.

Initially, analytical models have been developed to analyze melting and solidification process of PCM in various energy systems involving cylindrical annulus and rectangular enclosure for different thermal boundary conditions. Variational formulation technique has been employed to solve the conduction equation with associated boundary conditions in cylindrical annulus. The model yields closed form solution for temperature distribution of PCM during melting and solidification process. The theoretical prediction is found to exhibit good agreement with available experimental results. Later on, the analytical models have been proposed to analyze melting and solidification of PCM inside rectangular energy storage system with internal plate fins. Heat balance integral method is employed to solve the conduction equation with associated boundary conditions. Closed form expressions have been obtained for various parameters such as temperature distribution, solid-liquid interface location and melt/solid fraction. The results obtained from the analytical models are compared with the available experimental, analytical and numerical results. Based on the theoretical analysis, correlations have been proposed for melt/solid fraction for different boundary conditions.

Subsequently, *computational fluid dynamics* (CFD) simulations have been performed to analyze the unconstrained and constrained melting of PCM inside the spherical capsule by using Ansys Fluent. Numerous models involving symmetric/axisymmetric formulations with varying density, constant density and Boussinesq approximation have been simulated to analyze the melting behavior. Volume of fluid model and solidification and melting model are used to simulate

the melting of PCM. The results obtained from numerical simulation such as melting pattern and melt fraction of PCM are found to be in good agreement with the available test data.

Furthermore, a test facility has been developed to analyze the heat transfer performance of PCM based heat sinks for thermal management of electronic devices. Tests have been carried out to investigate the thermal performance of PCM based heat sinks involving fin number, inclination angle and heat flux values. The evolution and propagation of melt front inside the heat sink is studied through photographic observation. For two different cases such as unfinned heat sink without PCM and PCM based three finned heat sink configurations, the operating time is found to be relatively independent of inclination angle.

In addition, metallic foams are employed in different unfinned and finned heat sinks. Thermal performance of different configurations of unfinned and finned heat sinks involving pure PCM and metallic foam (MF) PCM composite have been compared. The effect of various parameters such as volume fraction of PCM, effect of heat flux and type of heat sink on the stretching of operating time to achieve a set point temperature has been studied. Enhancement ratios are obtained for various heat sink configurations. It has been observed that four finned heat sink assembly with MF integrated with PCM exhibits the highest enhancement ratio. In addition to this, nanoparticles are embedded in PCM based unfinned and finned heat sinks to study the thermal performance of nano-enhanced PCM based heat sinks through experimental investigation. The thermal performance of nano-enhanced PCM based heat sinks are compared with pure PCM based heat sink configuration. Lower nanoparticle concentration in PCM is found to provide better thermal performance and beneficial for thermal management applications.

Keywords: *thermal management, thermal energy storage, phase change materials, melting/solidification, melt/solid fraction, unconstrained, constrained, heat sink, unfinned/finned, enhancement ratio*

TABLE OF CONTENTS

ABSTRACT	i
LIST OF FIGURES	ix
LIST OF TABLES	xxi
NOMENCLATURE	xxiii
Chapter 1	
Introduction and literature survey	1
1.1 General background	1
1.2 Thermal management techniques	2
1.3 Thermal energy storage techniques	3
1.3.1 Sensible heat storage (SHS)	4
1.3.2 Thermochemical heat storage (TCHS)	5
1.3.3 Latent heat storage (LHS)	6
1.4 Phase change materials	7
1.4.1 Selection of PCM	8
1.4.2 Classification of PCMs	9
1.4.3 Limitation of PCMs	10
1.4.3 Application of PCMs	11
1.5 Thermal conductivity enhancement	13
1.6 Review of literature	15
1.6.1 Analytical investigations	15
1.6.2 Numerical investigations	18
1.6.3 Experimental investigations	27

1.7 Scope of present investigation	39
Chapter 2	
Theoretical investigation on melting and solidification of phase change material inside the thermal energy storage system	43
2.1 General background	43
2.2 Melting and solidification analysis of phase change material inside annular thermal energy storage system	44
2.2.1 Physical model	45
2.2.2 Mathematical formulation	47
2.2.3 Results and discussion	59
2.3 Melting and solidification analysis of phase change material inside rectangular thermal energy storage system involving fins	70
2.3.1 Physical model	70
2.3.2 Mathematical formulation	76
2.3.3 Results and discussion	94
2.4 Concluding remarks	132
Chapter 3	
Unconstrained and constrained melting behavior of phase change material inside the spherical capsule through numerical investigation	135
3.1 General background	135
3.2 Unconstrained melting analysis of phase change material in a spherical capsule	136

3.2.1	Physical model	136
3.2.2	Mathematical formulation and computational procedure	137
3.2.3	Results and discussion	144
3.3	Constrained melting of phase change material in a spherical capsule	154
3.3.1	Physical model	154
3.3.2	Mathematical formulation and computational procedure	155
3.3.3	Results and discussion	161
3.4	Concluding remarks	169
Chapter 4		
	Experimental investigation of phase change materials inside the heat sink for thermal management applications	171
4.1	General background	171
4.2	Experimental preparations	172
4.2.1	Test facility	172
4.2.2	Heat sinks and measurement schemes	175
4.2.3	Preparation of PCM metallic foam composite and nano enhanced phase change material (NePCM)	181
4.2.4	Characterization and thermo-physical properties of PCM, NePCM and TCE	184
4.2.5	Experimental procedure, data reduction and comparison of results	190
4.3	Results and discussion	197

4.3.1	Effect of inclination angle on the performance of phase change material based finned heat sink configurations	198
4.3.2	Effect of metal foam and phase change material composite on the thermal performance of various finned and unfinned heat sink configurations	218
4.3.3	Analysis of thermal performance of nano enhanced phase change material (NePCM) based finned and unfinned heat sink configurations	235
4.4	Concluding remarks	246
Chapter 5		
	Summary and conclusions	249
5.1	Theoretical investigation on melting and solidification of phase change material inside the thermal energy storage system	250
5.1.1	Melting and solidification analysis of phase change material inside annular thermal energy storage system	250
5.1.2	Melting and solidification analysis of phase change material inside rectangular thermal energy storage system involving fins	251
5.2	Unconstrained and constrained melting behavior of phase change material inside the spherical capsule through numerical investigation	253
5.2.1	Unconstrained melting analysis of phase change material in a spherical capsule	254

5.2.2	Constrained melting analysis of phase change material in a spherical capsule	255
5.3	Experimental investigation of phase change materials inside the heat sink for thermal management applications	255
5.3.1	Effect of inclination angle on the performance of phase change material based finned heat sink configurations	256
5.3.2	Effect of metal foam and phase change material composite on the thermal performance of various finned and unfinned heat sink configurations	257
5.3.3	Analysis of thermal performance of nano enhanced phase change material (NePCM) based finned and unfinned heat sink configurations	258
5.4	Recommendations for further investigation	259
	<i>References</i>	261
	Appendix I	285
	Appendix II	289
	List of Publications	293
	Resume	301

LIST OF FIGURES

Fig. 1.1	Different available techniques for thermal energy storage	4
Fig. 1.2	Rise in temperature during the storage of heat in SHS material	5
Fig. 1.3	Thermochemical heat storage cycle	5
Fig. 1.4	Phase transition during the storage of heat in LHS material	6
Fig. 1.5	Stages involved during phase change process	8
Fig. 1.6	Classification of PCM	9
Fig. 1.7	Photograph of 72 pin fin heat sink considered by Baby and Balaji [45]	29
Fig. 1.8	Different heat sink geometry considered by Mahmoud et al. [147]	30
Fig. 1.9	Square cross finned heat sink considered by Leong et al. [150]	33
Fig. 2.1	Schematic of PCM based annular TES system	45
Fig. 2.2(a-e)	Typical phase change curves for melting process for (a) substage-1(a), (b) substage1(b), (c) stage-2, and (d) stage-3	46
Fig. 2.3	Comparison of present prediction with the test data of Duan and Naterer [40] during melting of RPCM with constant heat flux at inner surface and convective heat transfer at outer surface	60
Fig. 2.4	Comparison of present prediction with the test data of Liu et al. [193] during melting of PCM with constant heat flux at inner surface and insulation at outer surface	60
Fig. 2.5	Comparison of present prediction with the test data of Liu et al. [194] during solidification of PCM with insulated inner surface and convective heat transfer at	62

	outer surface	
Fig. 2.6(a-b)	PCM inner surface temperature distribution for different values of heat flux (a) melting and solidification with convection at outer surface of cylinder, (b) melting with insulation at outer surface of cylinder	64
Fig. 2.7(a-b)	PCM inner surface temperature distribution for different values of heat transfer coefficient (a) melting with insulation and convection at outer surface of cylinder, (b) melting and solidification with convection at outer surface of cylinder	64
Fig. 2.8(a-b)	Dimensionless time (t_0/t_m) for melting and heat penetration with radial distance for various PCM with $T_\infty = 18^\circ\text{C}$, $r_1 = 0.002$ m and $h = 5$ W/m ² -K (a) $q'' = 500$ W/m ² , (b) $q'' = 2000$ W/m ²	66
Fig. 2.9(a-b)	Variation of transient interface location with time for various values of (a) q'' , (b) h	67
Fig. 2.10	Variation of melt fraction with time for various values of (a) q'' (b) h	67
Fig. 2.11	Effect of radius ratio (η) on melting of PCM	68
Fig. 2.12	Effect of TCE on melting and solidification of PCM	69
Fig. 2.13	Finite storage system for PCM with fins	70
Fig. 2.14(a-c)	Schematic of different regions in a PCM based two-dimensional storage system with various boundary conditions (a) constant heat flux, (b) constant temperature and (c) convective air environment	71
Fig. 2.15(a-c)	Schematic of different regions in a two-dimensional PCM storage with different boundary wall conditions (a) constant heat flux, (b) constant temperature, and (c) constant convective air environment	75
Fig. 2.16	Energy balance in a differential element of the PCM	78

	storage during melting	
Fig. 2.17	Energy balance in a differential element of the PCM storage during solidification	88
Fig. 2.18	Comparison of current prediction for temperature distribution with the results obtained from two-dimensional numerical and analytical models [87]	96
Fig. 2.19	Comparison of present prediction for interface location with two-dimensional numerical and analytical models [87]	96
Fig. 2.20(a-f)	Comparison of solid-liquid interface locations at different time for (a) $q_w'' = 500 \text{ W/m}^2$, $\sigma = 0.5$, (b) $q_w'' = 500 \text{ W/m}^2$, $\sigma = 1$, (c) $q_w'' = 500 \text{ W/m}^2$, $\sigma = 2$, (d) $q_w'' = 1000 \text{ W/m}^2$, $\sigma = 0.5$, (e) $q_w'' = 1000 \text{ W/m}^2$, $\sigma = 1$, and (f) $q_w'' = 1000 \text{ W/m}^2$, $\sigma = 2$	100
Fig. 2.21(a-b)	(a) Melt fraction variation of PCM, (b) Melting time of PCM for different σ	102
Fig. 2.22	Melting time variation of PCM for various imposed q_w''	102
Fig. 2.23	Comparison of predicted and computed melting time of PCM	103
Fig. 2.24(a-f)	Comparison of solid-liquid interface locations at different time for (a) $T_w = 48^\circ\text{C}$, $\sigma = 0.5$, (b) $T_w = 48^\circ\text{C}$, $\sigma = 1$, (c) $T_w = 48^\circ\text{C}$, $\sigma = 2$, (d) $T_w = 58^\circ\text{C}$, $\sigma = 0.5$, (e) $T_w = 58^\circ\text{C}$, $\sigma = 1$, and (f) $T_w = 58^\circ\text{C}$, $\sigma = 2$	104
Fig. 2.25(a-b)	(a) Melt fraction variation of PCM, (b) Melting time of PCM for different σ	106
Fig. 2.26	Melting time variation of PCM for various imposed T_w	106
Fig. 2.27	Comparison of predicted and computed melting time of PCM	107
Fig. 2.28(a-f)	Comparison of solid-liquid interface locations for $h_w = 55$	108

W/m² at different time for (a) $T_{\infty} = 38^{\circ}\text{C}$, $\sigma = 0.5$, (b) $T_{\infty} = 38^{\circ}\text{C}$, $\sigma = 1$, (c) $T_{\infty} = 38^{\circ}\text{C}$, $\sigma = 2$, (d) $T_{\infty} = 48^{\circ}\text{C}$, $\sigma = 0.5$, (e) $T_{\infty} = 48^{\circ}\text{C}$, $\sigma = 1$, and (f) $T_{\infty} = 48^{\circ}\text{C}$, $\sigma = 2$

Fig. 2.29(a-b)	(a) Melt fraction variation of PCM, (b) Melting time of PCM for different σ	110
Fig. 2.30	Melting time variation of PCM for different h_w and T_{∞}	111
Fig. 2.31	Comparison of predicted and computed melting time of PCM	112
Fig. 2.32(a-c)	Comparison of solid-liquid interface locations obtained by present model with the existing numerical solutions for (a) $\sigma = 2$, $t = 800$ s, constant heat flux boundary condition, (b) $\sigma = 5$, $t = 1085$ s, constant end wall temperature boundary condition, and (c) $\sigma = 2$, $t = 1000$ s, constant convective air environment boundary condition	113
Fig. 2.33(a-e)	Comparison of solid-liquid interface locations obtained by present model with the one dimensional analytical, one dimensional numerical and two dimensional numerical solutions by Lamberg et al. [17] for (a) $\sigma = 0.2$, $t = 724$ s, (b) $\sigma = 5$, $t = 1085$ s, (c) $\sigma = 0.2$, $t = 169$ s, (d) $\sigma = 1$, $t = 4226$ s, and (e) $\sigma = 5$, $t = 1127$ s	117
Fig. 2.34(a-e)	Comparison of fin temperatures obtained by present model with the one-dimensional analytical, one-dimensional numerical and two-dimensional numerical solutions by Lamberg et al. [17] for (a) $\sigma = 0.2$, $t = 724$ s, (b) $\sigma = 5$, $t = 1085$ s, (c) $\sigma = 0.2$, $t = 169$ s, (d) $\sigma = 1$, $t = 4226$ s, and (e) $\sigma = 5$, $t = 1127$ s	118
Fig. 2.35(a-b)	(a) Variation of solid fraction of PCM with time, (b) Solidification time of PCM for different cell aspect ratios and PCMs	120

Fig. 2.36	Variation in total solidification time of PCM for different imposed temperature at the end walls	120
Fig. 2.37	Comparison of computed solidification temperature with those predicted by the proposed correlation	121
Fig. 2.38(a-f)	Comparison of solid-liquid interface locations obtained by present model with the one dimensional analytical and two dimensional numerical solutions by Talati et al. [16] with $q_w'' = -1000 \text{ W/m}^2$ for (a) $\sigma = 0.5$, $t = 400 \text{ s}$, (b) $\sigma = 0.5$, $t = 800 \text{ s}$, (c) $\sigma = 1$, $t = 400 \text{ s}$, (d) $\sigma = 1$, $t = 800 \text{ s}$, (e) $\sigma = 2$, $t = 400 \text{ s}$, and (f) $\sigma = 2$, $t = 800 \text{ s}$	123
Fig. 2.39(a-c)	Comparison of fin temperatures obtained by present model with the one dimensional analytical and two dimensional numerical solutions by Talati et al. [16] with $q_w'' = -1000 \text{ W/m}^2$ for (a) $\sigma = 0.5$, $t = 400 \text{ s}$ and $t = 800 \text{ s}$ (b) $\sigma = 1$, $t = 400 \text{ s}$ and $t = 800 \text{ s}$, and (c) $\sigma = 2$, $t = 400 \text{ s}$ and $t = 800 \text{ s}$	124
Fig. 2.40(a-b)	(a) Variation of solid fraction of PCM with time, (b) Solidification time of PCM for different cell aspect ratios	125
Fig. 2.41	Variation in total solidification time of PCM for different imposed heat flux at the end walls	126
Fig. 2.42	Comparison of computed solidification temperature with those predicted by the proposed correlation	126
Fig. 2.43(a-f)	Comparison of solid-liquid interface locations obtained by present model with the one-dimensional analytical and two-dimensional numerical solutions by Maosaffa et al. [67] with $h = 65 \text{ W/m}^2\text{-K}$ and $T_\infty = 10^0\text{C}$ for (a) $\sigma = 0.5$, $t = 350 \text{ s}$, (b) $\sigma = 0.5$, $t = 700 \text{ s}$, (c) $\sigma = 1$, $t = 500 \text{ s}$, (d) $\sigma = 1$, $t = 1000 \text{ s}$, (e) $\sigma = 2$, $t = 500 \text{ s}$, and (f) $\sigma = 2$, $t = 1000 \text{ s}$	129
Fig. 2.44(a-c)	Comparison of fin temperatures obtained by present	130

model with the one-dimensional analytical and two-dimensional numerical solutions by Mosaffa et al. [67] with $h = 65 \text{ W/m}^2\text{-K}$ and $T_\infty = 10^\circ\text{C}$ for (a) $\sigma = 0.5$, $t = 350 \text{ s}$ and $t = 700 \text{ s}$, (b) $\sigma = 1$, $t = 500 \text{ s}$ and $t = 1000 \text{ s}$, and (c) $\sigma = 2$, $t = 500 \text{ s}$ and $t = 1000 \text{ s}$

Fig. 2.45(a-b)	(a) Variation of solid fraction of PCM with time, (b) Solidification time of PCM for different cell aspect ratios at $h = 65 \text{ W/m}^2\text{-K}$ and $T_\infty = 10^\circ\text{C}$	131
Fig. 2.46	Variation in total solidification time of PCM for different convective air conditions at the end walls	131
Fig. 2.47	Comparison of computed solidification temperature with those predicted by the proposed correlation	132
Fig. 3.1	Schematic diagram of the computational domain	137
Fig. 3.2	The computational mesh	143
Fig. 3.3	Melt fraction for (a) different grid refinements, and (b) different time step values	143
Fig. 3.4(a-d)	Comparison of melt fraction obtained from present computational study for (a) case I, (b) case II, (c) case III, and (d) case V with existing experimental/computational studies	145
Fig. 3.5	Comparison of computational and experimental melting patterns for different cases	147
Fig. 3.6	Comparison of computational and experimental melt fraction for different cases	151
Fig. 3.7	Temperature (left) and streamline (right) contour for different cases	153
Fig. 3.8	Air region contraction history	154
Fig. 3.9	Schematic diagram of the computational domain	155
Fig. 3.10	Computational grid	160
Fig. 3.11(a-b)	Melt fraction rates for (a) different grid refinements, and	160

	(b) different time step values	
Fig. 3.12	Comparison of melt fraction obtained from present computational study with existing experimental/computational studies	162
Fig. 3.13	Comparison of computational and experimental melting pattern for different cases	163
Fig. 3.14	Comparison of computational and experimental melting pattern for different cases	166
Fig. 3.15	Temperature (left) and streamline (right) contour for different cases	168
Fig. 4.1	(a) Schematic of experimental setup, and (b) Actual photograph of experimental setup	173
Fig. 4.2	Photographs of various heat sinks	176
Fig. 4.3	Arrangement of thermocouples in (a) unfinned, (b) one finned, (c) two finned, and (d) three finned heat sinks	177
Fig. 4.4	(a) Isometric, and (b) top views of location of thermocouples on heat sink	178
Fig. 4.5	(a) Schematic, and (b) Photographic view of tracking mechanism with heat sink assembly	180
Fig. 4.6	Microscopic image of metallic foam (10 PPI)	181
Fig. 4.7	Photograph of four finned MF heat sink without PCM	182
Fig. 4.8	Schematic diagram of the preparation of NePCM	182
Fig. 4.9	Metallurgical composition of heat sink and TCE material	184
Fig. 4.10	(a) SEM image of NePCM, (b) TEM image of NePCM at 1 μm , and (c) TEM image of NePCM at 100 nm	185
Fig. 4.11	(a) Latent heat measurement, (b) Specific heat measurement curve of paraffin wax obtained using Differential Scanning Calorimeter	186
Fig. 4.12	Differential scanning calorimeter heating of PCM dispersed with various nanoparticle concentrations of	188

Al₂O₃

Fig. 4.13	Comparison of temperature of heat sink base obtained from present results with the existing results for (a) without PCM, and (b) with PCM based heat sinks	196
Fig. 4.14	Repeatability of readings of the base temperature of PCM based unfinned heat sink at 2.0 kW/m ²	197
Fig. 4.15	Photographs of (a) unfinned (b) one finned, (c) two finned and (d) three finned heat sinks used in the present study	198
Fig. 4.16	Dimensions of (a) one finned, (b) two finned and (c) three finned heat sinks	199
Fig. 4.17	Time histories of base temperature at different inclination angle of 0°, 15°, 30°, 45°, 60°, 75° and 90° for (a) unfinned, (b) one finned, (c) two finned, and (d) three finned PCM based heat sinks	201
Fig. 4.18(a-f)	Time history of temperature of PCM at different horizontal and vertical locations for unfinned PCM based heat sink	202
Fig. 4.19(a-f)	Time history of temperature of PCM at different horizontal and vertical locations for three finned PCM based heat sink	203
Fig. 4.20	Sequential photographs of solid-liquid interface progression at inclination angle of 0°, 45° and 90° for unfinned heat sink	205
Fig. 4.21	Sequential photographs of solid-liquid interface progression at inclination angle of 0°, 45° and 90° for one finned heat sink	206
Fig. 4.22	Sequential photographs of solid-liquid interface progression at different inclination angle of 0°, 45° and 90° for two finned heat sink	207

Fig. 4.23	Sequential photographs of solid-liquid interface progression at different inclination angle of 0°, 45° and 90° for three finned heat sink	208
Fig. 4.24	Operating time at different inclination angle of 0°, 15°, 30°, 45°, 60°, 75°, and 90° for different configuration of PCM based heat sink	212
Fig. 4.25(a-d)	Operating time at different inclination angle of 0°, 45° and 90° at different SPT of 65°, 70°, 75° for (a) unfinned, (b) one finned, (c) two finned and (d) three finned PCM based heat sinks	213
Fig. 4.26(a-d)	Enhancement ratio at different inclination angle of 0°, 45° and 90° and different heat flux of 1.3, 2.0, and 2.7 kW/m ² for (a) unfinned, (b) one finned, (c) two finned and (d) three finned PCM based heat sinks	215
Fig. 4.27	Melting time at different heat flux of 1.3, 2.0, and 2.7 kW/m ² for different configurations of heat sinks filled with PCM	216
Fig. 4.28(a-d)	Melt fraction of PCM at various inclination angles and different time duration for various heat sink configurations such as heat sinks (a) unfinned, (b) one finned, (c) two finned, and (d) Three finned heat sinks	217
Fig. 4.29	Melting time at different inclination angle of 0°, 15°, 30°, 45°, 60°, 75°, and 90° for different configurations of PCM based heat sinks	218
Fig. 4.30	Photographs of various heat sinks used in this investigation	219
Fig. 4.31(a-d)	Dimensions of various plate fin heat sinks: (a) one fin, (b) two fins, (c) three fins, (d) four fins (fin thickness 1.06 mm), and (d) four fins (fin thickness 1.59 mm)	220
Fig. 4.32	Comparison of time-temperature distribution of base	222

	temperature for unfinned heat sink without and with PCM at 2.0 kW/m ²	
Fig. 4.33(a-d)	Time-temperature distribution filled with different at 2.0 kW/m ² for different configuration of heat sinks: (a) unfinned, (b) one finned, (c) two finned, (d) three finned, (d) four finned heat sinks	223
Fig. 4.34(a-e)	Time-temperature distribution at different input heat flux for different heat sinks: (a) unfinned, (b) one finned, (c) two finned, (d) three finned, (e) four finned heat sinks	224
Fig. 4.35(a-c)	Comparison of time-temperature distribution of different configurations of heat sinks at 2.0 kW/m ² for (a) $\psi = 0.50$, (b) $\psi = 0.86$, (c) $\psi = 1.00$	225
Fig. 4.36(a-b)	Time to attain SPT at $q'' = 1.3, 2.0, \text{ and } 2.7 \text{ kW/m}^2$ for $\psi = 0.86$, (a) 65°C, and (b) 70°C	227
Fig. 4.37(a-b)	Time to attain SPT at $q'' = 1.3, 2.0, \text{ and } 2.7 \text{ kW/m}^2$ for different values of ψ in four finned heat sink case, (a) 65°C, and (b) 70°C	228
Fig. 4.38(a-b)	Enhancement ratio at $q'' = 1.3, 2.0, \text{ and } 2.7 \text{ kW/m}^2$ and $\psi = 0.86$ for different SPT (a) 65°C, and (b) 70°C	230
Fig. 4.39	MF-PCM composite enhancement ratio at $q'' = 1.3, 2.0, 2.7 \text{ kW/m}^2$ for four finned MF-PCM at $\psi = 0.86$	231
Fig. 4.40	Thermal conductance of various heat sink configurations for different heat flux values at $\psi = 0.86$	232
Fig. 4.41(a-b)	Time to attain SPT at $q'' = 1.3, 2.0, \text{ and } 2.7 \text{ kW/m}^2$ for different ξ in four finned heat sink case, (a) 65°C, and (b) 70°C	233
Fig. 4.42(a-b)	Enhancement ratio at different heat flux of 1.3, 2.0, and 2.7 kW/m ² for different ξ and SPT of (a) 65°C, and (b) 70°C	234

Fig. 4.43(a-c)	Heat sink base temperature at various nanoparticle concentrations (0%, 2%, 4% and 6%) for different configuration of heat sinks (a) unfinned, (b) one finned, and (c) three finned heat sinks	237
Fig. 4.44(a-d)	Heat sink base temperature at different configuration of heat sinks (unfinned, one finned and three finned heat sinks) for various nanoparticle concentrations (a) 0%, (b) 2%, (c) 4%, and (d) 6%	239
Fig. 4.45	Binary photographs of the melting front propagation of PCM in various configurations of heat sinks (unfinned, one finned and three finned)	240
Fig. 4.46(a-c)	Melt fraction of PCM at various nanoparticle concentration and different time duration for various HS configurations such as heat sinks (a) unfinned, (b) one finned, and (c) three finned heat sinks	242
Fig. 4.47	Complete melting time of PCM at various nanoparticle concentration (0%, 2%, 4% and 6%) and heat sink configurations (unfinned, one finned and three finned)	243
Fig. 4.48(a-c)	Effect of nanoparticle concentration and different heat sink configurations at different set point temperature of (a) 60°C, (b) 65°C, and (c) 70°C	244
Fig. 4.49(a-c)	Enhancement ratio at various nanoparticle concentration and heat sink configurations for different set point temperature of (a) 60°C, (b) 65°C, and (c) 70°C	246

LIST OF TABLES

Table 1.1	Comparisons between various available techniques [11]	3
Table 1.2	Review studies on different applications of PCM	12
Table 1.3	Summary of existing computational studies on unconstrained/constrained melting of PCM	25
Table 1.4	Summary of experimental investigations on inclination of PCM based system	31
Table 1.5	Summary of experimental investigation on finned heat sink with PCM	32
Table 1.6	Summary of experimental investigation on MF-PCM composite	37
Table 1.7	Summary of experimental investigation on NePCM	38
Table 2.1	Temperature distributions obtained in various stages	57
Table 2.2	Thermo-physical properties of paraffin wax	59
Table 2.3	Thermo-physical Properties of various PCMs	65
Table 2.4	Properties of TCE (Aluminum)	68
Table 2.5	Thermo-physical properties of fin and PCM materials	78
Table 2.6	Thermal properties of PCM and fin material [16]	88
Table 2.7	Different parameters of storage system	95
Table 2.8(a)	Comparison of melting time obtained with current model and existing test results [202]	96
Table 2.8(b)	Comparison of temperature distribution obtained with current model, existing numerical and analytical models [87] at $t = 3600$ s	97
Table 2.8(c)	Comparison of solid/liquid interface obtained with current analytical model, existing numerical and analytical models [87] at $t = 3600$ s	98
Table 2.9(a)	Comparison of present analytical and two-dimensional numerical models [16] for constant heat flux boundary condition in different test cases	114

Table 2.9(b)	Comparison of present analytical and two-dimensional numerical models [17] for constant temperature boundary condition in different test cases	114
Table 2.9(c)	Comparison of present analytical model and two-dimensional numerical model [67] for convective air boundary condition in different test cases	115
Table 2.10	Thermal properties of PCMs and fin materials [17]	115
Table 2.11	Dimensions of PCM storage, end wall temperature, and materials used in different test cases	116
Table 2.12	Thermal properties of PCM and fin material [16]	122
Table 2.13	Dimensions of PCM storage unit	122
Table 2.14	Thermal properties of PCM and fin material [67]	127
Table 2.15	Dimensions of PCM storage unit	127
Table 3.1	Thermo-physical properties of PCM	137
Table 3.2	Various cases considered in this study	138
Table 3.3	Thermo-physical properties of PCM	155
Table 3.4	Various cases considered in this study	156
Table 4.1	Thermo-physical properties of paraffin wax, TCE and insulator	174
Table 4.2	Thermocouples location on respective walls	179
Table 4.3	Melting temperature and latent heat variation of NePCMs	188
Table 4.4	Specific heat capacity and thermal conductivity variation of NePCMs	190
Table 4.5	Uncertainty in measurement	193
Table 4.6	Fin dimensions for different configuration of heat sinks	200
Table 4.7	Fin dimensions for different configurations of heat sink	221
Table I.1	Error associated with measurement of various parameters	286

NOMENCLATURE

English symbols

a	Constant in Eq. (2.7)
a ₁	Constant in Eq. (2.52b)
a ₂	Constant in Eq. (2.61a)
A	Area, m ²
A ₁ (t)	Function in Eq. (2.40)
A ₂ (t)	Function in Eq. (2.49)
A ₃ (t)	Function in Eq. (2.75)
A ₄ (t)	Function in Eq. (2.89)
b	Constant in Eq. (2.7)
b ₁	Constant in Eq. (2.52b)
b ₂	Constant in Eq. (2.61a)
B ₁ (t)	Function in Eq. (2.40)
B ₂ (t)	Function in Eq. (2.49)
B ₃ (t)	Function in Eq. (2.75)
B ₄ (t)	Function in Eq. (2.89)
<i>Bi</i>	Biot number, hL_c / k
<i>c</i>	Specific heat at constant pressure, J/kg-K
<i>C</i>	Porosity constant in Eq. (3.15), kg/m ³ -s
C ₂ (t)	Function in Eq. (2.49)
C ₄ (t)	Function in Eq. (2.89)

D_i	Inner diameter of spherical capsule, m
E	Small computational constant in Eq. (3.15 and 3.33)
g	Gravitational acceleration, m^2/s
G	Thermal conductance (Eq. 4.15), J/K
Z	h/k (Eq. 2.62, 2.102), m^{-1}
h	Heat transfer coefficient, W/m^2-K
H	Total enthalpy, J/kg
H_c	Length of cylinder, m
k	Thermal conductivity, $W/m-K$
l_c	Half height of cell, m
l_f	Length of fin, m
L	Latent heat of PCM, J/kg
L_c	Characteristic length (m)
m	Mass, kg
Nu	Nusselt number
P	Pressure, N/m^2
P_o	Power, W
Pr	Prandtl number
q''	Heat flux, W/m^2
Q_{loss}	Heat loss, W
r	Radius, m

r_1	Inner radius of cylinder, m
r_2	Outer radius of cylinder, m
R_i	Inner radius of spherical capsule, m
R_o	Outer radius of spherical capsule, m
$R(t)$	Melt interface location, m
Ra	Rayleigh number
S	Source term in momentum equation in Eq. 3.2 and 3.7
St	Stefan's number, $c\Delta T / L$
t	Time, s
t_0	Thermal penetration time, s
t_m	Time for start of melting, s
t_s	Time for start of solidification, s
t_w	Thickness of shell, m
t'	Time for complete melting, s
t'''	Time for complete solidification, s
$t_{CR_{withTCE}}$	Time to reach critical SPT by PCM based heat sink with TCE, s
$t_{CR_{withoutTCE}}$	Time to reach critical SPT by PCM based heat sink with TCE, s
$t_{CR_{withMF-PCM}}$	Time to reach critical SPT by PCM based heat sink with MF-PCM, s
$t_{CR_{withoutMF-PCM}}$	Time to reach critical SPT by PCM based heat sink without MF-PCM, s

$t_{cr,with\ nanoparticles}$	Time to attain critical SPT by PCM based HS with nanoparticles, s
$t_{cr,without\ nanoparticles}$	Time to attain critical SPT by PCM based HS without nanoparticles (s)
Δt	Time interval, s
T	Temperature, °C
T_i	Initial temperature of PCM, °C
T_m	Melting/solidification temperature of PCM, °C
T_b	Heat sink base temperature, °C
T_{max}	Maximum heat sink base temperature, °C
ΔT	Temperature difference, °C
v_r	Radial velocity component, m/s
v_θ	Polar velocity component, m/s
V_{PCM}	Volume of PCM filled inside heat sink in Eq. (3.12), m ³
V_{HS}	Total volume of heat sink in Eq. 3.12, m ³
V_{TCE}	Volume of TCE in Eq. (3.12), m ³
x	Coordinate, m
$X(t)$	Solid-liquid interface in x direction, m
Δx	Thickness of insulation in Eq. (3.2), m
y	Coordinate, m
$Y(t)$	Solid-liquid interface in y direction, m

Greek symbols

α	Thermal diffusivity, m ² /s
α_q	Phase volume fraction in Eq. 3.1-3.7
β	Thermal expansion coefficient, °C ⁻¹
δ	Half thickness of fin, m
$\varepsilon(t)$	Thermal penetration depth, m
ϕ	MF-PCM composite enhancement ratio in Eq. 4.14
φ	Substitute of $k\Delta T / q''$ in chapter 2.2, m
γ	Radius ratio during melt/solid front (Eq. 2.12a), $\frac{r_2}{R(t)}$
η	Radius ratio of annulus (Eq. 2.10), $\frac{r_1}{r_2}$
λ	Liquid volume fraction in Eq. 3.12 and 3.30
μ	Dynamic viscosity of PCM, kg/m-s
θ	Angle, (°) or rad
ρ	Density of PCM, kg/m ³
σ	Aspect ratio, l_f / l_c
ζ	Volume fraction of TCE, Eq. 4.12b
ν	Kinematic viscosity, m ² /s
ω	Weight fraction of nanoparticles, m_N / m_P
ξ	Enhancement ratio, Eq. 4.13
ψ	Volume fraction of PCM, Eq. 4.12a
Υ	Liquid PCM volume fraction in computational cell, Eq. 3.12, 3.30

∇ Laplace operator in Eq. 3.4 and 3.19

Φ Volume fraction of nanoparticles (Eq. 4.7), $\frac{Wt_N / \rho_N}{(Wt_N / \rho_N) + (Wt_P / \rho_P)}$

Subscripts

f Fin

i, j Components in chapter 3.1 and 3.2

ins Insulation

l Liquid

$liquidus$ Above melting point

m Melting point

N Nanoparticle

P Phase change material

q q^{th} fluid

ref Reference point

s Solid

$solidus$ Before melting point

w Wall

∞ Ambient

Abbreviations

DSC Differential scanning calorimeter

HS Heat Sink

<i>MF</i>	Metallic foam
NePCM	Nano enhanced phase change material
PCM	Phase change material
SPT	Set point temperature
TCE	Thermal conductivity enhancers
TES	Thermal energy storage
Wt	Weight

Chapter 1

Introduction and Literature Survey

1.1 General background

Fastest growth in global population, increase in industrialization and sharp rise in modernization have led to increase in the energy demand. Global demand for energy is expected to rise by nearly 50% between 2018 to 2050 [1]. In general, fossil fuels supply about 80% of total energy consumption [2]; while the unrestricted use of fossil fuels because of rise in population growth and industrialization has led to depletion of fossil fuel reserves and imbalance to the nature [3]. In order to meet the higher energy demand, maintain the ecological balance and reserve the resources for the future generation, it is high time to develop and use sustainable sources of energy. Solar energy is abundant, freely available and one of the most promising alternatives to fossil fuels. In recent years, significant efforts have been made across the globe to harness the solar energy and subsequently reduce the use of fossil fuels that found to affect the environment and global temperature. One of the limitations for widespread usage of solar energy is its intermittent nature and fluctuating intensity [4]. In view of this, suitable thermal energy storage system needs to be developed that can store and utilize energy during requirement.

Rapid growth in industrialization and modernization has necessitated the development of advanced electronic components and gadgets with enhanced multifunctional features, higher computational capabilities, and compact sizes. Large scale integration and miniaturization of electronic components in various devices including laptop, smart phones have led to higher packing density resulting in higher power dissipation. In addition to this, the battery modules of electric vehicles, light emitting diodes (LED), and control systems in missiles result in large amount of heat generation. A delay in effective removal of generated heat may lead to increase the temperature of device. It may be noted that temperature plays a crucial role on the performance and life of electronic

devices. A survey by US air force reports that 55% of the electronic components fail due to rise in temperature [5]. Therefore, it is necessary to incorporate an efficient thermal management system in the electronic devices to maintain the desired temperature of electronic components/devices. This will increase the performance, reliability, and life of the devices. In order to address the above issues, a host of techniques have been adopted by various researchers. Some of the important techniques/methods are summarized below.

1.2 Thermal management techniques

Effective thermal management of electronic components is required to prevent failures that take place due to higher operating temperature and improve long term reliability of electronic components/devices. In general, two different cooling techniques such as active and passive are employed to dissipate heat from the electronic components [6]. Active cooling techniques require external power source to cool electronic devices and improve heat transfer rate. In this technique, desired cooling effect is obtained by circulating the heat transfer fluid at a higher rate. These include circulation of air, liquid on the electronic components and use of thermoelectric coolers (TECs). Passive cooling techniques usually do not have any rotating parts and therefore external power is not required to achieve the required cooling [6]. In this technique, capillary or gravitational buoyancy forces tend to circulate the heat transfer fluid. One can use heat sinks, heat pipes, heat spreader, phase change materials (PCMs) and combination of these methods to achieve the cooling.

Active thermal cooling techniques such as liquid and air cooling techniques are not preferred for certain applications due to various reasons such as large space requirement, higher maintenance, higher power requirement and higher noise level which in turn result in higher operating cost [7-10]. On the contrary, passive thermal management techniques are found to be cost effective and efficient because of various advantages and the comparison between various available techniques is summarized in Table 1.1 [11].

Table 1.1 Comparisons between various available techniques [11]

Parameters	Air	Liquid	Heat pipe	PCM
Ease of use	Easy	Difficult	Moderate	Easy
Integration	Easy	Difficult	Moderate	Easy
Efficiency	Low	High	High	High
Temperature drop	Small	Large	Large	Large
Temperature distribution	Uneven	Even	Moderate	Even
Maintenance	Easy	Difficult	Moderate	Easy

Currently, the combination of heat spreaders and heat sinks are employed for effective heat removal from the electronic components. In such a case, the heat dissipation is limited due to lower value of natural convection inside the closed space. Many a times, the portable devices operate with sharp rise in heat generation for a certain time period followed by rest period/less heat generation phase [12]. In such cases, these power spikes increase the possibility of failure of electronic components. Passive air and liquid cooling techniques may enhance the thermal cycling effect caused due to sharp power spikes. However, phase change material (PCM) based thermal energy storage can absorb the excessive heat generated during spikes and able to dissipate during the rest period. This arrangement can significantly reduce the temperature related failure of electronic components [12].

1.3 Thermal energy storage techniques

Thermal energy storage (TES) systems are found to be the promising candidates to smoothen and manage the temporal variation of energy demands and subsequently act as a thermal management tool. In addition, TES offers various advantages such as reduced size, less cost, improve in the energy

efficiency. The TES systems mainly store energy through the change in the internal energy of a material. In general, TES utilize sensible, latent, and thermochemical energy or combination of these methods for its application. Fig. 1.1 shows different available techniques for TES.

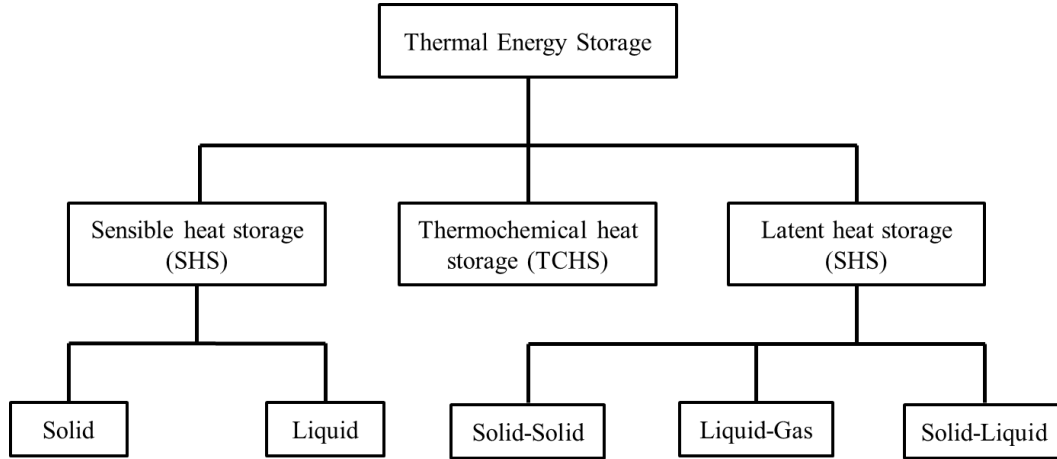


Fig. 1.1 Different available techniques for thermal energy storage

1.3.1 Sensible heat storage

In case of sensible heat storage (SHS) system, the heat is stored/released due to the change in the temperature of a storage material without changing the phase as shown in Fig. 1.2 [13]. The amount of heat storage is found to depend on various parameters such as the mass, specific heat, and change in temperature of materials [14] and is given by [15]:

$$Q = \int_{T_1}^{T_2} mcdT = mc(T_2 - T_1) \quad (1.1)$$

Where Q is the sensible heat stored, m is the mass of storage material, c is the specific heat capacity, and T₁ and T₂ denote the range of operating temperature. It is observed that the use of SHS systems is limited because of the utilization of large quantity of material and subsequently large space requirement.

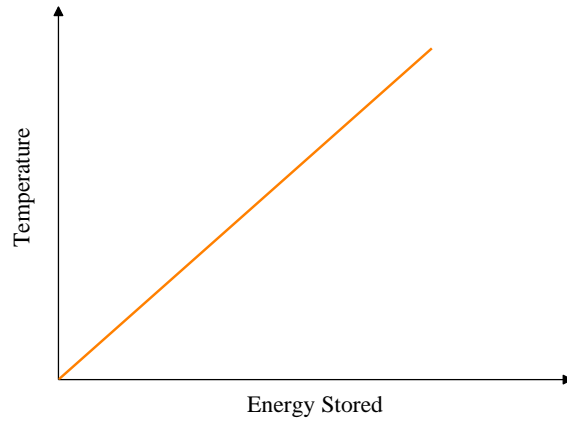


Fig. 1.2 Rise in temperature during the storage of heat in SHS material

1.3.2 Thermochemical heat storage (TCHS)

In case of thermochemical heat storage (TCHS) system, the heat is stored/released during the breaking and reforming of molecular bonds during exothermic and endothermic reaction, which is usually reversible (Fig. 1.3).

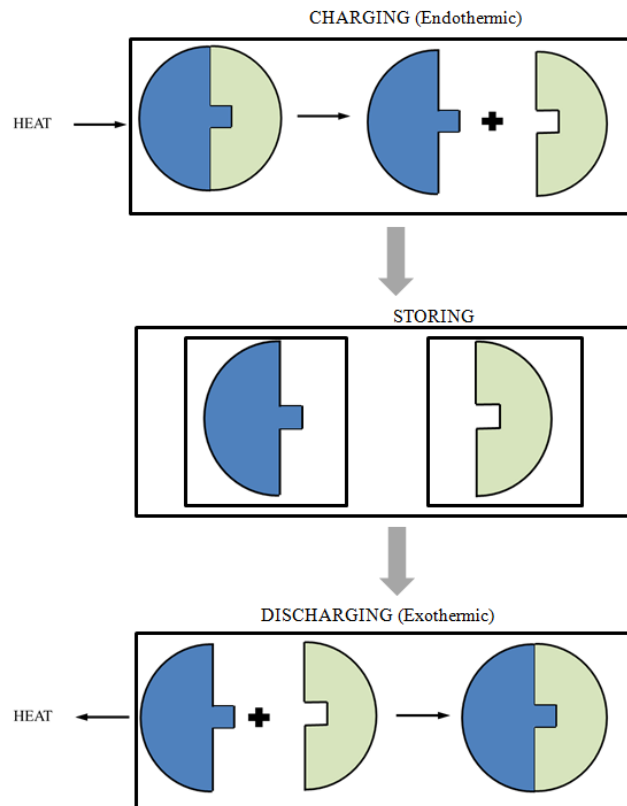


Fig. 1.3 Thermochemical heat storage cycle

The amount of heat storage is found to depend on various parameters namely, the mass, extent of conversion and heat of reaction of material and is given by [15]:

$$Q = ma_r \Delta R \quad (1.2)$$

Where Q , m , a_r and ΔR denote the thermochemical heat storage, the mass of storage material, extent of conversion, and the heat of reaction, respectively. In such a case, usually high temperature is needed in the chemical reaction to break the molecular bonds due to higher binding energy. The use of TCHS systems is limited because of different issues such as higher level of complexity and higher operating cost [6].

1.3.3 Latent heat storage (LHS)

In latent heat storage (LHS) system, heat is stored/released during the phase transition of the storage material, often termed as charging and discharging [15]. Fig. 1.4 shows the phase transition during the storage of heat in LHS material.

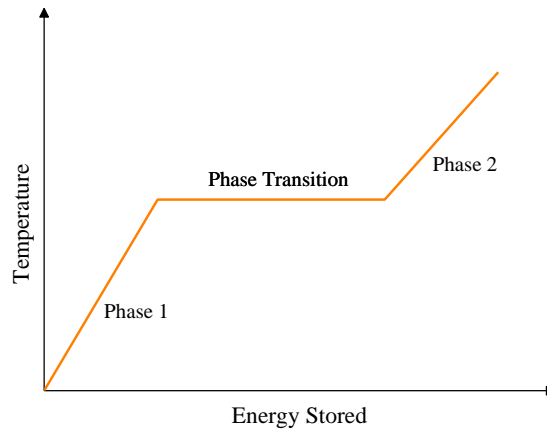


Fig. 1.4 Phase transition during the storage of heat in LHS material

The amount of stored heat energy depends on various parameters such as mass, specific heat, latent heat and temperature change of materials and is given by [14]:

$$Q = \int_{T_1}^{T_m} mcdT + mL + \int_{T_m}^{T_2} mcdT = mc(T_m - T_1) + mL + mc(T_2 - T_m) \quad (1.3)$$

Where Q , m , c , L , T_m denote the sensible heat storage, mass, specific heat capacity, latent heat, and melting temperature, respectively. While, T_1 and T_2 denote the range of the operating temperature.

1.4 Phase change materials

The latent heat storage can be achieved by various material phases such as solid-solid, solid-liquid, liquid-gas, and vice versa. The heat energy is stored in solid-solid LHS materials because of the transition of lattice structure. In case of solid-solid PCM, the amount of latent heat and the change in volume are less compared to solid-liquid LHS materials. It is argued that the liquid-gas phase transition can store higher latent heat compared to solid-solid and solid-liquid LHS material; however these are not commonly employed for LHS application because of the requirement of large volume and high pressure. Therefore, solid-liquid phase change material is a good choice and widely used for various applications.

The LHS involving solid-liquid PCMs is widely used because of its inherent advantages including phase transition at constant temperature and higher energy storage per unit volume [16, 17]. Initially, the supplied heat energy is absorbed in the PCM and the temperature of PCM rises due to gain in sensible heat (Stage-1). During this stage, PCM material acts as SHS material. This process continues till the PCM attains melting temperature. After PCM attains the melting temperature, it absorbs latent heat and the temperature of PCM remains stable during that period (Stage-2). Also, PCM tends to change its phase from solid to liquid. As the time progresses, the complete melting of PCM take place and the temperature of PCM again increases due to sensible heating of molten PCM (Stage-3). On the contrary, during cooling period the PCM tends to solidify as it losses heat energy. Cooling of PCM follows similar pattern but in reverse order. This process can be seen from Fig. 1.5.

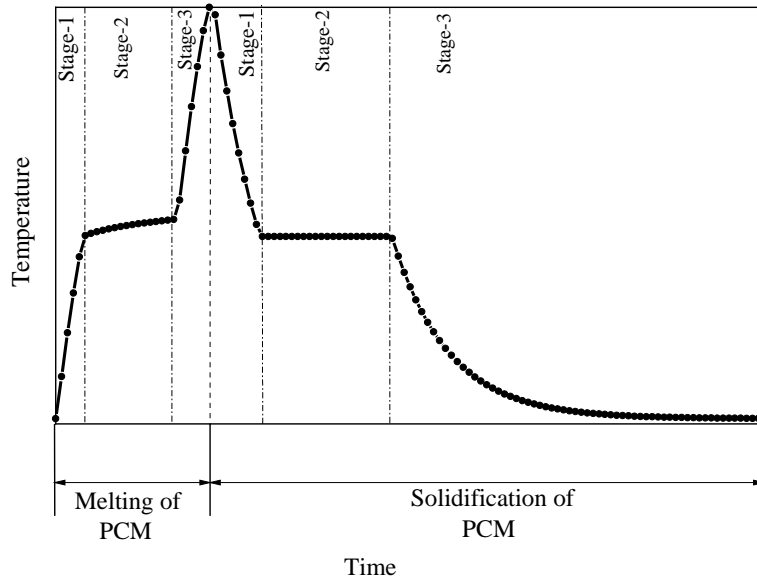


Fig. 1.5 Stages involved during phase change process

1.4.1 Selection of PCM

Selection of PCM plays a crucial role in the design of TES and thermal management system. The following criteria should be used to select PCM for a given application [15, 18, 19].

- Melting point of PCM must be lower than the maximum operating temperature of the component.
- The PCM melting temperature should be in desired working temperature range.
- It should possess high thermal conductivity to achieve higher charging and discharging rates.
- PCM should have high specific heat capacity and enthalpy of fusion on volumetric basis, which can reduce the size of the system.
- PCM should be corrosion resistant, chemically stable, and non-toxic.
- In order to avoid the issues of confinement of PCM, the change in volume during phase change and vapor pressure at operating temperature should be low.
- It should possess little or no subcooling during melting and solidification.

- It should be non-flammable and non-explosive.
- PCM must be recyclable, cost effective and easily available so that it can be used on large scale.

1.4.2 Classification of PCMs

Fig. 1.6 shows the classification of PCMs. Broadly PCMs are classified into three different categories such as organic, inorganic and eutectics.

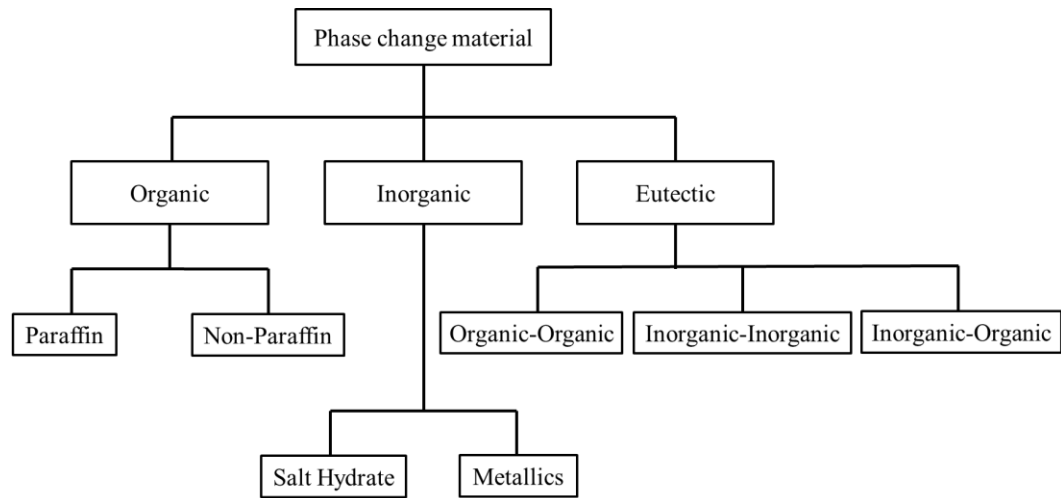


Fig. 1.6 Classification of PCM

The organic PCMs are divided into paraffin (C_nH_{2n+2}) and non-paraffin such as fatty acid ($CH_3(CH_2)_{2n}COOH$) [20]. These PCMs are found to be thermally stable, non-toxic, non-corrosive and possess no or little subcooling [21, 22]. The major limitation of organic PCMs is its lower value of thermal conductivity [20]. The organic PCMs are widely used in thermal management of electronic devices, preservation of medicines/food, and thermal comfort in buildings [23]. The inorganic PCMs are divided into salt hydrates and metallic alloys [15]. The salt hydrates are alloys of salt and water with a general formula $(AB.nH_2O)$. These PCMs exhibit higher value of thermal conductivity compared to organic PCMs, while they possess lower thermal stability values and higher value in supercooling, incongruent melting, corrosion, and phase separation. Metallic alloys usually have higher value of thermal conductivity and specific heat

compared to organic PCMs; while their use is limited because of their higher value in phase change temperature [24]. Also, the metallic alloys increase the weight of the system. In general, inorganic PCMs are used in medium to high temperature energy storage applications such as thermal power plants and process industries. The eutectics are a mixture of different phase change materials (organic/inorganic) that have nearly same melting/solidification temperature [24]. The mixture can be organic-organic, organic-inorganic, and inorganic-inorganic. Further investigation is required to analyze their thermo-physical properties.

Wide varieties of PCMs are available having different melting/solidification temperature range. Various review studies have been made by Sharma et al. [15], Zalba et al. [19], Sharma and Sangara [25], Kensarin and Mahkamov [26] that report the various available PCMs and their thermo-physical properties.

1.4.3 Limitations of PCMs

The criteria for selection of PCM have been discussed in section 1.4.1. It may be noted that a single PCM cannot completely satisfy various selection criteria as discussed in the previous section. Various researchers have made an effort to study the thermo-physical properties and addressed the challenges associated with PCM and are elaborated below.

- *Incongruent melting*: During melting of PCM, the solid and liquid phases undergo phase separation due to their different composition. With the repeated thermal cycles and incongruent melting, the storage efficiency of PCM decreases. This problem occurs during the use of inorganic PCM and their eutectics. Addition of stabilizers, mechanical stirring and encapsulation are some of the options to address this issue.
- *Super cooling*: Cooling of PCM below its melting temperature is termed as super cooling, which occurs due to poor nucleation rate in PCM. Super cooling effect reduces the ability to retrieve the energy from the PCM storage system. This phenomenon is found to be more common in inorganic PCM and can be avoided by adding nucleating agents.

- *Thermal stability:* PCM is assumed to undergo large number of thermal cycles during its lifetime, which decreases the storage efficiency of the PCM based system. Therefore, PCM must be stable during different thermal cycles. Many a times, PCMs are encapsulated to increase the heat transfer area, avoid leakage and increase the thermal stability.
- *Thermal conductivity:* The major challenge for the widespread application of PCM is its lower thermal conductivity. Poor thermal conductivity decreases the heat transfer rate resulting in localized superheating of liquid phase; keeping most of the PCM in solid phase. Therefore, the thermal conductivity of PCM needs to be enhanced which can make it suitable for higher heat load applications and enhance the solidification/melting rates.

In addition to this, various challenges such as corrosion of storage material, toxicity, and flammability of PCM are observed during its application. In general, the organic PCMs are found to be thermally stable, non-toxic, non-corrosive and possess no or little subcooling [21, 22]. Organic PCMs have wide temperature range and can be suitable for thermal management and thermal energy storage applications. However, major limitation of organic PCMs is its lower thermal conductivity [20]. Various thermal conductivity enhancers namely, metallic fins, metallic foams, nanoparticles, expanded graphite and encapsulation are incorporated with PCM to enhance the thermal conductivity of PCM and described in the subsequent section.

1.4.4 Application of PCMs

PCMs are found to be widely used in different applications including thermal management of batteries, electronic devices and photovoltaic panels. In addition, PCM are used in solar space heating and cooling, solar water heating, solar still, solar cooker, and waste heat recovery. Various application of PCM are elaborated below.

- *Solar power plants:* The PCMs (salt hydrates) are used to store solar energy. The salt hydrates possess various advantages such as low cost, high specific heat and compatibility with the temperature range of power plants.

- *Spacecraft*: High latent heat of fusion of PCMs can be utilized in spacecraft application to maintain the temperature of subsystems and electronic components within the desirable limits.
- *Conservation of food products and transport of temperature sensitive materials*: PCMs can be used to maintain the temperature of food products within the desired limit and restrict the defrosting of frozen food. Also, it is used to maintain the temperature of drugs during transportation.
- *Solar cooking*: PCM is a good option to store the solar energy during sunshine hours and can be utilized for cooking in late evening or off sunshine hours.
- *Waste Heat Recovery*: In order to improve the utility of waste heat, PCM based TES systems are used in various systems such as chimneys, air conditioning system, IC engine exhaust systems for long and short terms utilization of stored energy and subsequent use.

Numerous recent review studies are available on different applications of PCMs and listed in Table 1.2.

Table 1.2 Review studies on different applications of PCM

Applications	References
Electronic cooling	Sahoo et al. [6]
Battery thermal management	Malik et al. [11], Kim et al. [27],
Thermal management of PV panels	Islam et al. [28], Waqas et al. [29]
Solar absorption system	Mumtaz et al. [30]
Solar drying	Kant et al. [31]
Solar still	Shukla et al. [32]
Solar water and space heating	Abokersh et al. [33], Kee et al. [34],
Solar thermal plants	Xu et al. [35]
Solar cooker	Panchal et al. [36]
Waster heat recovery	Gutierrez et al. [37]

1.5 Thermal conductivity enhancement

Phase change materials (PCMs) based latent heat thermal energy storage (LHTES) system finds application in various areas such photovoltaic (PV) system and solar water heating. Also, PCM based passive cooling system is useful for thermal management of light emitting diodes (LED), laptop, cellular phones, power electronic equipment [38, 39], battery modules of electric vehicles [40], and control systems in missile [41, 42] and spacecraft [43, 44]. During peak loads PCMs can extract excessive heat from various electronic components and change its phase from solid to liquid with very little temperature fluctuation. This reduces the failure of critical components during their operation and maintains the designed operating temperature of critical components.

However, the dissipation of heat from the components is limited because of the poor conductivity of PCMs. Also, lower value of thermal conductivity of PCM results in slower melting and solidification rates, which leads to the decrease in heat storage efficiency of the system. In order to make PCMs suitable for thermal energy storage and thermal management applications, it is necessary to enhance the thermal conductivity of PCM which will promote the heat conduction. Various thermal conductivity enhancers namely, metallic fins [45-49], metallic foams [50, 51], nanoparticles [52, 53], expanded graphite [54], and encapsulation [55] are incorporated to enhance the thermal conductivity of PCM. The details are elaborated below.

- *Metallic fins*: The incorporation of extended surface (fins) is one of the most simple, effective and reliable technique to enhance heat transfer performance of heat sinks filled with PCM. Fins are usually classified into two categories such as plate and pin fins. Thermal performance of the system is found to depend on various parameters such as fin geometry, fin arrangement, and fin number.
- *Metallic foams*: Apart from fins, high porosity metallic foams (MFs) are considered to be excellent candidates to enhance the heat removal rate.

MFs provide extended surface area, high porosity, lesser weight, stable thermophysical properties and enhance the heat transfer rate due to high thermal conductivity of the webbed ligaments. The MFs possess different porosity values and available in different pore sizes which are usually characterized by pores per inch (PPI).

- *Nanoparticles*: Although, the fins and MFs increase the thermal conductivity of PCM and enhance the thermal performance of PCM based heat sinks, they increase the size and weight of the system [56]. Therefore, efforts have been made to use metallic [57-60] and non-metallic [61] nanoparticles to enhance the thermal conductivity of PCM system, keeping the system light weight. However, agglomeration and sedimentation of high conductivity nanoparticles take place at the base of the heat sink enclosure over long term operation and higher value of nanoparticle concentration.
- *Expanded Graphite*: The expanded graphite possesses excellent thermo-physical properties which makes it suitable candidate to enhance the thermal conductivity of PCM. It possesses higher aspect ratio, high thermal conductivity, lower density and chemical stability.
- *Encapsulation*: Encapsulation of PCM in a container or shell with different shapes can increase the overall heat transfer surface area which in turn increases the thermal performance of the system. These shells possess high thermal conductivity and stable properties. Also, encapsulation eliminates various issues such as leakage, phase separation, and corrosiveness.

Numerous recent studies have been made by different researchers namely, Lin et al. [62], Qureshi et al. [63], Wu et al. [64], Fan and Khodadadi [65], Ibrahim et al. [66] on various thermal enhancement techniques for different applications.

1.6 Review of literature

Wide varieties of studies have been made that reports the heat transfer characteristics of phase change materials (PCMs) during melting/solidification through theoretical and experimental investigations [3-8, 16, 17]. These studies report the thermal performance of various PCM based systems in terms of various parameters such as temperature distribution, melting/solidification time, operating time to attain the set point temperature and melt fraction. In case of passive cooling with PCM based system, the heat removal rate from the components is limited due to poor conductivity of PCMs. Also, lower value of thermal conductivity of PCM results in slow melting and solidification rates and leads to decrease in heat storage efficiency of the system. Most of the studies utilize different thermal conductivity enhancers (TCEs) such as metallic fins, metallic foams, nanoparticles, expanded graphite, and encapsulation with PCM to enhance the performance of PCM based systems for different applications. It is argued that PCM integrated with TCEs promote heat conduction and enhances the heat transfer performance of PCM based systems. In addition, studies have been carried out that consider the effect of various parameters such as geometry, aspect ratio of system, boundary conditions, type of PCMs and TCEs, and set point temperature (SPT) on the thermal performance of heat sink assembly. Some of the important studies relevant to present work are summarized in the following section.

1.6.1 Analytical investigations

The heat transfer behavior during melting/solidification process for the phase change materials (PCMs) is complex in nature because of nonlinear problem and moving solid-liquid interface. The moving solid-liquid problem is commonly termed as moving boundary problem (MBP) [16, 17, 67]. The analytical solution for the one-dimensional MBP is termed as Stefan's problem [68, 69]. The theoretical solution for MBP (Stefan's problem) for one-dimensional domain is reported by various researchers [68-70]. These include perturbation method, quasi-stationary approximation, Megerlin method, Kantorovich method and heat

balance integral method (HBIM). Several theoretical models [38, 71-77] were proposed to obtain the PCM temperature variation and solid-liquid interface movement during melting and solidification of PCM and are summarized in the following section.

Pure PCM

The PCM based cooling systems are widely used due to its isothermal phase transition behavior. This has generated interest to study the melting/solidification behavior of PCM for different geometries with various boundary conditions [38, 72-91]. Lu [38] presented one-dimensional conduction heat transfer model to analyze the melting behavior of PCM slab. The model considered specified heat flux on top layer of PCM, while the bottom layer was exposed to convective air environment. Temperature distribution in the PCM slab was obtained as a function of time and Biot number. Subsequently, the solutions obtained were analyzed to optimize the phase change cooling strategies for high power electronics. Chakraborty and Dutta [72] developed an analytical model for cyclic melting and solidification of PCM. The authors obtained the temperature distribution by employing either semi-infinite or quasi steady state assumptions and the results were compared with the results obtained by Laouadi and Lacroix [73]. Saha and Dutta [75] proposed one-dimensional heat conduction model to analyze the temperature distributions for both melting and solidification inside the PCM slab. In their model specified heat flux was imposed on the bottom layer of the PCM, while the top layer was maintained either insulated or exposed to convective air environment. The effect of various parameters such as applied heat flux, heat transfer coefficient and height of PCM on the temperature distribution were analyzed in their investigation.

Jiji and Gaye [76] proposed a one-dimensional conduction model to analyze the effect of volumetric energy generation on solidification and melting of PCM. The solutions were obtained by considering quasi steady approximation. Kalaiaselvam et al. [77] proposed a one-dimensional quasi-steady conduction model to investigate the effect of volumetric heat generation on melting and

solidification characteristics of PCM inside a cylindrical enclosure. The deviation between experimental and analytical results was found to be 16.11%. In addition to this, the generalized differential quadrature method (GDQM) has been employed to solve the one-dimensional Stefan problem [79]. It is argued that the GDQM method is more accurate compared to integral method for Stefan number less than 0.2. Khatra and Qarnia [80] employed perturbation method to solve the conduction equation during solidification of PCM. In their study, cold water is allowed to flow inside the storage system to ensure the solidification of PCM. Subsequently, the effect of various parameters on thermal performance was investigated in their analysis. Zhang et al. [81] proposed a one-dimensional analytical model to study the solid-liquid interface during melting of PCM inside the semi-infinite and finite PCM storage systems. The conduction equation along with boundary conditions is solved by employing integral approximation method. The authors considered both pure and composite PCM for the analysis. Bansal et al. [82] analyzed the thermal behavior of PCM during charging and discharging in cylindrical configuration by employing Bessel's function. Janghel et al. [83] proposed a one-dimensional semi-analytical model for the finite domain of air-PCM systems to analyze the formation of void during the solidification shrinkage. The authors employed separation of variable method and reported that the effect of void growth due to shrinkage is more significant when density ratio is 1.1.

PCM with fins

In case of PCM based systems, the heat transfer rate of various components are limited due to poor conductivity of PCM. Numerous studies have been made that report different methods to enhance the thermal conductivity of PCMs. These include inclusion of high conductivity metal particles, metal foam and fins in the PCM [84-86]. Fins are widely used to enhance the thermal conductivity of PCMs and heat transfer in latent heat thermal energy storage (LHTES) system. It was argued that melting and solidification rate increases with PCM storage involving fins [87].

Lamberg and Siren [87] proposed an analytical model to analyze the temperature variation and interface position during melting of PCM in a semi-infinite storage system having fins for constant temperature boundary condition. The results exhibited good agreement with the numerical solution obtained using finite element method. The thermal behavior during solidification of PCM in two-dimensional PCM storage system with internal fins is studied by both analytical and numerical techniques for constant heat flux wall condition [16]. The solid-liquid interface position and the temperature variation in the rectangular finned PCM storage system for convective air environment at the boundaries were studied by Mosaffa et al. [67]. The solidification behavior of PCM in finned rectangular thermal energy storage system was studied through both analytical and numerical methods. The authors used constant temperature boundary condition and effective thermophysical properties for the analysis. The effect of various parameters on solidification time of PCM was discussed in the study [89]. Taghilou and Talati [90] proposed a two-dimensional analytical model for solidification of PCM in a rectangular finned container with time dependent temperature boundary condition at the walls. The temperature distribution and location of solid front obtained from analytical model are compared with simulation results obtained using lattice Boltzmann method. Mosaffa et al. [91] proposed an analytical model to estimate the solidification behavior of PCM in a shell and tube configuration. The authors employed separation of variable method and Bessel's function to obtain temperature distribution and position of solid-liquid interface.

1.6.2 Numerical investigations

Various numerical models have been proposed to analyze the heat transfer behavior of PCM during melting/solidification process. Studies utilize different thermal conductivity enhancers such as fins, metal foams, and nanoparticles with PCM. Studies have also been reported to analyze the effect on thermal performance of PCM based systems. Some of the important studies relevant to the present work are summarized in the following sections.

Pure PCM

Voller et al. [92] proposed a numerical model with enthalpy formulation technique to study the convection/diffusion phase change problem valid for either isothermal phase change or over a range of temperature. The moving boundary problem (MBP) are analyzed with the help of enthalpy method due to the exclusion of explicit treatment of phase change interface condition [92]. Zivkovich and Fuji [93] proposed a mathematical model with enthalpy formulation and simulated the transient behavior of PCM filled in a container. Good agreement was obtained between the results and test data. Saman et al. [94] reported the thermal characteristics of TES system in a rectangular container with several PCM layers. They used the enthalpy formulation method based on finite difference scheme and reported the influence of inlet temperature and flow rate of air on melting time and heat transfer rate. Esen [95] reported the numerical solution of cylindrical LHTES with heat pipe system by employing enthalpy method. Bennon et al. [96] numerically proposed a consistent set of continuum equations for the conservation of mass, momentum, and energy for a binary solid-liquid phase change system. Hassab et al. [97] carried out numerical investigation and compared the melting process of wax with and without volumetric expansion. Authors reported that significant difference in the melting time is obtained at low Biot number.

Inclination of PCM based systems

Wang et al. [98] investigated the effect of orientation of portable electronic devices on the thermal performance of heat sink with plate fins through numerical investigation. Five fins of 1 mm thickness were considered in their study. Different angles of inclination such as $\theta = 0^\circ$, 45° , 90° , 135° , and 180° were examined, where $\theta = 0^\circ$ and 180° is horizontal position with PCM at the bottom and top of the heater, respectively. While $\theta = 90^\circ$ is vertical position of the heat sink. The effect of angle of inclination was found to be less significant in their study. Zennouhi et al. [99] conducted numerical investigation to analyze the melting process at different inclination angles ($\theta = 30^\circ$, 60° , and 90°) with respect

to horizontal position ($\theta = 0^\circ$). Investigation has been carried out by maintaining the right wall at constant temperature of 35°C . Melting rate was found to increase with the decrease in angle of inclination from 90° to 0° .

PCM with fins

Several numerical studies have been made that report the heat transfer enhancement of LHTES systems with internal fins [100-102]. Costa et al. [101] numerically analyzed the thermal performance of LHTES system with and without internal fins using enthalpy based method. It was reported that the fins significantly enhance the thermal conductivity of PCMs. Also, the authors reported the melt fraction and energy storage of the PCM during melting/solidification. Lamberg and Siren [101] performed experimental and numerical investigation to analyze the thermal performance of PCM storage without and with fins during melting and solidification. It has been found that the results obtained by employing heat capacity method are more correct compared to enthalpy method. Oliveski et al. [102] performed numerical investigation to analyze the effect of inverted fin on the melting of PCM in a rectangular storage system. It was reported that melting time decreases with decrease in aspect ratio and increase in fin length.

In addition, various studies have been made on geometric optimization of finned heat sinks [48, 103-109]. Saha et al. [104, 105] examined the optimum distribution of fins as TCE inside the heat sink, and reported that 8% volume fraction of TCE provide improved thermal performance compared to other volume fraction of TCE. Various correlations were proposed involving Stefan, Reynolds, Fourier and Nusselt numbers and characteristic length [48]. Pakrouh et al. [106] carried out optimization analysis on pin fin heat sink filled with PCM through numerical investigation. The authors adopted the genetic algorithm (GA) technique [48, 107, 108] for optimization of heat sink configuration. Baby and Balaji performed optimization by employing artificial neural network for plate fin [48] and pin fin [107] heat sinks of different volume fractions. The PCM based heat sink with TCE exhibits better thermal performance compared to PCM based

heat sinks without TCE. The volume fraction of TCE for better performance is found to be 15% and 9% for plate fin [48] and pin fin [107], respectively.

PCM with metallic foams

Lafdi et al. [110] studied effect of various parameters such foam properties (porosity, pore size and pore density), heat sink shape, and orientation on thermal performance. The decrease in porosity and increase in pore size is found to improve the thermal performance. The authors also reported that orientation and shape of heat sink can affect the heat sink performance for steady heat generation. Zhu et al. [111] performed numerical investigation to analyze the thermal performance of MF-PCM composite and reported that high pores per inches (PPI) aluminum foam promotes the heat transfer performance of metallic foam (MF)-PCM composite. Chamkha et al. [112] analyzed heat transfer characteristic of MF-PCM in L shaped heat sink for pulse load condition through numerical investigation. It was reported that MF-PCM enhances the heat sink efficiency during pulse load condition. Also, the heat sink efficiency increases with the rise in the pulse heat load. Similar results were reported by Veismoradi et al. [113] in their numerical investigation that consider MF-PCM for thermal management of Li-ion battery pack. Strong pulse load was found to increase the efficiency of MF-PCM heat sink by seven times.

PCM with nanoparticles

Sahoo et al. [56] performed numerical simulation to study the NePCM based finned heat sinks and compared their thermal performance with pure PCM based finned heat sinks. In their study, copper nanoparticles with 5 and 20 nm diameters are mixed with eicosane to prepare NePCM. Significant reduction in base temperature of heat sink was found with NePCM compared to pure PCM for short time duration during heating period. However, the effect of NePCM on thermal performance is insignificant during cooling period. Farsani et al. [114] analyzed the melting process of heat sink with cavities of square cross section. In their study, constant heat flux is supplied from the center of the cavity. It was reported that the pure PCM performs better compared to NePCM for heat sink with square

cavities. The result obtained with the configuration is found to contradict the reported results obtained for other geometries. Bondareva et al. [115] evaluated the thermal performance of finned heat sink with NePCM and reported that the addition of nanoparticle increases the melting rate of PCM. The optimum volume concentration of nanoparticles was found to be a function of fin height. Bayat et al. [116] analyzed the performance of NePCM based heat sink with four plate fins. The authors used Al_2O_3 and CuO nanoparticles in the investigation. The performance of heat sink is found to improve with the addition of small percentage of nanoparticles. Ghalambaz et al. [117] studied the heat transfer characteristics of differentially heated square enclosure with NePCM. The non-dimensional fusion temperature is found to play a crucial role for the enhancement in thermal performance. Babazadeh et al. [118] carried out numerical simulation to study the heat release rate for heat sink with fins associated with NePCM. The size of nanoparticles significantly affects the heat transfer rate and the optimum diameter was found to be 40 nm by considering the effect of fouling in heat release unit. Faraji et al. [119] analyzed the melting of NePCM in inclined rectangular enclosure. The concentration of nanoparticles in PCM was found to affect the heat transfer performance. The organic PCM was found to be better option to reduce heat sink temperature compared to inorganic PCM.

Encapsulation of PCM

The melting process of PCM in spherical capsules can be classified as unconstrained and constrained melting process. In *constrained* melting process, the solid PCM is retained in a fixed position with the help of fixture mechanism. Here, natural convection is the main driving force for the melting of PCM as heat transfer occurs from bottom of the capsule to unmelted solid PCM [120-123]. Various studies have been reported to analyze the effects of PCM properties, shell material, external temperature condition and container size on the melting rate during constrained melting of PCM [121-125]. On the contrary, in case of *unconstrained* melting, the solid PCM is not fixed and can drift due to density

difference between the solid and liquid PCM inside the capsule. The solid PCM migrates towards bottom as solid is heavier compared to liquid PCM (except water) and the melting at the bottom occurs due to close contact between bottom of capsule and solid PCM [126-128]. Therefore, it is also termed as close contact melting. A number of computational studies have been performed on the unconstrained and constrained melting of PCM in a spherical capsule (Table 1.3).

Unconstrained melting

Assis et al. [55] carried out both experimental and numerical investigation on melting of PCM in a spherical capsule. The melting process was assumed to be axisymmetric and an air region with the orifice at the top of capsule was considered to accommodate the volume expansion during melting of PCM. Volume of fluid (VOF) model was applied to model PCM-air system. The density variation was defined as constant, linearly varying and $\rho_v = \rho_l / [\beta(T - T_l) + 1]$ in the solid, mushy and liquid regions, respectively. Hosseinizadeh et al. [129] adopted similar approach as studied by Assis et al. [55] and reported that close contact melting occurs at the bottom of the capsule, while a thin layer of liquid PCM present between the capsule surface and solid PCM at the bottom reduces the melting rate. Also, the authors proposed the correlation for melt fraction based on Grashof, Fourier and Stefan numbers. Archibold et al. [130, 131] analyzed the melting of high temperature PCM with and without air region on the top of spherical capsule. Unlike previous studies, the capsule was closed from the top. The authors assume axisymmetric melting and considered constant density, constant or varying density and linearly varying density in solid, liquid and mushy region, respectively. They proposed the correlation for melt fraction based on Grashof, Fourier and Stefan numbers for high temperature PCM. Elmozughi et al. [132] carried out numerical study on melting of high temperature PCM in a spherical capsule with hot air or therminol/VP-1 flowing outside the capsule. For the ease of computation, the author considered symmetric melting and Boussinesq approximation for density variation. The VOF approach was used to model PCM-air system. Furthermore, Junior et al. [133] studied melting of medium

temperature PCM for cross flow boundary condition over the spherical capsule. It has been reported that the position of capsule in an array moderately changes the phase change phenomena. Also, effect of Reynold number and external flow temperature has been reported in their investigation. Their study also considered axisymmetric melting with density variation in liquid phase. Boukani et al. [134] investigated the melting of nano-enhanced PCM in an elliptical container involving various aspect ratios. They assumed symmetric melting and Boussinesq approximation with constant heat flux at the outer walls. They reported that aspect ratio 1.0 and 2.0 results in lowest and highest melting rates, respectively.

Constrained melting

Studies have also been made that consider the constrained melting of phase change materials inside the sphere. Tan et al. [122] carried out experimental and numerical investigation of PCM in spherical capsule. In their numerical investigation, authors have assumed axisymmetric melting with constant density in solid and liquid phase. However, Boussinesq approximation was taken for the variation in density within the liquid phase. It has been reported that numerical results agree well with the test data and can anticipate the chaotic flow structure at the bottom of the spherical capsule. Li et al. [124] studied the effect of radii of sphere, thermal conductivity of PCM, capsule material and external surface temperature during constrained melting of PCM. Axisymmetric melting with Boussinesq approximation has been assumed for the numerical investigation. Fan et al. [4] investigated the constrained melting in a spherical capsule with circumferential fins through experimental and numerical investigations. In their numerical investigation, they assumed axisymmetric melting with Boussinesq approximation. Effect of different fin heights has been investigated. Also, correlations have been proposed for melt fraction and Nusselt number in terms of dimensionless fin height. Sattari et al. [125] investigated the effect of capsule geometry and operating condition such as capsule diameter, initial and boundary temperature, and Stefan number on the melting process for similar spherical geometry. Unlike Tan et al. [122], they assumed symmetric melting of PCM.

Tables 1.3 Summary of existing computational studies on unconstrained/constrained melting of PCM

Source	PCM	Geometry	Boundary Condition	Modelling condition	Density variation	Conclusion
Assis et al. [55]	RT27 (Rubitherm GmbH)	Air region with open cavity at the top	Constant temperature	Axisymmetric	Linear density variation in mushy and liquid regions and constant density in solid region	Phase change process depends on geometrical and thermal parameters of the system
Hosseinizadeh et al. [129]	n-Octadecane	Air region with open cavity at the top	Constant temperature	Axisymmetric	Linear density variation in mushy region and constant density in solid/liquid regions	A thin layer of liquid PCM present between the bottom surface of capsule and solid PCM reduces the melting rate of PCM
Archibold et al. [130]	Sodium nitrate	Air region at the top in the closed capsule	Constant temperature	Axisymmetric	Linear density variation in mushy region and constant density in solid/liquid regions	Melting rate increases with increase in Grashof and Stefan numbers
Archibold et al. [131]	Sodium nitrate	No air region and closed capsule at the top	Constant temperature	Axisymmetric	Linear density variation in mushy and liquid regions and constant density in solid region	Melting rate increases with increase in Grashof and Stefan numbers

Elmozughi et al. [132]	Sodium nitrate	Air region at the top in the closed capsule	External heat convection	Symmetric	Boussinesq approximation in mushy region	PCM takes longer time to melt and solidify in the presence of air voids
Junior et al. [133]	Erythritol	Air region at the top in the closed capsule	External heat convection	Symmetric	Linear density variation in mushy region and constant density in solid/liquid regions	Sphere position, Reynold number and temperature difference directly affect the melting rate

1.6.3 Experimental investigation

Various studies have been made to investigate the heat transfer performance of PCM based systems through experimental investigation. Most of these experimental studies utilize different thermal conductivity enhancers such as fins, metal foams, and nanoparticles with PCMs. In addition, studies have been reported that consider the effect of various parameters, such as heat flux values, set point temperature, volume fraction of TCE and PCM on the thermal performance. Studies have also been reported to analyze the effect of inclination on the thermal performance of PCM systems for different applications. Some of the important studies relevant to the present work are summarized in the following sections.

Inclination of PCM based systems

Efforts have been made to evaluate the effect of angle of inclination, volume fraction and type of PCM on the thermal performance of PCM based systems [134-139]. Kandasamy et al. [134] analyzed the effect of power level and orientation on melting and freezing time for cyclic steady state conditions through experimental and numerical investigation. The effect of inclination angle on thermal performance was found to be minimal for transient cooling of electronic devices. Fok et al. [136] studied the effect of thermal performance of finned heat sink for portable electronic devices at constant heat flux condition. The volume fraction of thermal conductivity enhancers (TCE) is found to vary with different heat sink configurations in their analysis. The effect of inclination angle on thermal performance was found to be insignificant in their study. Baby and Balaji [137] studied the effect of orientation of heat sink filled with PCM integrated copper porous matrix on thermal performance. In their study, the orientation angle (θ) is varied from 0° to 210° , where $\theta = 0^\circ$ and $\theta = 90^\circ$ is considered as the horizontal and vertical positions, respectively. Effect of inclination was found to be minimum on the heat transfer performance of heat sink integrated with PCM embedded copper porous matrix. Lu et al. [138] investigated the effect of angle of inclination on the thermal performance of heat sinks filled with PCM for pulsed

heat load condition. The optimum inclination angle (α) was found to vary between 60° and 75° with the horizontal ($\alpha = 0^\circ$). Avci and Yazici [135] conducted experimental study to investigate the effect of angle of inclination (θ) on the thermal performance of the heat sink. It was reported that the change in angle of inclination from horizontal ($\theta = 90^\circ$) to vertical ($\theta = 0^\circ$) position significantly affects thermal performance of PCM based heat sink. While, the inclination angle does not has any effect on thermal performance of heat sink without PCM. Also, studies have been made to examine the effect of number of fins and inclination angle on the base temperature distribution of heat sink assembly. The integrated effect of both the angle of inclination (θ) and number of fin on the thermal performance of PCM based heat sink was studied by Yazici and Avci [139]. The studies were conducted for five different configurations of fin (1, 2, 3, 4, and 5 fins) and were tested for different angles of inclination ($\theta = 0^\circ$ - 90°) with constant heat load of 16 W. The effect of inclination angle was found to be significant for one and three finned heat sink assembly compared to five finned heat sink assembly.

Pal and Joshi [140] conducted numerical and experimental study to investigate the melting behavior of PCM in a vertical enclosure at constant heat flux. The authors reported that convection dominates in the PCM at the early stage of melting operation. However, as the time progresses the influence of free convection decreases. Kamkari et al. [141] studied the melting behavior of lauric acid in the rectangular enclosure at different angle of inclination (θ). Constant temperature condition is maintained at one wall of the enclosure, while the other walls are kept insulated. The angle of inclination at the horizontal and vertical position is taken as 0° and 90° , respectively. The melting rate was found to increase with the decrease in the angle of inclination from vertical ($\theta = 90^\circ$). This may be due to the formation of chaotic flow structure and increase in convection current. Shokouhmand and Kamkari [142] analyzed the melting of lauric acid in a vertical rectangular enclosure. Initially, the heat conduction was found to play a dominant role succeeded by natural convection at the later stage. The strength of free convection decreases with the increase in temperature of liquid PCM.

Kamkari and Groulx [143] investigated the effect of inclination angle on the melting process of PCM inside the rectangular enclosure with plate fins. The melting rate was found to enhance with the increase in angle of inclination from $\theta = 90^\circ$ (vertical) to $\theta = 0^\circ$ (horizontal). In another study, Kamkari and Shokouhmand [144] analyzed the effect of inclusion of adding partial fins on the heated surface. The increase in fin number leads to decreases the melting time significantly. Partial fins were found to be more advantageous in the initial melting operation. Both the studies by Kamkari and Groulx [143] and Kamkari and Shokouhmand [144] were performed by maintaining one wall at constant temperature by using water bath. Experimental studies that consider the effect of inclination of PCM based thermal systems is summarized in Table 1.4.

PCM with fins

Numerous experimental studies have been made that consider the extended fins as the TCE in PCM based heat sinks [145-150]. Baby and Balaji [45] performed experiments to study the thermal performance of PCM based heat sink with no fin, 3 plate fins and 72 pin fins. The photographic view of heat sink with 72 pin fins is shown in Fig. 1.7. Tests were conducted at various power input values (2 to 7 W). The authors reported that the value of maximum enhancement in operating time is found to be 18 for PCM based finned heat sink at higher input heat flux values.



Fig. 1.7 Photograph of 72 pin fin heat sink considered by Baby and Balaji [45]

Also, tests have been made to analyze the thermal performance of heat sinks with pin fins (33, 72, 120) and maximum enhancement in thermal performance

was obtained for heat sink with 72 pin fins [145]. It was argued that there must be critical fin number above which the increase in fin numbers leads to decrease in heat transfer performance of heat sink. Hosseinizadeh et al. [146] reported that compared to thickness, the height and number of fins significantly improve the performance of heat sink. Mahmoud et al. [147] carried out experimental investigation on cross and parallel finned heat sinks with honey-comb matrix for six different PCMs (Fig. 1.8). They reported that honey-comb structure is more advantageous compared to finned heat sink assembly manufactured by machining processes.

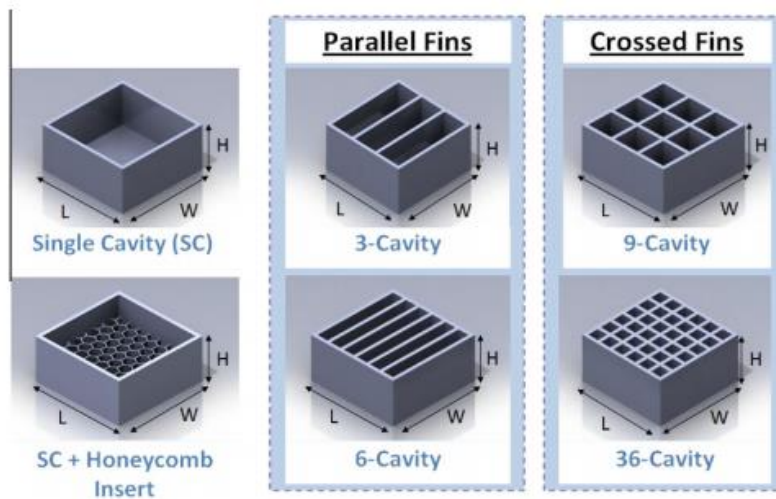


Fig. 1.8 Different heat sink geometry considered by Mahmoud et al. [147]

Ali and Arshad [148] experimentally investigated different configurations of heat sinks such as no fin, and circular pin fins with varying thickness (2-4 mm) for a fixed volume fraction (9%) of TCE. It was reported that heat sink with 3 mm thickness provides maximum enhancement ratio, higher thermal conductance and best thermal performance. The effect of fin thickness (1, 2 and 3 mm) and PCM volume fraction (0, 0.33, 0.66 and 1) corresponding to constant 9% volume fraction of TCE was experimentally studied by Arshad et al. [149]. The authors reported that pin fin with 2 mm thickness and PCM volume fraction of 1 result in maximum operating time.

Table 1.4 Summary of experimental investigations on inclination of PCM based system

Source	Boundary condition	PCM (m.p. in °C)	Heat flux/ Temperature	Dimensions of the PCM container (mm ³)	Inclination angle	Configurations
Baby and Balaji [136]	Constant heat flux	N-Eicosane (36.5)	1.984 to 3.968 kW/m ²	80×62×25	0, 25, 45, 60, 75, 90, 110, 130, 150, 180 and 210°	No fins with metal foam and PCM composite
Lu et al. [137]	Constant heat flux	1-hexadecanol (49)	12.5, 25 kW/m ²	80×80×30	0°, 15°, 30°, 45°, 60°, 75°, and 90°	No fin heat sink
Avci and Yazici [138]	Constant heat flux	N-Eicosane (35-37)	3.33 kW/m ²	100×48×34	0°, 15°, 30°, 45°, 60°, 75°, and 90°	No fin heat sink
Kamkari et al. [141]	Constant temperature	Lauric acid (43.5-48.2)	55, 60, 70°C	120×120×50	0°, 45°, 90°	No fins
Kamkari and Shokouhmand [144]	Constant temperature	Lauric acid (43.5-48.2)	55, 60, 70°C	120×120×50	0°, 45°, 90°	No fin, one fin and three fin (partial fins)

Table 1.5 Summary of experimental investigation on finned heat sink with PCM

Source	PCM type (M.P. in °C)	Heat flux (kW/m ²)	Dimensions (mm ³)	Configurations	Observations
Baby and Balaji [45]	n-Eicosane (36.5)	0.794 to 2.77	80×62×25	0, 3 plate, 72 pin fins	Improved operational performance with PCM based heat sink
Baby and Balaji [145]	n-Eicosane (36.5) Paraffin wax (53-57)	1.587 to 3.968	80×62×25	33, 72 and 120 pin fins	Heat sink with pin fins is superior compared to heat sink without fins
Mahmoud et al. [147]	Paraffin wax (42)	1.2, 1.6 and 2	50×50×25	Single cavity, parallel fin and cross fin, Honeycomb inserts	Honeycomb insert can replace machined fin structures
Ali and Arshad [148]	n-Eicosane (36.5)	0.8 to 2.8	114×114×25	0, 2, 3 and 4 mm fins	Improved result with 3 mm pin fin
Arshad et al. [149]	Paraffin wax (56-58)	1.58 to 3.174	114×114×25	0, 2 and 3 mm fins	PCM amount and number of fins are major effectiveness criteria
Leong et al. [150]	Paraffin wax (54.8), 1-hexadecanol (50.6)	0.81	110×110×26	0, 9, 16 cross-fins	16 cross fins heat sinks filled with paraffin wax is more effective compared to heat sink filled with 1-hexadecanol

Leong et al. [150] analyzed the thermal performance of different cross fin heat sinks such as no fin, 9 square cross fins, and 16 square cross fins filled with different PCM volume fraction through experimental investigation (Fig. 1.9). The authors used 1-hexadecanol and paraffin wax in their study. Paraffin wax based heat sink involving 16 square cross fins exhibit better heat transfer performance compared to heat sink with other configurations involving 1-hexadecanol. Table 1.5 summarizes experimental studies reported by different researchers on PCM based finned heat sink.



Fig. 1.9 Square cross finned heat sink considered by Leong et al. [150]

Various studies have been reported on PCM based thermal energy storage system with fins. Shell and tube heat exchanger with PCM on the shell side and heat transfer fluid (HTF) flowing inside the tube was studied by Lacroix [86]. It was reported that the melting and solidification rate increases with the incorporation of fins inside TES system [86]. Velraj et al. [151] reported that adding internal longitudinal fins in vertical shell type heat exchanger with paraffin wax as PCM reduces solidification time. The solidification time was found to vary inversely with the number of fins. Also, the authors reported that v shape fins give improved heat transfer performance [151]. Liu and Groulx [152] compared the straight and angled fin configuration for dodecanoic acid as PCM in their experimental study. During charging process, melting time of PCM is relatively lower for angled fin configuration compared to straight fin configuration for low inlet temperature (50°C) of HTF. While, there is negligible difference in melting time of angled and straight fin configurations for high temperature (60°C) of HTF. Also, no significant difference is obtained in solidification time for straight and

angled fin configurations [152]. This may be due to conduction dominant heat transfer during solidification of PCM. Rahimi et al. [153] experimentally investigated melting and solidification process of RT35 using finned tube heat exchanger and compared it with heat exchanger without fins. The inlet water temperature does not influence significantly on the melting time for the heat exchanger with fins. Also, the flow rate is found to effect significantly on solidification time for heat exchanger without fins [153].

PCM with metallic foams

Apart from fins, high porosity metallic foams (MFs) are considered to be excellent candidates to enhance the heat removal rate. Wide varieties of experimental studies were performed to investigate the heat transfer characteristics of PCM based MF heat sink [154-159]. These studies use aluminum [110, 154] and copper foams [156, 157, 160] in their experimental investigations. It was argued that the melting and solidification time decreases with the addition of MFs in PCM based heat sink systems. Also, numerous studies have been made that exhibit the enhancement in thermal performance of the heat sink with MF-PCM composite [159-160].

Gharbi et al. [155] analyzed different configurations of heat sink such as graphite, silicon matrix and fins. Graphite matrix provides improved thermal control, while longer fin with appropriate pitch leads to higher operating time. Rehman and Ali [156] analyzed the effect of inclusion of copper foam (95% and 97% porosities) and iron-nickel foam (95% porosity) in PCM on thermal performance of PCM based heat sink through experimental investigation. Compared to iron-nickel foam, copper foam is found to be more beneficial in the reduction in the base temperature of heat sink. It was reported that copper foam with 95% porosity involving 0.8% volume fraction of PCM provides best performance for thermal management applications. Studies were also carried out to analyze the effect of pulse and variable heat load on MF-PCM composite. Jackson and Fisher [157] reported that size of pores of the MF significantly affects heat transfer for rapid pulse load. The thermal conductivity of paraffin-MF

composite was found to be 15 times greater compared to pure paraffin [158]. Rehman and Ali [159] conducted tests to analyze the performance of MF-PCM at variable heat load with RT-54HC as the PCM and copper and nickel as foam materials. It was reported that the reduction in base temperature (T_b) is 26% higher in case of copper foam compared to nickel foam at PCM volume fraction of 0.8.

Zhang et al. [160] reported that more uniformity in temperature can be obtained for paraffin and copper foam composite compared to pure paraffin. The authors also reported the enhancement in thermal performance of copper foam and paraffin composite. Wang et al. [161] tests to investigate the thermal performance of the paraffin and porous MF sintered felt (PMFSF) composite PCM. The authors reported that PMFSF embedded with PCM provides higher thermal performance compared to pure PCM and MF-PCM. Zheng et al. [162] reported that complete melting time of PCM inside the MF is 20.5% higher compared to pure PCM. However, the melting rate depends on the heating position and therefore, the effect of free convection inside the PCM must be considered. Fan and Jin [163] performed experiments with paraffin based open cell MF and visualized the local thermal non-equilibrium effect at pore scale. It is argued that the local thermal non-equilibrium effect increases from 0 to 10°C with the progression of melting. Local thermal non-equilibrium effect and thermal response characteristics are also analyzed by Yao et al. [167] in their visualization study of melting of pure PCM and MF-PCM. It was reported that incorporating MF with PCM enhances the melting rate of PCM by two times. In another study, Yao and Wu [168] carried out experiments to study the effect of density and MF porosity on the thermal transport through MF-PCM. Further, it was reported that lower porosity and lower density of MF increases the thermal diffusion process and leads to enhanced temperature uniformity of MF-PCM. Table 1.6 summarizes various experimental studies on MF-PCM based composite reported by numerous researchers.

PCM with nanoparticles

Efforts have also been made to use metallic [166-168] and non-metallic [169] nanoparticles to enhance the thermal conductivity of PCM system. Various studies have been reported that address the thermal performance of nano enhanced phase change materials (NePCM). These studies focus different aspects such as preparation, characterization, thermophysical properties and applications of NePCM [169-175]. Different studies [170, 171] report the suitability of NePCM for electronic cooling and thermal energy storage applications. However, it is very challenging to estimate the optimum nanoparticle concentration in NePCM to obtain the best performance while optimizing the thermal conductivity and latent heat of PCM.

Wide varieties of studies have been made to analyze the heat transfer behavior of nano enhanced phase change material (NePCM) [176-190] and summarized in Table 1.7. Alimohammadi et al. [178] experimentally investigated different configurations of heat sinks such as heat sink (HS) without PCM, heat sink with PCM and heat sink with NePCM in both forced and free convection conditions. The authors used $Mn(NO_3)_2$ and Fe_3O_4 as PCM and nanoparticles, respectively. Significant reduction in heat sink temperature is observed with PCM embedded with heat sink. Tariq et al. [180] considered various mass fractions (0.002, 0.005 and 0.008%) of graphite nanoparticles (GNPs) with RT-44HC and RT-64HC for the thermal management of electronic devices. The RT-44HC/GNPs and RT-64HC/GNPs were found to be suitable for lower and higher heat loads, respectively. Studies were also conducted on use of NePCM in heat pipes and PV panels. Krishna et al. [187] analyzed water, tricosane (pure PCM) and Al_2O_3 impregnated with tricosane (NePCM) in the heat pipe for electronic cooling applications. The authors investigated the effect of PCM filling ratio, power input and fan speed on the cooling of electronic modules. The NePCM based heat pipe was found to save 53% fan power compared to conventional heat pipe.

Table 1.6 Summary of experimental investigation on MF-PCM composite

Source	PCM type (M.P. in °C)	Heat flux /Temperature	Dimensions (mm ³)	Configurations	Observations
Rehman et al. [159]	RT-54HC paraffin (52–54)	0.8, 1.6, 2.4 kW/m ²	100×100×25	No fin with MF	Lesser base temperature was obtained with copper foam based heat sink compared to nickel foam based heat sink
Zheng et al. [162]	Paraffin (50-58)	1.15 kW/m ²	100×100×30	No fin with MF	Uniformity in distribution of temperature distribution of the PCM using MF-PCM
Fan and Jin [163]	Paraffin wax (52-54)	71°C	26×14×10	No fin with MF	The local thermal non-equilibrium between a copper ligament and PCM increases as melting proceeds
Zhang et al. [160]	Paraffin (54.43-64.11)	6.208 kW/m ²	100×100×10	No fin with MF	Better heat transfer performance using MF-PCM

Table 1.7 Summary of experimental investigation on NePCM

Source	PCM type (M.P. in °C)	Nanoparticles (mass fraction)	Dimensions (mm ² /mm ³)	Configurations	Observation
Sharma et al. [177]	RT42 Rubitherm (38-43)	CuO (0.5 wt%)	36×35×35	Unfinned and 20 micro- finned	Higher reduction in base temperature of 10.7°C and 12.5°C with PCM and NePCM based microfinned HS than unfinned HS
Alimoha- mmadi et al. [178]	Mn(NO ₃) ₂ (37)	Fe ₃ O ₄ (1 wt%)	75×75×40	14 plate fins	Greater reduction in temperature with PCM and NePCM was found for heat sink with fins compared to HS without fins in both forced and free convection
Joseph and Sajith [179]	Paraffin (59.6)	Graphene (0.05 to 0.5 wt%)	42×42×32	4 plate finned	Higher energy saving for HS with PCM-GR composite than HS with and without PCM.
Tariq et al. [180]	RT-44HC (41-44) and RT-64HC (63-65)	Graphene nanoparticles (0.002 to 0.008 wt%)	102×102×25	Unfinned	Maximum 23% base temperature reduction is obtained with 0.008 wt% of RT- 44HC/GNPs.
Bahiraee et al. [190]	Paraffin wax (60)	CNF, GNP, and Graphite (2.5 to 10 wt%)	D _i = 10, D _o = 50	Annulus without fins	NePCM leads to lesser temperature control than pure PCM.

Kazemi et al. [189] analyzed the effect of varied mass fraction (0.2% and 0.5%) of MWCNT nanoparticles on the thermal performance of PCM for building applications with paraffin wax as PCM. The latent heat of fusion and thermal conductivity were found to decrease and increase, respectively with the addition of nanoparticles in PCM. Bahiraei et al. [190] embedded carbon nanofiber (CNF), graphite nanoplatelets (GNP), and graphite nanopowder in PCM to analyze the thermal performance. The PCM embedded with graphite nanopowder was found to exhibit higher thermal performance. Arshad et al. [191] reported the preparation of various mono and hybrid NePCMs. The hybrid NePCMs were prepared by mixing various nanoparticles such as graphene nanoplatelets (GNPs), multiwall carbon nanotubes (MWCNTs), aluminum oxide (Al_2O_3) and copper oxide (CuO) in PCM. The NePCM with 75% GNPs and 25% MWCNTs exhibit the maximum enhancement in the thermal conductivity.

1.7 Scope of present investigation

The present literature review reports the heat transfer performance of various PCM based system through theoretical and experimental investigations. These include the analytical and numerical investigation on pure PCM and PCM with TCEs for different geometries and boundary conditions. The solutions are obtained by employing various analytical techniques and numerical models. In addition, a host of tests have been conducted to analyze the thermal performance of PCM based heat sink system with different TCEs such as fins, metallic foams and nanoparticles. Efforts have been made to analyze the effect of various parameters such as heat flux values, volume fraction of PCM and TCEs, set point temperature and inclination angle on the heat transfer rate. Nevertheless, various issues pertaining to melting and solidification of PCM for thermal storage and thermal management applications need further investigations. These are detailed below:

- a) Most of the analytical models for cylindrical geometry consider the phase change material initially at melting/solidification temperature. Therefore,

there is a need to develop theoretical models during melting and solidification of PCM in cylindrical geometry considering various temporal regimes; namely, completely solid, partially molten and completely molten.

- b) Theoretical model to predict the melting and solidification of PCM in a finite TES with internal fins are limited in literature. Therefore, there is a need to develop theoretical models during melting and solidification of PCM involving different important parameters.
- c) Most of the studies consider one-dimensional approximation and neglect the effect of convection in PCM during melting. Moreover, numerous studies consider the constant temperature boundary condition. Therefore, it is needed to develop the theoretical model for melting process of PCM in a finite TES considering different boundary conditions.
- d) Efforts should be made to study the effect of boundary conditions and aspect ratio (σ) of thermal energy storage system on the temperature variation and interface location.
- e) Numerous studies have been made to analyze the unconstrained and constrained melting of PCM in a sphere through numerical investigation. The effect of the axisymmetric/symmetric modeling, linear density variation in mushy and liquid regions, linear density variation in mushy region but constant density in liquid and solid regions, Boussinesq approximation in mushy region and constant density in liquid and solid regions needs to be investigated in systematic manner.
- f) Various experimental studies report the thermal performance of PCM based heat sink with different thermal conductivity enhancers such as fins, metal foams and nanoparticles. Efforts should be made to study the thermal performance of PCM based heat sink with combination of different TCEs such as fins and MF, and fins and nanoparticles through experimental investigation.
- g) Limited experimental studies are available that report the effect of angle of inclination on the thermal performance of heat sinks filled with PCM. In

addition, the combined effects of fin number, inclination angle, and heat flux values on the thermal performance must be investigated for thermal management applications.

- h) Visual observation to analyze solid-liquid interface position and melt fraction through photographic observation needs to be studied to analyze the melting process.

The present study is aimed to obviate some of the issues highlighted above. The objective of the present thesis is to analyze the heat transfer performance of different PCM based systems for thermal storage and thermal management applications. Here, theoretical models have been proposed to analyze melting and solidification of PCM in annular and rectangular geometries. A variety of boundary conditions involving constant heat flux, adiabatic condition and convective conditions are used for the analysis. Efforts have been made to propose correlations to predict solidification and melting time as a function of aspect ratio and end wall boundary conditions for all the cases. Also, the unconstrained and constrained melting behavior of PCM in the spherical capsule is analyzed through computational fluid dynamics (CFD) numerical technique. Further, tests have been carried out to investigate the effect of various parameters such as fin number, inclination angle and heat flux values on the thermal performance of heat sinks through experimental investigation. The solid-liquid interface position and the melt fraction are analyzed for different angle of inclination and heat sink configurations through photographic observation. In addition, tests are performed to study the thermal performance of PCM based heat sinks with the combination of different TCEs such as fins, MF, nanoparticles and combination of these TCEs.

The organization of the thesis is as follows:

Chapter 1: This chapter introduces the phase change materials, their classification and applications. A brief review of the literature on various theoretical and experimental investigations of PCMs for thermal storage and thermal management applications are reported. The use of various thermal conductivity

enhancers to augment the thermal conductivity of PCM based systems is discussed. Finally, the scope of the present investigation is highlighted.

Chapter 2: This chapter reports the analytical models to predict the temperature distribution and position of solid-liquid interface in annular and rectangular geometries during melting and solidification of PCM. Host of boundary conditions involving constant heat flux, adiabatic condition and convective conditions are used for the analysis. Based on the analysis, closed form expressions are obtained for temperature distribution. Results obtained from the analytical model are validated with the existing test data.

Chapter 3: Here, numerical investigations are performed to analyze unconstrained and constrained melting of PCM in spherical capsule. Efforts have been made to investigate the effect of various modeling parameters on melt fraction and temperature distribution of PCM.

Chapter 4: In this chapter, tests are performed to investigate the thermal performance of different heat sink configurations. Combined effects of fin number, inclination angle and heat flux values on the thermal performance of PCM based heats sinks are analyzed. In addition, the effect of various TCEs such as fins, metallic foam, and nanoparticles and their combined effect on heat transfer performance of heat sinks is investigated. Various parameters such as PCM and TCE volume fractions, heat flux values, set point temperatures on the enhancement in operating time have been studied for thermal management of electronic devices.

Chapter 5: Conclusions obtained from the present theoretical, and experimental investigations are presented in this chapter. Scope for further investigation is also discussed.

Chapter 2

Theoretical investigation on melting and solidification of phase change material inside the thermal energy storage system

2.1 General background

Recently, efforts have been made to harness the solar energy which can reduce the use of fossil fuels and mitigate the imbalance of the nature. The limitation of solar energy is its intermittent nature and fluctuating intensity. Therefore, different designs of thermal energy storage (TES) systems with phase change material (PCM) have been developed to store energy. This has motivated various researchers to analyze the thermal performance of TES systems. Numerous analytical studies have been performed to analyze the melting/solidification process of PCMs inside cylindrical and rectangular storage systems. Most of the models, for cylindrical TES, consider the PCM initially at melting/solidification temperature. In real practice, PCM will be either at lower temperature or at higher temperature compared to melting and solidification temperature, respectively. Therefore, there is a need to develop theoretical models during melting and solidification of PCM in cylindrical geometry considering various temporal regimes. Also, the PCMs usually possess lower value of thermal conductivity, which alters the thermal performance. In view of this, various thermal conductivity enhancers including fins are employed to enhance the thermal performance. Therefore, it is necessary to analyze the thermal performance of finned TES for different configurations with various thermal boundary conditions.

Most of the analytical studies employ separation of variable method (SV) to analyze the melting and solidification of PCM. These techniques compute the solution by truncating the series of complex function, which may lead to errors in the solution. Heat balance integral method (HBIM) is one of many analytical methods used to solve conduction problems. HBIM has been used to solve Stefan

problems due to its simplicity, short computation time while providing the solutions with reasonable accuracy. In this study, HBIM has been used to solve the conduction equation with the associated boundary conditions.

Here, an effort has been made to analyze melting and solidification of phase change material (PCM) in an annulus for variety of boundary conditions such as constant heat flux, adiabatic and convective conditions. The solution for temperature distribution for each temporal regime is obtained either by employing variational formulation or using a method of quasi-steady state. Closed form expressions have been obtained for the temperature distribution for all the cases. Also, an effort has been made to obtain the behavior of PCM during melting and solidification processes in two-dimensional rectangular TES involving horizontal internal fins with various end wall boundary conditions, namely, constant heat flux, end wall temperature and convective air environment. HBIM is employed to obtain the solution. The study predicts the temperature variation in PCM, location of solid-liquid interface, melting and solidification time. Correlations have been proposed to predict melting and solidification time for all the cases.

2.2 Melting and solidification analysis of phase change material inside annular thermal energy storage system

In this work, a one-dimensional conduction heat transfer model has been proposed to study the melting and solidification of phase change material (PCM) inside an annulus. The entire problem is divided into two main sub-processes, namely, melting and solidification. Subsequently, each sub-process is analyzed for various temporal regimes. The temporal regimes include completely solid, partially molten and completely molten for melting sub-process and in reverse order for solidification sub-process. Later on, the solution for temperature distribution for each temporal regime is obtained either by employing variational formulation or using a method of quasi-steady approximation.

2.2.1 Physical model

Fig. 2.1 depicts the schematic diagram of thermal storage unit considered in this analysis. It consists of a cylindrical container with a centrally located electric heater and PCM surrounding to the electric heater. Initially, the heat generated by the heater is absorbed by the PCM and the temperature of PCM increases till the melting point of PCM is reached. After the PCM attains the melting temperature, it absorbs latent heat and the temperature of PCM remains stable during that period. As the time progresses, the complete melting of PCM take place and the temperature of PCM again increases due to sensible heating of molten PCM. On the contrary, PCM solidified during the cooling period as it losses heat.

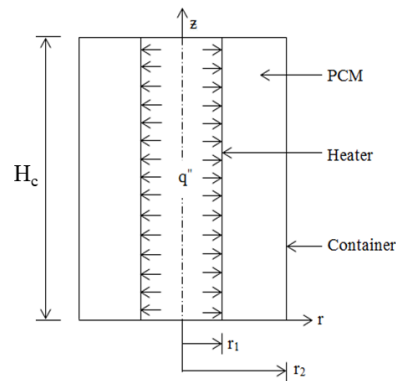


Fig. 2.1 Schematic of PCM based annular TES system

The problem depicted in Fig. 2.2 is categorized as the *Stefan problem*. It consists of cylinder having inner surface of radius r_1 and outer surface of radius r_2 . Uniform constant heat flux is applied at the inner surface of the annulus. The length of PCM cylinder (H_c) is assumed to be much larger than its thickness ($r_2 - r_1$), that is, ($H_c \gg r_2 - r_1$). The loss of heat from upper and lower surfaces of cylinder is assumed to be negligible and the entire heat is assumed to be conducted in radial direction. Therefore, the problem can be modeled as one-dimensional. Following assumptions have been made for the analysis and are detailed below.

- (i) PCM is assumed to be pure material and its melting is considered as isothermal.

- (ii) Heat transfer in PCM is assumed to be one-dimensional and conduction dominated.
- (iii) An equivalent thermal conductivity for liquid phase is considered in order to account the melt convection.
- (iv) Properties of solid and liquid phases are different but are assumed to be constant within the operating range of temperature.
- (v) The change of volume of PCM after phase change is neglected in the analysis.

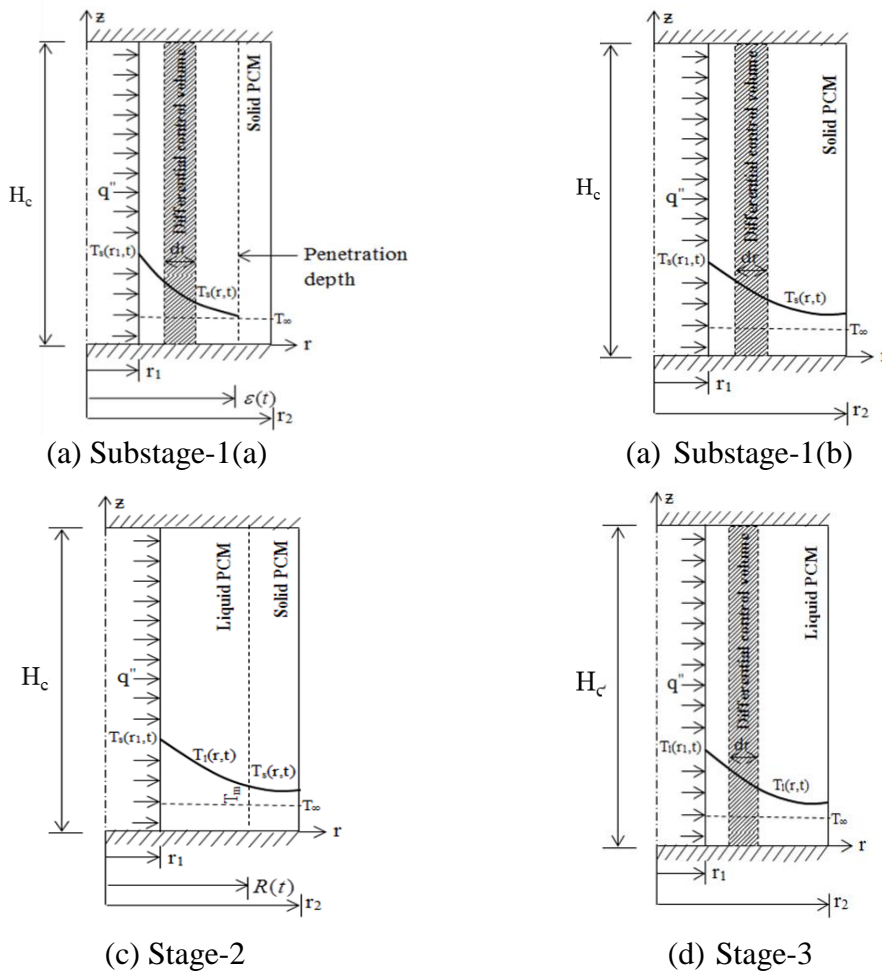


Fig. 2.2 Typical phase change curves for melting process for (a) substage-1(a), (b) substage1(b), (c) stage-2, and (d) stage-3

2.2.2 Mathematical formulation

Fig. 2.2 depicts the temperature distribution during the phase change process of PCM in the cylindrical container. Here, the problem involves two different domains; namely, melting and solidification. Each domain is formulated separately in subsequent sections.

Melting analysis

The melting domain is divided into three stages. Stage 1 represents the case where the entire PCM remains in solid state and heat transfer takes place due to conduction. The supplied heat energy is absorbed in PCM and the temperature of PCM rises due to gain in sensible heat. In stage 2, the melting of PCM takes place with partial solid and partial liquid state of PCM. In this stage, the melt front propagates from inner layer to the outermost layer of PCM. After complete melting of PCM (stage 3), the temperature of molten PCM increases due to sensible heat gain.

The one-dimensional transient heat conduction equation valid for all the three stages can be written as follows:

Stage 1: PCM is completely solid $0 \leq t \leq t_m$:

$$\frac{1}{r} \frac{\partial}{\partial r} \left(r \frac{\partial T_s}{\partial r} \right) = \frac{1}{\alpha_s} \frac{\partial T_s}{\partial t} \quad r_1 \leq r \leq r_2 \quad (2.1a)$$

Stage 2: PCM is partially molten $t_m \leq t \leq t'$:

$$\frac{1}{r} \frac{\partial}{\partial r} \left(r \frac{\partial T_l}{\partial r} \right) = \frac{1}{\alpha_l} \frac{\partial T_l}{\partial t} \quad r_1 \leq r \leq R(t) \quad (2.1b)$$

$$\frac{1}{r} \frac{\partial}{\partial r} \left(r \frac{\partial T_s}{\partial r} \right) = \frac{1}{\alpha_s} \frac{\partial T_s}{\partial t} \quad R(t) \leq r \leq r_2 \quad (2.1c)$$

Stage 3: PCM is completely liquid $t' \leq t \leq t''$:

$$\frac{1}{r} \frac{\partial}{\partial r} \left(r \frac{\partial T_l}{\partial r} \right) = \frac{1}{\alpha_l} \frac{\partial T_l}{\partial t} \quad r_1 \leq r \leq r_2 \quad (2.1d)$$

Here $R(t)$ denotes the position of solid-liquid interface at time t .

The initial and boundary conditions are given by:

$$T_j(r, t) = T_\infty \quad \text{at } t = 0 \quad (2.2a)$$

$$-k_j \frac{\partial T_j}{\partial r} = q'' \quad \text{at } r = r_1 \quad (2.2b)$$

$$R(t) = r_1 \quad \text{for } t \leq t_m \quad (2.2c)$$

$$k_s \frac{\partial T_s}{\partial r} - k_l \frac{\partial T_l}{\partial r} = \rho L_p \frac{\partial R(t)}{\partial t} \quad \text{at } r = R(t) \quad (2.2d)$$

$$T_j(r, t) = T_m \quad \text{at } r = R(t) \quad (2.2e)$$

In this study, outer surface is subjected to two different boundary conditions and are given as:

$$-k_j \frac{\partial T_j}{\partial r} = 0 \quad \text{at } r = r_2 \quad (2.3)$$

$$-k_j \frac{\partial T_j}{\partial r} = h\{T_j(r, t) - T_\infty\} \quad \text{at } r = r_2 \quad (2.4)$$

where

$$k_j = \begin{cases} k_s, & \text{for solid} \\ k_l, & \text{for liquid} \end{cases} \quad (2.5a)$$

$$(2.5b)$$

$$T_j = \begin{cases} T_s, & \text{for solid} \\ T_l, & \text{for liquid} \end{cases} \quad (2.6a)$$

$$(2.6b)$$

Here, Eqs. (2.3) and (2.4) represent the adiabatic and convective boundary conditions at the outer surface of the PCM ($r = r_2$), respectively.

In addition to the initial and boundary conditions, another initial condition is required to solve the conduction equation. The details are elaborated below.

Outer surface subjected to convective environment

Stage 1: ($0 \leq t \leq t_m$)

The governing equation, initial condition and boundary conditions for stage 1 are valid upto the time when melting starts at the inner surface (t_m). Stage 1 is further subdivided into two distinct time domains as below:

Case 1: Initiation of melting after the penetration of thermal disturbance at the outer layer of PCM, i.e. $t_m \geq t_0$.

Case 2: Initiation of melting before the thermal disturbance penetrates the outer layer of PCM, i.e. $t_m \leq t_0$.

Case 1: $t_m \geq t_0$

This stage is further divided into the following two substages:

(a) $0 \leq t \leq t_0$

(b) $t_0 \leq t \leq t_m$

In order to solve the above mentioned problem, one needs to assume a guess temperature profile and is given as:

$$T_j(r,t) - T_\infty = a + b\{\ln(r)\} \quad (2.7)$$

Here, a simplified variational profile, satisfying the boundary conditions (Eqs. 2.2a and 2.2b, for substage (a) and Eqs. 2.2a and 2.4, for substage (b) coupled with Kantorovich method [192], is employed to obtain the solution for both the substages and expressed below.

$$T_s(r,t) - T_\infty = \begin{cases} \frac{q''r_1}{k_s} \ln\left(\frac{\varepsilon(t)}{r}\right) & \text{for } 0 \leq t \leq t_0 \quad (2.8a) \\ \frac{q''r_1}{k_s} \left[\ln\left(\frac{r_2}{r}\right) + \frac{1}{\eta Bi_s} \left\{ 1 - e^{\left\{ \frac{Bi_s \alpha_s (t-t_0)}{(1-\eta)r_2^2} \right\}} \right\} \right] & \text{for } t_0 \leq t \leq t_m \quad (2.8b) \end{cases}$$

where the depth of penetration $\varepsilon(t)$ is defined as below:

$$\varepsilon(t) = r_1 + \frac{\alpha_s t}{r_1} \quad \text{for } 0 \leq t \leq t_0 \quad (2.9)$$

It may be noted that the penetration time (t_0) for thermal disturbance to penetrate to the outer surface of PCM can be obtained by substituting $T_s(r_2, t) = T_\infty$ in Eq. (2.8b) as follows:

$$t_0 = \frac{\eta(1-\eta)r_2^2}{\alpha_s} \quad (2.10)$$

Depth of penetration $\varepsilon(t)$ and penetration time t_0 are independent of amount of heat flux applied at the inner surface of PCM cylinder.

The solutions given by Eqs. (2.8a) and (2.8b) are valid upto $t = t_m$. Therefore, it is needed to evaluate the value of t_m . By substituting $T_s(r_1, t) = T_m$ at $t = t_m$ in Eqs. (2.8a) and (2.8b), and with $\Delta T = T_m - T_\infty$, we can obtain:

$$\frac{t_m}{t_0} = \begin{cases} \frac{\eta}{(1-\eta)} \left[e^{\frac{\varphi_s}{\eta r_2}} - 1 \right], & t_m \leq t_0 \quad (2.11a) \\ 1 - \frac{1}{\eta Bi_s} \ln \left[1 - Bi_s \left\{ \frac{\varphi_s}{r_2} + \eta \ln(\eta) \right\} \right] & t_m \geq t_0 \quad (2.11b) \end{cases}$$

It may be noted from Eqs. (2.11a) and (2.11b) that the melting analysis of PCM consist of two parts, one with melting time less than penetration time and other with melting time longer than penetration time. For the above case $t_m \geq t_0$ (Eq. 2.11b), one can obtain the condition for the heat flux $q'' \leq \frac{k_s \Delta T}{\eta r_2 \ln \eta}$.

Stage 2: ($t_m \leq t \leq t'$)

The solution for this stage is obtained by employing an approximate analytical method, termed as quasi steady method. This method assumes that

during melting of PCM, temperature variation with time is small. Although the temperature may vary with time, one can assume the temperature gradient both in solid and liquid phases to be constant. By using governing equation (Eqs. 2.1b and 2.1c) and employing the initial and boundary conditions (Eqs. 2.2b, 2.2c and 2.2e, for liquid state and Eqs. 2.2c, 2.2e and 2.4, for solid state), the temperature distribution for both solid and liquid phases can be expressed as follows:

$$T_j(r,t) = \begin{cases} T_m + \frac{Bi_s \Delta T}{\{1 + Bi_s \ln(\gamma)\}} \ln \left\{ \frac{R(t)}{r} \right\} & \text{for solid } t_m \leq t \leq t' \quad (2.12a) \\ T_m + \frac{\eta r_2 \Delta T}{\phi_l} \ln \left(\frac{R(t)}{r} \right) & \text{for liquid } t_m \leq t \leq t' \quad (2.12b) \end{cases}$$

The melt interface location $R(t)$ can be found by substituting Eqs. (2.12a) and (2.12b) into Eq. (2.2d).

$$\frac{\alpha_l \eta_1 S t_l r_2 (t - t_m)}{\phi_l} = \frac{\{R(t)\}^2}{2} \left[1 + 2e^{\left\{ \frac{2}{Bi_s} - 2\phi_s \right\}} E_1 \left\{ 2 \ln \left(\gamma - \phi_s + \frac{1}{Bi_s} \right) \right\} \right] \quad \text{for interface } t_m \leq t \leq t' \quad (2.13)$$

where

$$E_1 = - \int \frac{e^{-v}}{v} dv \quad (2.14a)$$

$$v = 2 \left\{ \ln \left(\gamma - \phi_s + \frac{1}{Bi_s} \right) \right\} \quad (2.14b)$$

$$\phi_s = \frac{k_s \Delta T}{q''} \quad (2.14c)$$

$$\phi_l = \frac{k_l \Delta T}{q''} \quad (2.14d)$$

For thin PCM layer coupled with air convection $Bi_s \ll 1$, thus Eq. 2.13 can be rewritten as:

$$R(t) = \sqrt{r_1^2 + \frac{2\alpha_l \eta_l S t_1 r_2 (t - t_m)}{\phi_l}} \quad \text{for interface } t_m \leq t \leq t' \quad (2.15)$$

Now, the temperature distribution in solid and liquid phases can be obtained by substituting Eq. 2.15 in Eqs. 2.12a and 2.12b, respectively.

The time duration at which melt front reaches the outer surface of PCM can be obtained by substituting $R(t) = r_2$ and $t = t'$ in Eq. 2.15:

$$t' = t_m + \frac{(1 - \eta^2) \phi_l r_2}{2\alpha_l \eta S t_1} \quad (2.16)$$

The difference between time t' and t_m gives the duration of time in which latent heat is absorbed by the PCM and temperature of the outer surface of heater can be made stable.

Stage 3: ($t' \leq t \leq t''$)

In this stage, melt interface $R(t)$ reaches at the outermost layer of the PCM which is completely in the liquid state. The initial condition for this stage is $t = t'$. Using earlier method described in stage 1, governing equation (Eq. 2.1d) and employing the initial and boundary conditions (Eqs. 2.2b and 2.4), the temperature distribution in the molten PCM for $t' \leq t \leq t''$ can be obtained as:

$$T_l(r, t) = T_m + \frac{\eta r_2 \Delta T}{\phi_l} \left[\ln\left(\frac{r_2}{r}\right) + \frac{1}{\eta Bi_l} \left\{ 1 - e^{\left\{ \frac{\alpha_l Bi_l (t - t')}{(1 - \eta) r_2^2} \right\}} \right\} \right] \quad \text{for } t' \leq t \leq t'' \quad (2.17)$$

Outer surface of cylinder is insulated

Stage 1: ($0 \leq t \leq t_m$)

Here, the governing equations (Eqs. 2.1a-2.1d), boundary and initial conditions (Eqs. 2.2a-2.2e and 2.3) are used to obtain the solution. In addition, different cases for melting (stage 1) as applicable for earlier section are same for this model and also, the solution for substage (a) is similar to the earlier section as

there is no effect of outside boundary condition of cylinder in this substage of melting and hence not presented here for the sake of brevity.

Temperature distribution for substage (b) applicable in the time domain $t_0 \leq t \leq t_m$, is obtained by using governing Eq. (2.1a) and initial and boundary conditions (Eqs. 2.2b and 2.3) and is expressed below.

$$T_s(r, t) - T_\infty = \frac{q'' r_1}{k_s} \left[\ln \left(\frac{r_2}{r} \right) + \frac{\alpha_s (t - t_0)}{\eta (1 - \eta) r_2^2} \right] \quad \text{for } t_0 \leq t \leq t_m \quad (2.18)$$

The solution given by Eq. (2.18) is valid upto $t = t_m$. Therefore, it is needed to evaluate the value of t_m . By substituting $T_s(r_1, t) = T_m$ at $t = t_m$ in Eq. (2.18), and with $\Delta T = T_m - T_\infty$, one can obtain:

$$\frac{t_m}{t_0} = 1 + \frac{\varphi_s}{\eta r_2} \left[1 - \frac{\eta r_2}{\varphi_s} \ln \eta \right], \quad t_m \geq t_0 \quad (2.19)$$

For the above case (Eq. 2.19), one can obtain the condition for the heat flux $q'' \leq \frac{k_s \Delta T}{\eta r_2 \ln \eta}$ while for $t_m \leq t_0$, the expression remains same as reported in earlier section (stage 2).

Stage 2: ($t_m \leq t \leq t'$)

By using governing Eqs. (2.1b) and (2.1c), and employing the initial and boundary conditions (Eqs. 2.2b, 2.2c and 2.2e, for liquid state and Eqs. 2.2c, 2.2e and 2.3, for solid state), the temperature distribution for both solid and liquid phases can be obtained. It may be noted that the solution for liquid phase is similar to that of the earlier section (stage 2) and temperature distribution for solid phase is expressed as follows:

$$T_s(r, t) = T_m \quad \text{for solid } t_m \leq t \leq t' \quad (2.20)$$

Stage 3: ($t' \leq t \leq t''$)

In this stage, melt interface $R(t)$ reaches at the outermost layer of the PCM which is completely in the liquid state. The initial condition for this stage is $t = t'$.

By using governing Eq. (2.1d) and employing the initial and boundary conditions (Eq. 2.2b and 2.3), the temperature distribution in the molten PCM for $t' \leq t \leq t''$ can be obtained as:

$$T_l(r,t) = T_m + \frac{\eta r_2 \Delta T}{\phi_l} \left[\ln\left(\frac{r_2}{r}\right) + \frac{\alpha_l(t-t')}{\eta(1-\eta)r_2^2} \right] \quad \text{for } t' \leq t \leq t'' \quad (2.21)$$

Solidification analysis

It is considered that the solidification of PCM begins when zero heat flux applied at the inner wall of cylindrical annulus. This occurs in the case of cyclic or periodic heat loading situation. The governing Eqs. (2.1a)-(2.1d), boundary and initial conditions (Eqs. 2.2a, 2.2c-2.2e and 2.4) are same as in the case of melting problem discussed earlier. In addition to this, following boundary conditions are used to obtain the solution.

$$-k_j \frac{\partial T_j}{\partial r} = 0 \quad \text{at } r = r_1 \quad (2.22)$$

Here, different stages of solidification of PCM are same as discussed in the melting problem. However, these stages occur in the reverse order compared to the melting problem. Different stages are elaborated below.

Stage 1: ($t'' \leq t \leq t_s$)

The temperature distribution in the liquid PCM after the start of solidification ($t \geq t''$) can be expressed as:

$$T_l(r,t) - T_\infty = \tau_2 \left\{ 1 + Bi_l \ln\left(\frac{r_2}{r}\right) \right\} \quad \text{for } t'' \leq t \leq t_s \quad (2.23a)$$

where

$$\tau_2 = [T_l(r,t'') - T_\infty] \exp[-\alpha_l m(t-t'')] \quad (2.23b)$$

$$m = \frac{Bi_l}{r_2^2 [1 - \eta + Bi_l \{1 + \eta(\ln \eta - 1)\}]} \quad (2.23c)$$

The solution given by Eq. (2.23a) is valid upto $t = t_s$. Therefore, it is needed to evaluate the value of t_s . By substituting $T_l(r_2, t) = T_m$ at $t = t_s$ in Eq. (2.23a), and with $\Delta T = T_m - T_\infty$, one can obtain:

$$t_s = t'' + \frac{1}{\alpha_s m} \ln \left[\frac{T(r_2, t'') - T_\infty}{\Delta T} \right] \quad (2.24)$$

t_s denotes the time at which solidification at the outer surface of PCM starts.

Stage 2: ($t_s \leq t \leq t'''$)

After the start of solidification, solid-liquid interface moves from outer surface to inner surface of PCM layer (frozen front) and PCM dissipates latent heat. The temperature distribution for both solid and liquid phases can be expressed as:

$$T_j(r, t) = \begin{cases} T_m + \frac{Bi_s \Delta T}{\{1 + Bi_s \ln(\gamma)\}} \ln \left\{ \frac{R(t)}{r} \right\} & \text{for solid } t_s \leq t \leq t''' \quad (2.25a) \\ T_m & \text{for liquid } t_s \leq t \leq t''' \quad (2.25b) \end{cases}$$

The frozen front location $R(t)$ can be found by substituting Eqs. (2.25a and 2.25b) in Eq. (2.2e).

$$4\alpha_s Ste_s = \{R(t)\}^2 \left\{ 1 + 2 \ln(\gamma) + \frac{2}{Bi_s} \right\} \quad \text{for interface } t_s \leq t \leq t''' \quad (2.26)$$

For thin PCM layer coupled with air convection $Bi_s \ll 1$, thus Eq. (2.26) can be rewritten as:

$$R(t) = \sqrt{r_2^2 - 2\alpha_s Bi_s St_s (t - t_s)} \quad \text{for interface } t_s \leq t \leq t''' \quad (2.27)$$

The time duration at which frozen front reaches the inner surface of PCM can be obtained by substituting $R(t) = r_1$ and $t = t'''$ in Eq. (2.27):

$$t''' = t_s + \frac{r_2^2 (1 - \eta^2)}{2\alpha_s Bi_s St_s} \quad (2.28)$$

The difference between time t''' and t_s gives the duration of time in which latent heat is dissipated by the PCM.

Stage 3: ($t \geq t'''$)

This stage begins when the frozen front $\{R(t)\}$ reaches at the innermost layer of the PCM. The initial condition for this stage is $t = t'''$. The temperature distribution in the solid PCM can be expressed as:

$$T_s(r, t) - T_\infty = \tau_3 \left\{ 1 + Bi_s \ln \left(\frac{r_2}{r} \right) \right\} \quad \text{for } t \geq t''' \quad (2.29a)$$

where

$$\tau_2 = [T_l(r, t''') - T_\infty] \exp[-\alpha_s m(t - t''')] \quad (2.29b)$$

$$m = \frac{Bi_s}{r_2^2 [1 - \eta + Bi_s \{1 - \eta + Bi_s (\ln \eta - 1)\}]} \quad (2.29c)$$

Temperature distributions for all domains, stages and sub-stages are summarized in Table 2.1.

Table 2.1 Temperature distributions obtained in various stages

Stages		Melting of PCM		Solidification of PCM (Inner surface is insulated and outer surface of cylinder is subjected to convective environment)
		Outer surface of cylinder is subjected to convective environment	Outer surface of cylinder is insulated	
Stage-1 (Melting: $0 \leq t \leq t_m$ Solidification: $t'' \leq t \leq t_s$ [Figure 2.2(a), 2.2(b)]	Sub stage-1(a) ($0 \leq t \leq t_0$) [Figure 2.2(a)]	$T_s(r,t) - T_\infty = \frac{q'' r_1}{k_s} \ln \left\{ \frac{\varepsilon(t)}{r} \right\}$ <p>Where, $\varepsilon(t) = r_1 + \frac{\alpha_s t}{r_1}$</p> $t_0 = \frac{\eta r_2^2 (1-\eta)}{\alpha_s}$	$T_s(r,t) - T_\infty = \frac{q'' r_1}{k_s} \ln \left\{ \frac{\varepsilon(t)}{r} \right\}$ <p>Where, $\varepsilon(t) = r_1 + \frac{\alpha_s t}{r_1}$</p> $t_0 = \frac{\eta r_2^2 (1-\eta)}{\alpha_s}$	$T_l(r,t) - T_\infty = \tau_2 \left\{ 1 + Bi_l \ln \left(\frac{r_2}{r} \right) \right\}$ $\tau_2 = [T_l(r, t'') - T_\infty] \exp[-\alpha_l m (t - t'')]$ $m = \frac{Bi_l}{r_2^2 [1 - \eta + Bi_l \{1 + \eta (\ln \eta - 1)\}]}$
	Sub stage-1(b) ($t_0 \leq t \leq t_m$) [Figure 2.2(b)]	$T_s(r,t) - T_\infty = \frac{q'' r_1}{k_s} \left[\ln \left(\frac{r_2}{r} \right) + \frac{1}{\beta Bi_s} \left\{ 1 - e^{-\left\{ \frac{Bi_s \alpha_s (t-t_0)}{r_2^2 (1-\beta)} \right\}} \right\} \right]$ $\frac{t_m}{t_0} = \begin{cases} \frac{\eta}{(1-\eta)} \left[e^{\frac{\varphi_s}{\eta r_2}} - 1 \right], & t_m \leq t_0 \\ 1 - \frac{1}{\eta Bi_s} \ln \left[1 - Bi_s \left\{ \frac{\varphi_s}{r_2} + \eta \ln(\eta) \right\} \right], & t_m \geq t_0 \end{cases}$	$T_s(r,t) - T_\infty = \frac{q'' r_1}{k_s} \left[\ln \left(\frac{r_2}{r} \right) + \frac{\alpha_s (t - t_0)}{r_2^2 \eta (1-\eta)} \right]$ $\frac{t_m}{t_0} = \begin{cases} \frac{\eta}{(1-\eta)} \left[e^{\frac{\varphi_s}{\eta r_2}} - 1 \right], & t_m \leq t_0 \\ 1 + \frac{\varphi_s}{\eta r_2} \left[1 - \frac{\eta r_2}{\varphi_s} \ln \eta \right], & t_m \geq t_0 \end{cases}$	$t_s = t'' + \frac{1}{\alpha_l m} \ln \left(\frac{T(r_2, t'') - T_\infty}{\Delta T} \right)$

<p>Stage-2</p> <p>(Melting: $t_m \leq t \leq t'$, Solidification: $t_s \leq t \leq t'''$)</p> <p>[Figure 2.2(c)]</p>	$T_p(r,t) = \begin{cases} T_m + \frac{Bi_s \Delta T}{\{1 + Bi_s \ln(\gamma)\}} \ln\left(\frac{R(t)}{r}\right) \\ T_m + \frac{\beta r_2 \Delta T}{\phi_l} \ln\left(\frac{R(t)}{r}\right) \end{cases}$ <p>Where $T_p = T_s, T_l$ for solid and liquid phase respectively.</p> $R(t) = \sqrt{r_1^2 + \frac{2\alpha_l \eta_l St_l r_2 (t - t_m)}{\phi_l}}$ $t' = t_m + \frac{(1 - \eta^2) \phi_l r_2}{2\alpha_l \eta St_l}$	$T_p(r,t) = \begin{cases} T_m \\ T_m + \frac{\eta r_2 \Delta T}{\phi_l} \ln\left(\frac{R(t)}{r}\right) \end{cases}$ <p>Where $T_p = T_s, T_l$ for solid and liquid phase respectively.</p> $R(t) = \sqrt{r_1^2 + \frac{2\alpha_l \eta_l St_l r_2 (t - t_m)}{\phi_l}}$ $t' = t_m + \frac{\rho L_p (r_2^2 - r_1^2)}{2q'' r_1}$	$T_s(r,t) = T_m + \frac{Bi_s \Delta T}{\{1 + Bi_s \ln(\gamma)\}} \ln\left(\frac{R(t)}{r}\right)$ $T_l(r,t) = T_m$ $R(t) = \sqrt{r_2^2 - 2\alpha_s Bi_s St_s (t - t_s)}$ $t''' = t_s + \frac{r_2^2 (1 - \eta^2)}{2\alpha_s Bi_s St_s}$
<p>Stage-3</p> <p>(Melting: $t' \leq t \leq t''$, Solidification: $t \geq t''''$)</p> <p>[Figure 2.2(d)]</p>	$T_l(r,t) = T_m + \frac{\eta r_2 \Delta T}{\phi_l} \left[\ln\left(\frac{r_2}{r}\right) + \frac{1}{\eta Bi_l} \left\{ 1 - e^{\left\{ \frac{\alpha_l Bi_l (t - t')}{(1 - \eta) r_2^2} \right\}} \right\} \right]$	$T_l(r,t) = T_m + \frac{\eta r_2 \Delta T}{\phi_l} \left[\ln\left(\frac{r_2}{r}\right) + \frac{\alpha_l (t - t')}{\eta (1 - \eta) r_2^2} \right]$	$T_s(r,t) - T_\infty = \tau_3 \left\{ 1 - Bi_s \ln\left(\frac{r}{r_2}\right) \right\}$ $\tau_2 = [T_s(r, t''') - T_\infty] \exp[-\alpha_s m (t - t''')]$ <p>and</p> $m = \frac{Bi_s}{r_2^2 [1 - \eta + Bi_s \{1 + \eta (\ln \eta - 1)\}]}$

2.2.3 Results and Discussion

In this section, an effort has been made to investigate the influence of heat flux, heat transfer coefficient, thermo-physical properties of PCM, thermal conductivity enhancers and physical dimension of storage system on the temperature distribution of PCM. Here, paraffin wax has been considered as the phase change material and its properties are given in Table 2.2. An annulus filled with PCM having inner or outer diameters 4 mm and 8 mm, respectively is considered for the analysis. The inner cylinder is assumed to be electric vehicle battery module. The dimensions of this annular geometry are summarized in Table 2.2. The length of PCM cylinder (H_c) is chosen as 400 mm.

Table 2.2 Thermo-physical properties of paraffin wax

Property	Magnitude
Thermal conductivity (W/m-K)	0.29 (solid), 0.21 (liquid)
Density (kg/m ³)	910 (solid), 822 (liquid)
Specific heat (kJ/kg-K)	1.77
Latent heat of fusion (kJ/kg)	195
Initial temperature (°C)	21
Melting temperature (°C)	56
Outer radius (m)	0.004
Inner radius (m)	0.002
Length (m)	0.4

Comparison of present theoretical model with available test data

Initially, the present predictions are compared with the test data of Duan et al. [40] and Liu et al. [193] as shown in Figs. 2.3-2.5. Here, the temperature distribution during melting is obtained at $r = r_1$ (shown in Fig. 2.3) for the condition $q'' = \frac{k_s \Delta T}{\eta r_2 \ln \eta}$. The solid region includes two sub stages: (i) heat is not reached to the outer surface ($0 \leq t \leq t_0$) and (ii) heat is reached to the outer surface with PCM in the solid state condition ($t_0 \leq t \leq t_m$).

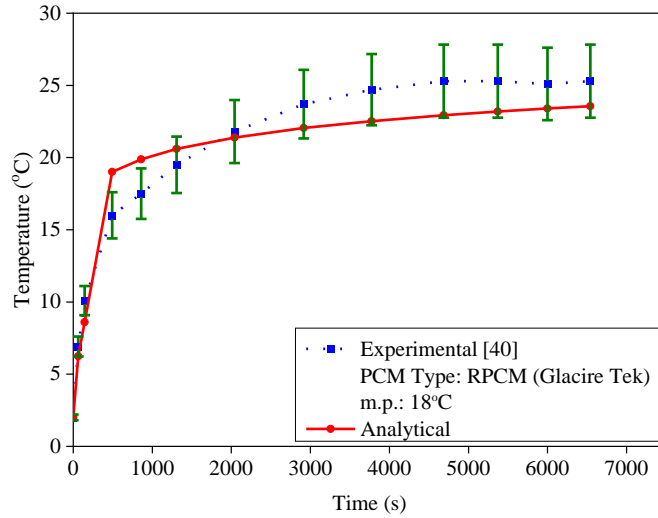


Fig. 2.3 Comparison of present prediction with the test data of Duan and Naterer [40] during melting of RPCM with constant heat flux at inner surface and convective heat transfer at outer surface

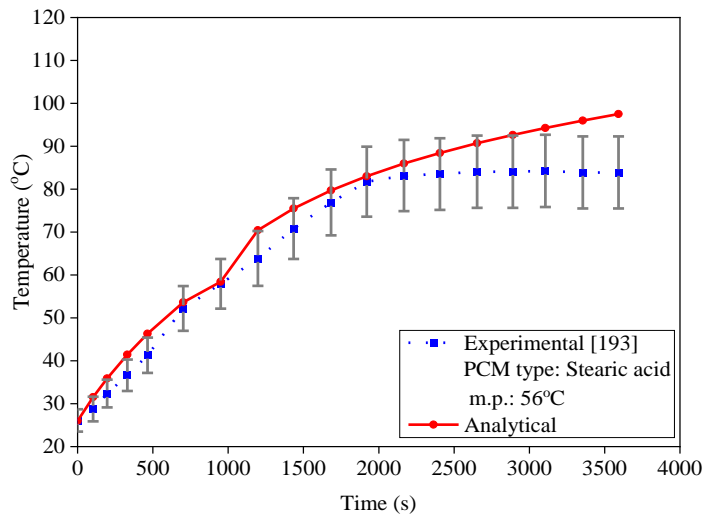


Fig. 2.4 Comparison of present prediction with the test data of Liu et al. [193] during melting of PCM with constant heat flux at inner surface and insulation at outer surface

Duan and Naterer [40] carried out experiments to simulate the battery cell by installing an electric heater at the center of a cylindrical container filled with RPCM as PCM. The container was made of aluminum with a thickness of 0.2

mm, diameter of 52 mm and height of 125 mm. The phase change temperature, specific heat, latent heat, density and thermal conductivity of RPCM was reported as 18°C, 2.1 kJ/kg-K, 195 kJ/kg, 840 kg/m³ and 0.55 W/m-K, respectively [40]. The electric heater is 101 mm long and 6.35 mm in diameter. The heater has heating rate of 1.36 W with a power supply of 14 V. Present predictions (Eqs. 2.8a-2.8b, 2.12b, 2.17) exhibit good agreement with the test data of Duan et al. [40] and are shown in Fig. 2.3. The temperature distribution (Fig. 2.3) depicts the melting of PCM involving various stages such as solid, partially molten and completely molten condition. It may be noted that the present prediction exhibits excellent agreement with the test data during solid state (0 - 232.49 s). While, there is some deviation between present prediction and test data during partial melting. This is attributed to the fact that the present analysis considers a quasi-steady assumption during the partial molten condition. The mean error is found to be less than 9.36% between both sets of results.

Here, efforts have also been made to compare present predictions during melting of PCM for insulated outer surface with the test data of Liu et al. [194] as shown in Fig. 2.4. In their experiments, electric heater of diameter 20 mm is placed concentrically with PCM tube made of stainless steel with inner diameter of 46 mm and length of 550 mm. The outside surface of cylindrical tube was well insulated with a porous polythene insulator. Stearic acid with melting temperature of 67.7°C was used as PCM. The initial temperature of PCM is kept at 26°C and heat flux of 1558 W/m² was considered during the tests. The properties of stearic acid are taken from Zalba et al. [19]. Fig. 2.4 depicts temperature distribution at the heater surface ($r = r_1$) obtained via both theoretical model and experiments. Present predictions exhibit good agreement with the test data. The error between both sets of results is found to be less than 7.86%.

The theoretical predictions obtained from the present analysis during solidification of PCM with the outer surface subjected to convective air environment are compared with the test data of Liu et al. [194] as shown in Fig. 2.5. In their experiments, electric heater with diameter 19.9 mm and 550 mm long is placed concentrically with heat exchanger made of two concentric cylindrical

pipes of stainless steel. The external tube was 600 mm long with inner diameter of 91 mm, while internal PCM tube was 550 mm long having 46 mm inner diameter and 2.5 mm wall thickness. The outside surface of external cylindrical tube was well insulated with a porous polythene insulator. Stearic acid with melting temperature of 67.7°C is used as PCM and was filled between electric heater and internal cylindrical tube. Cooling water was circulated in the space between internal and external cylindrical tubes. The initial temperature of PCM was maintained at 26°C and heat flux of 1558 W/m² was used during the experiment. Fig. 2.5 depicts the temperature distribution at the outer PCM surface ($r = r_2$) surrounded by pure stearic acid obtained through both theoretical model and experiments. The properties of stearic acid are taken from Zalba et al. [19]. The heat transfer coefficient is assumed to be 26.42 W/m²-K for all the stages of solidification process. The agreement between the present theoretical prediction and test data is found to be good and the maximum error is around 10.2%.

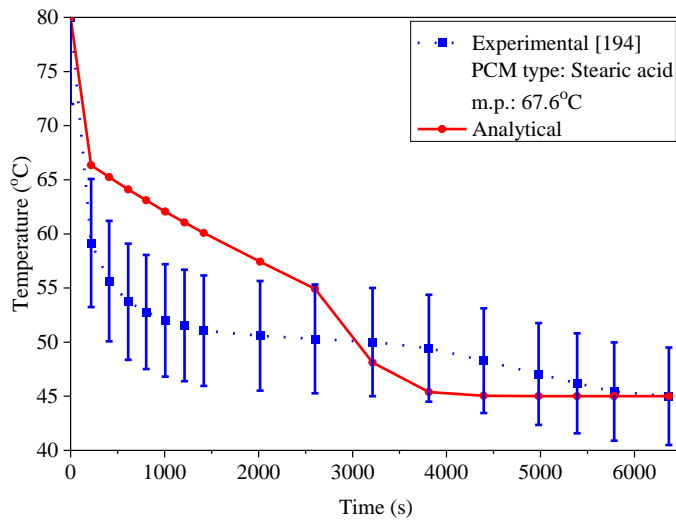


Fig. 2.5 Comparison of present prediction with the test data of Liu et al. [194] during solidification of PCM with insulated inner surface and convective heat transfer at outer surface

Effect of various parameters on melting and solidification of phase change material

Figs. 2.6(a) and 2.6(b) depict the distribution of temperature with time for various heat flux values. Fig. 2.6(a) illustrates the temperature distribution for different heat flux values for convective boundary condition at outer surface of cylinder containing PCM. The values of r_1 and r_2 are taken as 2 mm and 4 mm, respectively. The melting process completes when the temperature at the inside surface of PCM reaches a set point temperature of 100°C. The heat transfer coefficient at the outer surface of the PCM is assumed to be 5 W/m²-K. The heat flux values are varied between 250 W/m² to 2000 W/m². In earlier studies, heat flux values were found to be in the similar range [40, 195, 196]. It can be noticed that at lower heat flux values, the temperature of the inside surface of the PCM cylinder is stabilized for significant duration by absorbing the latent heat, while at higher heat flux values, the temperature rises very fast with short duration. Sensible heat storage is found to be significant for higher heat flux values compared to latent heat storage. Solidification of PCM initiates when heat flux at the inner surface becomes zero and outer surface of PCM is subjected to convective air environment. Therefore, it can be noticed from Fig. 2.6(a) that the heat flux values have no effect on the solidification process of PCM. Fig. 2.6(b) shows the distribution of temperature with time during melting of PCM for various heat flux values for adiabatic condition at the outer surface of PCM cylinder.

The effect of heat transfer coefficient on inner surface temperature of PCM during melting with insulated outer surface ($h = 0$ W/m²-K) and convective outer surface ($h = 5$ W/m²-K and 10 W/m²-K) is illustrated in Fig. 2.7(a). The melting process is assumed to be over when the temperature at the inner surface of PCM reaches a set point temperature of 100°C. Initially, the temperature remains same for different values of heat transfer coefficient. However, the start of melting of PCM is delayed by certain time period with the increase in the value of h . After certain time, as the melt front progresses, the temperature difference between insulated outer surface ($h = 0$ W/m²-K) and convective outer surface ($h = 5$ W/m²-

K, 10 W/m²-K) increases as shown in Fig. 2.7(a). This occurs because inner surface temperature of molten PCM depends on the heat transfer coefficient.

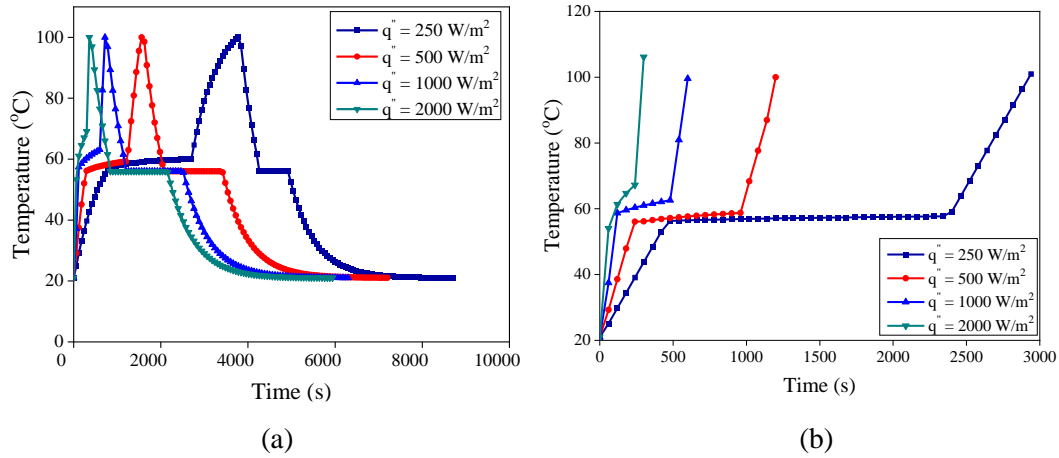


Fig. 2.6 PCM inner surface temperature distribution for different values of heat flux (a) melting and solidification with convection at outer surface of cylinder (b) melting with insulation at outer surface of cylinder

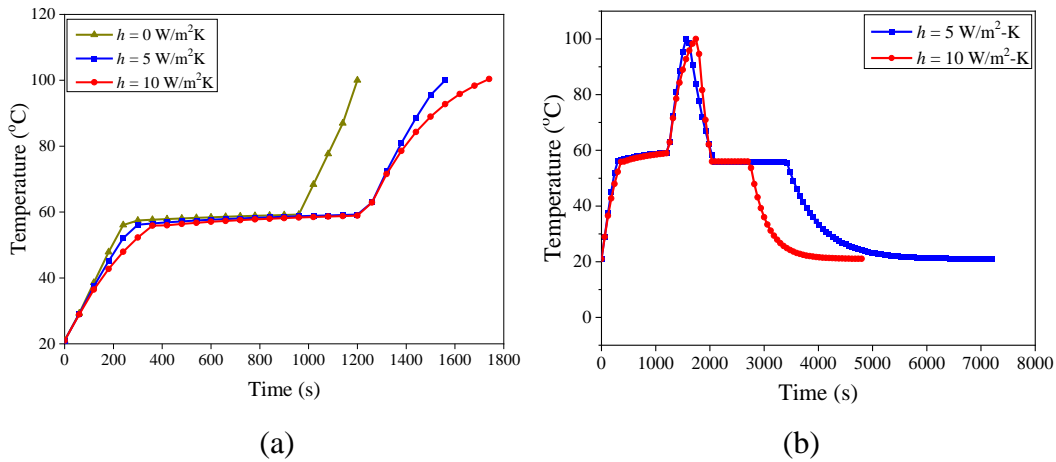


Fig. 2.7 PCM inner surface temperature distribution for different values of heat transfer coefficient (a) melting with insulation and convection at outer surface of cylinder (b) melting and solidification with convection at outer surface of cylinder

The effect of heat transfer coefficient on the inner surface temperature during melting and solidification of PCM with convective outer surface ($h = 5 \text{ W/m}^2\text{-K}$ and $10 \text{ W/m}^2\text{-K}$) is shown in Fig. 2.7(b). It can be noticed from the figure that increase in the value of heat transfer coefficient does not have significant effect

on melting duration. However, start of melting of PCM is delayed by certain time period with the increase in the value of h . Therefore, the time duration required by PCM to reach at the set point temperature increases. The solidification of PCM starts for $q'' = 0$ at the inner surface. Different values of heat transfer coefficient have significant effect on solidification of PCM. As the value of heat transfer coefficient increases at the outside surface of PCM, the time duration for inner surface to reach at ambient temperature decreases significantly.

Table 2.3 Thermo-physical properties of various PCMs

PCM	Melting Temperature (°C)	Latent heat of fusion (kJ/kg)	Thermal conductivity (W/m-K)	Density (kg/m ³)	Specific heat capacity (kJ/kg-K)
Paraffin	28	244	0.15	774	2.16
Paraffin wax	56	195	0.21	822	1770
Erythritol	120	340	0.326	1330	2.63
Eicosane	35	241	0.27	790	2.05
Stearic acid	69	202.5	0.172	848	2.30
KF.4H ₂ O	18.4	246	0.48	1450	2.59
Gallium	29.8	80.1	33.7	6093	0.40

In general, the analysis of melting of PCM in a cylindrical annulus of finite radii consists of two cases, one with t_0 less than t_m and other with t_0 greater than t_m . The former case is considered here. Figs. 2.8(a) and 2.8(b) depict the variation of (t_0/t_m) with radial distance for various PCMs and heat flux values. Here, four different categories of PCMs, namely, organic (paraffin, erythritol, eicosane, paraffin wax), fatty acid (stearic acid), salt hydrate (KF.4H₂O) and metal (gallium) are considered for analysis. The thermo-physical properties of PCM are reported by Zalba et al. [16] and Shamberger [197], are summarized in Table 2.3. It may be noted that for outer PCM layer of 0.5 mm and $q'' = 500 \text{ W/m}^2$, among various PCM materials, only KF.4H₂O starts to melt, when $t = t_0$ as shown in Fig. 2.8(a). On the contrary, with the increase of heat flux values to 2000 W/m^2 , in

addition to $\text{KF}\cdot 4\text{H}_2\text{O}$, paraffin wax starts to melt, when $t = t_0$ as shown in Fig. 2.8(b).

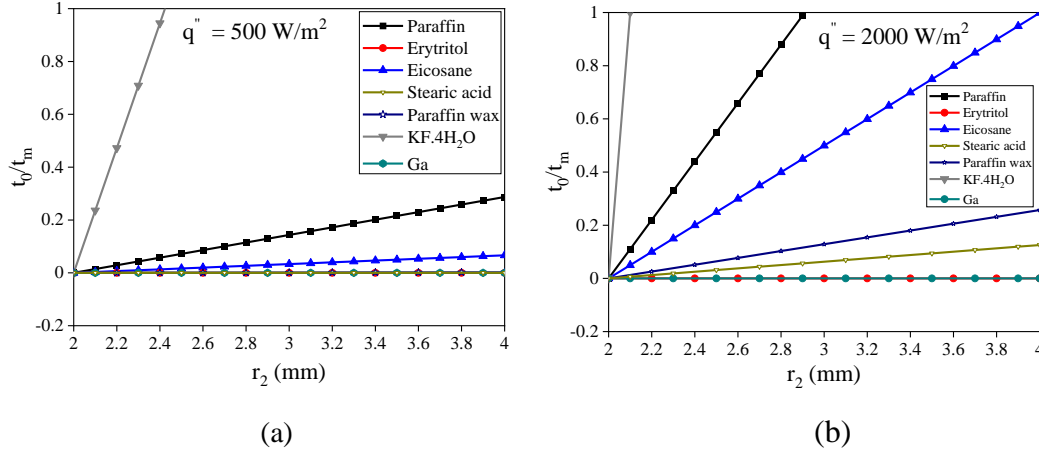


Fig. 2.8 Dimensionless time (t_0/t_m) for melting and heat penetration with radial distance for various PCM with $T_\infty = 18^\circ\text{C}$, $r_1 = 0.002$ m and $h = 5$ $\text{W}/\text{m}^2\text{-K}$
 (a) $q'' = 500$ W/m^2 (b) $q'' = 2000$ W/m^2

The variation of transient interface location with time for various heat flux values in case of melting of PCM and heat transfer coefficient in case of solidification of PCM is shown in Figs. 2.9(a) and 2.9(b), respectively. For analyzing the effect of heat flux on transient solid-liquid interface position, the PCM is assumed to be initially at its melting temperature. It is observed that with the increase in heat flux values the melt front speed increases and melt front reaches the outside surface of PCM cylinder in short duration as shown in Fig. 2.9(a). This indicates that with the increase of heat flux, PCM will melt quickly and results in reducing the temperature stabilization duration. It is observed that with the increase in the heat transfer coefficient, the time duration required to reach the frozen front at inside surface of PCM cylinder decreases. This indicates that with the increase of heat transfer coefficient, PCM will solidify quickly and can be considered as an important parameter for design.

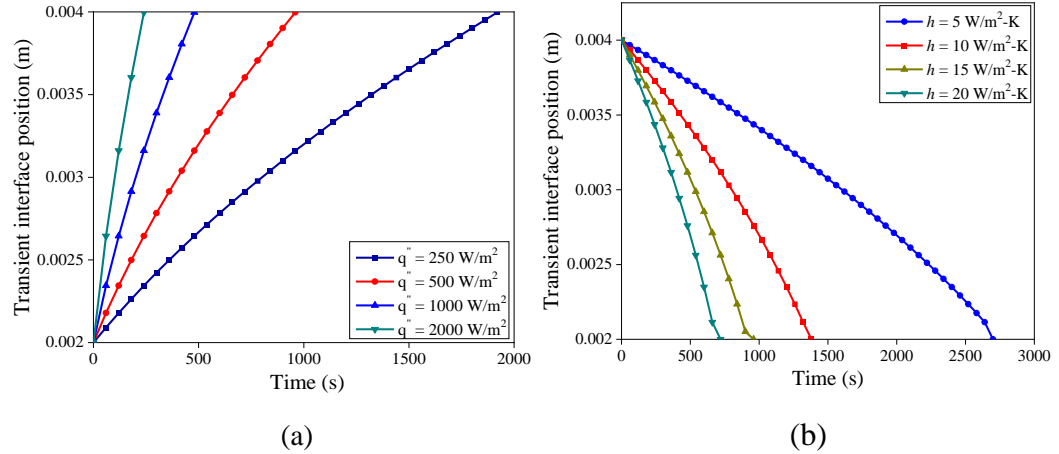


Fig. 2.9 Variation of transient interface location with time for various values of (a) q'' (b) h

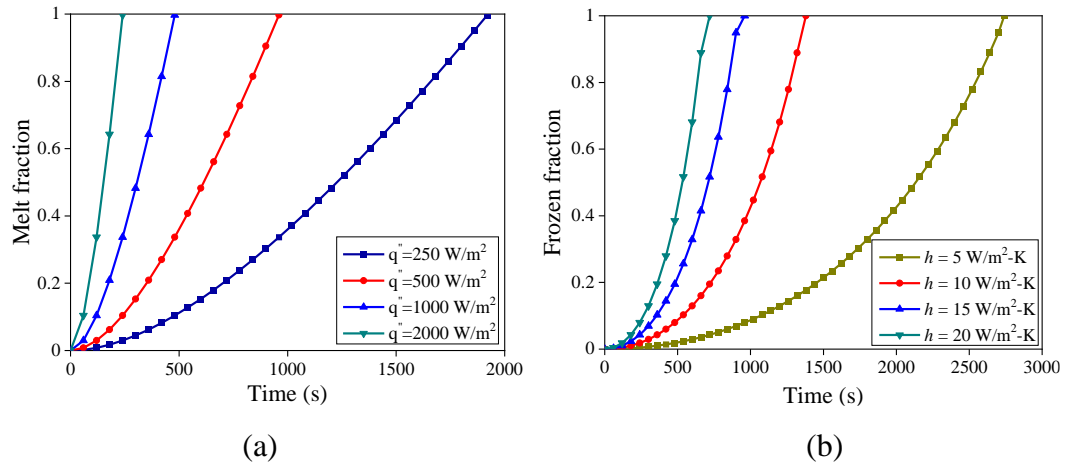


Fig. 2.10 Variation of melt fraction with time for various values of (a) q'' (b) h

Melt fraction is defined as the ratio amount of PCM melted to the total volume of PCM. While, the frozen fraction denotes the ratio of amount of PCM solidified to the total volume of PCM. Here, the PCM is assumed to be initially at its melting temperature. The variation of melt fraction with time for various heat flux values and variation of frozen fraction with time for various heat transfer coefficient is shown in Figs. 2.10(a) and 2.10(b), respectively. With the higher value of heat flux, the melting occurs quickly and the rate of melting is higher compared to lower heat flux values. It is observed that the solidification of PCM

occurs at faster rate with the increase in heat transfer coefficient as shown in Fig. 2.10(b) and frozen fraction rapidly approaches unity.

Fig. 2.11 depicts the effect of radius ratio (η) on melting of PCM. The melt duration for $\eta = 0.5$ and $\eta = 0.33$ was found to be 1238 s and 3046 s, respectively. This indicates that melt duration can be increased by increasing the thickness of PCM over the heater.

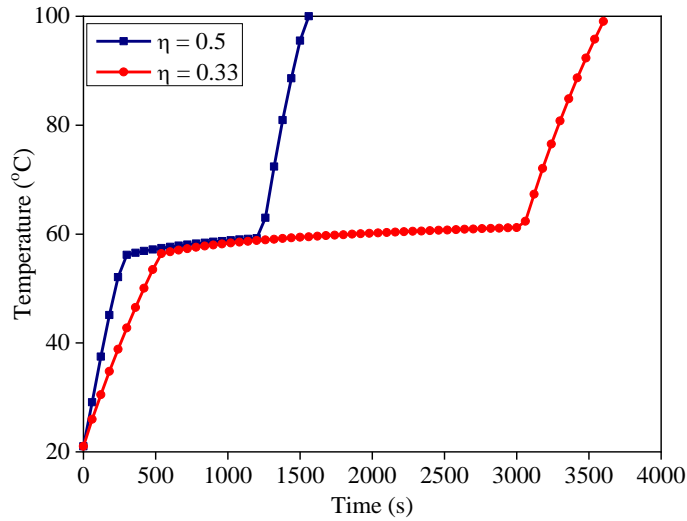


Fig. 2.11 Effect of radius ratio (η) on melting of PCM

Table 2.4 Properties of TCE (Aluminum)

Property	Magnitude
Thermal conductivity (W/m-K)	202.4
Density (Kg/m ³)	2719
Specific heat capacity (kJ/kg-K)	0.87
Melting Temperature (°C)	660.4

Here, an attempt has been made to analyze the effect of thermal conductivity enhancers (TCE) on the phase change process. For such investigation, aluminum is used as TCE and various volumetric percentage of aluminum (2% to 20%) is uniformly dispersed in PCM stored in the annulus of length of 400 mm. Thermo-

physical properties of aluminum are summarized in Table 2.4. The TCE has been assumed to be equally dispersed throughout the length of PCM cylinder.

The effective thermophysical properties of PCM and TCE are determined as follows [75].

$$k_{eff} = \delta k_{TCE} + (1 - \delta)k_{PCM} \quad (2.30a)$$

$$\rho_{eff} = \delta \rho_{TCE} + (1 - \delta)\rho_{PCM} \quad (2.30b)$$

$$(\rho c)_{eff} = \delta(\rho c)_{TCE} + (1 - \delta)(\rho c)_{PCM} \quad (2.30c)$$

$$(\rho L_p)_{eff} = (1 - \delta)(\rho L_p)_{PCM} \quad (2.30d)$$

It may be noted that linear variation with volumetric fraction of TCE is considered to evaluate the thermo-physical properties (Eqs. 2.30a-2.30d). Although the variation in effective thermal conductivity with volume fraction of TCE is complex, the linear approximation is valid for various properties of PCM such as density, specific heat and latent heat. Similar approximations have been made by earlier researchers in their investigations [75].

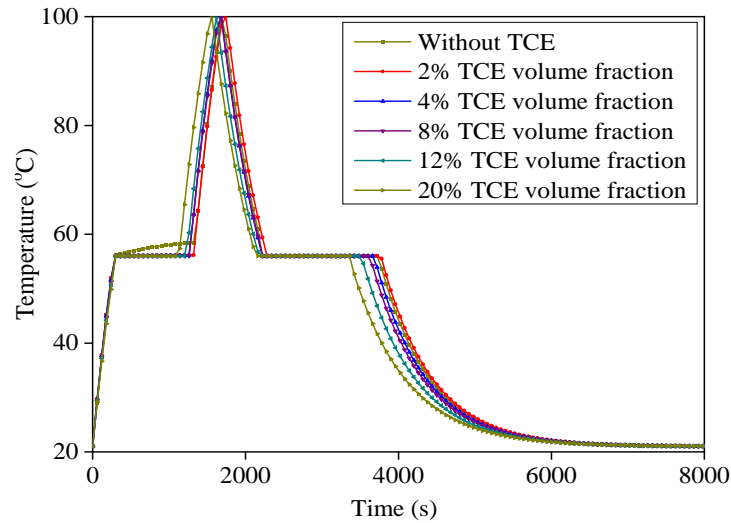


Fig. 2.12 Effect of TCE on melting and solidification of PCM

It is observed that with 2% TCE the time duration to reach at the set point temperature of 100°C increases. However, with further increase of TCE volume fraction, the time duration to reach at set point temperature decreases as shown in

Fig. 2.12. Also, the melt duration decreases due to the decrease in the amount of PCM in the thermal storage unit. Therefore, the volume fraction of TCE needs to be chosen wisely as there exists a particular percentage of TCE for each configuration at which the melt duration for thermal storage unit is maximum. It is observed that TCE have no effect on the solidification duration of PCM.

2.3 Melting and solidification analysis of phase change material inside rectangular thermal energy storage system involving fins

In this work, melting and solidification of PCM in two-dimensional rectangular storage system with horizontal internal fins have been analyzed. The storage unit involving PCM and internal fins is shown in Fig. 2.13. Various end wall boundary conditions, namely, constant heat flux, end wall temperature and convective air environment have been used. Heat balance integral method (HBIM) is employed to obtain the solution.

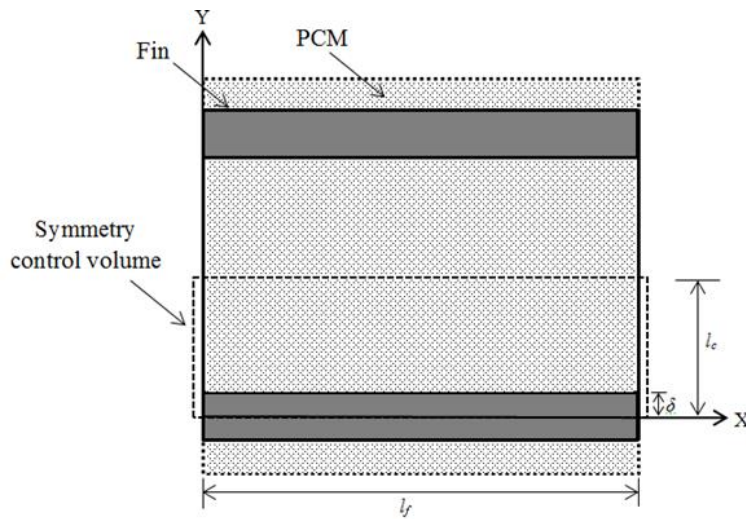
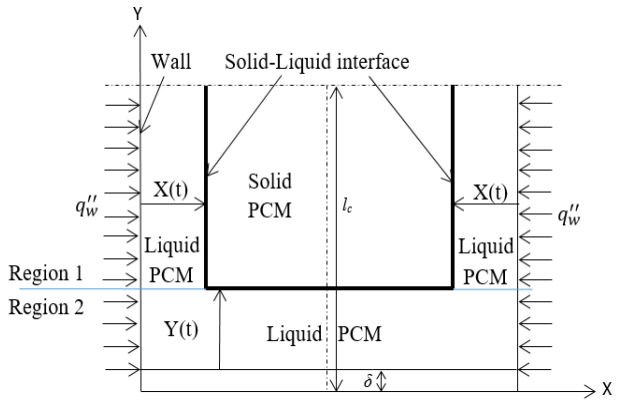


Fig. 2.13 Finite storage system for PCM with fins

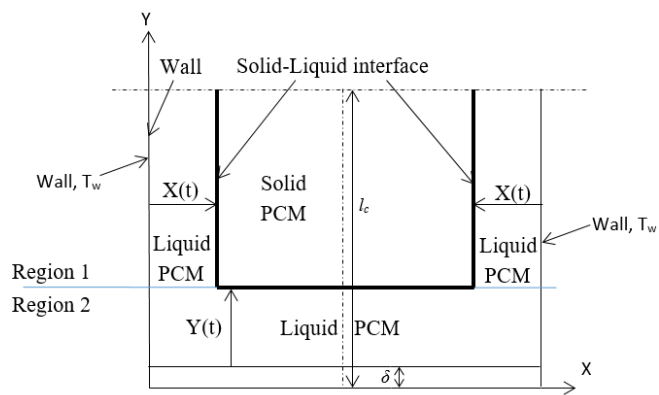
2.3.1 Physical model

Melting Analysis

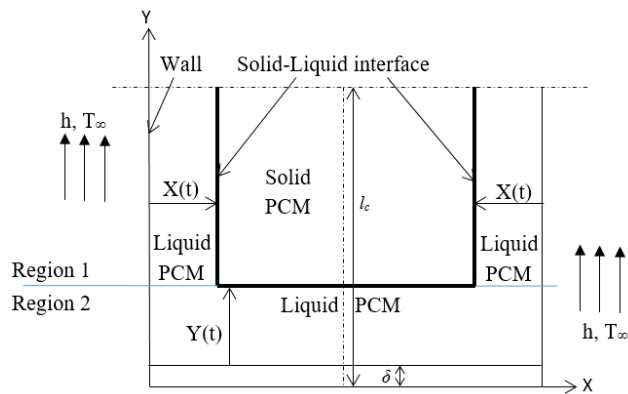
Here, the physical problem is divided into two regions (Region 1 and Region 2) by considering a single symmetry cell of the finite storage system (Fig. 2.14).



(a)



(b)



(c)

Fig 2.14 Schematic of different regions in a PCM based two-dimensional storage system with various boundary conditions (a) constant heat flux, (b) constant temperature and (c) convective air environment

In Region 1, the heat transfer takes place in X-direction (between wall and PCM) and fins do not influence the melting problem [17, 87]. Initially, the transfer of

heat occurs due to conduction, the mechanism of heat transfer changes from conduction to convection when Rayleigh number (Ra) is higher than 10^3 . Heat transfer to PCM takes place due to wall and fin in Region 2. The melting process in this region is divided into three stages, namely, conduction (hot wall and fin), combination of conduction (fin) and convection (hot wall), and natural convection (fin). In the initial phase, the heat transfer from fin to PCM occurs by conduction. For $Ra \geq 1708$, the mechanism of heat transfer from fin to PCM changes from conduction to convection [87]. Initially, the natural convection heat transfer from fin to PCM is insignificant because of lower value of temperature gradient in liquid PCM. With the progress of time, fins play a crucial role in the heat transfer process.

It is argued that convection heat transfer plays a crucial role during melting process in PCM storage unit involving fins. In order to simulate convection heat transfer, the value of heat transfer coefficient need to be provided prior to solve the conduction equation along with the initial and boundary conditions. It is further reported that transition of heat transfer from conduction to convection takes place for $Ra_{cr} = 1708$ [87, 198]. The Rayleigh number is expressed as:

$$Ra = \frac{g(T_f - T_m)\rho^2 c_l \{Y(t)\}^3 \beta}{\mu k_l} \quad (2.31)$$

For $Ra_{cr} = 1708$, Eq. (2.31) can be expressed as:

$$\{Y(t)\}_{cr} = \left(\frac{1708 \mu k_l}{g(T_f - T_m)\rho^2 c_l \beta} \right)^{1/3} \quad (2.32)$$

Here, β , μ , and g denote thermal expansion coefficient, dynamic viscosity and acceleration due to gravity, respectively.

Marshall [199, 200] performed tests and studied the effect of natural convection during the melting of paraffin with different boundary conditions and reported the correlation for Nusselt number (Nu) as:

$$Nu = 0.072 Ra^{1/3} \quad (2.33)$$

where

$$Nu = \frac{hY(t)}{k_l} \quad (2.34)$$

Utilizing Eqs. 2.31 and 2.34 in Eq. 2.33, the heat transfer coefficient is given by:

$$h = 0.072 \left(\frac{g(T_f - T_m) \rho^2 c_l k_l^2 \beta}{\mu} \right)^{1/3} \quad (2.35)$$

Eq. 2.35 denotes the h as a function of ρ , c_l , k_l , β , μ , g , ΔT_f . It is argued that the value of ΔT_f is found out to be small and hence compared to other parameters, the influence of ΔT_f on h is minimal [201]. At this juncture, one needs to find out the value of T_f for different thermal boundary conditions. Based on energy balance, one can evaluate the temperature of fin for different thermal boundary conditions as below:

$$T_f = \begin{cases} \frac{T_w + T_m}{2}, \text{End wall temperature [87]} \\ T_m + \frac{q'' l_f}{2k_l}, \text{Heat flux} \\ T_m + \frac{h_w l_f (T_\infty - T_m)}{2k_l}, \text{Convective air condition} \end{cases} \quad (2.36)$$

The value of h is evaluated by using Eqs. 2.35-2.36 and subsequently used as input condition to solve the conduction equation. This is discussed in subsequent sections. The value of h is obtained by using Eqs. 2.35 and 2.36 underestimates and overestimates for location nearer to wall and at location farther from the wall, respectively [87].

The melting behavior of PCM is complex due to transient behavior and moving of interface location. The assumptions considered in this study are as follows:

- (i) The fin surface and PCM are at melting temperature (T_m).
- (ii) Because of thinness of geometry and higher value of thermal conductivity, one-dimensional temperature distribution is considered in fin.

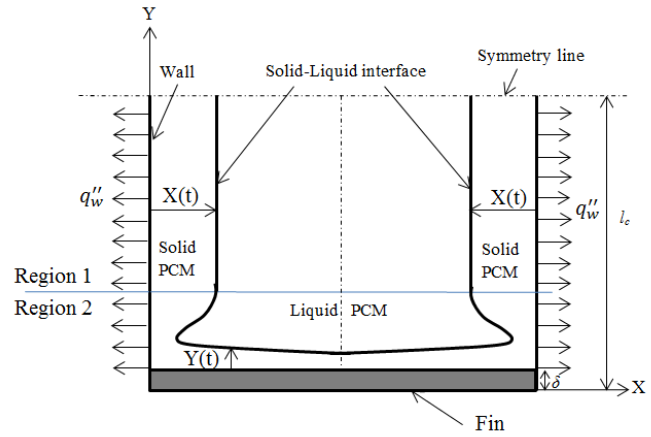
- (iii) The dominant mode of heat transfer in molten PCM is assumed to take place due to conduction and convection in Region 1 and Region 2, respectively.
- (iv) The variation of properties of HTF, fin and PCM are considered to be negligible.
- (v) Homogeneous behavior of PCM is considered and melting process is assumed to be isothermal.

Solidification Analysis

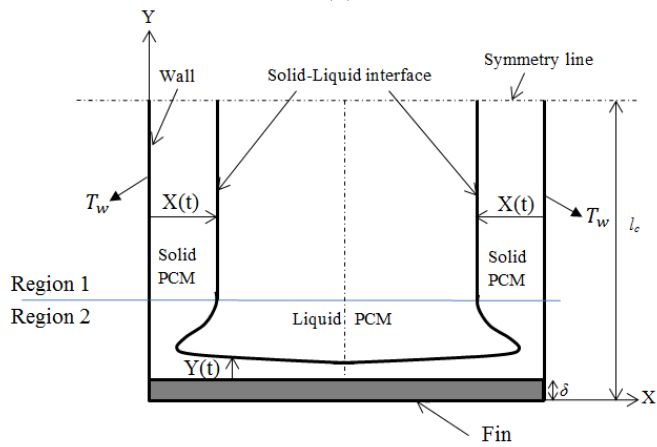
Fig. 2.13 represents the schematic of PCM storage unit with internal horizontal fins. Due to symmetry of PCM storage unit, a single symmetry cell was considered for the analysis and is shown in Fig. 2.15. Two regions, namely; Region 1 and Region 2 is considered for the analysis. In Region 1, the heat transfer is one-dimensional, towards direction X. Here, heat is transferred only by walls and the fin does not affect the solidification of PCM as reported by Lamberg and Siren [17, 87]. In Region 2, transfer of heat to the PCM takes place by the wall as well as the fin. After short duration, heat is mainly transferred by the fin. In such case, the solid-liquid interface is assumed to move one dimensionally in direction Y. In solidification process, conduction is assumed to be primary mode of heat transfer. The natural convection, at the solid-liquid interface due to the difference in temperature of liquid PCM, has minimal effect on location of solid-liquid interface compared to heat conduction in solid PCM [67]. Therefore, the natural convection is not considered in the analysis.

The following assumptions are made for the analysis [16, 17, 67].

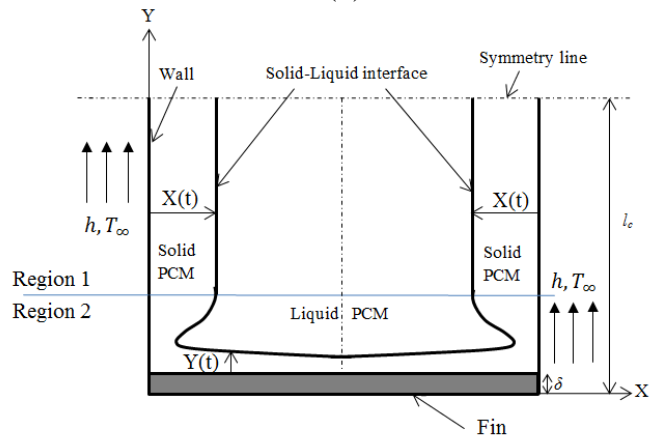
- (i) Initially, the temperature of PCM and fin are considered to be same as that of solidification temperature (T_m).
- (ii) The temperature variation of fin is one-dimensional because of small thickness, geometry and high thermal conductivity.
- (iii) Various properties of fin, PCM and HTF are considered to be constant irrespective of temperature.
- (iv) PCM is assumed to be homogeneous and solidification considered to takes place isothermally.



(a)



(b)



(c)

Fig. 2.15 Schematic of different regions in a two-dimensional PCM storage with different boundary wall conditions (a) constant heat flux, (b) constant temperature, and (c) constant convective air environment

2.3.2 Mathematical formulation

Melting analysis

Present model involves two different regions such as Region 1 and Region 2. The governing equations along with the initial condition and boundary conditions are solved for each region and elaborated in this section. The details are summarized below.

Constant heat flux

Fig. 2.14a depicts the schematic of melting process and interface location for constant heat flux condition. Here, two different regions (Region 1 and Region 2) are identified for the analysis.

Region 1, $\{0 \leq x \leq X(t)\}$

The energy equation valid for Region 1 is expressed as:

$$\frac{\partial^2 T_l}{\partial x^2} = \frac{1}{\alpha_l} \frac{\partial T_l}{\partial t}, \quad 0 \leq x \leq X(t), t = 0 \quad (2.37)$$

And, initial and boundary conditions are given by:

$$\rho L_p \frac{dX(t)}{dt} = -k_l \frac{\partial T_l(X(t), t)}{\partial x} \quad (2.38a)$$

$$T_l(x, 0) = T_m, \quad 0 \leq x \leq l_f \quad (2.38b)$$

$$-k_l \frac{\partial T_l}{\partial x} = q_w'' \quad (2.38c)$$

where $X(t)$ denotes the interface location. Here, $q_w'' > 0$ is considered for the analysis of melting process.

The energy equation (Eq. 2.37) is integrated in the X direction. Utilizing Equation 2.38a-2.38c, Eq. 2.37 can be rewritten as:

$$\frac{d}{dt} \int_0^{X(t)} \rho c_l [T_l(x, t) - T_m] dx = -\rho L_p X'(t) + q_w''(t) \quad \text{for } 0 < x < X(t) \quad (2.39)$$

At this juncture, one can assume a suitable guess profile for the analysis. The guess profile can be selected as a function of various parameters (c_l , q_w'' , k_l , ρ , L_p , $X(t)$, x and t) and expressed as:

$$T_l(x,t) = T_m + A_1(t)[x - X(t)] + B_1(t)[x - X(t)]^2 \quad (2.40)$$

Utilizing Equation 2.38a-2.38c, the value of $A_1(t)$ and $B_1(t)$ can be expressed as:

$$A_1(t) = \frac{L_p}{2c_l X(t)} \left[1 - \sqrt{1 + \frac{4c_l q_w'' X(t)}{k_l L_p}} \right] \quad (2.41)$$

$$B_1(t) = \frac{L_p}{8c_l \{X(t)\}^2} \left[1 - \sqrt{1 + \frac{4c_l q_w'' X(t)}{k_l L_p}} \right]^2 \quad (2.42)$$

Utilizing Equation 2.40-2.42, Eq. 2.39 can be solved and the solution is expressed in the polynomial form involving numerous parameters (c_l , q_w'' , k_l , ρ , L_p , $X(t)$ and t) as:

$$C_1 \{X(t)\}^4 + D_1 \{X(t)\}^3 + E_1 \{X(t)\}^2 + F_1 \{X(t)\} + G_1 = 0 \quad (2.43)$$

where

$$C_1 = [c_l q_w'']^2 \quad (2.44a)$$

$$D_1 = 10k_l c_l L_p q_w'' - 4k_l c_l \rho^2 L_p q_w'' \quad (2.44b)$$

$$E_1 = 25k_l^2 L_p^2 - 12k_l c_l (q_w'')^2 t - k_l^2 \rho^2 L_p^2 \quad (2.44c)$$

$$F_1 = -60k_l^2 L_p q_w'' t \quad (2.44d)$$

$$G_1 = [6k_l q_w'' t]^2 \quad (2.44e)$$

$X(t)$ can be obtained by using the value of various properties of PCM (c_l , q_w'' , k_l , ρ , L_p and t) summarized in Table 2.5.

Region 2, $\{0 \leq x \leq Y(t)\}$

As discussed in the previous section, in the initial stage, the heat transfer from fin to PCM takes place due to conduction. With the increase in Rayleigh number (Ra) upto 1708, the mode of convection changes from conduction to convection.

Table 2.5 Thermo-physical properties of fin and PCM materials

Property	Paraffin (PCM)	Aluminum (fin)
Density, ρ (kg/m ³)	777	2,713
Thermal conductivity, k_l (W/m-K)	0.149	180
Heat capacity, C_l (J/kg-K)	2,600	960
Melting temperature, T_m (°C)	28	-
Latent heat of fusion, L_p (J/kg)	241360	-
Thermal expansion coefficient, β (K)	0.001	-
Viscosity, μ (kg/m-s)	0.00385	-

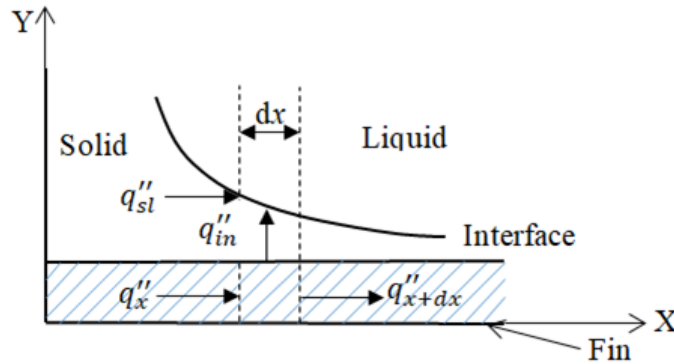


Fig. 2.16 Energy balance in a differential element of the PCM storage during melting

The balance of energy for differential element dx of PCM storage unit (Fig. 2.16) can be expressed as:

$$-q''_x + q''_{x+dx} - q''_{in} = \dot{E}_{st} \quad (2.45)$$

Here, \dot{E}_{st} denotes the storage rate of heat flux in fin. Utilizing the rate equation, Eq. 2.45 is expressed as:

$$\frac{\partial^2 T_f}{\partial x^2} - M(T_f - T_m) = \frac{1}{\alpha_f} \frac{\partial T_f}{\partial t} \quad (2.46)$$

Here, $M = \frac{h}{k_f \delta}$, and δ is the half thickness of fin.

Subjected to following initial and boundary conditions:

$$T_f(x, 0) = T_m \quad 0 \leq x \leq l_f \quad (2.47a)$$

$$-k_f \frac{\partial T_f(0, t)}{\partial x} = k_f \frac{\partial T_f(l_f, t)}{\partial x} = q_w'' \quad (2.47b)$$

Eq. 2.46 is integrated in X direction and expressed as:

$$\frac{1}{\alpha_f} \frac{d}{dt} \int_0^{l_f/2} (T_f - T_m) dx = \left(\frac{\partial T_f(x, t)}{\partial x} \right)_{l_f/2} - M \int_0^{l_f/2} (T_f - T_m) dx \quad (2.48)$$

As discussed earlier, the guess profile is selected as a function of various parameters (c_l , q_w'' , k_l , ρ , L_p , $Y(t)$, h , x and t) and expressed as:

$$T_f(x, t) = T_m + t \left[A_2(t) e^{\sqrt{M}x} + B_2(t) e^{-\sqrt{M}x} + C_2(t) \right] \quad (2.49)$$

Utilizing Eqs. 2.47a, 2.47b and 2.49, Eq. 2.48 can be solved and the temperature variation of fin can be expressed as:

$$T_f(x, t) = T_m + t P_1 + \frac{q_w''}{k_f \sqrt{M}} \left[\frac{e^{\sqrt{M}x} + e^{-\sqrt{M}x} + e^{\sqrt{M}(x-l_f)} + e^{-\sqrt{M}(x-l_f)}}{e^{\sqrt{M}l_f} - e^{-\sqrt{M}l_f}} \right] \quad (2.50)$$

where

$$P_1 = \frac{2\alpha_f q_w''}{l_f k_f (1 + M\alpha_f t)} - \frac{Q_1}{l_f \sqrt{M}} (e^{\sqrt{M}l_f} - 1) - \frac{R_1}{l_f \sqrt{M}} (1 - e^{-\sqrt{M}l_f}) \quad (2.51a)$$

$$Q_1 = \frac{q_w''}{k_f t \sqrt{M}} \left[\frac{1 + e^{-\sqrt{M}l_f}}{e^{\sqrt{M}l_f} - e^{-\sqrt{M}l_f}} \right] \quad (2.51b)$$

$$R_1 = \frac{q_w''}{k_f t \sqrt{M}} \left[\frac{1 + e^{\sqrt{M}l_f}}{e^{\sqrt{M}l_f} - e^{-\sqrt{M}l_f}} \right] \quad (2.51c)$$

The balance of energy for differential element dx of PCM storage unit (Fig. 2.16) at solid-liquid interface can be expressed as:

$$q_{sl}'' + q_{in}'' = \dot{E}_p \quad (2.52a)$$

Here, \dot{E}_p , q_{in}'' , q_{sl}'' , denotes the heat storage rate to PCM, heat flow per unit length from fin to solid-liquid interface and heat flow per unit length from wall to solid-liquid interface, respectively. Utilizing the rate equation, Eq. 2.52a is expressed as [87]:

$$a_1 \frac{\partial Y(t)}{\partial X} + h(T_f - T_m) = b_1 \frac{\partial Y(t)}{\partial t} \quad (2.52b)$$

where

$$a_1 = q_w'' \quad (2.52c)$$

$$b_1 = \rho L_p \quad (2.52d)$$

Here,

$$Y(t) = 0, \text{ at } t = 0 \quad (2.52e)$$

Utilizing the method of characteristics for quasilinear equations [87] and Eqs. 2.52b-2.52e, one can obtain the solution for solid-liquid interface $Y(t)$ in Y direction as:

$$Y(t) = h(T_f - T_m) \left(\frac{-b_1 X + \sqrt{(b_1 X)^2 + 2a_1 b_1 t}}{a_1 b_1} \right) \quad (2.52f)$$

Here, the value of a_1 and b_1 is given by Eqs. 2.52c-2.52d and the value of h can be obtained for Eqs. 2.35 and 2.36. It may be noted by using Eqs. 2.35, 2.36, 2.50-2.51c, and 2.52d-2.52f, temperature variation of the fin and the solid-liquid interface position $[Y(t)]$ can be obtained.

Constant temperature

Fig. 2.14b shows the schematic of melting process and interface location for constant wall temperature condition. Here, two different regions (Region 1 and Region 2) are identified for the analysis.

Region 1, $\{0 \leq x \leq X(t)\}$

Energy equation (Eq. 2.37), initial condition (Eqs. 2.38a and 2.38b) and assumed temperature profile (Eq. 2.40) is valid in this section. In addition to this, constant wall temperature condition is expressed as:

$$T_l(0,t) = T_l(l_f,t) = T_w \quad (2.53)$$

The energy equation (Eq. 2.37) is integrated in the X-direction. Utilizing Eqs. 2.38a, 2.38b and 2.53, Eq. 2.37 can be rewritten as:

$$\frac{d}{dt} \int_0^{X(t)} \rho c_l [T_j(x,t) - T_m] dx = -\rho L_p X'(t) + k_l T_l(0,t) \quad \text{for } 0 < x < X(t) \quad (2.54)$$

In order to solve Eq. 2.54, we have used the guess temperature profile as discussed in earlier section (Eq. 2.40).

Here, $T_w > 0$ is considered for analysis of melting process. Utilizing Eq. 2.37-2.38b, 2.53-2.54, $A_1(t)$ and $B_1(t)$ as reported in Eq. 2.40 is expressed as:

$$A_1(t) = \frac{L_p}{c_l X(t)} \left[1 - \sqrt{1 + 2st_l} \right] \quad (2.55)$$

$$B_1(t) = \frac{L_p}{2c_l \{X(t)\}^2} \left[1 - \sqrt{1 + 2st_l} \right]^2 \quad (2.56)$$

Utilizing Eqs. 2.40, 2.55, and 2.56, Eq. 2.54 can be solved and the solution for solid-liquid interface is expressed as:

$$X(t) = 2 \left[\sqrt{\frac{3(1+2st_l - \sqrt{1+2st_l})}{5+2st_l + \sqrt{1+2st_l}}} \right] \sqrt{\alpha_l t} \quad (2.57a)$$

Region 2, $\{0 \leq x \leq Y(t)\}$

In this case, the energy equation (Eq. 2.46) and initial condition (Eq. 2.47a) is used for the analysis. In addition to this, constant wall temperature condition is expressed as:

$$T_f(0, t) = T_f(l_f, t) = T_w \quad (2.58)$$

The energy equation (Eq. 2.46) is integrated in Y-direction and can be expressed by Eq. 2.48. The guess temperature profile (Eq. 2.49) is used to solve the energy equation (Eq. 2.48). Utilizing Eqs. 2.47a, 2.49 and 2.58, Eq. 2.48 can be solved and the temperature variation of fin is expressed as:

$$T_f(x, t) = T_w + tP_2 \left[e^{\sqrt{M}(x-l_f)} + e^{-\sqrt{M}x} - (1 + e^{-\sqrt{M}l_f}) \right] \quad (2.59)$$

where

$$P_2 = \frac{(T_m - T_w)l_f \sqrt{M}}{2t \left[e^{-\sqrt{M}l_f} \left\{ e^{(\sqrt{M}l_f/2)} - 1 \right\} + \left\{ 1 - e^{(-\sqrt{M}l_f/2)} \right\} - \frac{l_f \sqrt{M}}{2} \left\{ 1 + e^{-\sqrt{M}l_f} \right\} + \frac{M \alpha_f t (e^{-\sqrt{M}l_f} - 1)}{1 + M \alpha_f t} \right]} \quad (2.60)$$

Utilizing the rate equation, Eq. 2.52a is expressed as [87]:

$$\frac{a_2}{X} \frac{\partial Y(t)}{\partial X} + h(T_f - T_m) = b_2 \frac{\partial Y(t)}{\partial t} \quad (2.61a)$$

where

$$a_2 = k_l(T_w - T_m) \quad (2.61b)$$

$$b_2 = \rho L \quad (2.61c)$$

Employing method of characteristics for quasilinear equation [87] and using Eqs. 2.61a-2.61c, and 2.52e, the solid/liquid interface $Y(t)$ in Y-direction is expressed as:

$$Y(t) = h(T_f - T_m)X \left(\frac{-b_2X + \sqrt{(b_2X)^2 + 2a_2b_2t}}{a_2b_2} \right) \quad (2.61d)$$

Here, the value of a_2 and b_2 is given by Eqs. 2.61b and 2.61c and the value of h can be obtained by using Eqs. 2.35 and 2.36. It may be noted by using Eqs. 2.35, 2.36, 2.59-2.60, 2.61b-2.61d, temperature variation of the fin and solid-liquid interface position [$Y(t)$] can be obtained.

Constant convective air environment

Here, Fig. 2.14c illustrates the melting process and interface location for convective air environment condition. These include two different regions (Region 1 and Region 2) for the analysis.

Region 1, $\{0 \leq x \leq X(t)\}$

Here, the energy equation and the associated boundary conditions (Eqs. 2.37, 2.38a-2.38b) are used for the analysis. In addition to this, constant convective air environment boundary condition is expressed as:

$$\frac{-\partial T_l(0,t)}{\partial x} - Z_l\{T_l(0,t) - T_\infty\} = 0 \quad (2.62)$$

The energy equation (Eq. 2.37) is integrated in the X-direction. Utilizing Eqs. 2.38a, 2.38b, and 2.62, Eq. 2.37 can be rewritten as:

$$\frac{d}{dt} \int_0^{X(t)} \rho c_l [T_j(x,t) - T_m] dx = -\rho L_p X'(t) + h[T_\infty - T(0,t)] \quad \text{for } 0 < x < X(t) \quad (2.63)$$

In this case, the guess profile (Eq. 2.40) is used to solve the Eq. 2.63.

Here $k_l \llll h$, therefore assuming

$$\frac{k_l}{h} \approx 0 \quad (2.64)$$

Here, $T_\infty > 0$ is considered for analysis of melting process. Utilizing Eqs. 2.37, 2.38a, 2.38b, 2.62-2.64, one can estimate $A_1(t)$ and $B_1(t)$ as reported in Eq. 2.40.

$$A_1(t) = \frac{L_p}{c_l X(t)} \left[1 - \sqrt{1 - 2st_l} \right] \quad (2.65)$$

$$B_1(t) = \frac{L_p}{2c_l \{X(t)\}^2} \left[1 - \sqrt{1 - 2st_l} \right]^2 \quad (2.66)$$

where, St_l is Stefan number and is expressed as $St_l = \frac{c_l(T_\infty - T_m)}{L_p}$.

Utilizing Eqs. 2.40, 2.65, and 2.66, Eq. 2.54 can be solved and the solution for solid-liquid interface is expressed as:

$$X(t) = \frac{6ht}{\rho c_l} \left[\frac{-st_l}{7 + 2st_l + \sqrt{1 - 2st_l}} \right] \quad (2.67)$$

Present solution yields the position of solid-liquid interface as a function of h , t , c_l , st_l , ρ and expressed in Eq. 2.67.

Region 2, $\{0 \leq x \leq Y(t)\}$

For Region 2, the energy equation (Eq. 2.46) and the initial condition (Eq. 2.47a) is used for the analysis. In addition to this, constant convective air environment boundary condition is expressed as:

$$\frac{-\partial T_f(0,t)}{\partial x} + Z_f \{T_f(0,t) - T_\infty\} = \frac{\partial T_f(l_f,t)}{\partial x} + Z_f \{T_f(l_f,t) - T_\infty\} = 0 \quad (2.68)$$

The energy equation (Eq. 2.46) is integrated in Y direction and can be expressed by Eq. 2.48. The guess temperature profile (Eq. 2.49) is used for the analysis.

Utilizing Eqs. 2.47a, 2.49 and 2.68, Eq. 2.48 can be solved and the temperature variation of fin and is expressed as:

$$T_f(x,t) = T_\infty + tP_3 \left[Q_3 e^{\sqrt{M}x} + e^{-\sqrt{M}x} + \left\{ Q_3 \times \left(\frac{\sqrt{M}}{Z_f} - 1 \right) - 1 - \frac{\sqrt{M}}{Z_f} \right\} \right] \quad (2.69)$$

where

$$P_3 = \frac{(T_m - T_\infty)l_f}{t \left[\left\{ Q_3 \left(\frac{\sqrt{M}}{Z_f} - 1 \right) - 1 - \frac{\sqrt{M}}{Z_f} \right\} \{l_f + 2R_3\} + \{Q_3 + e^{-\sqrt{M}l_f}\} \left\{ \left(\frac{e^{\sqrt{M}l_f} - 1}{\sqrt{M}} \right) + R_3(1 + e^{\sqrt{M}l_f}) \right\} \right]} \quad (2.70a)$$

$$Q_3 = \frac{\frac{\sqrt{M}}{Z_f} e^{-\sqrt{M}l_f} + \frac{\sqrt{M}}{Z_f} + 1 - e^{-\sqrt{M}l_f}}{\frac{\sqrt{M}}{Z_f} e^{\sqrt{M}l_f} + \frac{\sqrt{M}}{Z_f} - 1 + e^{\sqrt{M}l_f}} \quad (2.70b)$$

$$R_3 = \frac{\alpha_f Z_f t}{1 + M \alpha_f t} \quad (2.70c)$$

In order to determine the solid-liquid interface location, the rate equation is obtained and given by Eq. 2.52f.

where

$$a_1 = h_w(T_\infty - T_m) \quad (2.71a)$$

$$b_1 = \rho L_p \quad (2.71b)$$

It may be noted that the solid-liquid interface $Y(t)$ in Y-direction for Region 2 is expressed in Eq. 2.52f. The temperature variation of the fin and the solid/liquid interface position $[Y(t)]$ is obtained by using Eqs. 2.35, 2.36, 2.69-2.71b, and 2.52f.

Solidification analysis

The present analytical model is developed in two parts. The problem can be treated as Stefan's problem [70] in Region 1, which is specifically solvable

moving boundary problem. In Region 2, transfer of heat is assumed to follow the direction Y and energy balance is required for the analysis. The problem is further divided based on different boundary conditions. This has been elaborated in subsequent sections.

Constant imposed heat flux at the walls

Fig. 2.15a shows the location of solid-liquid interface during solidification in two different regions for constant heat flux at the end walls.

Region 1, $\{0 \leq x \leq X(t)\}$

The transient heat conduction equation in one-dimensional for the PCM (Fig. 2.15a) can be expressed as:

$$\frac{\partial^2 T_s}{\partial x^2} = \frac{1}{\alpha_s} \frac{\partial T_s}{\partial t}, \quad 0 \leq x \leq X(t), t = 0 \quad (2.72)$$

The initial and boundary conditions are given by:

$$T_s(x, 0) = T_m, \quad 0 \leq x \leq l_f \quad (2.73a)$$

$$-\rho L_p \frac{dX(t)}{dt} = -k_s \frac{\partial T_s(X(t), t)}{\partial x} \quad (2.73b)$$

$$-k_s \frac{\partial T_s}{\partial x} = q_w'' \quad q_w'' < 0 \quad (2.73c)$$

Here, $X(t)$ is the distance of solid-liquid interface in direction X.

On integrating the governing Eq. (2.72) from end wall to solid-liquid interface with respect to x and utilizing the initial and boundary conditions, Eqs. (2.73a-2.73c), Eq. (2.72) can be rewritten as:

$$\frac{d}{dt} \int_0^{X(t)} \rho c_s [T_s(x, t) - T_m] dx = -\rho L_p X'(t) - q_w''(t), \quad 0 < x < X(t) \quad (2.74)$$

In order to solve the above equation and boundary conditions (Eqs. 2.73a-2.73c), a guess temperature profile is assumed and is given as:

$$T_s(x,t) = T_m + A_3(t)[x - X(t)] + B_3(t)[x - X(t)]^2 \quad (2.75)$$

where $A_3(t)$ and $B_3(t)$ are the constants; given by:

$$A_3(t) = \frac{L_p}{2c_s X(t)} \left[-1 + \sqrt{1 - \frac{4c_s q_w'' X(t)}{k_s L_p}} \right] \quad (2.76)$$

$$B_3(t) = \frac{L_p}{8c_s \{X(t)\}^2} \left[-1 + \sqrt{1 - \frac{4c_s q_w'' X(t)}{k_s L_p}} \right]^2 \quad (2.77)$$

Utilizing Eqs. (2.75)-(2.77), polynomial form solution for various parameters such as c_s , q_w'' , k_s , ρ , L_p , $X(t)$ and t . This can be written in the following form.

$$C_2 \{X(t)\}^4 + D_2 \{X(t)\}^3 + E_2 \{X(t)\}^2 + F_2 \{X(t)\} + G_2 = 0 \quad (2.78)$$

where

$$C_2 = [c_s q_w'']^2 \quad (2.79)$$

$$D_2 = 16k_s c_s L_p q_w'' [\rho^2 - 1] \quad (2.80)$$

$$E_2 = 4k_s [16k_s L_p^2 - 3c_s (q_w'')^2 t - k_s \rho^2 L_p^2] \quad (2.81)$$

$$F_2 = 96k_s^2 L_p q_w'' t \quad (2.82)$$

$$G_2 = [6k_s q_w'' t]^2 \quad (2.83)$$

In order to obtain $X(t)$, we need values of various properties of PCM such as c_s , q_w'' , k_s , ρ , L_p and t . The values of various properties of PCM are summarized in Table 2.6.

Region 2, $\{0 \leq x \leq Y(t)\}$

Here, the solid-liquid interface moves only in one direction that is in direction Y. In such case, one can consider the heat transfer takes place because of conjugate effect of heat transfer through fin. Fig. 2.17 shows the arbitrary differential element dx, which is detached from the PCM storage.

Table 2.6 Thermal properties of PCM and fin material [16]

Property	Paraffin	Aluminum fin
Density, ρ (kg/m ³)	1,450	2,770
Specific heat, c (J/kg-K)	3,600	875
Thermal conductivity, k (W/m-K)	0.6	177
Latent heat of fusion, L_p (J/kg)	162,000	-
Melting/solidification temperature, T_m (°C)	28	-

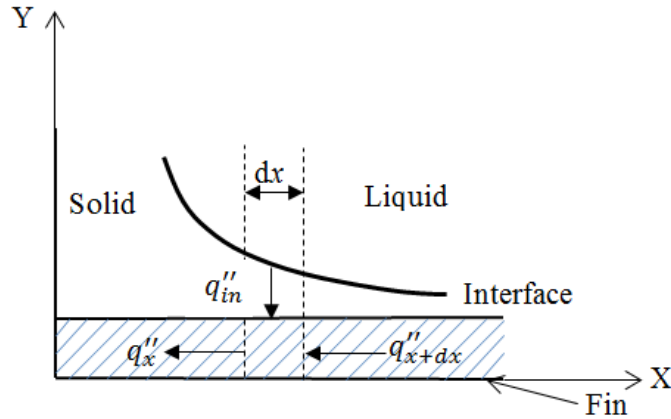


Fig. 2.17 Energy balance in a differential element of the PCM storage during solidification

An energy balance for the element dx can be written as:

$$-q''_x + q''_{x+dx} + q''_{in} = \dot{E}_{st} \quad (2.84)$$

where, \dot{E}_{st} is the rate of change of energy storage per unit area of the fin. Substituting rate equations, the energy balance equation (Eq. 2.84) can be rewritten as:

$$\frac{\partial^2 T_f}{\partial x^2} - M(T_f - T_m) = \frac{1}{\alpha_f} \frac{\partial T_f}{\partial t} \quad (2.85)$$

where

$$M = \frac{k_s}{k_f \delta Y(t)} \quad (2.86)$$

Here, δ is the half thickness of fin and $Y(t)$ is the distance of solid-liquid interface in direction Y .

The initial and boundary conditions of the fin are given by:

$$T_f(x, 0) = T_m \quad 0 \leq x \leq l_f \quad (2.87a)$$

$$-k_f \frac{\partial T_f(0, t)}{\partial x} = k_f \frac{\partial T_f(l_f, t)}{\partial x} = q_w'' \quad (2.87b)$$

On integrating the governing equation along the half length of fin with respect to x , Eq. (2.85) can be rewritten as:

$$\frac{1}{\alpha_f} \frac{d}{dt} \int_0^{l_f/2} (T_f - T_m) dx = \left(\frac{\partial T_f(x, t)}{\partial x} \right)_0^{l_f/2} - M \int_0^{l_f/2} (T_f - T_m) dx \quad (2.88)$$

The solution of Eq. (2.85) for different boundary conditions has been reported by several researchers [16, 17, 67]. While, for HBIM method, one need to assume the guess temperature profile and this can be written as:

$$T_f(x, t) = T_m + t[A_4(t)e^{\sqrt{M}x} + B_4(t)e^{-\sqrt{M}x} + C_4(t)] \quad (2.89)$$

Applying the initial and boundary conditions given by Eqs. (2.87a) and (2.87b) of the fin in Eq. (2.88), and substituting in Eq. (2.89), one can obtain the temperature variation of fin and is given by:

$$T_f(x, t) = T_m + tP_1 + \frac{q_w''}{k_f \sqrt{M}} \left[\frac{e^{\sqrt{M}x} + e^{-\sqrt{M}x} + e^{\sqrt{M}(x-l_f)} + e^{-\sqrt{M}(x-l_f)}}{e^{\sqrt{M}l_f} - e^{-\sqrt{M}l_f}} \right] \quad (2.90)$$

where

$$P_1 = \frac{2\alpha_f q_w''}{l_f k_f (1 + M\alpha_f t)} - \frac{Q_1}{l_f \sqrt{M}} (e^{\sqrt{M}l_f} - 1) - \frac{R_1}{l_f \sqrt{M}} (1 - e^{-\sqrt{M}l_f}) \quad (2.91a)$$

$$Q_1 = \frac{q_w''}{k_f t \sqrt{M}} \left[\frac{1 + e^{-\sqrt{M}l_f}}{e^{\sqrt{M}l_f} - e^{-\sqrt{M}l_f}} \right] \quad (2.91b)$$

$$R_1 = \frac{q_w''}{k_f t \sqrt{M}} \left[\frac{1 + e^{\sqrt{M}l_f}}{e^{\sqrt{M}l_f} - e^{-\sqrt{M}l_f}} \right] \quad (2.91c)$$

$$M = \frac{k_s}{k_f \delta Y(t)} \quad (2.91d)$$

The location of solid-liquid interface in Region 2, that is in direction Y, Y(t) is defined following the Megerlin method [70] as below.

$$Y(t) = 2 \left[\frac{\sqrt{1 + 2St} - 1}{2} \right]^{1/2} \sqrt{\alpha_s t} \quad (2.92)$$

where, St denotes the Stefan number and is provided by,

$$St = \frac{c_s (T_m - T_f)}{L_p}. \quad (2.93)$$

It may be noted by using Eqs. 2.90-2.93, one can obtain temperature variation of the fin and the location of solid-liquid interface Y(t).

Constant imposed temperature at the walls

Fig. 2.15b shows the location of solid-liquid interface during solidification in two different regions for constant imposed temperature at the end walls.

Region 1, $\{0 \leq x \leq X(t)\}$

Here, the solution of the model is obtained by considering similar governing equation (Eq. 2.72), initial condition (Eq. 2.73a-2.73b) and assumed temperature

profile (Eq. 2.74). In addition to this, boundary condition for constant imposed end wall heat flux (Eq. 2.73c) is replaced with constant end wall temperature boundary condition and is given as:

$$T_s(0,t) = T_s(l_f,t) = T_w \quad T_w < T_m \quad (2.94)$$

On integrating the governing equation (Eq. 2.72) from end wall to interface of solid and liquid with respect to x and utilizing the initial and boundary conditions given by Eqs. (2.73a-2.73b, 2.94), Eq. (2.72) can be rewritten as:

$$\frac{d}{dt} \int_0^{X(t)} \rho c_s [T_j(x,t) - T_m] dx = -\rho L_p X'(t) - k_s T_s(0,t) \quad \text{for } 0 < x < X(t) \quad (2.95)$$

$A_4(t)$ and $B_4(t)$ are the constants in assumed temperature profile and their values are obtained as:

$$A_4(t) = \frac{L_p}{c_s X(t)} \left[-1 + \sqrt{1 - 2st_s} \right] \quad (2.96)$$

$$B_4(t) = \frac{L_p}{2c_s \{X(t)\}^2} \left[-1 + \sqrt{1 - 2st_s} \right]^2 \quad (2.97)$$

Utilizing Eqs. (2.75), (2.95) – (2.97), the position of interface of solid and liquid is given as:

$$X(t) = 2 \left[\frac{3(-1 + 2st_s - \sqrt{1 - 2st_s})}{-7 - 2st_s + \sqrt{1 - 2st_s}} \right] \sqrt{\alpha_s t} \quad (2.98)$$

Region 2, $\{0 \leq x \leq Y(t)\}$

It may be noted that solution of Region 2 for this model is obtained by considering similar governing equation (Eq. 2.85), initial condition (Eq. 2.87a) and assumed temperature profile (Eq. 2.89). In addition, following boundary conditions for constant imposed end wall heat flux (Eq. 2.87b) is replaced with constant end wall temperature boundary condition and is given as:

$$T_f(0,t) = T_f(l_f,t) = T_w \quad (2.99)$$

Applying the initial and boundary conditions of the fin (Eqs. 2.87a, 2.99) in Eq. (2.88) and substituting in Eq. (2.89), one can obtain the temperature variation of fin and is given by:

$$T_f(x,t) = T_w + tP_2 \left[e^{\sqrt{M}(x-l_f)} + e^{-\sqrt{M}x} - (1 + e^{-\sqrt{M}l_f}) \right] \quad (2.100)$$

where

$$P_2 = \frac{(T_m - T_w)l_f\sqrt{M}}{2t \left[e^{-\sqrt{M}l_f} \left\{ e^{(\sqrt{M}l_f/2)} - 1 \right\} + \left\{ 1 - e^{(-\sqrt{M}l_f/2)} \right\} - \frac{l_f\sqrt{M}}{2} \left\{ 1 + e^{-\sqrt{M}l_f} \right\} + \frac{M\alpha_f t (e^{-\sqrt{M}l_f} - 1)}{1 + M\alpha_f t} \right]} \quad (2.101a)$$

$$M = \frac{k_s}{k_f \delta Y(t)} \quad (2.101b)$$

Here, the solid-liquid interface $Y(t)$ is defined similar to the Eq. (2.92). Also, variation in temperature of the fin and the location of solid-liquid interface $Y(t)$ can be obtained using the Eqs. (2.92-2.93, 2.100-2.101).

Convective air environment at the walls

The location of solid-liquid interface during solidification in two different regions for convective air environment boundary condition is shown in Fig. 2.15c.

Region 1, $\{0 \leq x \leq X(t)\}$

In addition to Governing Eq. (2.72), initial and boundary conditions (Eqs. 2.73a-2.74b) and assumed temperature profile (Eq. 2.75), constant air environment boundary condition is used instead of constant imposed end wall heat flux (Eq. 2.73c) to obtain the solution. And, the solution is given as:

$$\frac{-\partial T_s(0,t)}{\partial x} + Z_s \{T_s(0,t) - T_\infty\} = 0 \quad (2.102)$$

The governing equation (2.73) can be rewritten by integrating it with respect to x from end wall to interface of solid and liquid, and substituting the initial and

boundary conditions (Eqs. 2.73a-2.73b, 2.102) we can obtain the following relation:

$$\frac{d}{dt} \int_0^{X(t)} \rho c_s [T_s(x,t) - T_m] dx = -\rho L_p X'(t) - h[T_\infty - T(0,t)] \quad \text{for } 0 < x < X(t) \quad (2.102)$$

Here $k_s \llll h$, therefore assuming

$$\frac{k_s}{h} \approx 0 \quad (2.103)$$

The value of constants $A_4(t)$ and $B_4(t)$ assumed in temperature profile (Eq. 2.75) are obtained as:

$$A_4(t) = \frac{L_p}{c_s X(t)} \left[\sqrt{1 + st_s} - 1 \right] \quad (2.104)$$

$$B_4(t) = \frac{-L_p}{2c_s \{X(t)\}^2} \left[\sqrt{1 + st_s} - 1 \right]^2 \quad (2.105)$$

where, st_s is Stefan number for solid PCM and is given by $st_s = \frac{c_s (T_m - T_\infty)}{L_p}$.

Utilizing Eqs. 2.75, 2.102, 2.104 and 2.105, the solid-liquid interface position is given as:

$$X(t) = \frac{3ht}{\rho c_s} \left[\frac{st_s - 2 \left\{ 1 - \sqrt{1 + st_s} \right\}}{7 - st_s - \sqrt{1 + st_s}} \right] \quad (2.106)$$

Region 2, $\{0 \leq x \leq Y(t)\}$

In addition to governing Eq. (2.85), initial condition (Eq. 2.87a) and assumed temperature profile (Eq. 2.89), constant air environment boundary condition is used instead of constant imposed end wall heat flux (Eq. 2.87b) for obtaining the solution. The solution is given as:

$$\frac{-\partial T_f(0,t)}{\partial x} + Z_f \{T_f(0,t) - T_\infty\} = \frac{\partial T_f(l_f,t)}{\partial x} + Z_f \{T_f(l_f,t) - T_\infty\} = 0 \quad (2.107)$$

The temperature variation of fin is obtained by substituting Eqs. (2.87a, 2.88 and 2.107) in Eq. (2.89); given as:

$$T_f(x,t) = T_\infty + tP_3 \left[Q_3 e^{\sqrt{M}x} + e^{-\sqrt{M}x} + \left\{ Q_3 \times \left(\frac{\sqrt{M}}{Z_f} - 1 \right) - 1 - \frac{\sqrt{M}}{Z_f} \right\} \right] \quad (2.108)$$

where

$$P_3 = \frac{(T_m - T_\infty)l_f}{t \left[\left\{ R_3 \left(\frac{\sqrt{M}}{Z_f} - 1 \right) - 1 - \frac{\sqrt{M}}{Z_f} \right\} \{l_f + 2S_3\} + \{R_3 + e^{-\sqrt{M}l_f}\} \left\{ \left(\frac{e^{\sqrt{M}l_f} - 1}{\sqrt{M}} \right) + S_3(1 + e^{\sqrt{M}l_f}) \right\} \right]} \quad (2.109a)$$

$$Q_3 = \frac{\frac{\sqrt{M}}{Z_f} e^{-\sqrt{M}l_f} + \frac{\sqrt{M}}{Z_f} + 1 - e^{-\sqrt{M}l_f}}{\frac{\sqrt{M}}{Z_f} e^{\sqrt{M}l_f} + \frac{\sqrt{M}}{Z_f} - 1 + e^{\sqrt{M}l_f}} \quad (2.109b)$$

$$R_3 = \frac{\alpha_f Z_f t}{1 + M \alpha_f t} \quad (2.109c)$$

$$M = \frac{k_s}{k_f \delta Y(t)} \quad (2.109d)$$

Here, the solid-liquid interface $Y(t)$ is defined similar to the Eq. (2.92). Also, temperature variation of fin and location of solid-liquid interface $Y(t)$ can be obtained using the Eqs. 2.92-2.93, 2.108-2.109.

2.3.3 Results and discussion

Melting analysis

Present study utilizes aluminum and the laboratory grade n-octadecane as fin and PCM materials, respectively; the thermo-physical properties are summarized in Table 2.5 [87]. Here, l_f , l_c and l_f/l_c (σ) denotes the length of fin, half height of cell and aspect ratio of the cell, respectively. The value of σ is varied between 0.5 to 2 and fin thickness is considered as 2 mm for all the cases (Table 2.7). Here, T_i denotes the initial temperature of storage unit. The value of T_i is maintained at 28°C for the analysis.

Table 2.7 Different parameters of storage system

Parameters/Cases	I	II	III
Half height of cell, l_c (mm)	20	15	10
Fin length, l_f (mm)	10	15	20
Aspect ratio, $\sigma = l_f / l_c$	0.5	1	2

Validation of present analytical model

Here, the results of complete melting time obtained from the present analytical model are validated with the test results of Henze and Humphrey [202]. In their experimental study, n-octadecane and aluminum is used as PCM and fin material, respectively. The thermo-physical properties of n-octadecane and aluminum considered in the experimental study are shown in Table 2.5. Constant wall temperature condition is employed on one wall of the enclosure, while the other wall is insulated. Half height of cell (l_c) and length of fin (l_f) are kept as 127 mm and 15.875 mm, respectively for all the cases. Half thickness of fin is considered as 3.175 mm.

Table 2.8a shows the comparison of current predictions with the available test results. Maximum deviation between the current predictions and existing test results to obtain the complete melting time is found to be less than 12%. The deviation obtained is because various experimental aspects such as contact resistance between fin and wall, variable value of melt convection and difference in initial and melting temperature (1°C in the experimental model and 0°C in the present model). Although the assumptions and simplification in analytical modelling leads to deviation, it can be seen from Table 2.8a that good agreement is obtained between experimental and analytical results.

Also, the results obtained from the present model for constant end wall temperature are compared with the numerical and analytical solutions of Lamberg and Siren [87] to validate the present model. The comparison of current predictions with the available numerical and analytical models is shown in Fig. 2.18-2.19 and Table 2.8b-2.8c.

Table 2.8(a) Comparison of melting time obtained with current model and existing test results [202]

$T_w - T_m$ (°C)	Stefan number (St)	Melting time obtained with current model (I)	Melting time obtained from test results [202] (II)	Error $\left \frac{I - II}{II} \right $ ×100%
20	0.22	7480	7469	0.15%
10	0.11	16390	15170	8.04%
5	0.055	41500	37339	11.14%

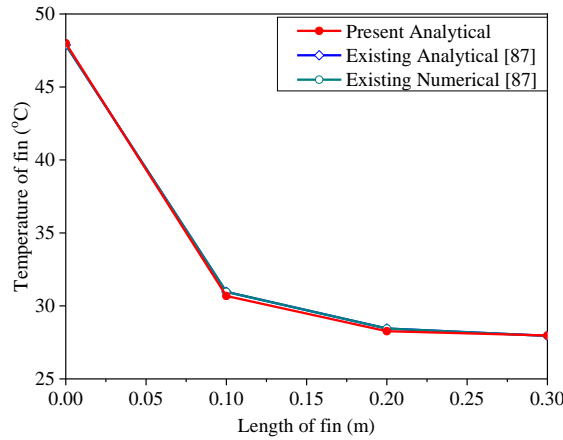


Fig. 2.18 Comparison of current prediction for temperature distribution with the results obtained from two-dimensional numerical and analytical models [87]

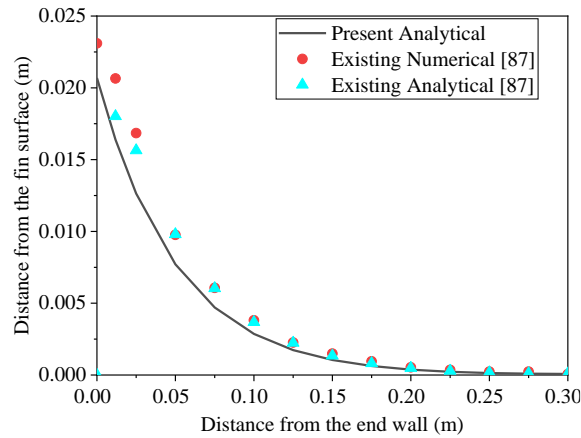


Fig. 2.19 Comparison of present prediction for interface location with two-dimensional numerical and analytical models [87]

Table 2.8(b) Comparison of temperature distribution obtained with current model, existing numerical and analytical models [87] at
t = 3600 s

Distance from the end wall surface (m)	Temperature of fin surface predicted from present study (°C) (I)	Temperature of fin surface obtained from existing numerical model [87] (°C) (II)	Temperature of fin surface obtained from existing analytical model [87] (°C) (III)	Error $\left \frac{I - II}{II} \right $ ×100%	Error $\left \frac{I - III}{III} \right $ ×100%
0	48	48	48	0	0
0.1	30.68	30.77	30.96	0.27	0.90
0.2	28.27	28.367	28.45	0.34	0.64
0.3	27.98	28.077	27.95	0.35	0.10

Table 2.8(c) Comparison of solid/liquid interface obtained with current analytical model, existing numerical and analytical models [87] at $t = 3600$ s

Distance from the end wall surface (m)	Distance of interface from fin surface predicted from present study (m) (I)	Distance of interface from fin surface obtained from existing numerical model [87] (m) (II)	Distance of interface from fin surface obtained from existing analytical model [87] (m) (III)	Error $ \text{II-I} \times 100\%$	Error $ \text{III-I} \times 100\%$
0	2.069×10^{-2}	2.31×10^{-2}	0	0.241	2.069
0.1	2.86×10^{-3}	3.81×10^{-3}	3.68×10^{-3}	0.095	0.082
0.2	3.76×10^{-4}	5.36×10^{-4}	4.86×10^{-4}	0.016	0.010
0.3	7.70×10^{-5}	5.95×10^{-5}	9.95×10^{-5}	0.002	0.002

Maximum deviation between the current predictions and existing numerical and analytical models to predict the surface temperature of fin is found to be 0.35% and 0.95%, respectively. While, the maximum deviation between the current model with the existing numerical and analytical models to anticipate solid-liquid interface location is obtained as 0.24% and 2.06%, respectively. Therefore, the results obtained from the current analysis can be used to design the TES systems.

Constant heat flux

In this study, three imposed heat flux ($q_w'' = 500, 1000$ and 2000 W/m^2) are considered for the analysis. Fig. 2.20 shows solid-liquid interface location for three different aspect ratio ($\sigma = 0.5, 1$ and 2) at different time duration of PCM during melting in the storage system.

It can be seen that the geometry of PCM storage influences the melting rate of PCM. The advancement of solid-liquid interface in X-direction is found to be 26.98%, 17.98% and 13.49% at $\sigma = 0.5, 1$ and 2 , respectively for the duration of 300 s. While, for the higher time duration of 600 s, the percentage advancement of solid-liquid interface in X-direction is found to be 67.56%, 45.04% and 33.78% at $\sigma = 0.5, 1$ and 2 , respectively. This indicates the amount of heat flow in X-direction (from wall to interface of solid-liquid) is greater for $\sigma < 1$. While, the percentage advancement of solid-liquid interface in Y-direction is obtained as 34.72%, 31.58% and 35.23% at $\sigma = 0.5, 1$ and 2 , respectively for the duration of 300 s. While, for the higher time duration of 600 s, the advancement of solid-liquid interface in X-direction is obtained as 11.57%, 44.97% and 51.06% at $\sigma = 0.5, 1$ and 2 , respectively. It implies that the amount of heat flow in Y-direction (from fin to interface of solid-liquid) is greater for $\sigma > 1$. At $\sigma = 1$, the heat flows from wall as well as fin to interface of solid-liquid (both in X and Y directions). In addition, it can be seen that the overall movement of solid-liquid interface is faster for $\sigma < 1$ in comparison to $\sigma \geq 1$. This may be because of the large amount of heat flow in X-direction for $\sigma < 1$. The ratio of flow of heat in X-direction and Y-direction decreases with the increase in the value of σ . This is because of decrease in the height of end wall and increase in length of fin with the increase in value of σ .

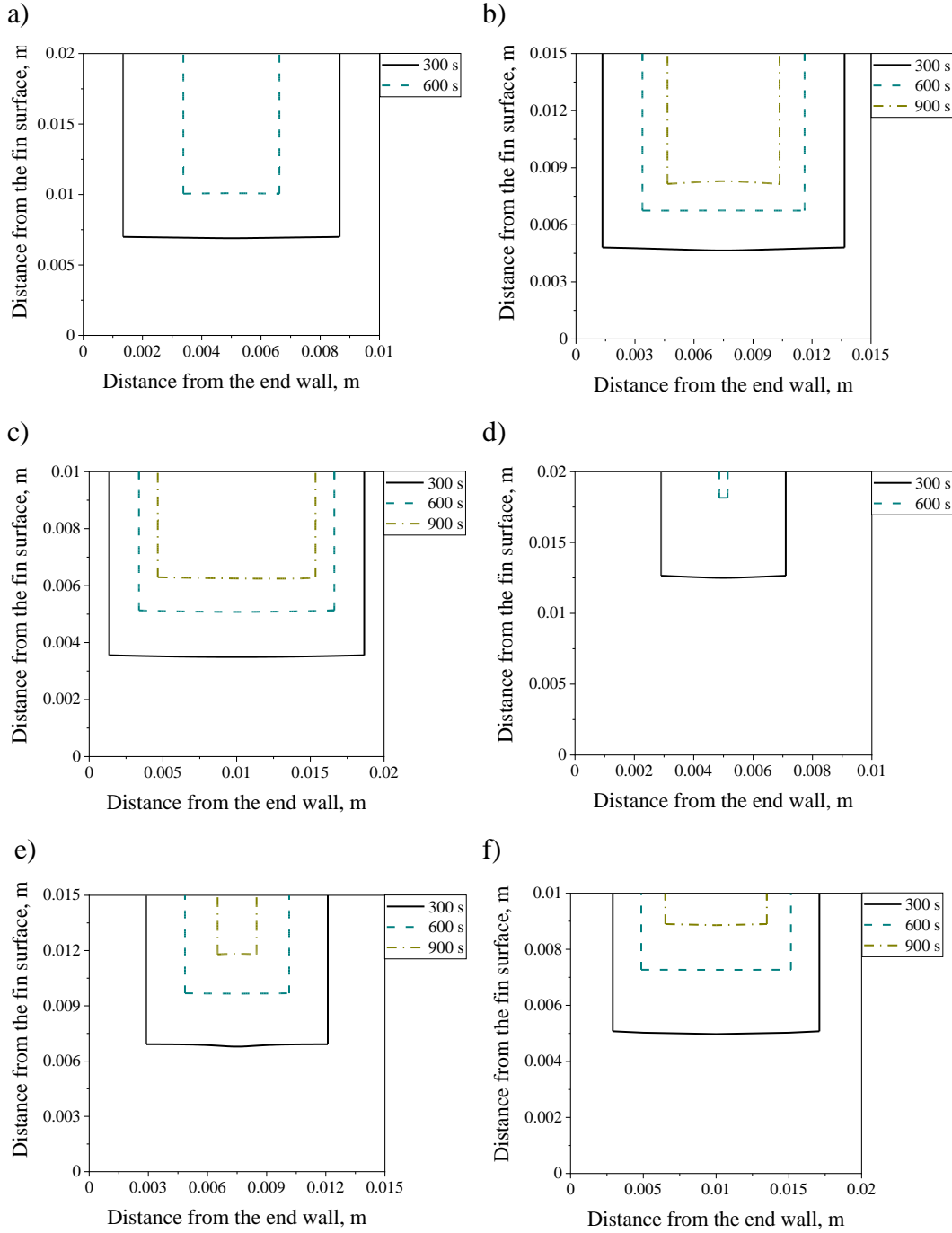


Fig. 2.20(a-f) Comparison of solid-liquid interface locations at different time for (a) $q_w'' = 500 \text{ W/m}^2, \sigma = 0.5$, (b) $q_w'' = 500 \text{ W/m}^2, \sigma = 1$, (c) $q_w'' = 500 \text{ W/m}^2, \sigma = 2$, (d) $q_w'' = 1000 \text{ W/m}^2, \sigma = 0.5$, (e) $q_w'' = 1000 \text{ W/m}^2, \sigma = 1$, and (f) $q_w'' = 1000 \text{ W/m}^2, \sigma = 2$

Also, the speed of movement of solid-liquid interface increases with the increase in imposed wall heat flux (q_w''). Difference in the percentage advancement of solid-liquid interface position (X, Y) with the increase in q_w'' from 500 W/m² to 1000 W/m² is found to be (31.02%, 28.18%), (20.68%, 14.25%), and (15.51%, 15.11%) for $\sigma = 0.5, 1$ and 2 , respectively at 300 s. While, at 600 s, difference in the percentage advancement of solid-liquid interface position (X, Y) with the increase in q_w'' from 500 W/m² to 1000 W/m² is found to be (29.60%, 40.47%), (19.73%, 19.50%), and (14.8%, 21.60%) for $\sigma = 0.5, 1$ and 2 , respectively. Here, it may be noted that the effect of increase in q_w'' on the percentage advancement of solid-liquid interface decreases with the increase in time duration in X-direction. While in Y-direction the advancement in solid-liquid interface increases with the increase in time duration.

The amount of liquid PCM in PCM storage at particular time duration is denoted by melt fraction of PCM (ε). The value of melt fraction lies between zero (PCM is entirely solid) and unity (PCM is entirely liquid) and is expressed as [16, 17, 67]:

$$\varepsilon = \frac{2X(t)[l_c - \delta - Y(t)] + l_f Y(t)}{[l_c - \delta]l_f} \quad (2.110)$$

The melt fraction (ε) and melting time (t_m) of PCM at different time duration obtained from the present model is shown in Fig. 2.21(a-b). The value of melt fraction (ε) attains unity value at faster rate for the PCM storage unit with smaller value of aspect ratio (σ). This implies that the storage system with lower σ needs lesser time for complete melting of PCM for same TCE and PCM volume fraction. The melting time is found to reduce by 49% with the reduction of σ from 2 to 0.5 for $q_w'' = 500$ W/m². This may be due to the fact that lower amount of heat flows from X-direction at $\sigma \geq 1$. Also, the ratio of amount of heat flow from end wall (X-direction) and fin (Y-direction) decreases with the increase in value of σ . That is due to decrease and increase in the height of end wall and

length of fin, respectively with the increase in σ . Also, t_m is found to decrease by 74% with the increase in q_w'' from 500 W/m^2 to 2000 W/m^2 for $\sigma = 2$.

Variation in melting time of PCM for different σ for same TCE and PCM volume fraction is shown in Fig. 2.22. Total t_m is found to be less for $\sigma = 0.5$ compared to $\sigma = 8$ (Fig. 2.22). The reduction in melting time is found to be $\sim 84\%$ with the reduction in value of σ from 8 to 0.125 for a given imposed q_w'' . Also, with the increase in the imposed q_w'' from 500 W/m^2 to 2000 W/m^2 , the t_m reduces by $\sim 55\%$ for the same aspect ratio.

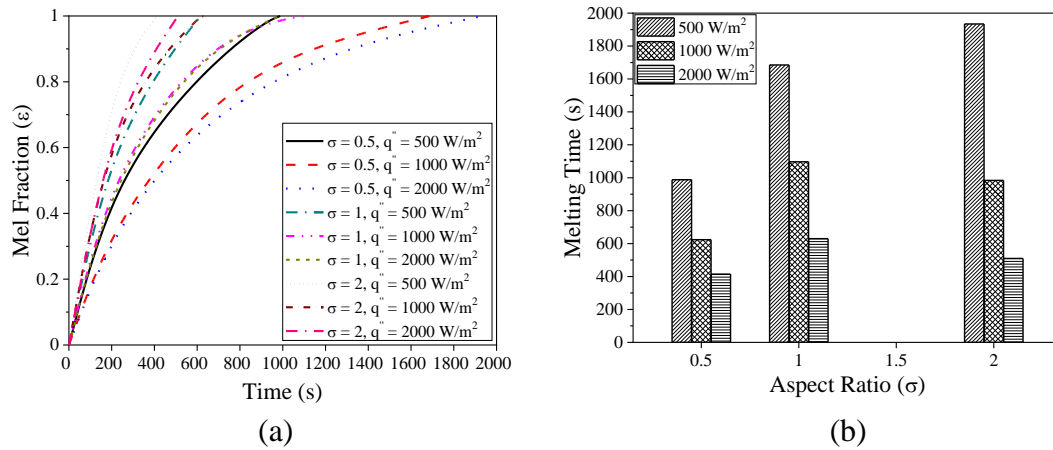


Fig. 2.21 (a) Melt fraction variation of PCM, (b) Melting time of PCM for different σ

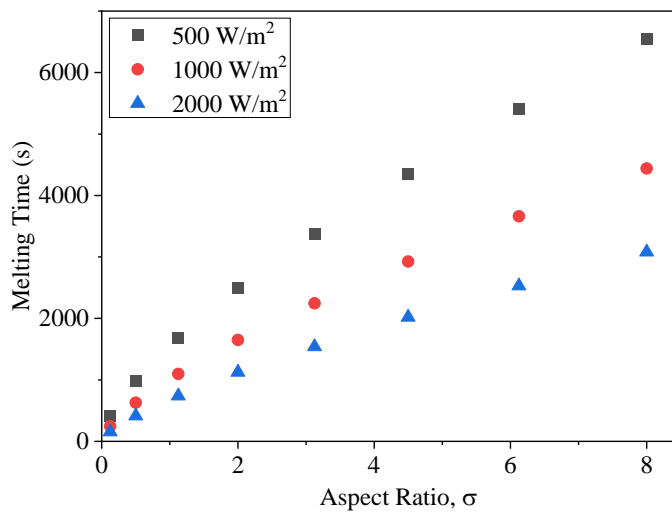


Fig. 2.22 Melting time variation of PCM for various imposed q_w''

Efforts have been made to propose a correlation for melting time (t_m) as a function of σ and q_w'' and is given in Eq. (2.111).

$$t_m = 48142.267(\sigma)^{0.7016} (q_w'')^{-0.5563} \quad 0.125 \leq \sigma \leq 8 \quad (2.111)$$

The correlation for t_m is valid for the aspect ratio varying between 0.125 and 8, is able to predict the 99% of the computed data within the error band of $\pm 6\%$ (Fig. 2.23).

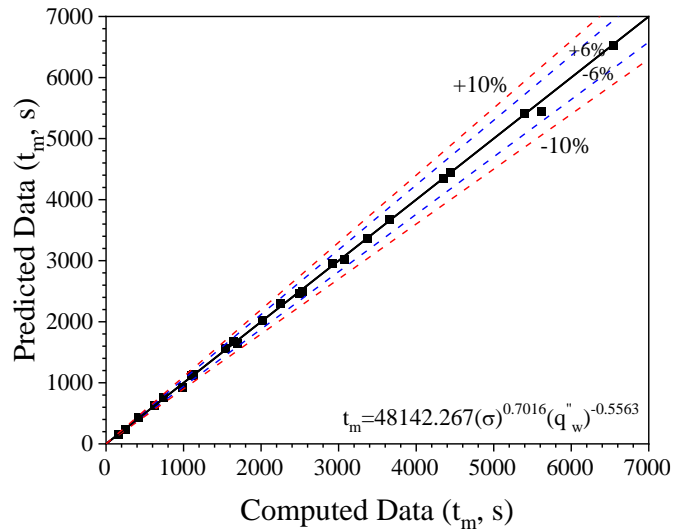


Fig. 2.23 Comparison of predicted and computed melting time of PCM

Constant temperature

In this study, three end wall temperatures ($T_w = 48^\circ\text{C}$, 58°C and 68°C) are chosen for the analysis. Fig. 2.24 shows solid-liquid interface position for $\sigma = 0.5$, 1 and 2 at different time during melting of PCM in the storage system. The geometry of PCM storage influences the melting rate of PCM. The advancement of interface of solid-liquid in X-direction is found to be 61.32%, 40.88% and 30.66% at $\sigma = 0.5$, 1 and 2, respectively for the duration of 300 s. While, the interface location advancement occurs at 86.70%, 57.80% and 43.35% for $\sigma = 0.5$, 1 and 2, respectively for the duration of 600 s. This indicates the heat flow in X-direction (from wall to interface of solid-liquid) is higher at $\sigma < 1$.

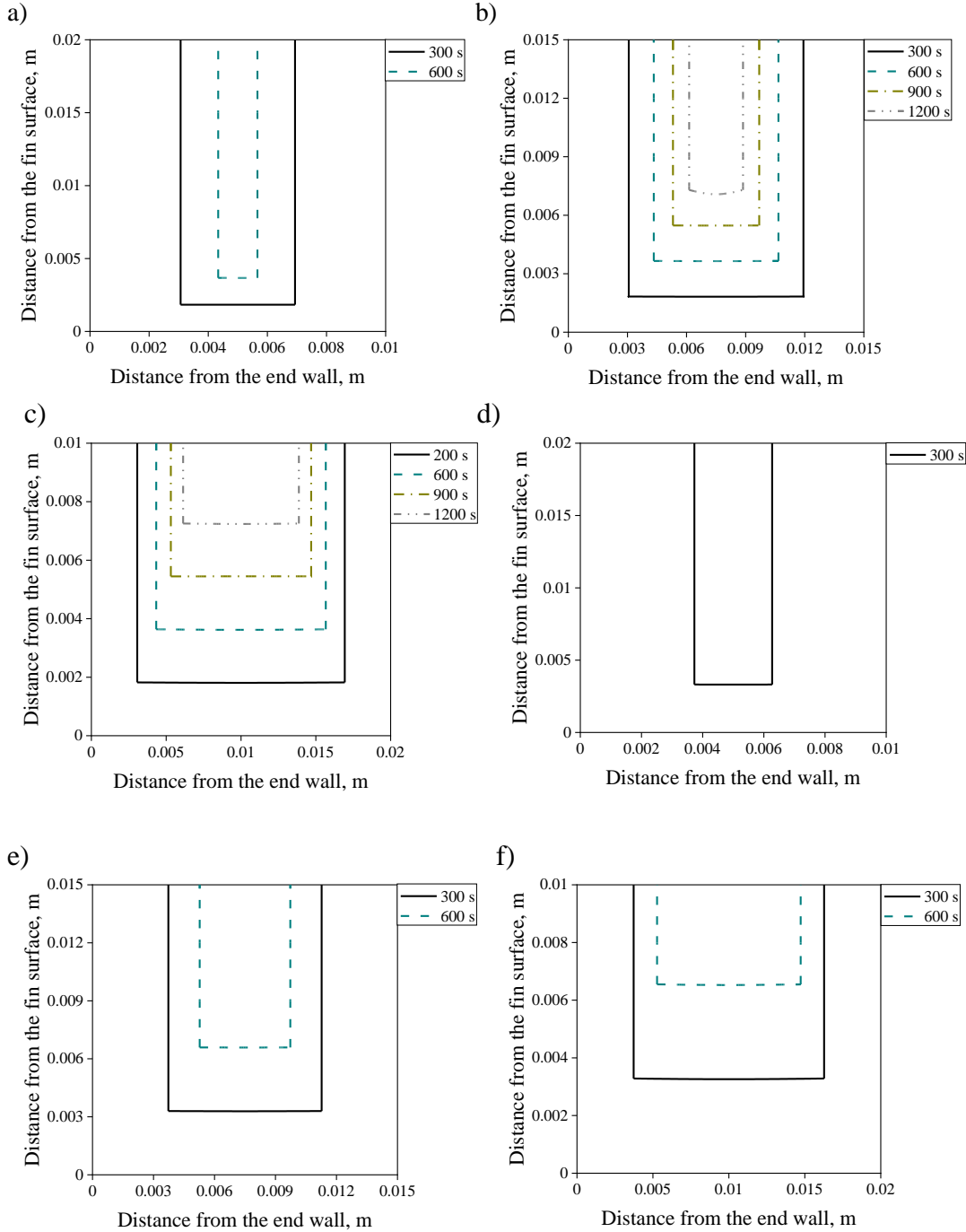


Fig. 2.24 (a-f) Comparison of solid-liquid interface locations at different time for (a) $T_w = 48^\circ\text{C}$, $\sigma = 0.5$, (b) $T_w = 48^\circ\text{C}$, $\sigma = 1$, (c) $T_w = 48^\circ\text{C}$, $\sigma = 2$, (d) $T_w = 58^\circ\text{C}$, $\sigma = 0.5$, (e) $T_w = 58^\circ\text{C}$, $\sigma = 1$, and (f) $T_w = 58^\circ\text{C}$, $\sigma = 2$

While, the percentage advancement of solid-liquid interface in Y-direction is found to be 9.17%, 12.17% and 18.16% at $\sigma = 0.5$, 1 and 2, respectively for the

duration of 300 s. While, the advancement of interface of solid-liquid interface occurs at 18.34%, 24.33% and 36.30% at $\sigma = 0.5, 1$ and 2 , respectively for the duration of 600 s. This indicates the heat flow in Y-direction (from fin to solid/liquid interface) is higher at $\sigma > 1$. At $\sigma = 1$, the heat flows equally in X and Y directions. In addition, figure shows that the overall movement of solid-liquid interface is faster at $\sigma = 0.5$ compared $\sigma \geq 1$. The ratio of heat flow from end wall (X-direction) and fin (Y-direction) decreases with the increase in value of σ . This is because the height of end wall decreases and length of fin increases with the increase in value of σ .

Also, the speed of movement of solid-liquid interface increases with the increase in end wall temperature (T_w). Difference in the percentage advancement of solid-liquid interface position (X, Y) with the increase in T_w from 48°C to 58°C are found to be (13.26%, 7.39%), (8.84%, 9.77%), and (6.63%, 14.57%) for $\sigma = 0.5, 1$ and 2 , respectively at 300 s. While, at 600 s, difference in the percentage advancement of solid-liquid interface position (X, Y) with the increase in T_w from 48°C to 58°C are found to be (12.50%, 19.57%), and (9.38%, 29.05%) for $\sigma = 1$ and 2 , respectively. With the increase in T_w , the advancement of interface of solid-liquid interface decreases in X-direction, while it increases in Y-direction.

Here, the melt fraction of PCM is estimated by using Eq. 2.110. The melt fraction and melting time (t_m) of PCM at different time duration obtained from the present model is shown in Fig. 2.25. The value of melt fraction (ε) attains unity value at faster rate for the PCM storage unit with smaller value of aspect ratio (σ). This implies that the storage unit with lower σ needs lesser time to complete melting of PCM for same TCE and PCM volume fraction. t_m is found to reduce by 53% with the reduction of σ from 2 to 0.5 for $T_w = 48^\circ\text{C}$. This may be due to the similar reason as explained for constant heat flux boundary condition. That is lower amount of heat flows from wall to interface of solid-liquid (X-direction) for $\sigma \geq 1$. Also, the ratio of amount of heat flow from end wall (X-direction) and fin (Y-direction) decreases with the increase in value of σ .

Also, t_m is found to decrease by 59% with the increase in T_w from 48°C to 68°C for $\sigma = 2$.

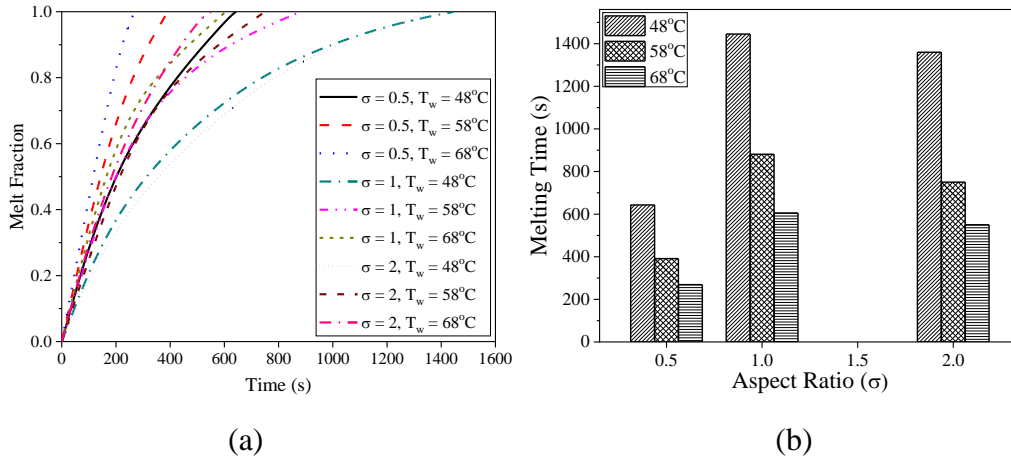


Fig. 2.25 (a) Melt fraction variation of PCM, (b) Melting time of PCM for different σ

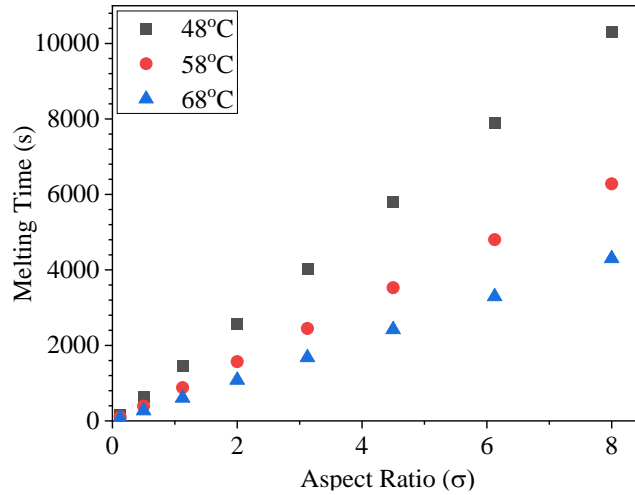


Fig. 2.26 Melting time variation of PCM for various imposed T_w

Total melting time of PCM for different σ at same TCE and PCM volume fraction is shown in Fig. 2.26. t_m is found to increase with the increase in σ . Total t_m of PCM is significantly less for $\sigma = 0.125$ compared to $\sigma = 8$ (Fig. 2.26). The reduction in t_m is found to be ~73% by reducing σ from 8 to 0.125 for given end wall temperature. In addition to this, with the increase in T_w from 48°C to 68°C, the melting time reduces by ~60% for the same aspect ratio.

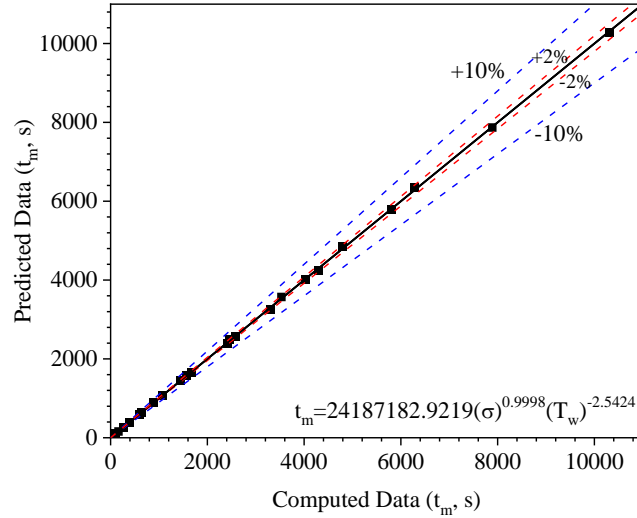


Fig. 2.27 Comparison of predicted and computed melting time of PCM

Efforts have been made to propose a correlation for melting time (t_m) in terms of σ and T_w and is given in Eq. (2.112).

$$t_m = 24187182.9219(\sigma)^{0.9998}(T_w)^{-2.5424} \quad 0.125 \leq \sigma \leq 8 \quad (2.112)$$

The correlation for melting time is valid for the aspect ratio varying between 0.125 and 8, is able to predict the 99% of the computed data within the error band of $\pm 7\%$ (Fig. 2.27).

Convective air environment

Here, constant imposed convective air environment has been considered for melting of PCM. Different heat transfer coefficient values ($h_w = 45, 55$ and 65 $\text{W/m}^2\text{-K}$) and heat transfer fluid (HTF) temperature ($T_\infty = 38^\circ\text{C}, 48^\circ\text{C}$ and 58°C) are chosen for the analysis. Fig. 2.28 shows solid-liquid interface location for three different aspect ratio ($\sigma = 0.5, 1$ and 2) at different time duration of PCM during melting in the storage unit. As discussed earlier, the geometry of PCM storage influences the melting rate of PCM. The advancement of interface of solid-liquid in X direction is found to be 27.14%, 18.09% and 13.57% at $\sigma = 0.5, 1$, and 2 , respectively for the duration of 300 s.

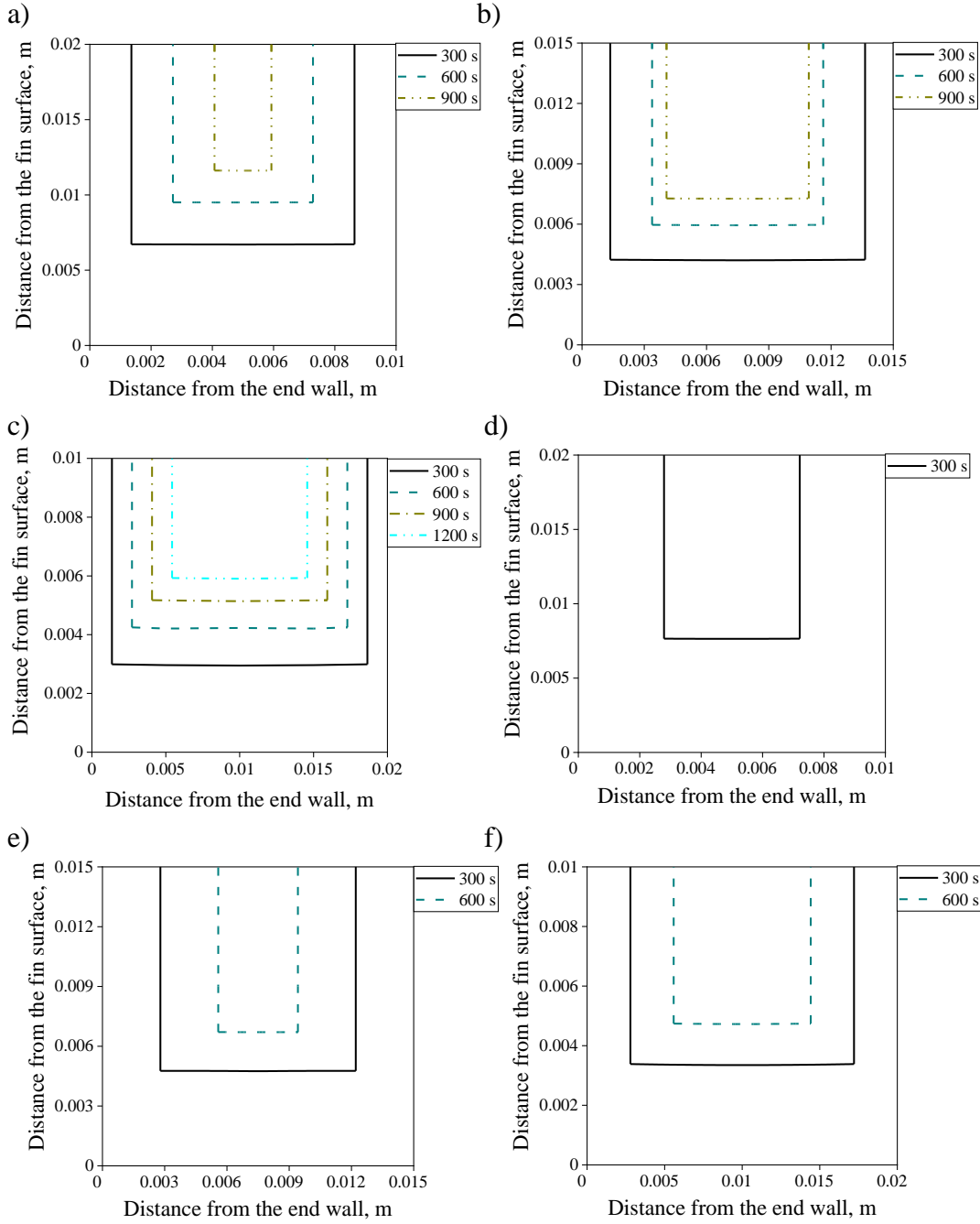


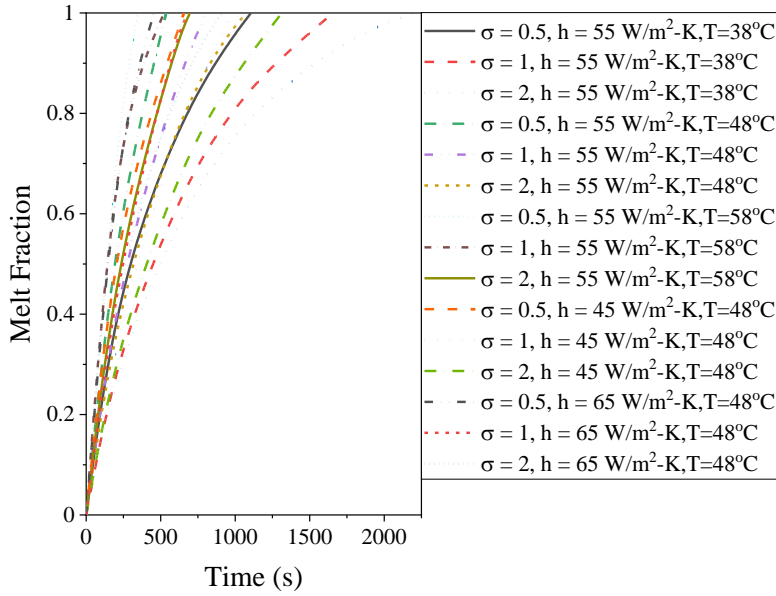
Fig. 2.28 (a-f) Comparison of solid-liquid interface locations for $h_w = 55 \text{ W/m}^2$ at different time for (a) $T_\infty = 38^\circ\text{C}$, $\sigma = 0.5$, (b) $T_\infty = 38^\circ\text{C}$, $\sigma = 1$, (c) $T_\infty = 38^\circ\text{C}$, $\sigma = 2$, (d) $T_\infty = 48^\circ\text{C}$, $\sigma = 0.5$, (e) $T_\infty = 48^\circ\text{C}$, $\sigma = 1$, and (f) $T_\infty = 48^\circ\text{C}$, $\sigma = 2$

While the propagation of solid-liquid interface in Y-direction is 54.28%, 36.18% and 27.14% at $\sigma = 0.5$, 1 and 2, respectively for the duration of 600 s. The heat

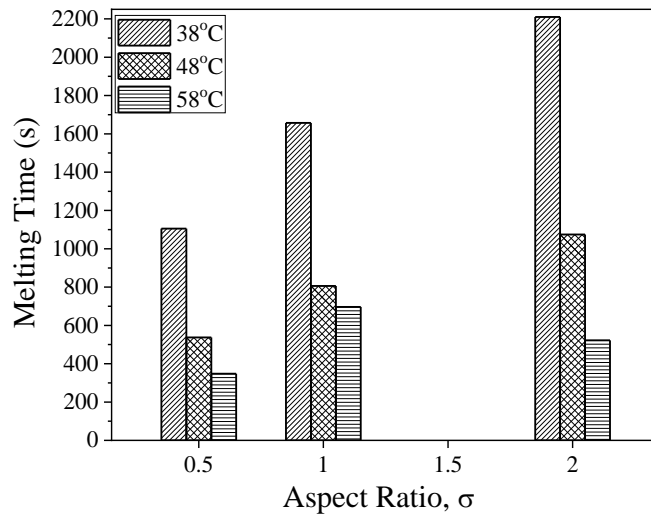
flow in X-direction (wall to interface of solid-liquid) is greater at $\sigma < 1$. While, the advancement of interface of solid-liquid in Y-direction is obtained as 33.56%, 28.12% and 29.72% at $\sigma = 0.5, 1$ and 2 , respectively for the duration of 300 s. While the advancement of interface of solid/liquid is found to be 47.50%, 39.70% and 42.28% at $\sigma = 0.5, 1$ and 2 , respectively for the duration of 600 s. As discussed earlier, the heat flow in Y-direction is greater at $\sigma > 1$. While, at $\sigma = 1$, heat flows towards both X-direction and Y-direction. This is similar to flow of heat in constant heat flux and end wall temperature cases. In addition, figure shows that the overall movement of solid-liquid interface is faster for $\sigma = 0.5$ compared $\sigma \geq 1$. This may be because of the large amount of heat flow in X-direction $\sigma < 1$ and the ratio of heat flow between X-direction and Y-direction decreases with the increase in value of σ .

Also, it can be noticed that the speed of movement of interface of solid-liquid increases with the increase in HTF temperature (T_∞) at constant heat transfer coefficient (h_w) value of 55 W/m²-K. Difference in the percentage advancement of solid-liquid interface position (X, Y) with the increase in T_∞ from 38°C to 48°C are found to be (55.82%, 38.22%), (37.21%, 31.73%), and (27.91%, 33.66%) for $\sigma = 0.5, 1$ and 2 , respectively at 300 s. While, at 600 s, difference in the percentage advancement of solid-liquid interface position (X, Y) with the increase in T_∞ from 38°C to 48°C are found to be (74.41%, 44.72%), and (55.81%, 51.22%) for $\sigma = 1$ and 2 , respectively. The effect of increase in T_∞ at $h_w = 55$ W/m²-K on the percentage advancement of solid-liquid interface decreases in X-direction and increases in Y-direction with the increase in time duration.

Here, the melt fraction of PCM is defined similar to Eq. 2.110. The melt fraction and melting time of PCM at different time duration obtained from the present model is shown in Fig. 2.29. The value of melt fraction (ε) attains unity value at faster rate for the PCM storage unit with smaller value of aspect ratio (σ). This implies that the storage system with lower σ needs lesser time for complete melting of PCM for same TCE and PCM volume fraction.



(a)



(b)

Fig. 2.29 (a) Melt fraction variation of PCM, (b) Melting time of PCM for different σ

The melting time is found to reduce by 50% with the reduction of σ from 2 to 0.5 for $T_\infty = 38^\circ\text{C}$ at constant $h_w = 55 \text{ W/m}^2\text{-K}$. This may be due to the similar reason as explained for constant heat flux boundary condition. That is lower amount of heat flows from wall to interface of solid-liquid (X-direction) for $\sigma \geq 1$. Also, the ratio of amount of heat flow from end wall (X-direction) and fin (Y-

direction) decreases with the increase in σ . The melting time is found to decrease by 30% with the increase in imposed h_w from 45 W/m²-K to 65 W/m²-K at given T_∞ and σ . Also, melting time (t_m) is found to reduce by ~69% for increasing the T_∞ from 38°C to 58°C for a given value of σ and h_w .

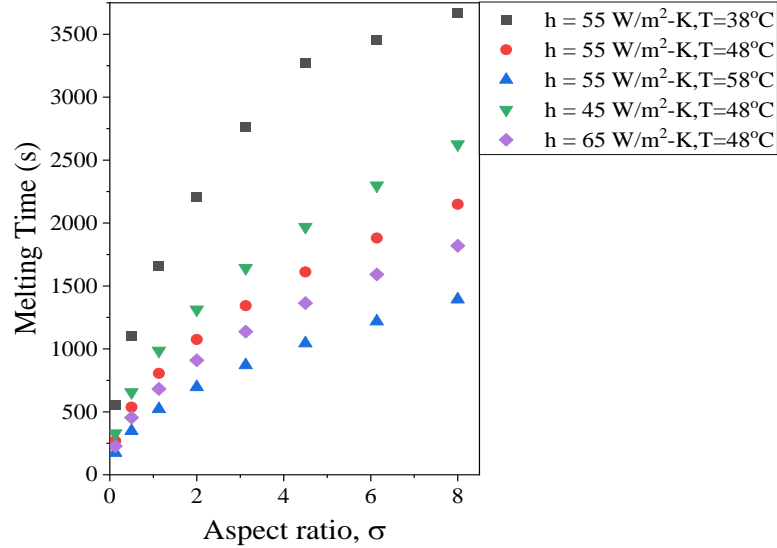


Fig. 2.30 Melting time variation of PCM for different h_w and T_∞

Fig. 2.30 shows variation in total melting time of PCM for different σ at same TCE and PCM volume fraction. Different values of T_∞ and h_w have been considered in this analysis. The reduction in t_m is obtained as ~88% by reducing the σ from 8 to 0.125 for a given h_w . Also, with the increase in h_w from 45 W/m²-K to 65 W/m²-K, the t_m reduces by ~31% at $T_\infty = 48^\circ$ C for the same σ . However, the reduction in t_m is obtained as ~69% by increasing T_∞ from 38°C to 58°C at $h_w = 55$ W/m²-K for the same value of σ . Here, the increase of T_∞ has greater effect on t_m in comparison to increase in h_w .

Efforts have been made to propose a correlation for melting time (t_m) in terms of σ and T_∞ and is given in Eq. (2.113).

$$t_m = 1993.4784(\sigma)^{0.4577} (h)^{-0.9685} (T_\infty)^{-2.6537} (T_m)^{3.9814} \quad 0.125 \leq \sigma \leq 8 \quad (2.113)$$

The correlation for melting time is valid for the aspect ratio varying between 0.125 and 8, is able to predict the 99% of the computed data within the error band of $\pm 20\%$ (Fig. 2.31).

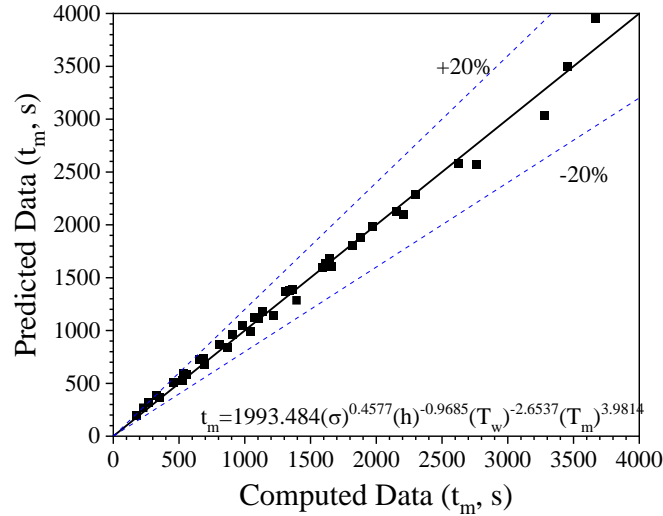


Fig. 2.31 Comparison of predicted and computed melting time of PCM

Solidification analysis

Here, the fraction of the fin length to the half-height of symmetry section (l_f/l_c) is considered as the cell aspect ratio (σ) (Fig. 2.15). Various cases with different values of σ are considered for the analysis. For all the cases, half of the thickness of fin is considered to be 0.5 mm. Initially, the liquid PCM is at the solidification temperature (T_m) inside the PCM storage unit.

Comparison of present prediction with other theoretical models

In order to verify the present analytical model, efforts have been made to compare the location of solid-liquid interface and solid fraction of PCM obtained from the present prediction with the two-dimensional numerical solution of Talati et al. [16], Lamberg et al. [17] and Mosaffa et al. [67] for constant heat flux, end wall temperature and convective air boundary condition, respectively and the results of the validation are shown in Fig. 2.32(a-c) and Table 2.9(a-c). For the sake of brevity, the location of solid-liquid interface in directions X and Y are compared at $\sigma < 1$. The average error, between the present predictions and two-

dimensional numerical results, in obtaining the location of solid-liquid interface in direction X is found to be 0.69 mm, 1.73 mm and 1.06 mm for constant heat flux, end wall temperature and convective air boundary condition, respectively. While, the average error in obtaining the location of solid-liquid interface in direction Y is found to be 0.19 mm, 0.39 mm and 0.57 mm in direction Y for constant heat flux, end wall temperature and convective air boundary condition, respectively.

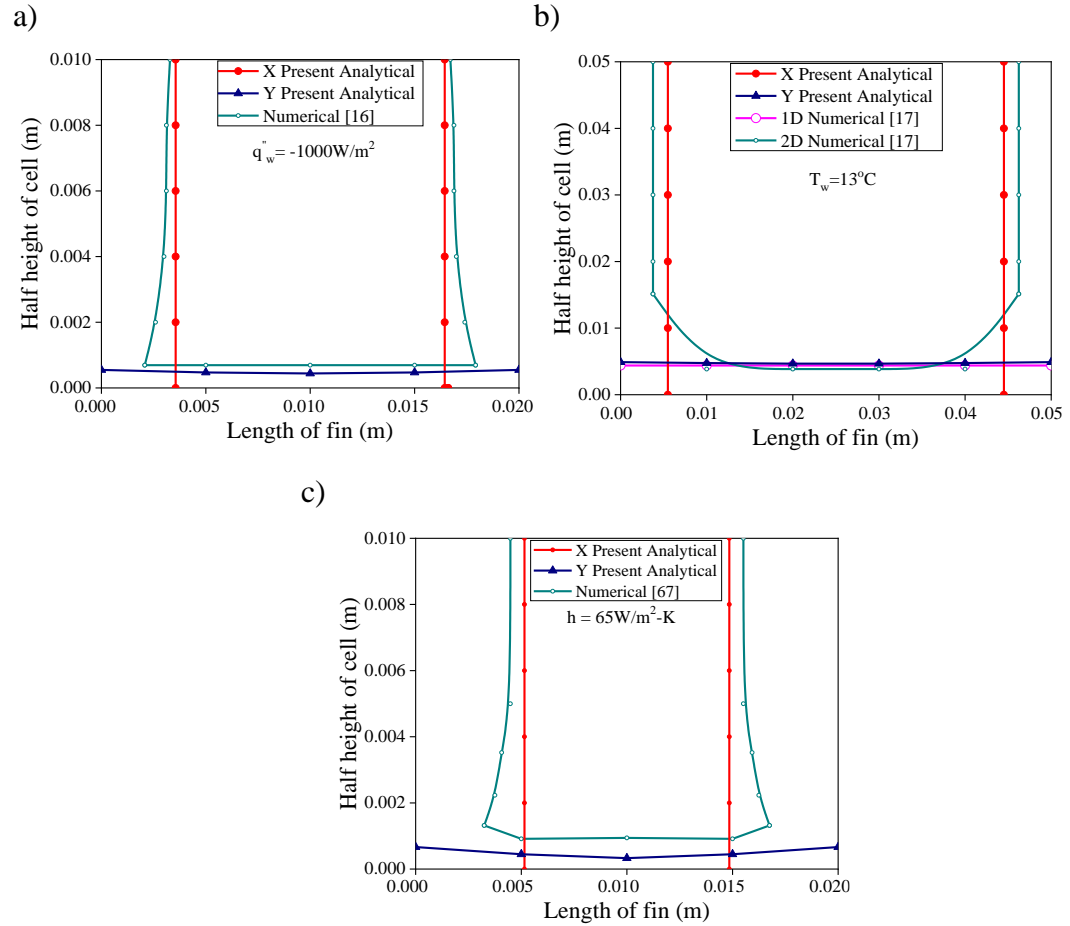


Fig. 2.32(a-c) Comparison of solid-liquid interface locations obtained by present model with the existing numerical solutions for (a) $\sigma = 2$, $t = 800$ s, constant heat flux boundary condition, (b) $\sigma = 5$, $t = 1085$ s, constant end wall temperature boundary condition, and (c) $\sigma = 2$, $t = 1000$ s, constant convective air environment boundary condition

The solid fraction of PCM during solidification for varied range of aspect ratio and different boundary condition are compared with the two-dimensional

numerical solutions and is summarized in Table 2.9(a-c). Present prediction exhibits good agreement with the numerical solution [16, 17, 67]. The maximum error between the present prediction and the two-dimensional numerical solution is found to be $\pm 13\%$. Therefore, the model can be useful in designing the PCM based thermal energy storage systems.

Table 2.9(a) Comparison of present analytical and two-dimensional numerical models [16] for constant heat flux boundary condition in different test cases

Aspect ratio (σ)	Time, s	Solid fraction predicted from present study (ε_{anal}) (I)	Solid fraction obtained from two- dimensional numerical model [16], (ε_{num}) (II)	Error (I- II) $\times 100\%$
0.5	400	0.43	0.35	6.7
1	400	0.30	0.25	3.3
2	400	0.26	0.21	1.4

Table 2.9(b) Comparison of present analytical and two-dimensional numerical models [17] for constant temperature boundary condition in different test cases

Aspect ratio (σ)	Time, s	Solid fraction predicted from present study (ε_{anal}) (I)	Solid fraction obtained from two- dimensional numerical model [17], (ε_{num}) (II)	Error (I- II) $\times 100\%$
Paraffin, 0.2	724	0.90	0.79	10.6
Paraffin, 1	1085	0.29	0.23	6.1
Paraffin, 5	1085	0.61	0.53	7.1

Table 2.9(c) Comparison of present analytical model and two-dimensional numerical model [67] for convective air boundary condition in different test cases

Aspect ratio (σ)	Time, s	Solid fraction predicted from present study (ε_{anal}) (I)	Solid fraction obtained from two-dimensional numerical model [6], (ε_{num}) (II)	Error (I-II) \times 100%
0.5	350	0.27	0.40	-13.0
1	500	0.27	0.36	-9.4
2	500	0.20	0.23	-3.0

Constant imposed temperature at the walls

In this study, pure n-octadecane paraffin is used as the PCM with aluminium as fins and commercial grade salt hydrate (Climsel 23) used as the PCM with steel as fins for the analysis. Table 2.10 summarizes the properties of fin materials and PCM. Different values of σ such as 0.2, 1 and 5 are considered for the analysis.

Table 2.10 Thermal properties of PCMs and fin materials [17]

Property	Paraffin Octadecane	Salt hydrate Climsel23	Aluminum fin	Steel fin
Density, ρ (kg/m ³)	777	1480	2,713	7854
Specific heat, c (J/kg-K)	2660	2660	960	434
Thermal conductivity, k (W/m-K)	0.149	0.6	180	60.5
Latent heat of fusion, L_p (J/kg)	241,360	148,000		
Solidification temperature, T_m (°C)	28	23	-	-
Viscosity, μ (kg/m-s)	0.00385	-	-	-
Thermal expansion coefficient, α (K ⁻¹)	0.001	-	-	-

Table 2.11 Dimensions of PCM storage, end wall temperature, and materials used in different test cases

Cases	Case 1	Case 2	Case 3	Case 4	Case 5	Case 6
PCM material	Paraffin	Paraffin	Paraffin	Salt hydrate	Salt hydrate	Salt hydrate
Fin material	Aluminum	Aluminum	Aluminum	Steel	Steel	Steel
wall temperature, T_w (°C)	13	13	13	8	8	8
Length of fin, l_f (mm)	10	50	50	10	50	50
Half height of cell, l_c (mm)	50	50	10	50	50	10
Aspect ratio, σ	0.2	1	5	0.2	1	5

Table 2.11 shows the dimensions of PCM storage unit for which the constant wall temperature was considered (Fig. 2.15b). It is observed from Fig. 2.33 that the aspect ratio (σ) of PCM storage unit affects the rate of solidification. The heat flows only in direction X, i.e. from wall to interface of solid and liquid when the value of σ is less than unity. However, the heat flows only in direction Y, i.e. from wall to solid-liquid interface. In case of σ equals to unity, heat flows from both wall to solid-liquid interface and fin to solid-liquid interface, i.e. both in X and Y directions.

Figs. 2.33(a-e) depict the comparison of locations of solid-liquid interface obtained from the present one-dimensional analytical predictions and two-dimensional numerical solutions of Lamberg et al. [17] for different values of t and σ . The maximum error in predicting solid-liquid interface by present model is found to be 1.82 mm and 0.37 mm in X- and Y-directions, respectively, at $\sigma = 5$ and $t = 1085$ s for n-octadecane. While, the maximum error for salt hydrate is found to be 1.23 mm and 1.43 mm in X-and Y-directions, respectively, at $\sigma = 1$ and $t = 4226$ s. However, present model exhibits excellent agreement with the two-dimensional numerical model for $\sigma = 0.2$.

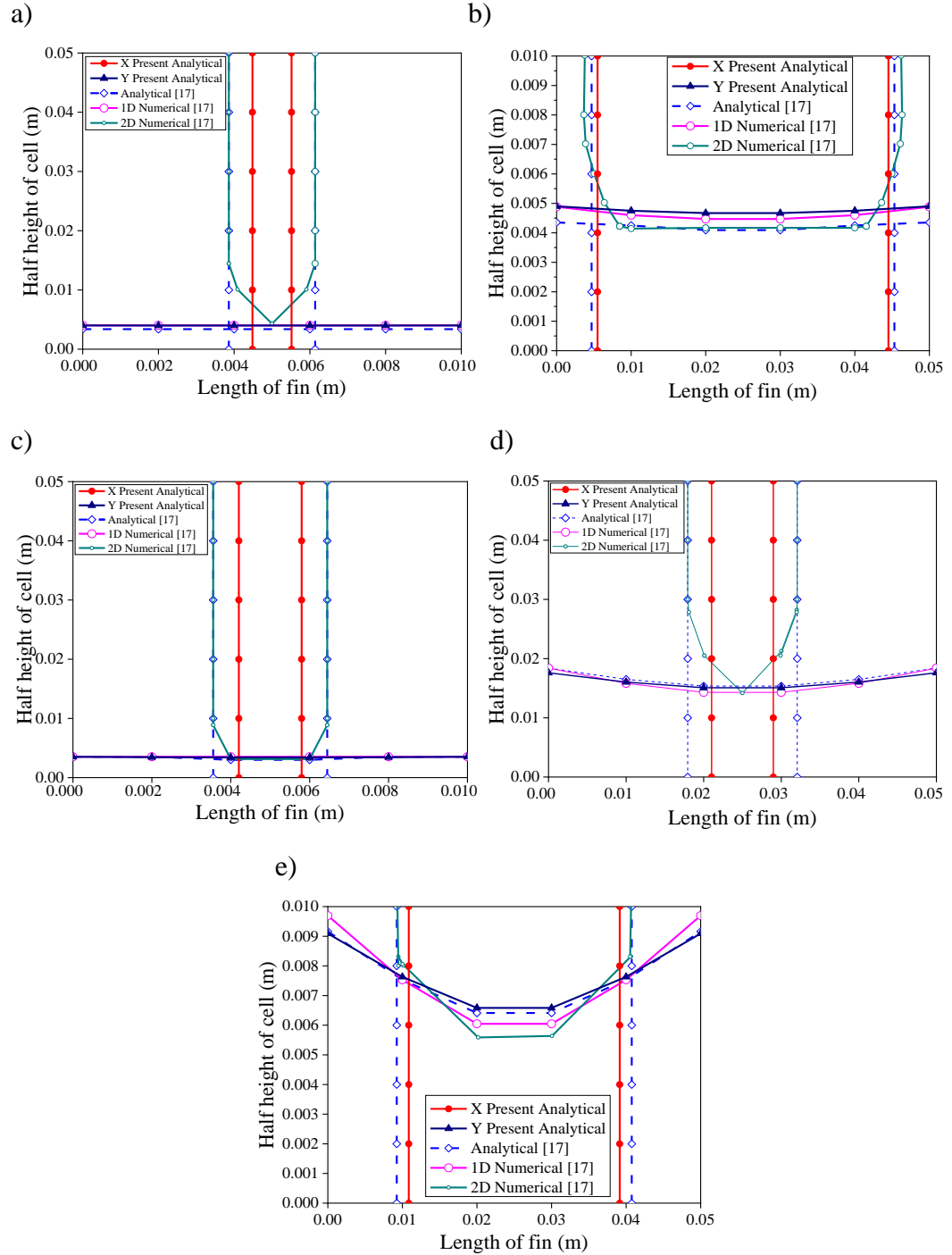


Fig. 2.33 (a-e) Comparison of solid-liquid interface locations obtained by present model with the one-dimensional analytical, one-dimensional numerical and two-dimensional numerical solutions by Lamberg et al. [17] for (a) $\sigma = 0.2, t = 724$ s, (b) $\sigma = 5, t = 1085$ s, (c) $\sigma = 0.2, t = 169$ s, (d) $\sigma = 1, t = 4226$ s, and (e) $\sigma = 5, t =$

1127 s

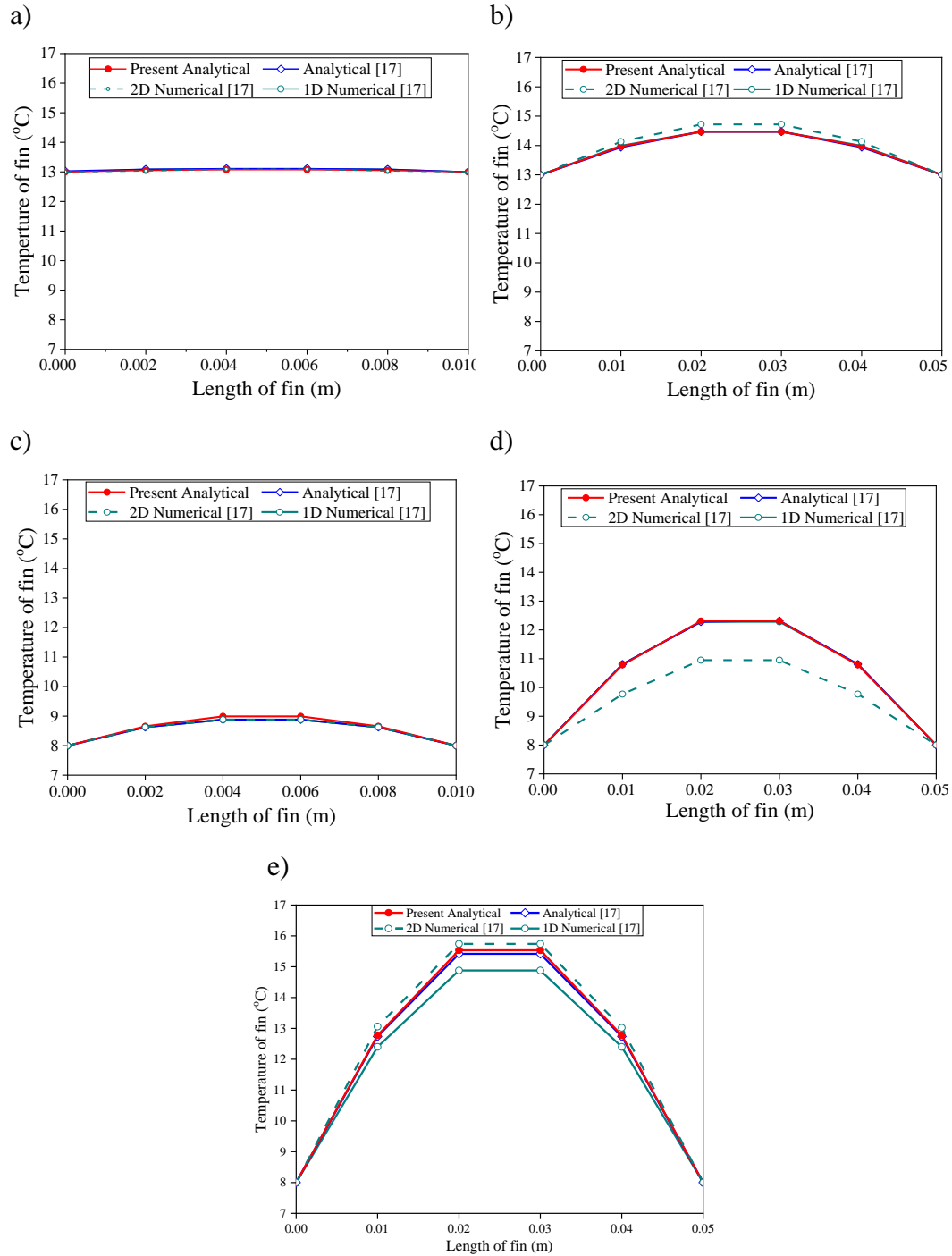


Fig. 2.34 (a-e) Comparison of fin temperatures obtained by present model with the one-dimensional analytical, one-dimensional numerical and two-dimensional numerical solutions by Lamberg et al. [17] for (a) $\sigma = 0.2, t = 724$ s, (b) $\sigma = 5, t = 1085$ s, (c) $\sigma = 0.2, t = 169$ s, (d) $\sigma = 1, t = 4226$ s, and (e) $\sigma = 5, t = 1127$ s

Here, efforts were also made to estimate the variation of temperature in fin and the same are presented in Fig. 2.34. The temperature variation of fin obtained from the present analytical model is compared with the results obtained by employing Fourier's ring theory and finite difference method [17]. The maximum error in temperature by the present model is found to be negligible (0.25°C) at $\sigma = 5$ and $t = 1085$ s for n-octadecane. While, the maximum error for salt hydrate is found to be -1.389°C at $\sigma = 1$ and $t = 4226$ s. The present results agree well with the existing numerical results [17].

Solid fraction of PCM usually denotes the amount of solidified PCM in the symmetric storage cell for a given duration. The solid fraction of PCM changes from entirely solid ($\varepsilon = \text{unity}$) to completely liquid ($\varepsilon = 0$) and is expressed as [16, 17, 67]:

$$\varepsilon = \frac{2X(t)[l_c - D - Y(t)] + l_f Y(t)}{[l_c - D]l_f} \quad (2.114)$$

The variation of solid fraction with time for two different PCMs for $\sigma = 0.2$ and $\sigma = 5$ is evaluated by using Eq. (2.114) and is demonstrated in Fig. 2.35. It may be noted that for the same aspect ratio the solidification rate is higher for salt hydrate as compared to paraffin because of better heat conductivity of salt hydrate compared to paraffin. This may be due to the difference in density and latent heat of fusion of two PCMs. The reduction in respective solidification rate is found to be 73.4% and 50% for $\sigma = 0.2$ and $\sigma = 5$ for paraffin and salt hydrate.

Total solidification time of PCM for solidification time of paraffin for different aspect ratio at constant volume of PCM and TCE is presented in Fig. 2.36. The solidification time is found to be less for lower aspect ratio of TES system. This may be because the distance between fins increases with the decrease in aspect ratio and a large amount of heat is discharged from the end walls. The PCM's total solidification time is remarkably less for lower value of aspect ratio ($\sigma = 0.05$) compared to $\sigma = 5$ (Fig. 2.36). The reduction in solidification time was found to be ~99% by reducing the aspect ratio from 5 to 0.05 for same imposed heat flux at the walls. In addition to this, with the decrease

in the imposed end wall from 18°C to 8°C, the solidification time reduces by ~54% for the same aspect ratio.

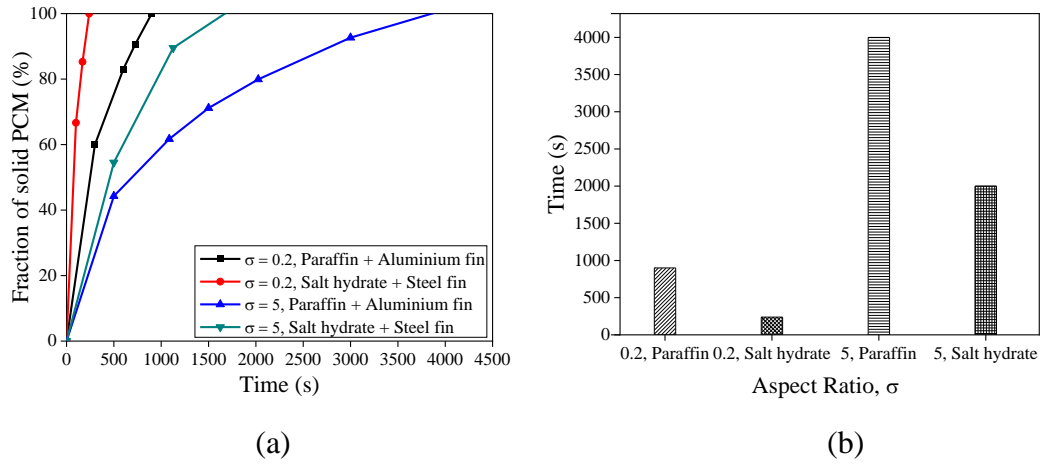


Fig. 2.35 (a) Variation of solid fraction of PCM with time, (b) Solidification time of PCM for different cell aspect ratios and PCMs

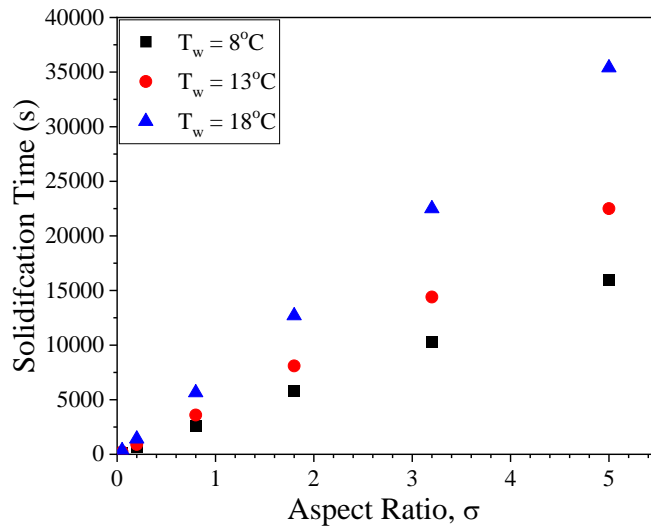


Fig. 2.36 Variation in total solidification time of PCM for different imposed temperature at the end walls

In the present investigation, a correlation has been proposed for solidification time (t_s) in terms of aspect ratio and end wall boundary condition and expressed in Eq. (2.115).

$$t_s = 329.3757(\sigma)^{1.0021}(T_w)^{1.0512} \quad (2.115)$$

The proposed correlation for t_s is valid for the range of $0.05 \leq \sigma \leq 8$ and the error band to anticipate 99% test data of the proposed correlation for solidification time (t_s) is found to be $\pm 10\%$ as shown in Fig. 2.37.

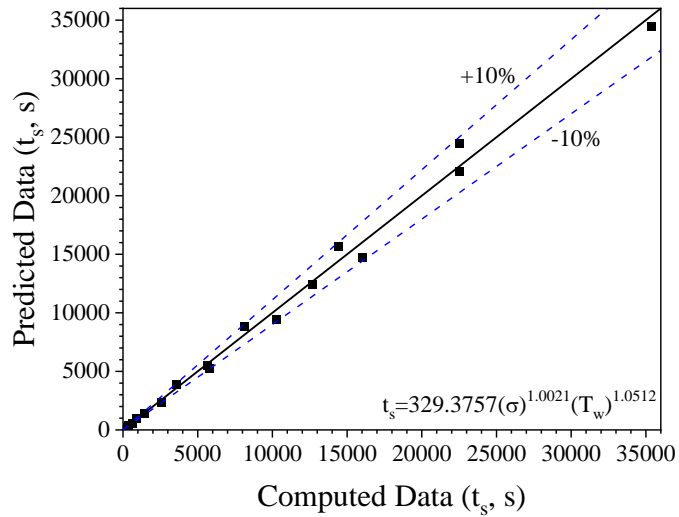


Fig. 2.37 Comparison of computed solidification temperature with those predicted by the proposed correlation

Constant imposed heat flux at the wall

The PCM and fin material considered for the present study are salt hydrate Climsel C28 and aluminium, respectively. Their properties are summarized in Table 2.12. The different values of σ are taken as 0.5, 1 and 2 for the analysis. Dimensions of PCM storage unit are shown in Table 2.13. Constant heat flux, $q_w'' = -1000 \text{ W/m}^2$, was taken for solidification of PCM in all the cases.

Figs. 2.38(a-f) depict the comparison of location of solid-liquid interface obtained from the present mathematical model with the one-dimensional analytical and two-dimensional numerical solutions of Talati et al. [16] for different values of time steps (t) and σ . Present predictions exhibit good agreement with the one-dimensional results obtained by employing separation of variable method and two-dimensional results obtained by finite difference method [16]. It is evident that geometry of PCM storage changes the solidification rate. When σ is very less than unity, heat flows only from wall to interface of solid and

liquid, in direction X. When σ is much larger than unity, heat flows only from fin to interface of solid and liquid, in direction Y. In case of σ equal to unity, heat flows from both wall and fin to interface of solid and liquid, in the directions X and Y.

Fig. 2.38 shows the comparison of results obtained by using integral method in the present study with various available mathematical models. Here, the results of one-dimensional analytical and two-dimensional numerical models of Talati et al. [16] are considered for comparison. In all the cases, sharp corners are formed on the interface of solid and liquid at the point near both the wall and the fin surfaces. This is because of the high temperature at the corners. The maximum error in solid-liquid interface between the two sets of results was found to be 0.96 mm in direction X and 0.40 mm in direction Y at $\sigma = 2$ and $t = 400$ s. However, present model exhibits excellent agreement with the two-dimensional numerical model when the value of $\sigma = 0.5$.

Table 2.12 Thermal properties of PCM and fin material [16]

Property	Paraffin	Aluminum fin
Density, ρ (kg/m ³)	1,450	2,770
Specific heat, c (J/kg-K)	3,600	875
Thermal conductivity, k (W/m-K)	0.6	177
Latent heat of fusion, L_p (J/kg)	162,000	-
Melting/solidification temperature, T_m (°C)	28	-

Table 2.13 Dimensions of PCM storage unit

Dimensions	Case 1	Case 2	Case 3
Length of fin, l_f (mm)	10	15	20
Half height of cell, l_c (mm)	20	15	10
Cell aspect ratio, $\sigma = \frac{l_f}{l_c}$	0.5	1	2

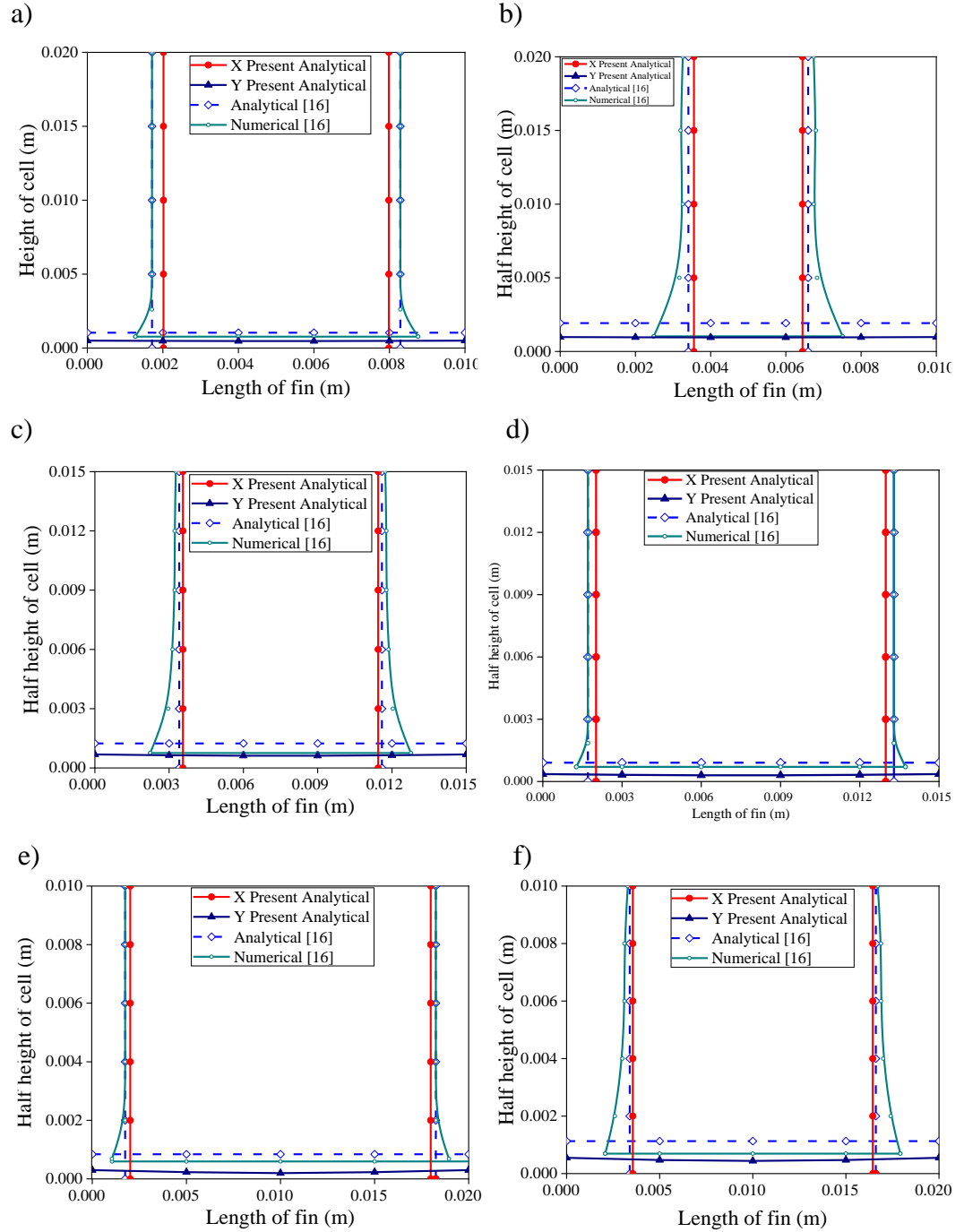


Fig. 2.38 (a-f) Comparison of solid-liquid interface locations obtained by present model with the one-dimensional analytical and two-dimensional numerical solutions by Talati et al. [16] with $q_w'' = -1000 \text{ W/m}^2$ for (a) $\sigma = 0.5$, $t = 400 \text{ s}$, (b) $\sigma = 0.5$, $t = 800 \text{ s}$, (c) $\sigma = 1$, $t = 400 \text{ s}$, (d) $\sigma = 1$, $t = 800 \text{ s}$, (e) $\sigma = 2$, $t = 400 \text{ s}$, and (f) $\sigma = 2$, $t = 800 \text{ s}$

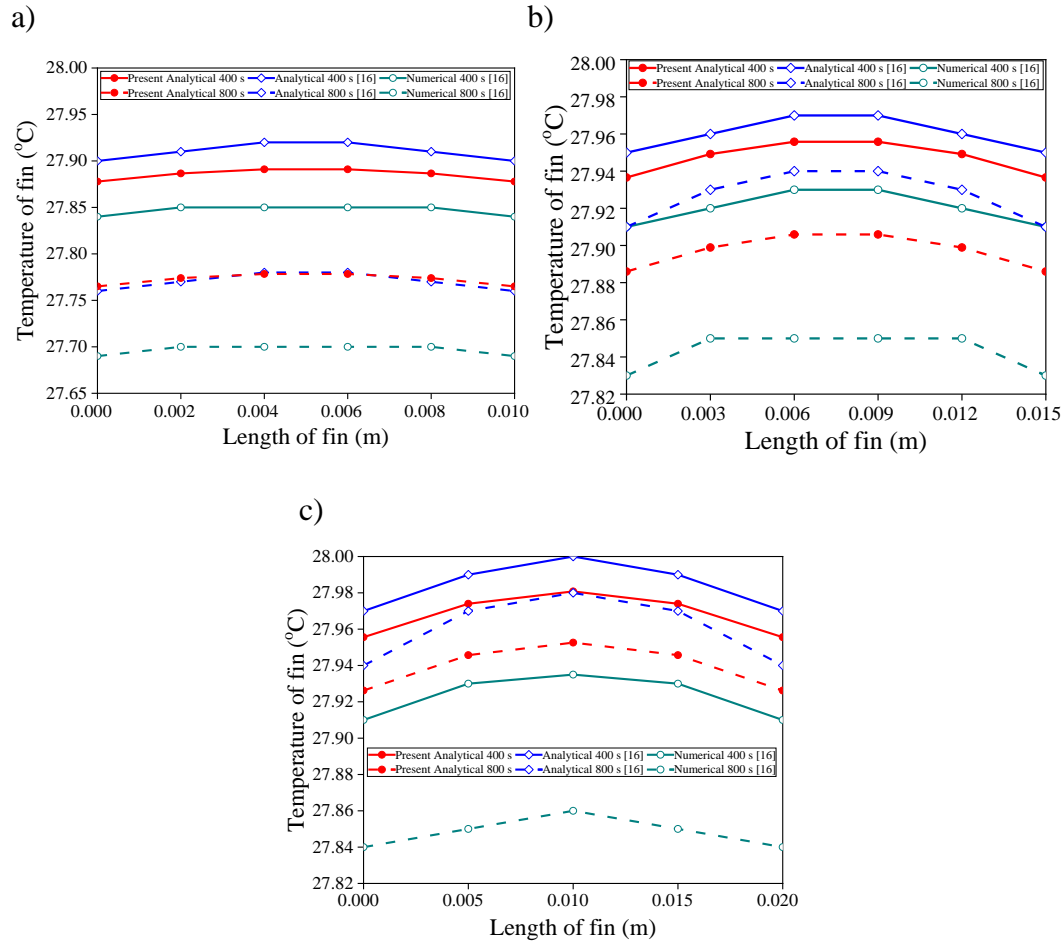


Fig. 2.39 (a-c) Comparison of fin temperatures obtained by present model with the one-dimensional analytical and two-dimensional numerical solutions by Talati et al. [16] with $q_w'' = -1000 \text{ W/m}^2$ for (a) $\sigma = 0.5$, $t = 400$ s and $t = 800$ s (b) $\sigma = 1$, $t = 400$ s and $t = 800$ s, and (c) $\sigma = 2$, $t = 400$ s and $t = 800$ s

The temperature distributions of fin obtained from the present analytical model are compared with the results obtained by employing separation of variable and finite difference methods [16], and are shown in Figs. 2.39(a-c). It is observed from Fig. 2.39(a) that the present predictions exhibit good agreement with the results obtained by separation of variable (SV) method. The maximum error in temperature difference between both sets of results is found to be negligible ($\sim 0.095^\circ\text{C}$) at $\sigma = 2$ and $t = 800$ s. It has been reported that one-dimensional heat transfer occurs in case of short fins when the value of σ is much smaller than unity. The temperature variation along the fin length is found to be low due to

high thermal conductivity and constant heat flux. However, the temperature variation increases as l_f increases. The current results exhibit excellent agreement with the numerical solutions obtained by Talati et al. [16]. Also, the present predictions agree well with the results obtained by employing separation of variable method.

Time of PCM solidification in a rectangular storage having fins for each symmetry cell was obtained using the analytical formulation for different cases and is presented in Fig. 2.40. It is noticed from figure that the PCM solidification is fast for smaller values of σ . Initially, the PCM solidification is faster because of small thickness of solid PCM layer. However, as the time progresses, the thickness of solid PCM layer increases, which increases the thermal resistance and solidification rate decreases.

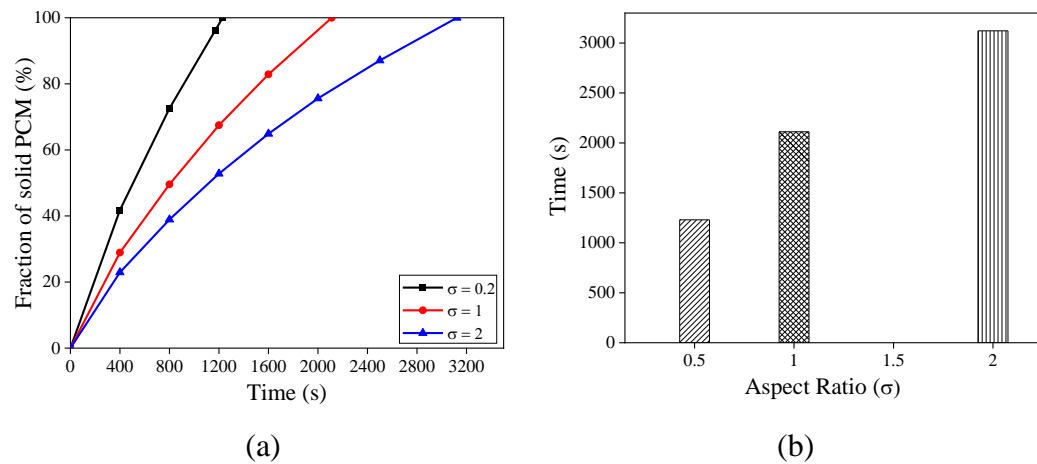


Fig. 2.40 (a) Variation of solid fraction of PCM with time, (b) Solidification time of PCM for different cell aspect ratios

Fig. 2.41 shows variation in PCM's total solidification time for different aspect ratio at constant volume of PCM and TCE. It may be noted from the figure that solidification time is less for lower aspect ratio of TES system for constant volume of PCM and TCE. This may be due to the fact that with the decrease in aspect ratio, distance between fins increases and a huge amount of heat is liberated from the end walls. The PCM's total solidification time is found to be less for lower aspect ratio ($\sigma=0.125$) compared to $\sigma=8$ (Fig. 2.41). The

reduction in solidification time is found to be ~93% by reducing the aspect ratio from 8 to 0.125 for a given imposed heat flux at the walls. In addition to this, with the increase in the imposed heat flux from 500 W/m² to 2000 W/m², the solidification time reduces by ~60% for the same aspect ratio.

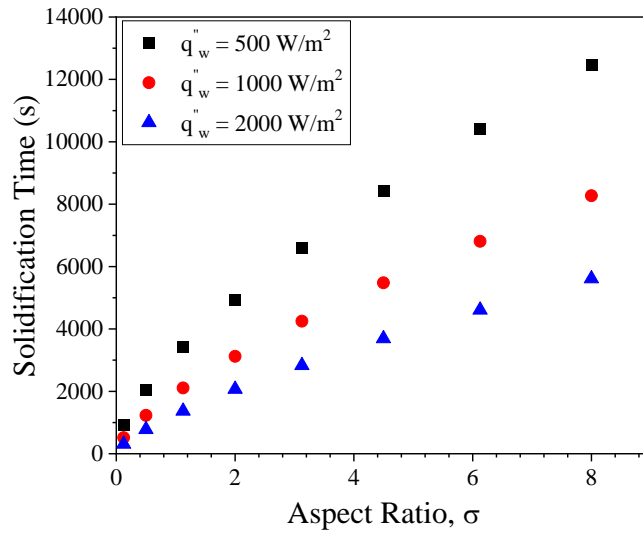


Fig. 2.41 Variation in total solidification time of PCM for different imposed heat flux at the end walls

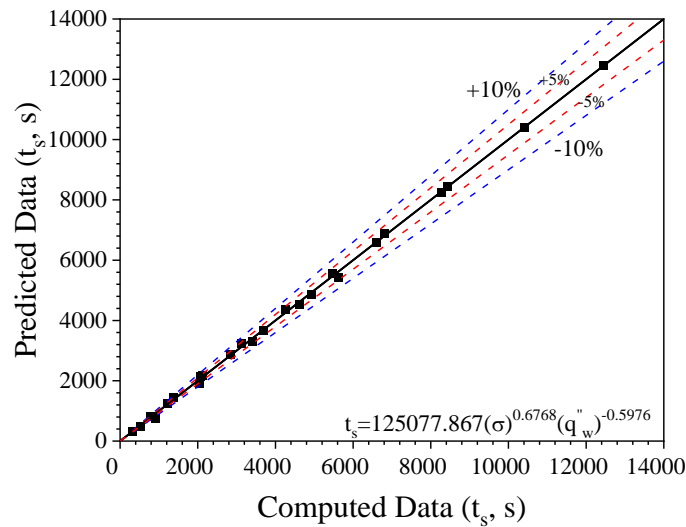


Fig. 2.42 Comparison of computed solidification temperature with those predicted by the proposed correlation

In the present study, a correlation has been proposed for solidification time (t_s) in terms of aspect ratio and end wall boundary condition and expressed in Eq. (2.116).

$$t_s = 125077.867(\sigma)^{0.6768} (q_w'')^{-0.5976} \quad (2.116)$$

The proposed correlation for t_s is valid for the range of $0.125 \leq \sigma \leq 8$ and the error band to anticipate 99% test data of the proposed correlation for solidification time (t_s) is found to be $\pm 5\%$ as shown in Fig. 2.42.

Convective air environment boundary conditions

In this section, paraffin and aluminum are taken as PCM and fin material, respectively. Their properties are summarized in Table 2.14. Here, different values of σ such as 0.5, 1 and 2 are considered. The dimensions of PCM storage unit are listed in Table 2.15. Constant air boundary condition was considered for PCM storage unit (Fig. 2.15). Heat transfer fluid (HTF) temperature and coefficient of heat transfer during convection for PCM solidification were assumed constant in all the cases (Fig. 2.15(c)). Air was chosen as HTF having the temperature of 10°C and the value of coefficient of heat transfer during convection at the wall was taken as 65 W/m²K [67].

Table 2.14 Thermal properties of PCM and fin material [67]

Property	Paraffin	Aluminum fin
Density, ρ (kg/m ³)	830	2770
Specific heat, c (J/kg-K)	1920 (Solid)	875
	3260 (Liquid)	
Thermal conductivity, k (W/m-K)	0.514 (Solid)	177
	0.224 (Liquid)	
Latent heat of fusion, L_p (J/kg)	251,000	-
Melting/solidification temperature, T_m (°C)	32	-

Table 2.15 Dimensions of PCM storage unit

Dimensions	Case 1	Case 2	Case 3
Length of fin, l_f (mm)	10	15	20
Half height of cell, l_c (mm)	20	15	10
Cell aspect ratio, $\sigma = \frac{l_f}{l_c}$	0.5	1	2

Rate of solidification is influenced by the aspect ratio of PCM storage unit. It can be seen from Fig. 2.43 that when σ is less than unity, heat flows only in direction X, that is, from wall to solid-liquid interface. However, heat flows only in direction Y, that is, from fin to interface of solid and liquid, when the value of σ is greater than unity. While, heat flows from both wall to solid-liquid interface and fin to interface of solid-liquid (both in the directions X and Y) at $\sigma = 1$. The comparison of location of solid-liquid interface obtained from the present analytical investigation with the one-dimensional mathematical and two-dimensional numerical solutions of Mosaffa et al. [67] for different values of t and σ is presented in Fig. 2.43(a-f). The maximum error in interface of solid-liquid by the present model is found to be 1.1477 mm in direction X at $\sigma = 1$ and $t = 1000$ s and 0.973 mm in direction Y at $\sigma = 2$ and $t = 1000$ s. The present model agrees well with the two-dimensional numerical model for $\sigma = 0.5$.

Here, the fin's temperature variation was determined and compared with the results obtained by employing separation of variable (SV) and enthalpy method [67], and is presented in Fig. 2.44(a-c). It is noticed from Fig. 2.45 that the present predictions exhibit good agreement with the result obtained by separation of variable method. The maximum error in temperature difference by the present model was found to be negligible at $\sigma = 2$ and $t = 1000$ s. It may also be observed that the length of fin significantly changes the temperature variation. For the small values of l_f , the temperature difference is small, while it increases with the values of l_f . This is attributed to the one-dimensional heat transfer in the small length of a fin and its higher thermal conductivity. The present predictions agree well with the existing numerical solutions [67].

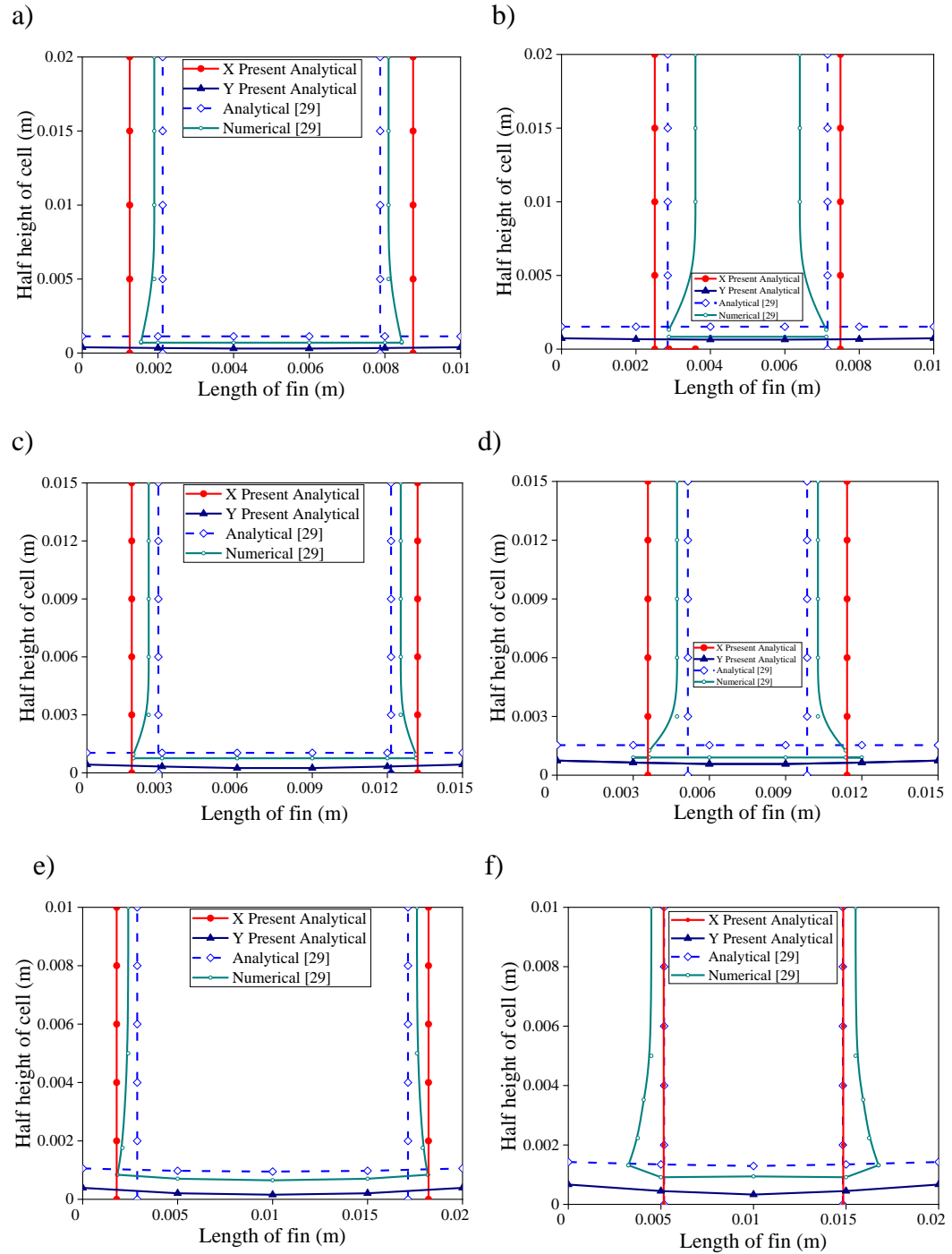


Fig. 2.43 (a-f) Comparison of solid-liquid interface locations obtained by present model with the one-dimensional analytical and two-dimensional numerical solutions by Maosaffa et al. [67] with $h = 65 \text{ W/m}^2\text{-K}$ and $T_\infty = 10^\circ\text{C}$ for (a) $\sigma = 0.5, t = 350$ s, (b) $\sigma = 0.5, t = 700$ s, (c) $\sigma = 1, t = 500$ s, (d) $\sigma = 1, t = 1000$ s, (e) $\sigma = 2, t = 500$ s, and (f) $\sigma = 2, t = 1000$ s

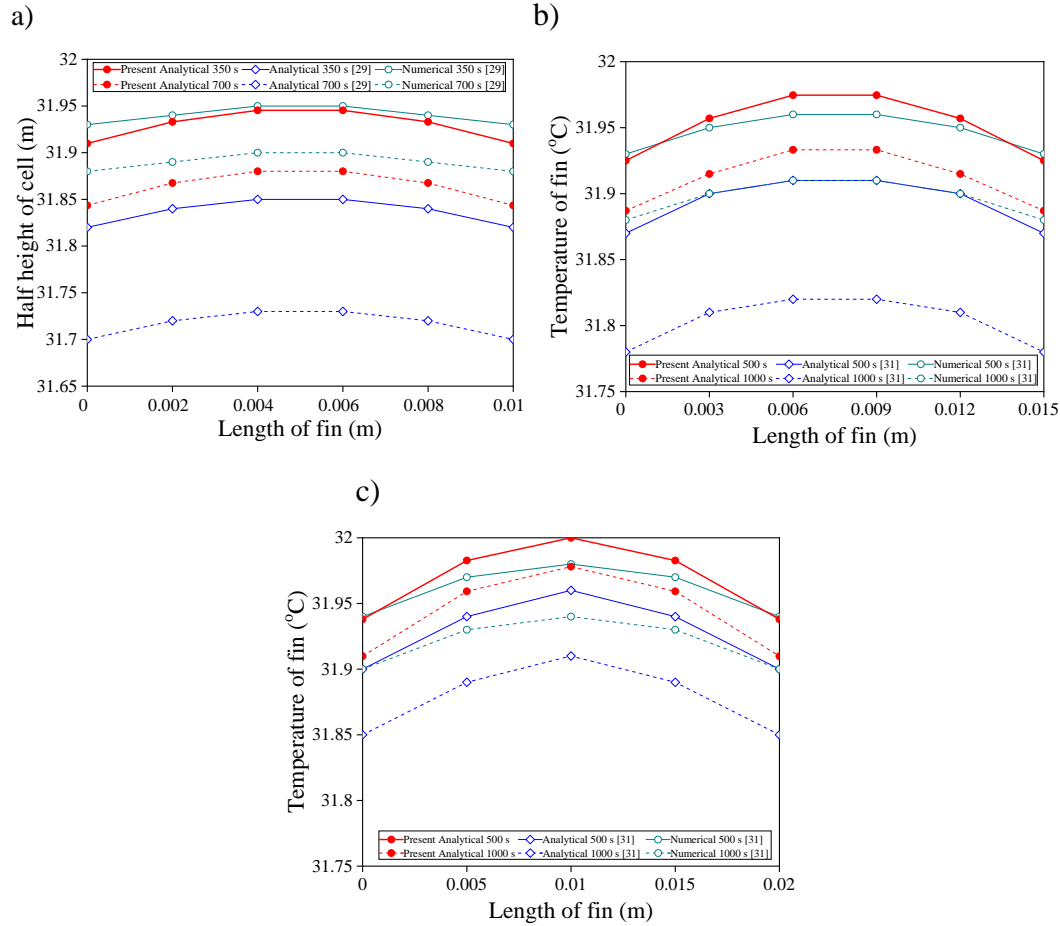


Fig. 2.44 (a-c) Comparison of fin temperatures obtained by present model with the one-dimensional analytical and two-dimensional numerical solutions by Mosaffa et al. [67] with $h = 65 \text{ W/m}^2\text{-K}$ and $T_{\infty} = 10^{\circ}\text{C}$ for (a) $\sigma = 0.5$, $t = 350 \text{ s}$ and $t = 700 \text{ s}$, (b) $\sigma = 1$, $t = 500 \text{ s}$ and $t = 1000 \text{ s}$, and (c) $\sigma = 2$, $t = 500 \text{ s}$ and $t = 1000 \text{ s}$

The variation of solid fraction with time for $\sigma = 0.5$ and $\sigma = 2$ was evaluated using Eq. (2.114) and is demonstrated in Fig. 2.45. It is noticeable from Fig. 2.45 that the PCM solidification is fast for smaller values of σ . Fig. 2.46 shows variation in PCM total solidification time for different aspect ratio at constant volume of PCM and TCE. Different values of temperature of HTF and coefficient of heat transfer during convection has been taken for the analysis. Here, the reduction in solidification time was found to be $\sim 88\%$ by reducing the aspect ratio from 8 to 0.125 for a given imposed convective environment at the walls. Also,

with the increase in the coefficient of heat transfer from $55 \text{ W/m}^2\text{-K}$ to $75 \text{ W/m}^2\text{-K}$, the solidification time reduces by $\sim 26\%$ at $T_\infty=10^\circ\text{C}$ for the same aspect ratio. However, the reduction in solidification time is obtained as $\sim 55\%$ by reducing T_∞ from 20°C to 10°C at $h = 65 \text{ W/m}^2\text{-K}$ for the same aspect ratio. Here, it may be noted the decrease of HTF temperature (T_∞) has more effect on solidification time compared to increase in coefficient of heat transfer during convection (h).

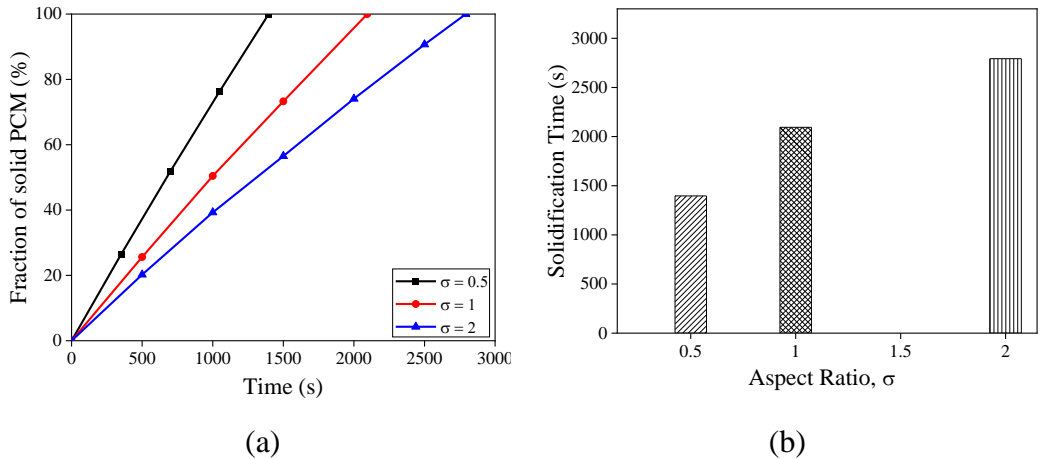


Fig. 2.45 (a) Variation of solid fraction of PCM with time, (b) Solidification time of PCM for different cell aspect ratios at $h = 65 \text{ W/m}^2\text{-K}$ and $T_\infty = 10^\circ\text{C}$

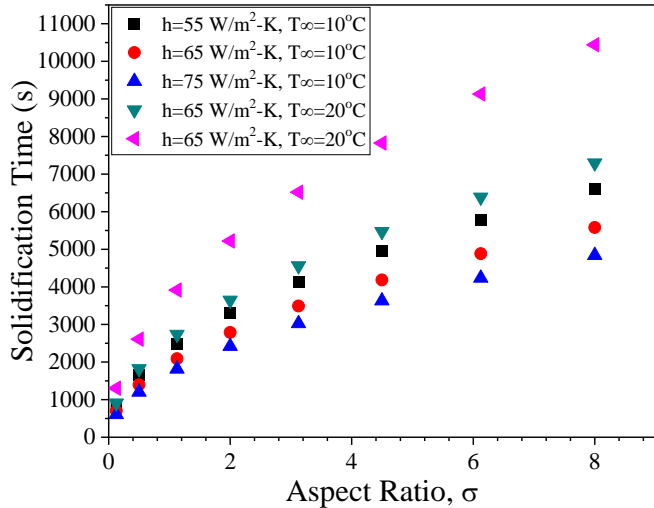


Fig. 2.46 Variation in total solidification time of PCM for different convective air conditions at the end walls

The proposed correlation for solidification time (t_s) in terms of aspect ratio and end wall boundary condition is expressed in Eq. (2.117).

$$t_s = 125077.867(\sigma)^{0.5014} (h)^{-0.5814} (T_m - T_\infty)^{-1.0002} \quad (2.117)$$

The proposed correlation for t_s is valid for the range of $0.125 \leq \sigma \leq 8$ and $T_m > T_\infty$. The error band to anticipate 99% test data of the proposed correlation for solidification time (t_s) is found to be $\pm 10\%$ as shown in Fig. 2.47.

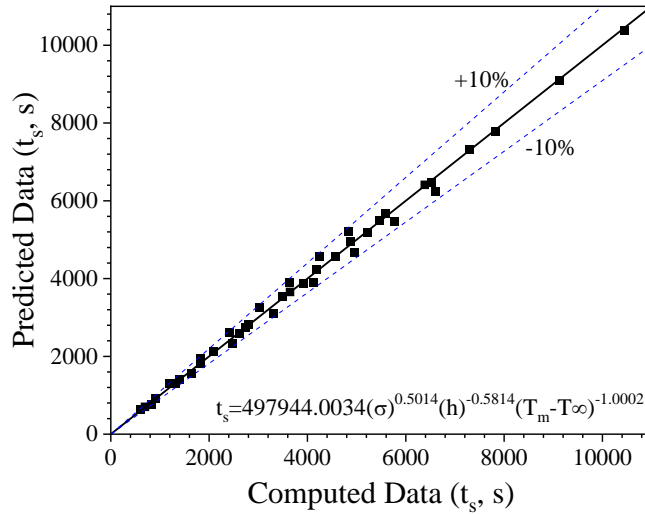


Fig. 2.47 Comparison of computed solidification temperature with those predicted by the proposed correlation

2.4 Concluding remarks

The analysis of melting and solidification phenomena of PCM in two different cases such as annular TES and rectangular TES with plate fins has been presented in this chapter.

In the first problem, a one-dimensional conduction heat transfer model has been proposed to study the melting and solidification of phase change material (PCM) inside an annulus. Here, the phase change process is divided into two main sub-processes such as melting and solidification sub-process. Subsequently, each sub-process is analyzed for various temporal regimes. The temporal regimes include completely solid, partially molten and completely molten for melting sub-

process and in reverse order for solidification sub-process. Later on, the solution for temperature distribution for each temporal regime is obtained either by employing variational formulation or using a method of quasi-steady state. The solution of each temporal regime is coupled to provide the solution for temperature distribution for the sub-process. Present model exhibits good agreement with the existing experimental data. The results indicate that melt duration can be increased by increasing the thickness of PCM in an annulus. It is also observed that for any thermal storage unit there exists a particular percentage of TCE-PCM distribution through which maximum melt duration can be achieved.

In the second problem, melting and solidification process of phase change material (PCM) is analyzed in a two-dimensional finite storage system with plate fins. Solutions are obtained for various boundary conditions namely, constant heat flux, constant temperature and convective air environment at the end walls. The model predicts the solid-liquid interface, temperature distribution and melt fraction. Melting time has been reported for various aspect ratios (σ) and different end wall conditions. The melting and solidification time is found to reduce by decreasing the value of σ and with the increase in wall heat flux, wall temperature and heat transfer coefficient. Correlations have been proposed to predict the melting and solidification time as a function of various parameters.

The analysis shows the ability of HBIM and vibrational technique to solve variety of problems involving phase change in TES without recourse to mathematical complexity and numerical computation. This technique is simple and provides the solutions with reasonable accuracy. Analysis of different design of TES is useful because of numerous applications. In the next section, the analysis of melting and solidification PCM is reported inside the spherical capsule.

Chapter 3

Unconstrained and constrained melting behavior of phase change material inside the spherical capsule through numerical investigation

3.1 General background

The PCM based latent heat storage is widely used because of various advantages such as higher storage density and ability to store energy within smaller temperature variation. Many a times, PCMs are encapsulated in small containers which increase the heat transfer area, decreases charging and discharge time and prevents any leakage, phase separation, and corrosiveness. The melting behaviors of encapsulated PCMs are usually studied by two different approaches such as constrained melting and unconstrained melting. In case of constrained melting, a support is provided that prevents the sinking of PCM to the bottom of the container during melting. On the contrary, in case of unconstrained melting, the solid PCM tends to sink to the bottom of sphere due to gravity. Numerous computational studies have been made that analyze the unconstrained and constrained melting of PCM inside the spherical capsule. In general two different approaches such as axisymmetric and symmetric modelling are adopted to obtain the solution. The governing equations associated with boundary conditions are solved by numerical techniques either for spherical coordinates and rectangular coordinate systems in case of axisymmetric modelling and symmetric modelling, respectively. In case of axisymmetric modelling, the variation in circumferential direction is neglected for the analysis. It is argued that the mode of density variation such as linear, constant, Boussinesq approximation in various regions such as solid, liquid and mushy affects the thermal performance. In this study, different models involving model of density variation in different regions are studied systematically through numerical investigation.

The objective of this study is to numerically investigate the unconstrained and constrained melting of PCM in a spherical capsule. CFD simulations are carried out with the help of commercial software Ansys Fluent 19.2. Simulations are performed for various configurations such as axisymmetric and symmetric modelling with different density variations such as linear density variation in mushy and liquid regions, linear density variation in mushy region but constant density in solid and liquid regions, Boussinesq approximation in mushy region and constant density in solid and liquid regions. The results are validated with the available experimental and numerical results for various cases. Finally, the parametric effects of these various configurations are examined in detail.

3.2 Unconstrained melting analysis of phase change material in a spherical capsule

Here, unconstrained melting of PCM in a spherical capsule is numerically investigated by using Ansys Fluent 19.2. Simulations are performed for various configurations such as axisymmetric and symmetric modelling with different density variations such as linear density variation in mushy and liquid regions, linear density variation in mushy region but constant density in solid and liquid regions, Boussinesq approximation in mushy region and constant density in solid and liquid regions.

3.2.1 Physical model

In this investigation, closed spherical capsule is considered with internal diameter (D_i) and wall thickness (t_w) of 80 mm and 2 mm, respectively. A glass spherical shell filled with solid PCM upto 85% of its volume is considered. To contemplate the significant increase in volume of PCM due to huge density difference between solid and liquid phases, air void is considered at the top of the PCM in 15% of volume of capsule. Here, computational domain is defined based on the symmetry of the considered model and the schematic is shown in Fig. 3.1. Spherical capsule glass shell with thermal conductivity of 0.81 W/m-K and the PCM RT27 (Rubitherm GmbH) having melting temperature of 28-30°C is used in

the analysis [55]. The thermo-physical properties of RT27 (PCM) are presented in Table 3.1. Similar to the study of Archibold et al. [130, 131], air is considered as ideal gas.

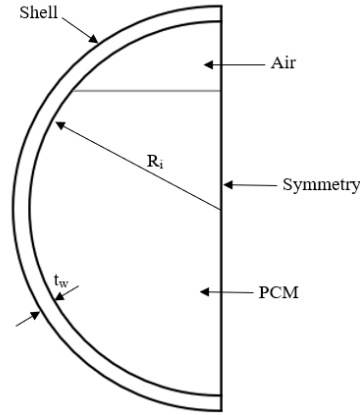


Fig. 3.1 Schematic diagram of the computational domain

Table 3.1 Thermo-physical properties of PCM

Properties (unit)	RT27
Density (kg/m^3)	870 (Solid), 760 (Liquid)
Dynamic viscosity (kg/m-s)	3.42×10^{-3}
Latent heat of fusion (kJ/kg)	179
Melting temperature ($^{\circ}\text{C}$)	28 (Solidus), 30 (Liquidus)
Specific heat (kJ/kg-K)	2.4 (Solid), 1.8 (Liquid)
Thermal expansion coefficient ($1/\text{K}$)	0.5×10^{-3}
Thermal conductivity (W/m-K)	0.24 (Solid), 0.15 (Liquid)

3.2.2 Mathematical formulations and computational procedure

Here, spherical capsule is modeled considering its symmetry and can be analyzed in two dimensions based on the assumption of axisymmetry/symmetry with symmetric axis along vertical direction. The mathematical model consists of continuity, momentum and energy equations. The mathematical model is described based on the following assumptions [55, 130, 131]:

- Both solid/liquid phases of PCM and air are homogeneous and isotropic.

- Viscous Newtonian liquid phase.
- Laminar flow with negligible viscous dissipation and surface tension effects.
- Different cases are considered for the variation in density of PCM and are shown in Table 3.2.
- The entire system is initially maintained at 23°C that is the marginally subcooled.

Table 3.2 Various cases considered in this study

Cases	Modelling	Density variations
I	Axisymmetric	Constant density- Solid region
		Linearly varying- Mushy region
		Varying as $\rho_l / [\beta(T - T_l) + 1]$ - Liquid region
II		Constant density- Solid/liquid region
Linearly varying- Mushy region		
III		Constant density- Solid/liquid region
Boussinesq approximation- Mushy region		
IV	Symmetric	Constant density- Solid region
		Linearly varying- Mushy region
		Varying as $\rho_l / [\beta(T - T_l) + 1]$ - Liquid region
V		Constant density- Solid/liquid region
Linearly varying- Mushy region		
VI		Constant density- Solid/liquid region
Boussinesq approximation- Mushy region		

Continuity, energy and momentum equations used for axisymmetric and symmetric melting are expressed as:

For axisymmetric melting

Continuity:

$$\frac{\partial(\alpha_q \rho_q)}{\partial t} + \frac{1}{r^2} \frac{\partial}{\partial r} (\alpha_q \rho_q v_r r^2) + \frac{1}{r \sin \theta} \frac{\partial}{\partial \theta} (\alpha_q \rho_q v_\theta \sin \theta) = 0 \quad (3.1)$$

Momentum in radial direction:

$$\begin{aligned} & \frac{\partial(\alpha_q \rho_q v_r)}{\partial t} + \frac{1}{r^2} \frac{\partial}{\partial r} (\alpha_q \rho_q v_\theta r^2 v_r) + \frac{1}{r \sin \theta} \frac{\partial}{\partial \theta} (\alpha_q \rho_q v_\theta \sin \theta v_r) - \frac{\alpha_q \rho_q v_\theta^2}{r} \\ &= -\frac{\partial P}{\partial r} + \mu \left[\nabla^2 (\alpha_q \rho_q v_r) - \frac{2\alpha_q \rho_q v_r}{r^2} - \frac{2}{r^2} \frac{\partial(\alpha_q \rho_q v_\theta)}{\partial \theta} - \frac{2\alpha_q \rho_q v_\theta \cot \theta}{r^2} \right] \\ & \quad + \alpha_q \rho_q g_r \beta (T - T_m) + S_i \end{aligned} \quad (3.2a)$$

Momentum in polar direction:

$$\begin{aligned} & \frac{\partial(\alpha_q \rho_q v_\theta)}{\partial t} + \frac{1}{r^2} \frac{\partial}{\partial r} (\alpha_q \rho_q v_r r^2 v_\theta) + \frac{1}{r \sin \theta} \frac{\partial}{\partial \theta} (\alpha_q \rho_q v_\theta \sin \theta v_\theta) + \frac{\alpha_q \rho_q v_r v_\theta}{r} \\ &= -\frac{1}{r} \frac{\partial P}{\partial \theta} + \mu \left[\nabla^2 (\alpha_q \rho_q v_\theta) + \frac{2}{r^2} \frac{\partial(\alpha_q \rho_q v_r)}{\partial \theta} - \frac{2\alpha_q \rho_q v_\theta}{r^2 \sin^2 \theta} \right] \\ & \quad + \alpha_q \rho_q g_\theta \beta (T - T_m) + S_i \end{aligned} \quad (3.2b)$$

Energy:

$$\begin{aligned} & \frac{\partial(\alpha_q \rho_q h)}{\partial t} + \frac{1}{r^2} \frac{\partial}{\partial r} (\alpha_q \rho_q r^2 v_r h) + \frac{1}{r \sin \theta} \frac{\partial}{\partial \theta} (\alpha_q \rho_q v_\theta \sin \theta h) \\ &= \frac{\alpha_q k_q}{c} \nabla^2 h - \frac{1}{c} \frac{\partial \lambda}{\partial t} - \frac{1}{r^2} \frac{\partial}{\partial r} (\alpha_q \rho_q r^2 v_r \lambda) + \frac{1}{r \sin \theta} \frac{\partial}{\partial \theta} (\alpha_q \rho_q v_\theta \lambda \sin \theta) \end{aligned} \quad (3.3)$$

Here, ∇ is a Laplace operator and is defined as:

$$\nabla^2 = \frac{1}{r^2} \frac{\partial}{\partial r} \left(r^2 \frac{\partial}{\partial r} \right) + \frac{1}{r^2 \sin \theta} \frac{\partial}{\partial \theta} \left(\sin \theta \frac{\partial}{\partial \theta} \right) \quad (3.4)$$

Initial and boundary conditions:

$$v_r(r, \theta, 0) = v_\theta(r, \theta, 0) = 0, \quad T(r, \theta, 0) = T_i \quad (3.5a)$$

$$T(R_o, \theta, t) = T_w \quad (3.5b)$$

$$k_w \frac{\partial T_w}{\partial r} \Big|_{r=R_i} = k_{pcm} \frac{\partial T_{pcm}}{\partial r} \Big|_{r=R_i} \quad (3.5c)$$

$$v_r(R_i, \theta, t) = v_\theta(R_i, \theta, t) = 0 \quad (3.5d)$$

For symmetric melting

Continuity:

$$\frac{\partial(\alpha_q \rho_q)}{\partial t} + v_i \frac{\partial(\alpha_q \rho_q)}{\partial x_i} = 0 \quad (3.6)$$

Momentum:

$$\frac{\partial(\alpha_q \rho_q v_i)}{\partial t} + \frac{\partial(\alpha_q \rho_q v_j v_i)}{\partial x_j} = -\frac{\partial P}{\partial x_i} + \mu \frac{\partial^2(\alpha_q \rho_q v_i)}{\partial x_j \partial x_j} + \alpha_q \rho_q g_i + S_i \quad (3.7)$$

Energy:

$$\frac{\partial}{\partial t}(\alpha_q \rho_q H) + \frac{\partial}{\partial x_i}(\alpha_q \rho_q v_i H) = \frac{\partial}{\partial x_i} \left(k \frac{\partial T}{\partial x_i} \right) \quad (3.8)$$

Initial and boundary conditions:

$$v_i(x, y, 0) = 0, \quad T(x, y, 0) = T_i \quad (3.9a)$$

$$T(x, y, t) = T_w \quad (3.9b)$$

$$k_w \frac{\partial T_w}{\partial x} \Big|_{x=R_i} = k_{pcm} \frac{\partial T_{pcm}}{\partial x} \Big|_{x=R_i} \quad (3.9c)$$

$$v_i(x, y, t) = 0, \quad (3.9d)$$

where

$$H = h + \lambda \quad (3.10)$$

h and λ are sensible enthalpy and latent heat of fusion, respectively and are defined as:

$$h = h_{ref} + \int_{T_{ref}}^T c dT \quad (3.11)$$

where h_{ref} and T_{ref} are reference sensible heat and temperature, respectively.

$$\lambda = \Upsilon L \quad (3.12)$$

Here, L is the latent heat and Υ is the volume fraction of liquid PCM of a computational cell in which the phase transition is taking place ($0 < \Upsilon < 1$). Υ is defined as:

$\Upsilon = 0$	T < T _{solidus}	solid	
$0 < \Upsilon < 1$	T _{solidus} < T < T _{liquidus}	mushy	(3.13)
$\Upsilon = 1$	T > T _{liquidus}	liquid	

Here, solid-liquid interface is tracked with the help of enthalpy-porosity technique introduced by Voller and Prakash [203] and Brent et al. [204]. This method introduces a source term in the momentum equation and is given by:

$$S_i = -A(\Upsilon)v, \quad (3.14)$$

where v is v_r or v_θ for radial and polar momentum equation in axisymmetric melting. While, v is taken as v_i for symmetric melting.

The porosity function $A(\Upsilon)$ is given by Brent et al. [204] and expressed as:

$$A(\Upsilon) = \frac{C(1-\Upsilon)^2}{\Upsilon^3 + E} \quad (3.15)$$

Here, E is a small computational constant used to avoid division by zero and its value is taken as $E = 0.001$. C is a constant reflecting the morphology of the melt interface. Generally, the value of C is taken between 10^4 - 10^7 . Similar to the previous studies, the value of C is adopted as 10^5 in this investigation [55].

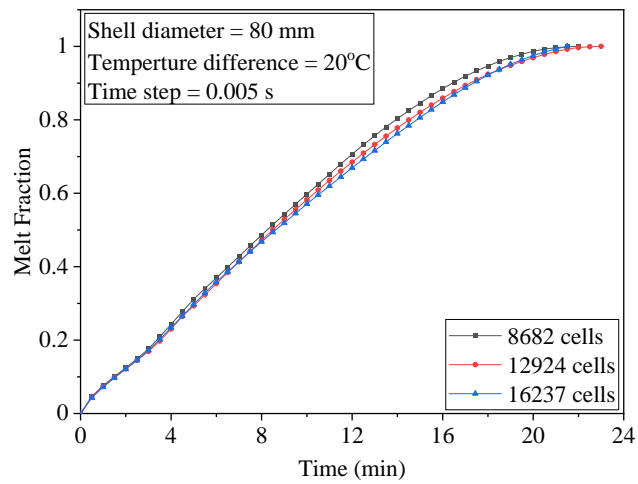
First, VOF model is used for the PCM-air system in which the interface moves without inter penetration of the two media. The volume fraction of the q^{th} fluid in the computational cell is defined by α_q and the value of α_q can vary from 0 to 1. If the cell is devoid then $\alpha_q = 0$ and its value is 1 for the cell entirely filled with the q^{th} fluid. If $0 < \alpha_q < 1$ then the computational cell contains interface between air and the other fluids. Various properties and variables are determined using the volume fraction value of the fluid in the computational cell. The motion of solid PCM can be approximately modeled by enthalpy-porosity method as have been done by numerous studies reported on melting of PCM by using enthalpy porosity model [55, 129, 205]. These studies use low value of Darcy constant to implement settling of solid PCM inside the spherical capsule, so the sinking phenomena is modeled. Therefore, the melting process in this study is simulated using the enthalpy porosity model.

The mathematical model is solved using control volume technique. PISO method has been adopted for the pressure-velocity coupling and PRESTO scheme is employed for the pressure corrections [206]. Momentum and energy equations are solved using second order upwind scheme and Geo-reconstruct method has been utilized to correct the VOF model liquid fraction [207]. The under relaxation factors used for pressure, density and body force is considered as 0.5, while it is taken as 0.2 for momentum and liquid fraction and 0.8 for energy. The convergence criteria for continuity, momentum equation is chosen as absolute residuals of 10^{-5} , while it is fixed at absolute residuals of 10^{-8} for energy equations.

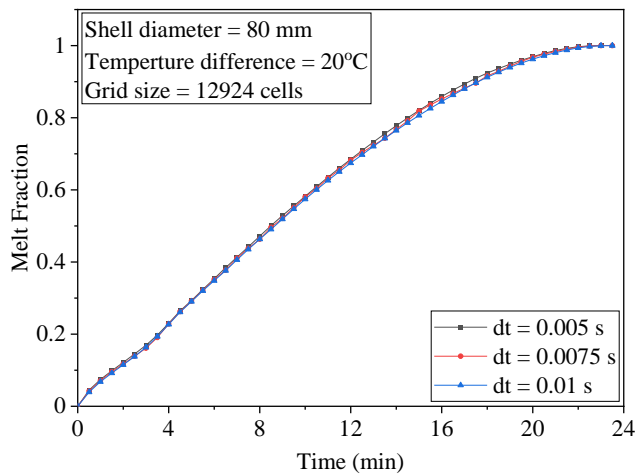
The computational domain is meshed with the quadrilateral structured grid as shown in Fig. 3.2. A finer mesh is applied near the wall of the capsule along with the marked consideration at PCM-air interface. While, the other part of the domain is meshed coarsely.



Fig. 3.2 The computational mesh



(a)



(b)

Fig. 3.3 Melt fraction for (a) different grid refinements, and (b) different time step values

In order to ensure the independency of the computational results, different grid sizes keeping the constant time step and different time step keeping the constant grid size have been examined for the axisymmetric melting of PCM in a spherical capsule for case 1 as this is the challenging case to be analyzed. Comparison of the melt fraction of PCM in a spherical capsule with different grid size such as 8682, 12924, 16237 for $dt = 0.005$ s have been shown in Fig. 3.3(a). No significant difference in the melt fraction of PCM has been reported for the grid sizes 12924 and 16237. Therefore, the grid size of 12924 has been chosen in the present study. Likewise, the comparison of the melt fraction with 12924 grid size at different time steps such 0.01, 0.0075, 0.005 have been shown in Fig. 3.3(b). Based on this study, the time step of 0.005 and grid size of 12924 were chosen for all the cases in this study.

3.2.3 Results and discussion

Validation results

Different cases are validated for the melt fraction of PCM with the existing experimental and numerical results and are shown in Fig. 3.4(a-d). Case I is validated with the experimental and numerical results of Assis et al. [55]. Assis et al. [55] considered a spherical capsule with 80 mm diameter and 2 mm thickness. The walls of the capsule are made from glass and is maintained at 10°C higher than the mean melting temperature of the PCM. RT27 (Rubitherm GmbH) has been taken as the PCM for the analysis. The initial temperature of the whole system was maintained at 23°C. Case II is validated with the experimental results of Assis et al. [55] and numerical results of Archibold et al. [131]. The results are validated for the same simulation conditions as opted in case I. Case III is validated against the experimental and numerical results of Tan et al. [122]. In their study, Tan et al. [122] considered n-octadecane as the PCM filled inside the spherical glass capsule of 101.66 mm diameter and 1.5 mm thickness. Sub-cooling of 1°C and outer wall temperature of 40°C were chosen for the analysis. Case V is validated with the experimental results of Assis et al. [55] and

numerical results of Junior et al. [133]. This validation is again for the same experimental conditions as chosen for case I.

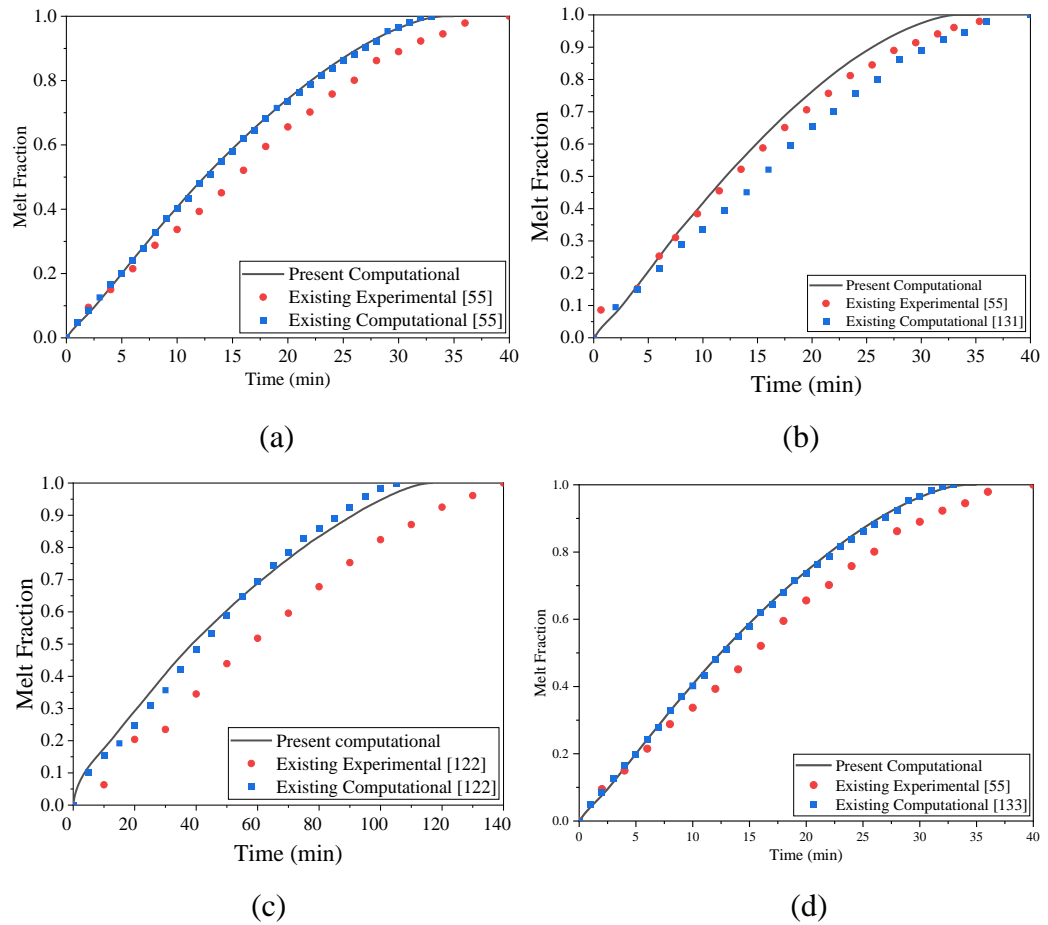


Fig. 3.4 Comparison of melt fraction obtained from present computational study for (a) case I, (b) case II, (c) case III, and (d) case V with existing experimental/computational studies

It is evident from the comparison curves that the present model is in good agreement with the existing numerical results for all the cases. However, the melting time obtain from the present model is slightly different compared to the existing experimental cases. This may be due to various reasons such as:

- In experiments, the capsule is kept in the water bath working at certain fixed temperature. While, in numerical model that fixed temperature is set over the outer wall. That is the thermal resistance; although small, exists in the experiments.

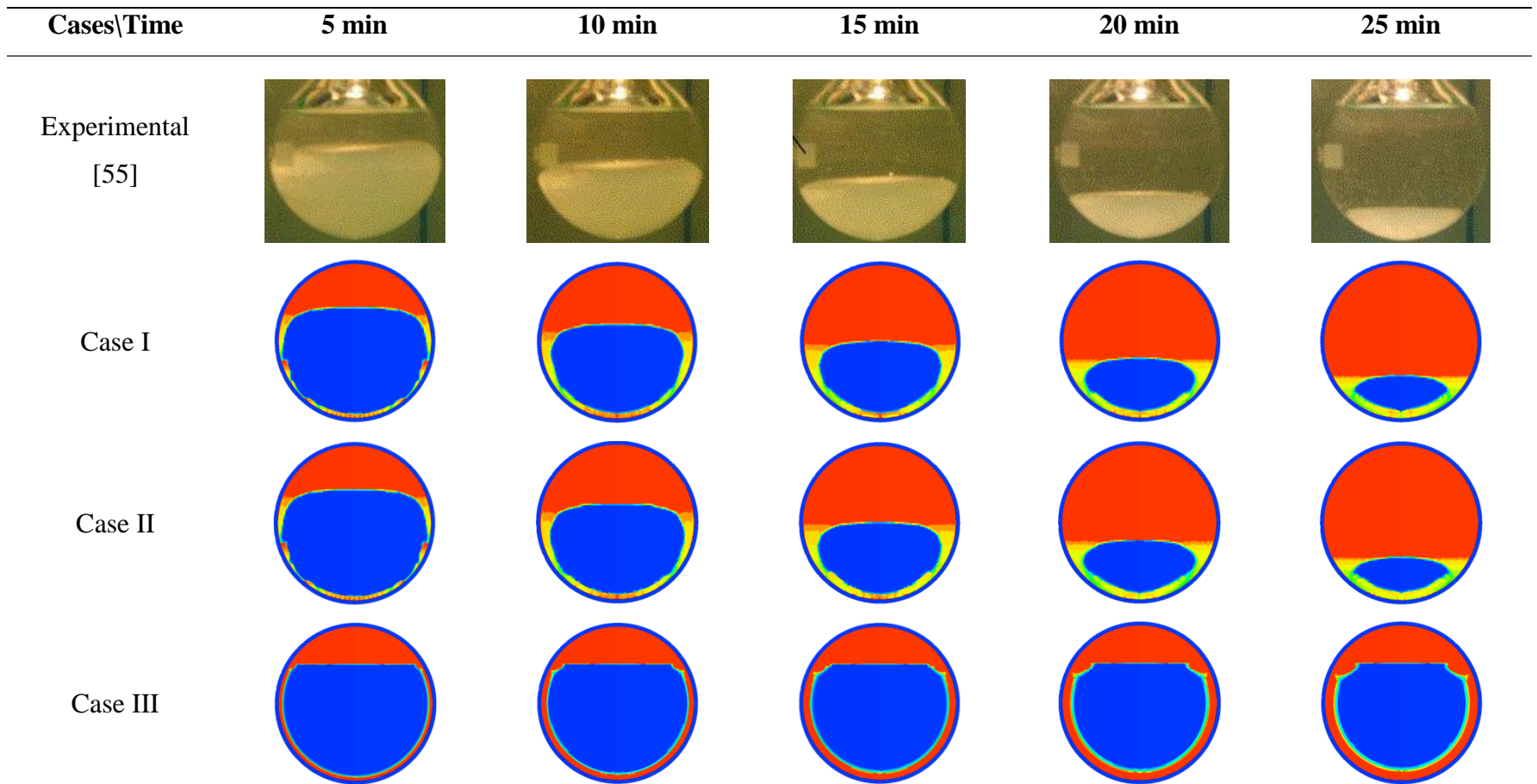
- Thermal conductivity of the capsule material is taken from the literature and not specifically measured.
- Also, different assumptions taken in the numerical simulations affected the obtained results.

It may be noted that the maximum difference in the value of melt fraction obtained using present computation model and existing experimental results are less than 11% for the cases I, II and V, while it is less than 16% for the case III. Considering all this, it can be concluded that the present numerical model is in good agreement with the experimental results. Notably, the effect of different assumptions considered in the different numerical simulations on unconstrained melting of PCM needs to be analyzed for the same boundary conditions and material properties.

Comparison of computational and visualized melting pattern

In this section, the melting of RT27 in a spherical capsule for six different conditions (reported in Table 3.2) are analyzed for similar boundary condition. Physical model discussed in Sec. 3.1.2 is considered for the analysis. Outer surface temperature of the capsule is kept 10°C higher than the mean melting temperature of the PCM. Melt fractions are obtained for various cases and compared with the existing experimental results. Composite diagrams are presented and discussed for the evolution of anticipated melt fraction distribution, streamline contours, isotherms and interface rise.

Fig. 3.5 shows melting pattern of PCM in a spherical capsule at different time instants with outer wall temperature of 40°C and subcooling of 1°C. The results obtained for the different cases listed in Table 3.2 are compared with the visualized melting pattern obtained during experimental investigation by Assis et al. [55] at different time instant. In the experimental melting pattern, solid and liquid PCM is represented by white and transparent parts, respectively. While, the computational melting patterns are shown colorized with solid and liquid PCM represented by blue and red colors, respectively.



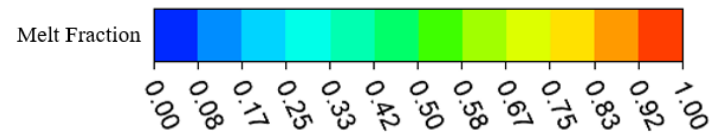
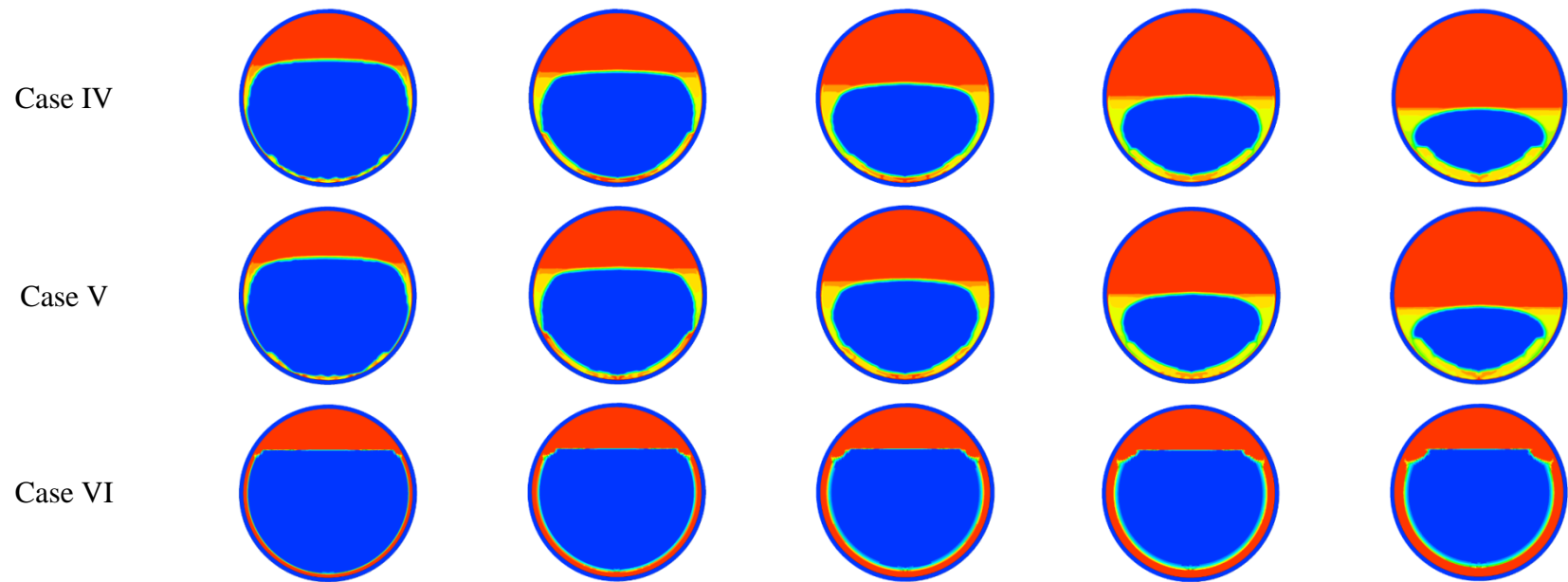


Fig. 3.5 Comparison of computational and experimental melting patterns for different cases

Fig. 3.5 shows the melting pattern at different time instants such as 5, 10, 15, 20, and 25 min. It can be seen from the figures that the cases I, II, IV and V show good agreement with the experimental observations compared to cases III and VI.

For all the cases, melting process begins with the transfer of heat through conduction at the outer surface of solid PCM and inner surface of capsule wall. Due to the heat transfer, the solid PCM starts melting and a thin layer is formed between the solid PCM and inner wall of the sphere. The thin liquid layer starts expanding with the progress of time for Boussinesq approximation but remains uniform throughout the inner surface of capsule. Afterwards, the strong natural convection at the bottom of capsule starts forcing the hot liquid PCM at the top and pushing the cold liquid PCM downwards. Therefore, the melting rate is more at the top of capsule. Due to little density variations between solid and liquid PCM in case of Boussinesq approximation, the melting rate is slower and also, air volume remains approximately same. The more interesting phenomena observed from the figure is that unlike experimental observations, the solid PCM does not sink down in Boussinesq approximation (cases III and VI). This is again due to little density variations associated with Boussinesq approximation, which is not true for real cases of unconstrained melting. Thus, cases III and VI do not agree with the experimentally observed melting pattern.

Similar to the melting during Boussinesq approximation, the melting is initially conduction dominated in cases such as linear density variation in mushy and liquid regions (cases I and IV), linear density variation in mushy region but constant density in solid and liquid regions (cases II and V). Thin liquid layer is formed at the bottom of inner surface of capsule. Like Boussinesq approximation case, thin layer starts expanding but unlike Boussinesq approximation case, the liquid layer at the bottom of inner surface of the wall is being squeezed down by the solid PCM. This is due to huge density variation between solid and liquid PCM considered in cases I, II, IV and V, which is more relatable to real case unconstrained melting of PCM. The squeezed liquid layer at bottom of the inner surface of the capsule is forced to move towards the top along the side walls and the cold liquid PCM at the top is pushed downwards. This forms the basis of

buoyancy driven convection in cases I, II, IV and V. Thus, the melting is dominated by buoyancy driven convection at the top and side of PCM. Solid PCM which squeezes the liquid PCM at the bottom of the capsule comes in contact with the bottom wall of the capsule and therefore, melting at the bottom is dominated by conduction heat transfer, also referred as close contact melting. Due to the aforementioned reason, the melting rate is more at the top and side surface compared to the bottom of the PCM surface. Also, the melting rate decreases with time at the bottom because of the decrease in contact area of solid PCM with time. Due to lower density of liquid PCM compared to solid PCM, the layer of air at the top of the capsule is compressed and the air volume decreases with time. More detailed observations about the volume of air before and after the complete melting of PCM is presented in subsequent section. It can be concluded from the Fig. 3.5 that cases I, II, IV and V agree well with the experimentally observed melting pattern.

Comparison of melt fraction

As discussed in earlier section, cases I, II, IV and V show similar melting pattern as observed in the experimental investigation. Here, melt fraction of PCM obtained for cases I, II, IV and V are compared with the experimentally obtained melt fraction by Assis et al. [55] at different time instant as shown in Fig. 3.6. It may be noted that the melt fraction at different time for the case I is approximately similar to case II with maximum variation of less than 1%. Like cases I and II, the values of melt fraction for cases IV and V are also approximately similar with maximum variation of less than 2% between the values. Furthermore, it can be seen from the figure that the axisymmetric cases I and II underestimate, while the symmetric cases IV and V overestimate the complete melting time of PCM in a spherical capsule. The difference in the complete melting time is 12.5% for axisymmetric cases, while it is found to be 20% for symmetric cases. Therefore, it can be noted that axisymmetric cases I and II show close agreement compared to symmetric cases IV and V.

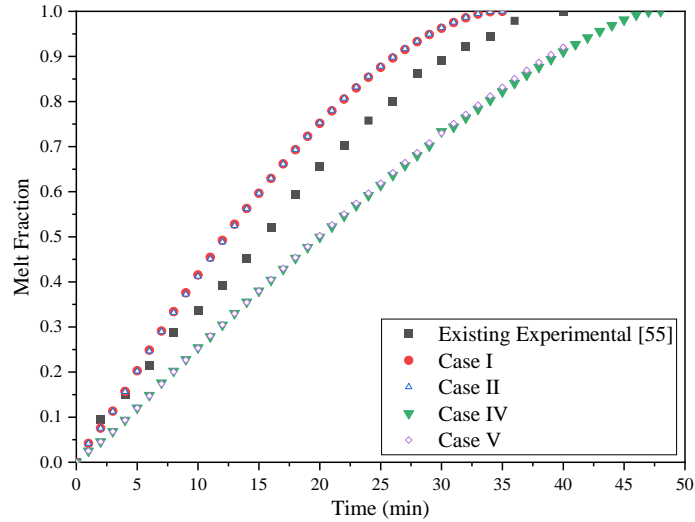


Fig. 3.6 Comparison of computational and experimental melt fraction for different cases

Time dependent streamlines contours, isotherms and interface rise

In order to better understand the melting of PCM inside the spherical capsule and compare the melting patterns for the cases I and II, composite diagrams are shown in Fig. 3.7. Figure depicts the evolution of streamline contours, isotherms, solid PCM fraction and interface rise of PCM in a spherical capsule for cases I and II at different time instant such as 5, 10, 15, 20 and 25 min. Temperature contours are shown on the left part, while the streamline contours, solid PCM fraction and interface rise on the right side of the capsule. Melting of PCM in spherical capsule are described by various researchers but here, the difference in the melting process of PCM for two different cases are analyzed.

Initially, the heat is transferred through the capsule wall to the PCM by conduction during the melting process and convection plays a very little role in the melting process. It may be noted from the figure that the temperature contours are same in both the cases till the time instant of 5 min. Melting of PCM starts along the inner boundary of the capsule. As the time progresses, amount of liquid PCM increases inside the capsule and convection starts dominating the melting process. Counterclockwise circulation starts inside the mushy region and liquid PCM region for case I. while for case II, the counterclockwise circulation is only

in mushy region because there is no density variation in the liquid region. In addition, the rate of increase in temperature of liquid PCM is fast in case I compared to case II. This may be due to the density of liquid PCM varies in case I, which increases the buoyancy circulation of liquid PCM and make the temperature more uniform compared to the case II where liquid density is constant. However, the temperature contours for the solid phase remains almost same for both the cases, this is due to constant density in solid phase for both the cases. In mushy region, temperature is more in case I compared to case II. Moreover, it can be seen here that at time instant 20 and 25 min, counter clockwise circulations cover major area that is throughout the mushy and liquid PCM for case I. While, the counter clockwise circulations cover small area that is only mushy regions for case II. This phenomenon decreases the heat transfer and underestimate the total heat storage of the capsule in case II.

Different circulation patterns can be seen in the air and PCM region as the two regions are immiscible. Also, figure shows that the temperature of air is more than the PCM at all the time instant; this is because of the higher thermal diffusivity of air than the PCM. Circulation patterns in air are same for all the cases. Also, as the PCM melts the air region gets compressed due to expansion of PCM during melting process. Air region contraction history for cases I and II is shown in Fig. 3.8. Interface rise is reported as approximately 12.138 mm and 11.712 mm in cases I and II respectively. Lower interface rise in case II is due to the assumption of constant density variation in liquid region, which is not true in the real case and therefore, although the melt fractions are similar for both the cases at different time instant but case II underestimate the interface rise of PCM during melting process as well as heat storage capacity of the PCM in the capsule.

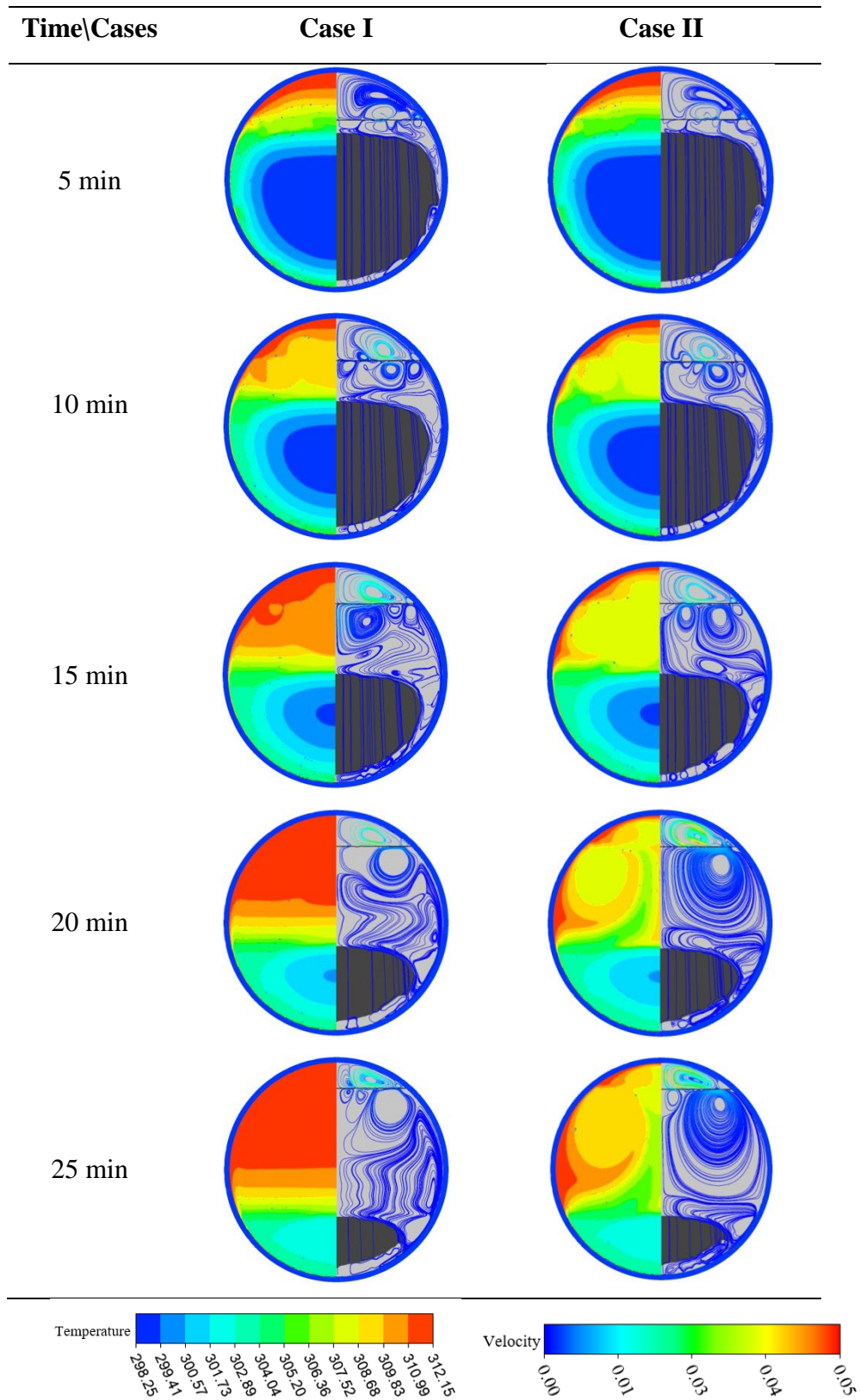


Fig. 3.7 Temperature (left) and streamline (right) contour for different cases

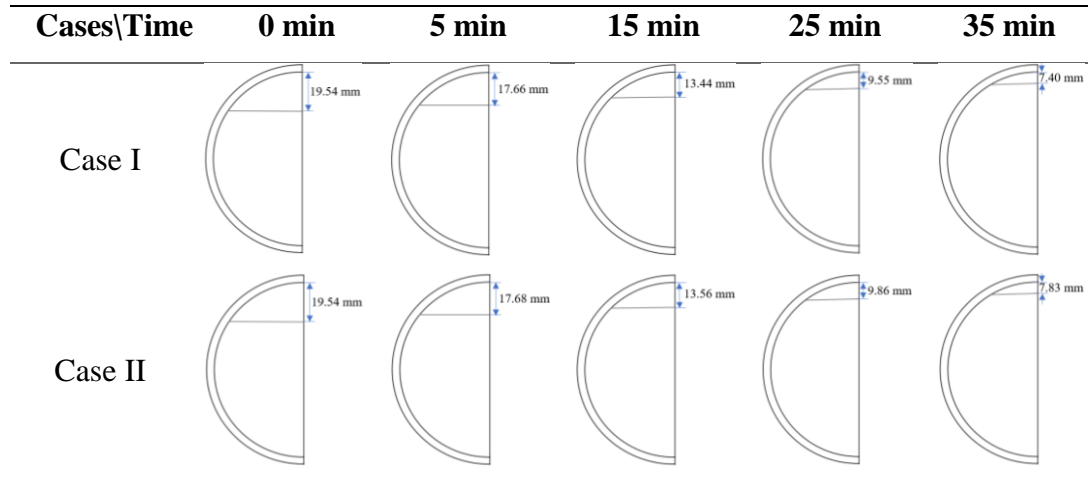


Fig. 3.8 Air region contraction history

3.3 Constrained melting of phase change material in a spherical capsule

Constrained melting of PCM inside the sphere for different cases such as axisymmetric modelling with constant density variation, axisymmetric modelling with Boussinesq approximation, symmetric modelling with constant density variations, and symmetric modelling with Boussinesq approximation in different phases have been numerically investigated by using Ansys Fluent 19.2.

3.3.1 Physical model

Present study considers the glass spherical capsule with inner radius and thickness of 50.83 mm and 1.5 mm, respectively. The considered physical model in this computational investigation is similar as studied by Tan et al. [122] in their experimental and numerical investigation. Glass spherical capsule has a thermal conductivity of 1.14 W/m-K [125]. Initially, the capsule is filled with solid phase change material. Here, n-octadecane is chosen as the PCM and its thermo-physical properties [122, 125] are shown in Table 3.3. The schematic diagram of the computation domain based on the symmetry of the model is presented in Fig. 3.9.

Table 3.3 Thermo-physical properties of PCM

Properties (unit)	n-octadecane
Density (kg/m ³)	772
Kinematic viscosity (m ² /s)	5×10 ⁻⁶
Latent heat of fusion (kJ/kg)	243.5
Melting temperature (°C)	28.2
Specific heat (kJ/kg-K)	2.33
Thermal expansion coefficient (1/K)	0.91×10 ⁻³
Thermal conductivity (W/m-K)	0.1505

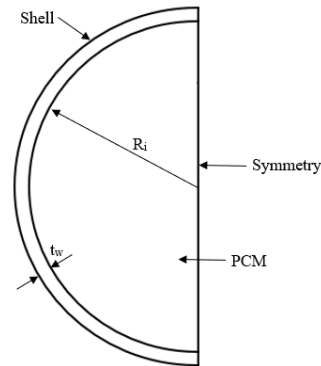


Fig. 3.9 Schematic diagram of the computational domain

3.3.2 Mathematical formulation and computational procedure

In this study, computational model is analyzed in two-dimensional with axisymmetric/symmetric modelling and taking the axis of symmetry along the vertical direction. The mathematical model consists of continuity, momentum and energy equations. Following assumptions have been taken in this numerical study [122, 124, 125].

- Isotropic and homogeneous phases of PCM with thermal equilibrium at the interface of solid and liquid phase.
- Unsteady, incompressible and laminar flow without viscous dissipation and surface tension effects.

- Cases with different density variations of PCM as shown in Table 3.4.
- Marginally subcooled system maintained at 1°C lower than the melting temperature of PCM.

Table 3.4 Various cases considered in this study

Cases	Modelling	Density variations
I	Axisymmetric	Constant density
II		Boussinesq approximation
III	Symmetric	Constant density
IV		Boussinesq approximation

As mentioned previously, continuity, energy and momentum equations used for axisymmetric and symmetric melting are solved for spherical and rectangular coordinates and are expressed as:

For axisymmetric melting

Continuity:

$$\frac{\partial \rho}{\partial t} + \frac{1}{r^2} \frac{\partial}{\partial r} (\rho v_r r^2) + \frac{1}{r \sin \theta} \frac{\partial}{\partial \theta} (\rho v_\theta \sin \theta) = 0 \quad (3.16)$$

Momentum in radial direction:

$$\begin{aligned} & \frac{\partial(\rho v_r)}{\partial t} + \frac{1}{r^2} \frac{\partial}{\partial r} (\rho v_\theta r^2 v_r) + \frac{1}{r \sin \theta} \frac{\partial}{\partial \theta} (\rho v_\theta \sin \theta v_r) - \frac{\rho v_\theta^2}{r} \\ & = -\frac{\partial P}{\partial r} + \mu \left[\nabla^2(\rho v_r) - \frac{2\rho v_r}{r^2} - \frac{2}{r^2} \frac{\partial(\rho v_\theta)}{\partial \theta} - \frac{2\rho v_\theta \cot \theta}{r^2} \right] + \rho g_r \beta (T - T_m) + S_i \end{aligned} \quad (3.17a)$$

Momentum in polar direction:

$$\begin{aligned} & \frac{\partial(\rho v_\theta)}{\partial t} + \frac{1}{r^2} \frac{\partial}{\partial r} (\rho v_r r^2 v_\theta) + \frac{1}{r \sin \theta} \frac{\partial}{\partial \theta} (\rho v_\theta \sin \theta v_\theta) + \frac{\rho v_r v_\theta}{r} \\ & = -\frac{1}{r} \frac{\partial P}{\partial \theta} + \mu \left[\nabla^2(\rho v_\theta) + \frac{2}{r^2} \frac{\partial(\rho v_r)}{\partial \theta} - \frac{2\rho v_\theta}{r^2 \sin^2 \theta} \right] + \rho g_\theta \beta (T - T_m) + S_i \end{aligned} \quad (3.17b)$$

Energy:

$$\begin{aligned} & \frac{\partial(\rho h)}{\partial t} + \frac{1}{r^2} \frac{\partial}{\partial r} (\rho r^2 v_r h) + \frac{1}{r \sin \theta} \frac{\partial}{\partial \theta} (\rho v_\theta \sin \theta h) \\ &= \frac{k}{c} \nabla^2 h - \frac{1}{c} \frac{\partial \lambda}{\partial t} - \frac{1}{r^2} \frac{\partial}{\partial r} (\rho r^2 v_r \lambda) + \frac{1}{r \sin \theta} \frac{\partial}{\partial \theta} (\rho v_\theta \lambda \sin \theta) \end{aligned} \quad (3.18)$$

Here, ∇ is a Laplace operator and is defined as:

$$\nabla^2 = \frac{1}{r^2} \frac{\partial}{\partial r} \left(r^2 \frac{\partial}{\partial r} \right) + \frac{1}{r^2 \sin \theta} \frac{\partial}{\partial \theta} \left(\sin \theta \frac{\partial}{\partial \theta} \right) \quad (3.19)$$

Initial and boundary conditions:

$$v_r(r, \theta, 0) = v_\theta(r, \theta, 0) = 0, \quad T(r, \theta, 0) = T_i \quad (3.20a)$$

$$T(R_o, \theta, t) = T_w \quad (3.20b)$$

$$k_w \frac{\partial T_w}{\partial r} \Big|_{r=R_i} = k_{pcm} \frac{\partial T_{pcm}}{\partial r} \Big|_{r=R_i} \quad (3.20c)$$

$$v_r(R_i, \theta, t) = v_\theta(R_i, \theta, t) = 0 \quad (3.20d)$$

For symmetric melting

Continuity:

$$\frac{\partial \rho}{\partial t} + \frac{\partial(\rho v_i)}{\partial x_i} = 0 \quad (3.21)$$

Momentum:

$$\frac{\partial(\rho v_i)}{\partial t} + \frac{\partial(\rho v_j v_i)}{\partial x_j} = -\frac{\partial P}{\partial x_i} + \mu \frac{\partial^2 v_i}{\partial x_j \partial x_j} + \rho g_i + S_i \quad (3.22)$$

Energy:

$$\frac{\partial}{\partial t}(\rho H) + \frac{\partial}{\partial x_i}(\rho v_i H) = \frac{\partial}{\partial x_i} \left(k \frac{\partial T}{\partial x_i} \right) \quad (3.23)$$

Initial and Boundary conditions:

$$v_i(x, y, 0) = 0, \quad T(x, y, 0) = T_i \quad (3.24a)$$

$$T(x, y, t) = T_w \quad (3.25b)$$

$$k_w \frac{\partial T_w}{\partial x} \Big|_{x=R_i} = k_{pcm} \frac{\partial T_{pcm}}{\partial x} \Big|_{x=R_i} \quad (3.26c)$$

$$v_i(x, y, t) = 0, \quad (3.27d)$$

where

$$H = h + \lambda \quad (3.28)$$

h and λ are sensible enthalpy and latent heat of fusion, respectively and are defined as:

$$h = h_{ref} + \int_{T_{ref}}^T c dT \quad (3.29)$$

where h_{ref} and T_{ref} are reference sensible heat and temperature, respectively.

$$\lambda = \Upsilon L \quad (3.30)$$

Here, L is the latent heat and Υ is the volume fraction of liquid PCM of a computational cell in which the phase transition is taking place ($0 < \Upsilon < 1$). Υ is defined as:

$\Upsilon = 0$	$T < T_{\text{solidus}}$	solid
$0 < \Upsilon < 1$	$T_{\text{solidus}} < T < T_{\text{liquidus}}$	mushy
$\Upsilon = 1$	$T > T_{\text{liquidus}}$	liquid

(3.31)

Here, solid liquid interface is tracked with the help of enthalpy-porosity technique introduced by Voller and Prakash [203] and Brent et al. [204]. This method introduces a source term in the momentum equation and is given by:

$$S_i = -A(\Upsilon)v, \quad (3.32)$$

Where v is v_r or v_θ for radial and polar momentum equation in axisymmetric melting. While, v is taken as v_i for symmetric melting.

Here, the porosity function $A(\Upsilon)$ is given by Brent et al. [204] and expressed as:

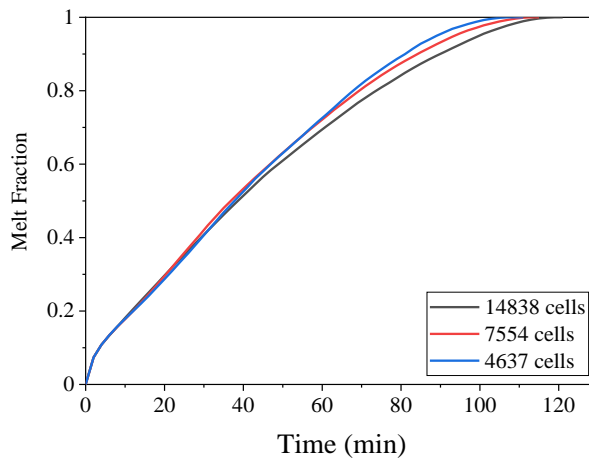
$$A(\varphi) = \frac{C(1-\Upsilon)^2}{\Upsilon^3 + E} \quad (3.33)$$

Here, E is a small computational constant used to avoid division by zero and its value is taken as $E = 0.001$. C is a constant reflecting the morphology of the melt interface. Generally, the value of C is taken between 10^4 - 10^7 . Similar to the previous studies, the value of C is adopted as 10^5 in this investigation [122, 125].

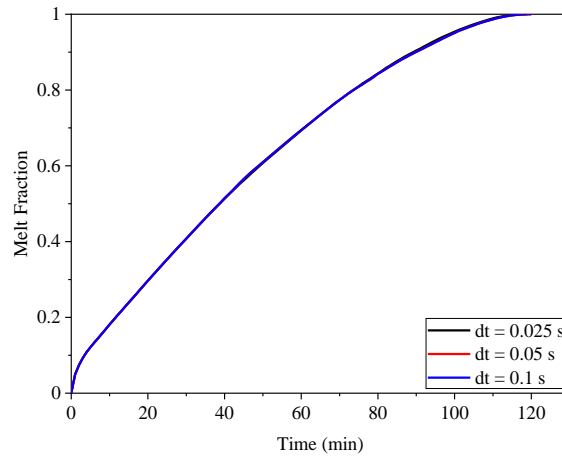
The mathematical model is solved using control volume technique. PISO method has been adopted for the pressure-velocity coupling and PRESTO scheme is employed for the pressure corrections [207]. Momentum and energy equations are solved using second order upwind scheme and Geo-reconstruct method has been utilized to correct the VOF model liquid fraction [207]. The under relaxation factors used for pressure, density and body force is considered as 0.5, while it is taken as 0.2 for momentum and liquid fraction and 0.8 for energy. The convergence criteria for continuity, momentum equation is chosen as absolute residuals of 10^{-5} , while it is fixed at absolute residuals of 10^{-8} for energy equations.



Fig. 3.10 Computational grid



(a)



(b)

Fig. 3.11 Melt fraction rates for (a) different grid refinements, and (b) different time step values

The computational domain is meshed with the quadrilateral structured grid as shown in Fig. 3.10. A finer mesh is applied near the wall of the capsule. While, the other part of the domain is meshed coarsely. In order to ensure the independency of the computational results, different grid sizes keeping the constant time step and different time steps keeping the constant grid size have been examined for the axisymmetric melting of PCM in a spherical capsule for case 1 as this is the challenging case to be analyzed. Comparison of the melt fraction of PCM in a spherical capsule with different grid sizes such as 4637, 7554, 14838 for $dt = 0.1$ s have been shown in Fig. 3.11(a). No significant difference in the melt fraction of PCM has been reported for the grid sizes. Therefore, the grid size of 7554 has been chosen in the present study. Likewise, the comparison of the melt fraction with 7554 grid size at different time steps such 0.025 s, 0.05 s, 0.1 s have been shown in Fig. 3.11(b). Based on this study, the time step of 0.1 s and grid size of 7554 have been chosen for all the cases in this study.

3.3.3 Results and discussion

Validation results

Fig. 3.12 shows the comparison of instantaneous values of melt fraction obtained from the present numerical investigation are compared with the existing experimental and numerical results of Tan et al. [122]. In their study, constrained melting of PCM has been investigated inside the glass spherical capsule. The capsule radii and thickness are 50.83 mm and 1.5 mm. PCM filled inside the capsule is taken as n-octadecane. The thermo-physical properties of PCM and glass are taken as reported by Tan et al. [122]. Initial and outer wall temperatures are reported as 27.2°C and 40°C, respectively. Axisymmetric modelling with Boussinesq approximation is chosen for the analysis as opted by Tan et al. [122] for their numerical investigation.

It may be noted from the figure that the melt fraction values obtained numerically lag behind the experimental results that is the melting rate of PCM is

higher in case of computational study. This may be because during the experiments, PCM capsule is kept inside the bath which is fixed at certain temperature, while outer wall temperature is kept constant during simulation study and this additional thermal resistance is ignored in the numerical investigation. Also, thermal conductivity of glass wall is not specifically measured during experiments. Another reason for the deviation of results is the various assumptions taken during simulation as reported in Sec. 3.2.3. In general, the present simulation results agree well with the existing numerical and experimental results of Tan et al. [122].

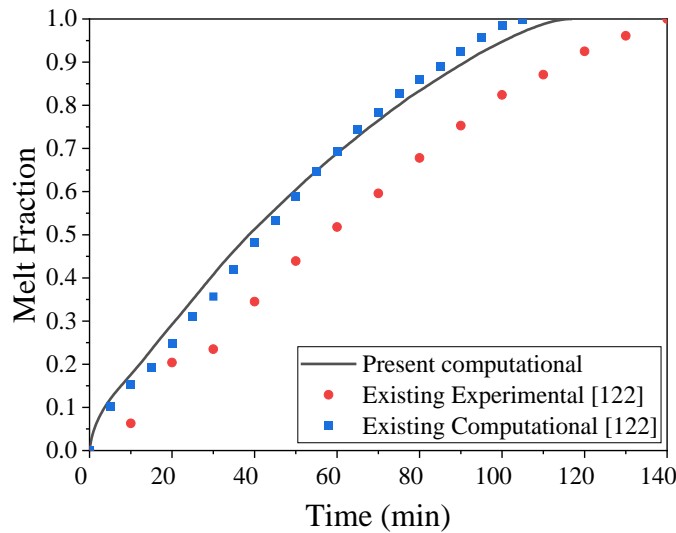
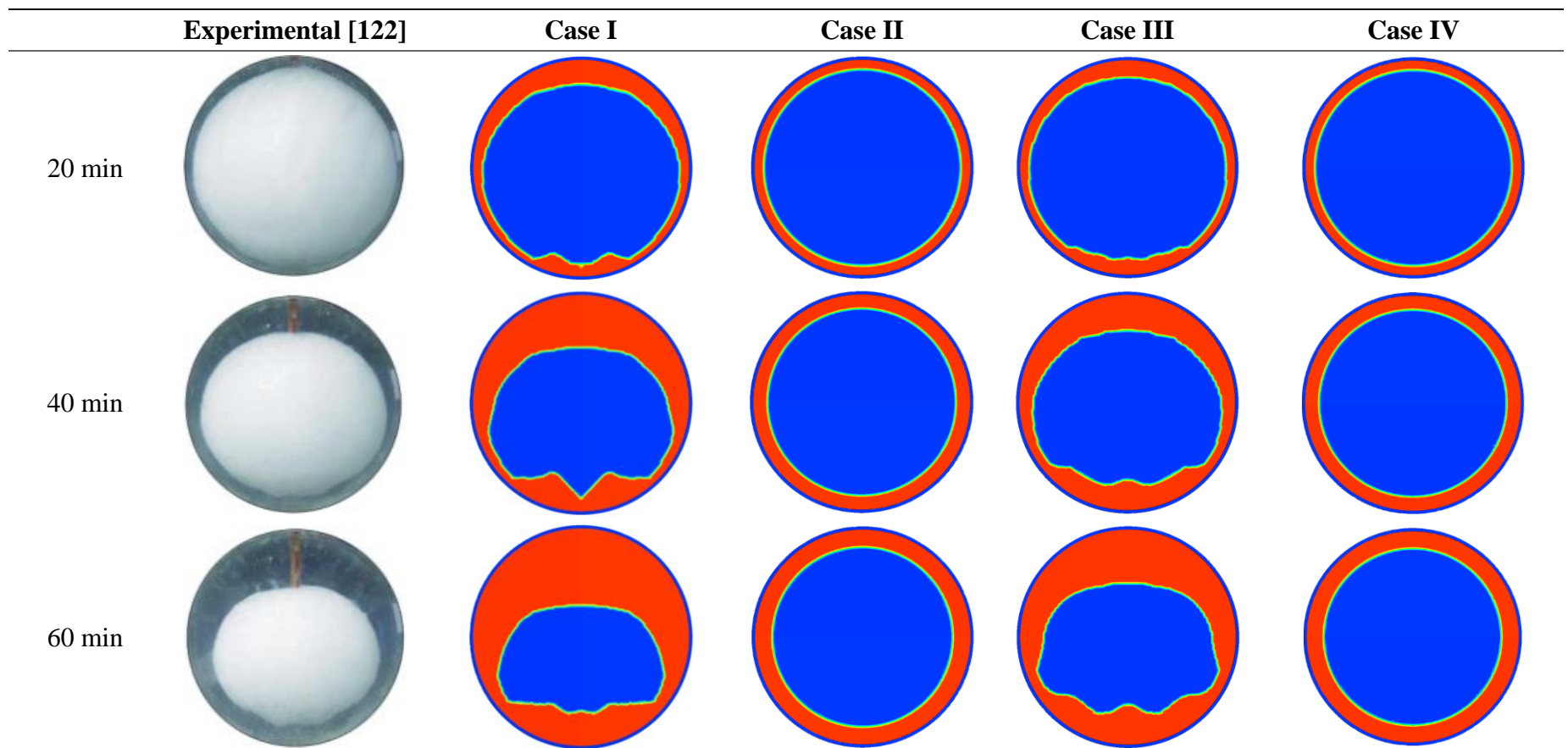


Fig. 3.12 Comparison of melt fraction obtained from present computational study with existing experimental/computational studies

Comparison of computational and visualized melting pattern

Here, results obtained from simulations of four different conditions as reported in Table 3.4 for similar geometry, initial and boundary conditions. Initial and boundary temperatures are kept as 27.2°C and 40°C, respectively. Results are obtained for four different cases in terms of melt fraction and compared with the existing experimental results. Composite diagrams are presented and discussed for the evolution of anticipated melt fraction distribution, temperature and streamline contours.



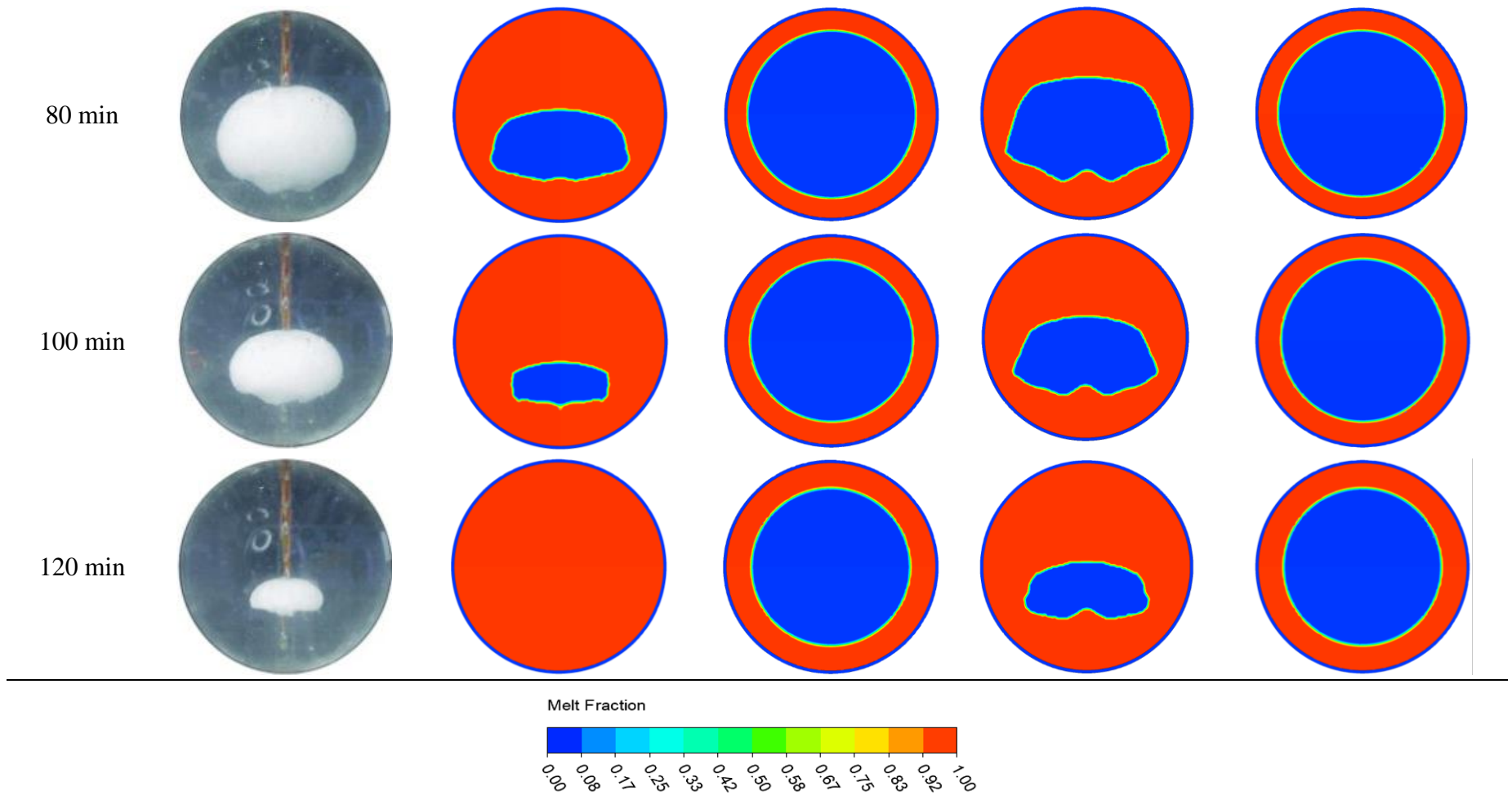


Fig. 3.13 Comparison of computational and experimental melting pattern for different case

Here, computationally obtained melt front contours for the constrained melting of PCM inside the spherical capsule have been compared with the experimentally visualized contours of Tan et al. [122] and are shown in Fig. 3.13. Different cases are considered for the comparison of melt front contours as reported in Table 3.4. The cases are compared for different time instant such as 20, 40, 60, 80, 100 and 120 min. White and transparent colors in the visualized contours represents solid and liquid PCM, respectively. While, blue and red colors are used for solid and liquid PCM respectively in the computationally obtained melt front contours. Figure shows that the cases I and III agree well with the experimentally obtained melt fraction contours in comparison to cases II and IV. Cases II and IV represent cases with constant density in solid and liquid phase. In these cases, melting of PCM inside the sphere occurs with conduction as the dominate mode of heat transfer because of the absence of circulation of buoyancy driven convection current in the liquid PCM inside the capsule. Therefore, symmetric melting occurs from all the sides of the capsule in cases II and IV. However, it can be seen from the visualized melting patterns that the constrained melting of PCM inside the spherical capsule is not symmetric from the walls. Melt fractions contours confirms that cases II and IV do not match with the existing results and therefore, those cases are not discussed hereafter.

Cases I and III represent axisymmetric and symmetric modelling cases with Boussinesq approximations, respectively. In these cases, initially the melting is conduction dominated similar to the cases II and IV. This is because solid PCM is sitting over the inner shell wall. However, this mode continues for small time duration as the subcooling of solid PCM is only 1°C. Soon, thin layer of liquid PCM is formed between the inner shell wall and solid PCM. This thin liquid layer expands with the progress of time. Liquid PCM layer growing at the bottom of the capsule is forced to move at the top of the solid PCM. In this way, warm liquid takes the position of the cold liquid and buoyancy driven convection currents start circulating. Figure shows the non-symmetric melting having more liquid layer thickness at the top compared to the bottom of the solid PCM. This can be exactly seen in the existing experimental results. In addition, the waviness is observed at

the bottom of the solid PCM at all the time instant. The reason for this is stable and unstable thermal layers at the bottom part of the sphere as reported by various authors [122, 124, 125]. Similar waviness can be seen in the experimentally visualized melt front contours of Tan et al. [122]. It may be noted from the figures that pattern of melting of PCM observed using axisymmetric and symmetric modeling with Boussinesq approximations agrees well with the existing experimental results. However, still dissimilarity exist between the two cases. It can be seen from the figures that symmetric modelling (case III) closely approximate the waviness at the bottom of the solid compared to the axisymmetric modelling (case I). Also, figure shows that the two cases have different rate of melting, which is discussed in the next section.

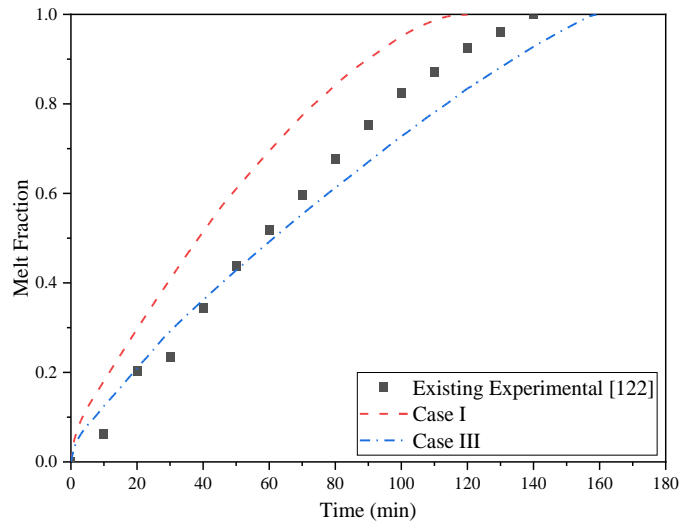


Fig. 3.14 Comparison of computational and experimental melting pattern for different cases

Comparison of melt fraction

Fig. 3.14 shows the comparison of melt fraction of PCM inside the spherical capsule for different cases with the melt fraction obtained by Tan et al. [122] in their experimental investigation. Here, axisymmetric and symmetric melting with Boussinesq approximation (cases I and III) are considered. It can be seen from the figure that the modelling conditions influences the melting rate and pattern of the

PCM inside the spherical capsule. The melting rate obtained in case I is faster compared to experimental melting rate. That is case I underestimate the melt fraction of PCM inside the spherical capsule for the constrained melting. However, case III overestimates the melt fraction of PCM that is the melting rate is slower in case III compared to the experimentally obtained melting rate. Difference in the complete melting of PCM inside the spherical capsule obtained using cases I and III with the existing experimental results are approximately 14% for both the cases.

Time dependent temperature and streamline contours

The computational and visualized melt pattern are unable to represent the intensity, flow pattern of natural convection and heat transfer characteristics inside the PCM filled spherical capsule. Therefore, composite diagrams are presented in Fig. 3.15, which shows the temperature and streamline contours for cases I and III at different time instant such as 20, 40, 60, 80, 100 and 120 min. Case I considers axisymmetric melting with Boussinesq approximation, while symmetric melting with Boussinesq approximation is considered for case III. Left half of the circle in the figure shows the colored temperature contours, where the color bar shows the temperature between initial and outer wall boundary conditions. Whereas, the right half of the circle shows the streamline contours and solid/liquid PCM. Grey color on the right side shows the solid PCM in the spherical capsule.

It can be seen from the figures that the temperature contours are nonconcentric, which shows the presence of convection driven melting of PCM. The PCM in contact with the wall melt faster and move towards the top due to convection and hence take more heat from the walls during its transit and therefore, temperature of PCM is more at the top of the sphere. This hot liquid PCM moving towards the top pushes the cold liquid PCM and takes its place. Cold liquid PCM moves downward and recirculating vortex is formed. This is the basis of existence of stable and unstable thermal layers in the proximity of the symmetric axis, which can be seen in the streamline contours.

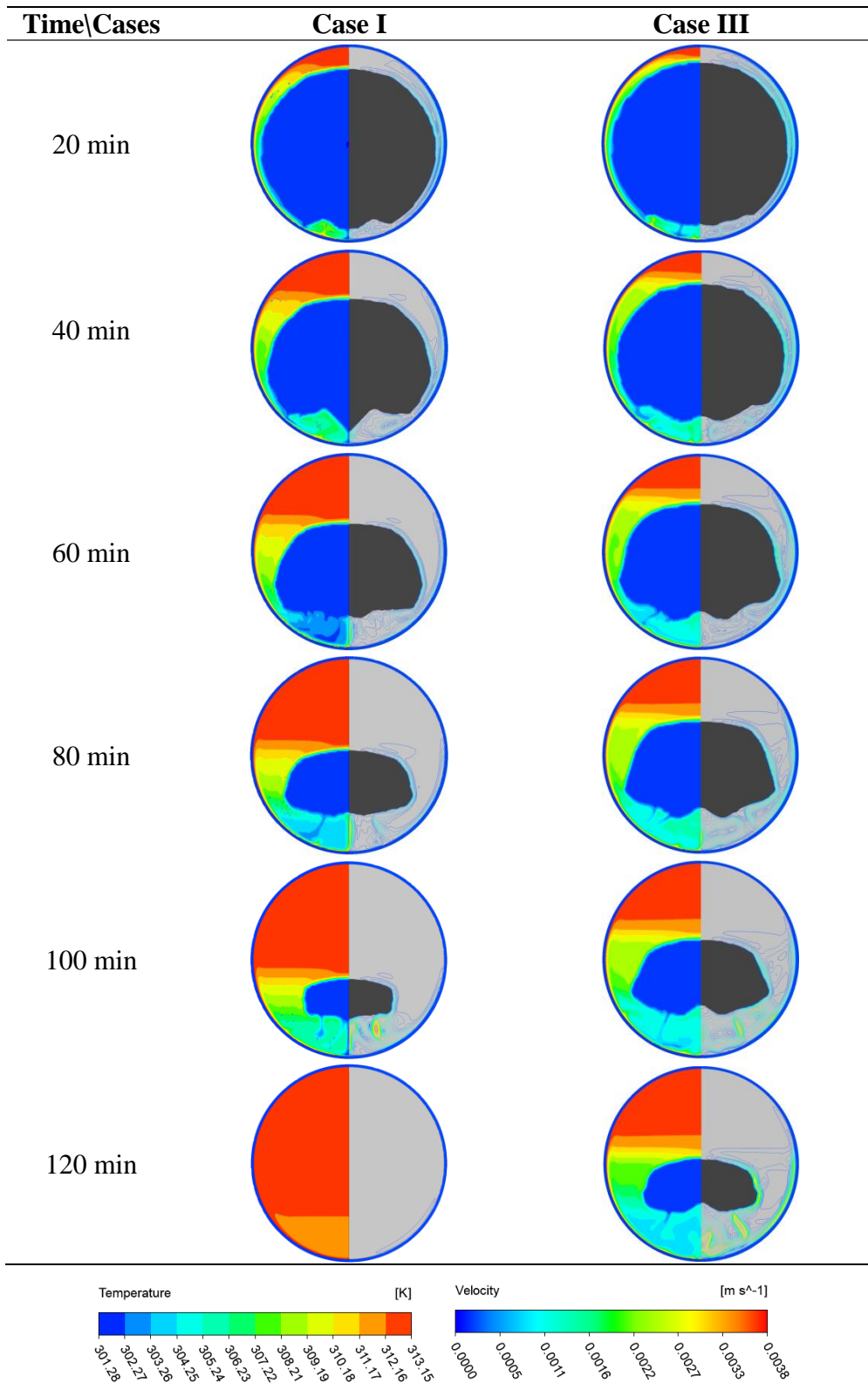


Fig. 3.15 Temperature (left) and streamline (right) contour for different cases

In the upper side the velocity of PCM is negligible that is stable structure is formed, while unstable structure can be seen at the bottom side of the symmetric axis. This unstable structure is responsible for the waviness at the bottom of the solid PCM. Also, it can be seen as unstable fluid motion is more dominant in the axisymmetric modelling during early stage of melting and therefore, more waviness can be seen at the bottom of solid PCM at 20 and 40 min. This higher unstable fluid motion increase the melting rate of PCM in case of axisymmetric modelling. However, in case of symmetric melting the waviness at the bottom increases after 60 min of melting and therefore, the melting rate is slower in case of symmetric modelling compared to axisymmetric modelling. But, as can be seen from Fig. 3.13 that the waviness pattern in symmetric modelling more closely resembles with the experimentally observed melting patterns.

3.3 Concluding remarks

The unconstrained melting behavior of phase change material (PCM) in the spherical capsule is analyzed through CFD numerical technique. Transient two dimensional axisymmetric and symmetric melting models are simulated for different cases such as linear density variation in mushy and liquid regions, linear density variation in mushy region but constant density in liquid and solid regions, Boussinesq approximation in mushy region but constant density in liquid and solid regions using Ansys Fluent 19.2 software. Validations of the computationally obtained results are carried out with the existing experimental and numerical results. Furthermore, various cases are simulated for the similar boundary and initial temperature conditions. Melting pattern and melt fraction of PCM for different cases are compared with the existing experimental results at different time instant. Simulation results depict that the axisymmetric melting underestimate, while symmetric melting overestimate the total melting time of PCM in a spherical capsule. Moreover, results of this study show that axisymmetric modelling with varying density in liquid region (case I) more

closely simulate the unconstrained melting of PCM in a spherical capsule compared to the other cases.

Also, constrained melting of phase change material (PCM) inside the spherical capsule has been numerically investigated. Computations are performed for different cases such as axisymmetric modeling with Boussinesq approximation, axisymmetric modeling with constant density, symmetric modeling with Boussinesq approximation and symmetric modeling with constant density of PCM. Melting patterns and melt fractions are compared with the existing experimental and numerical results. Results obtained using axisymmetric and symmetric modelling with constant density of PCM in different phases do not matches with the visualized melting patterns, while axisymmetric and symmetric modelling using Boussinesq approximation agrees well with the experimentally obtained melting patterns. Axisymmetric modelling with Boussinesq approximation underestimate, while symmetric modelling with Boussinesq approximation overestimate the melting time. Waviness pattern obtained in case of symmetric modelling more closely resembles with the visualized pattern.

Chapter 4

Experimental investigation of phase change materials inside the heat sink for thermal management applications

4.1 General background

Phase change materials (PCMs) are widely used for green buildings, thermal energy storage and thermal management of electronic components because of the constant temperature solid-liquid phase transition. Among various available PCMs, paraffin based PCMs are extensively used for thermal management application of portable electronic components because of high enthalpy of fusion, higher heat capacity, nontoxicity, noncorrosive and chemical stability. Lower value of thermal conductivity of PCMs is a challenge for their possible use in different applications. In view of this, high thermal conductivity enhancers (TCEs) namely, fins, metallic foams (MFs), and nanoparticles are embedded in the phase change material (PCM) system.

It may be noted that the portable electronic devices are handy and can be inclined to any angle during/after its use. It is important to examine the possible effect of inclination angle on the thermal performance of various PCM based heat sinks with and without fins. However, limited studies are available that report the effect of angle of inclination on the thermal performance of heat sinks filled with PCM. In addition, the combined effects of fin number, inclination angle, and heat flux values on the thermal performance have not been comprehensively reported in the literature for thermal management applications. Numerous studies have been made to analyze thermal management of portable electronic components with pure PCM involving different TCEs (fins, nanoparticles and MFs). The experimental studies on the combined effect of fins, MFs and nanoparticles with PCM based heat sinks on thermal performance have not been studied extensively especially for thermal management application. In this work, efforts have been made to investigate the combined effect of fins with metallic foams and

nanoparticles inside PCM based heat sink on thermal performance for thermal management application.

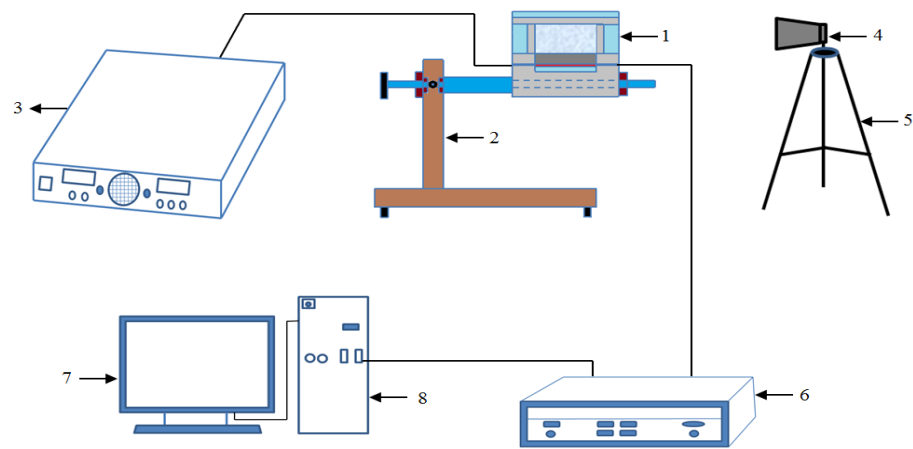
In this chapter, a systematic study has been carried out to analyze the thermal performance of heat sinks with the combined effects of fin number, inclination angle and heat flux values through experimental investigation. The thermal performance of various heat sink configurations such as pure PCM without fin, PCM with fin, PCM with MF matrix and PCM with MF matrix and fin systems during melting process is studied through experimental investigation. In addition, the combined effect of fins (0, 1, and 3 fins) and nanoparticles (2, 4, and 6 wt%) with PCM based heat sink for thermal management application have been analyzed. The operating time to stretch a critical set point temperature is studied for various heat sink configurations and design parameters.

4.2 Experimental preparations

4.2.1 Test facility

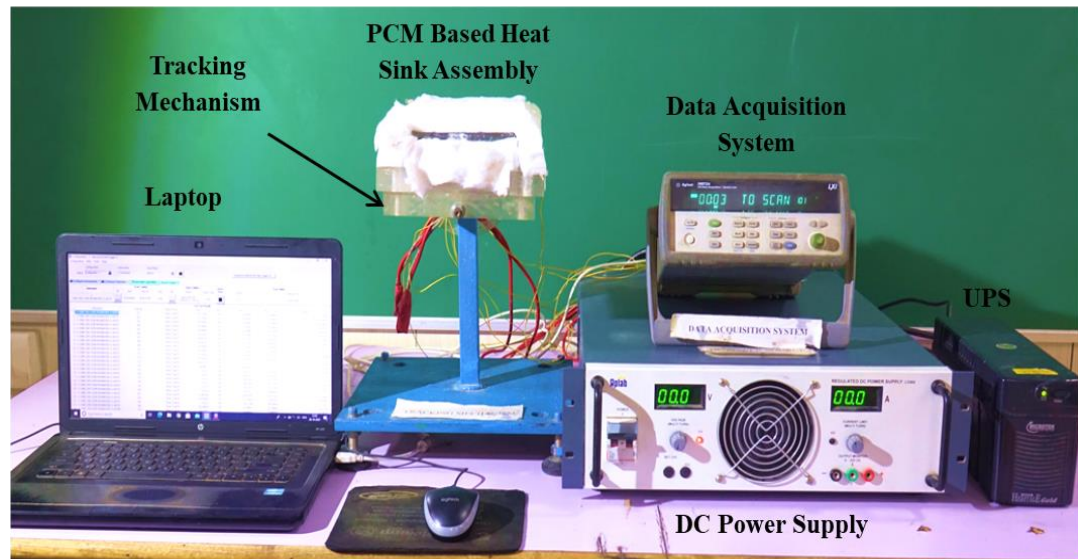
Fig. 4.1 depicts schematic diagram and actual photograph of test facility for analyzing the thermal performance of PCM based heat sinks. It consists of various modules such as PCM based heat sink assembly, data acquisition system (DAS), thermocouples, DC power supply, and laptop. PCM based heat sink assembly includes (i) heat sink container insulated with ceramic glass wool to prevent heat losses to the environment, and (ii) a plate heater (Sunrise products, India) with dimension of $100 \times 100 \text{ mm}^2$ to mimic the heat generated by the electronic devices, adhered to the heat sink base. Thermal paste (OT-201, OMEGATHERM, Omega India) having thermal conductivity of 2.30 W/m-K has been used to bond the heater and base surface of heat sink. Thermal paste minimizes the thermal resistance between interfacial surfaces that is heater and base surface of heat sink. The maximum heat flux that can be generated by plate heater is 15.0 kW/m^2 . A DC power supply (Aplab L3260, 0-32V/0-60A, India) is used to provide required electrical power to the plate heater. Three input heat fluxes of 1.3, 2.0 and 2.7 kW/m^2 are chosen for the present analysis. These are usually the power inputs for

portable electronic devices and lies between the ranges of power inputs considered in various studies that are based on thermal performance of PCM based heat sink [45, 48, 145, 148, 149, 159, 160, 212].



1	PCM based heat sink assembly	2	Support
3	DC power supply	4	Digital camera
5	Camera stand	6	Data acquisition system
7	Laptop	8	UPS

(a)



(b)

Fig. 4.1 (a) Schematic of experimental setup, and (b) Actual photograph of experimental setup

Table 4.1 Thermo-physical properties of paraffin wax, TCE and insulator

Properties	Paraffin Wax		Aluminum (TCE)	Plexiglas	Ceramic glass wool
	Datasheet	Measured property			
Melting Temperature (°C)	58-62	61.5	660.37	-	-
Latent heat (kJ/kg)	194.2	202.4	-	-	-
Specific Heat (kJ/kg-K)	2.89	2.13 (at 58°C), 3.12 (at 62°C)	0.896	1.470	-
Density (kg/m ³)	750 (l), 900 (s)	775 (l), 900 (s)	2719	-	128
Thermal Conductivity (W/m-K)	0.12 (l), 0.21 (s)	0.2 (l)	218	0.19	0.12

Among other parameters, selection of PCM plays a crucial role in the design of thermal energy storage system. This is due to the fact that the melting point of PCM must be lower than the maximum operating temperature of the component. In addition to this, PCM should have high specific heat capacity and enthalpy of fusion on volumetric basis, which can reduce the size of the system. Also, PCM should be corrosion resistant, chemically stable and non-toxic. In order to avoid the issues of confinement of PCM, the change in volume during phase change and vapor pressure at operating temperature should be low. Paraffin wax (Sigma Aldrich, USA) is used as PCM in the present investigation. Earlier, Gantara et al. [208] utilized paraffin wax (Sigma Aldrich, USA) in their experimental investigation. The thermo-physical properties of paraffin wax (PCM), aluminum (TCE), plexiglas (heat sink enclosure) and ceramic glass wool (insulator) are summarized in Table 4.1.

4.2.2 Heat sinks and measurement schemes

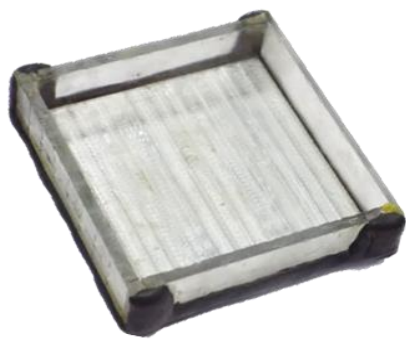
Heat sink preparation

In this study, each heat sink has constant overall internal dimensions of $100 \times 100 \times 22 \text{ mm}^3$. Here, aluminum is selected as the heat sink material due to its good thermal conductivity, low density, corrosion resistant and light weight. Although copper has higher thermal conductivity (two times higher than aluminum) but also has higher density (three times higher than aluminum), which makes it unsuitable for application of portable electronic components. In the present investigation, E350 CNC milling machine (Emcomill E350, Emco group, Austria) has been used to fabricate the heat sinks. Material is removed from the heat sink with help of HSS end mill cutter (Addision & Co., Ltd., Chennai, India) with 10 mm diameter and 22 mm cutting edge length. Photographs of various heat sinks are presented in Fig. 4.2. Plate heater having same dimensions and 4 mm thickness is attached at the heat sink base. Each heat sink assembly is enclosed with 5 mm thick transparent plexiglas sheet, which acts as an insulator. Similar plexiglas sheet is attached to cover the heat sink from the top. A gap of 2 mm is kept between the heat sink and top plexiglas surface to allow volume expansion of PCM. All four side walls, bottom surface of heater and top surface of heat sink are again insulated with ceramic glass wool of thickness 25 mm to minimize heat losses from test assembly.

Thermocouple location

Chromel-Alumel K type thermocouples are located at various positions of heat sink assembly to record temperature during the experiments. The diameter of the bare Chromel-Alumel wire is 0.19 mm. The bare wires are Teflon sheathed and the entire assembly is insulated with Teflon, leads to an overall diameter of 1.5 mm. Araldite™ epoxy resin is applied to mount the thermocouples at different location. The transient temperature variation inside the heat sinks is recorded by incorporating various thermocouples at the middle plane of the enclosure. Number of thermocouples fixed inside the enclosure for unfinned, one finned, and

three finned heat sinks are 14, 12, and 12, respectively. The arrangement of thermocouples in unfinned and finned enclosures is shown in Fig. 4.3.



(a) No fin



(b) One plate fin



(c) Two plate fins



(d) Three plate fins



(e) Four plate fins

Fig. 4.2 Photographs of various heat sinks

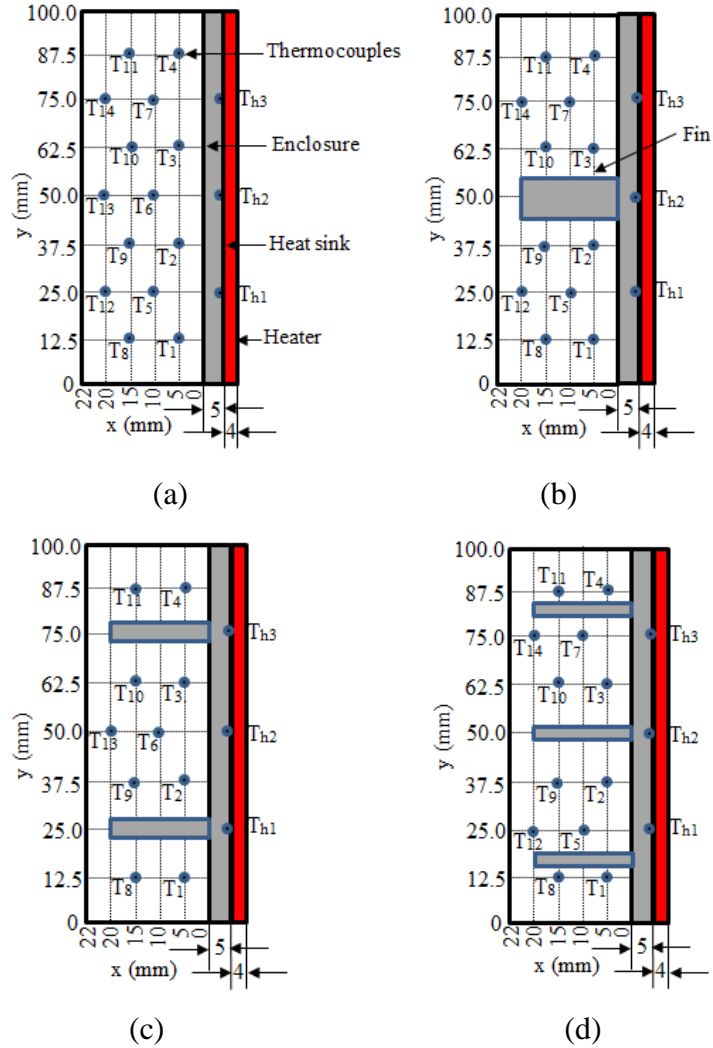


Fig. 4.3 Arrangement of thermocouples in (a) unfinned, (b) one finned, (c) two finned, and (d) three finned heat sinks

In addition, three thermocouples T_{h1} , T_{h2} , and T_{h3} are fixed at the junction of heater and heat sink. Thermocouples T_{s1} , T_{s2} , and T_{s3} are fixed at the three side walls, and T_{s4} is placed at the top surfaces of heat sink enclosure. Thermocouples T_{s5} to T_{s7} are placed over the side wall insulations, and T_{s8} and T_{s9} are placed over top and bottom insulations to analyze the heat losses after the insulation. T_{s10} is used to record the temperature of environment. The exact position of each thermocouple on the side, top and bottom surface of heat sink configurations are summarized in Fig. 4.4 and Table 4.2. Each thermocouple is connected to laptop

through DAS (Agilent 34972A, USA). The readings of thermocouples are recorded after every 10 s.

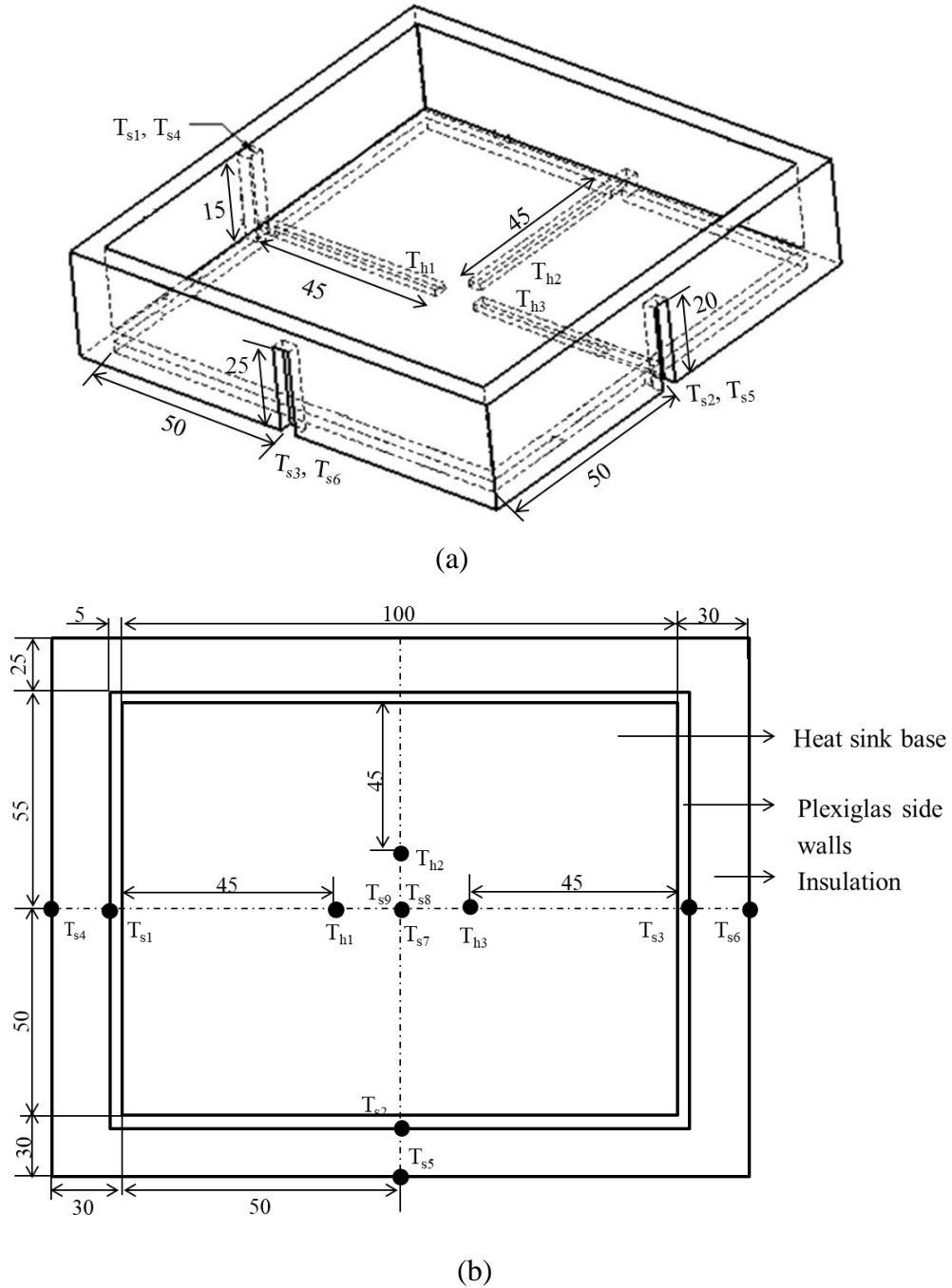


Fig. 4.4 (a) Isometric, and (b) top views of location of thermocouples on heat sink

Table 4.2 Thermocouples location on respective walls

Thermo- couple	Height from bottom of heat sink (mm)	Position from side walls	Location on walls	Location on the heat sink assembly
T _{h1}	0.75	25×50 mm ²	Base	Heat sink surface
T _{h2}	0.75	25×50 mm ²	Base	Heat sink surface
T _{h3}	0.75	25×50 mm ²	Base	Heat sink surface
T _{s1}	15	50 mm	Side 1	Heat sink surface
T _{s2}	20	25 mm	Side 2	Heat sink surface
T _{s3}	25	50 mm	Side 3	Heat sink surface
T _{s4}	32	50×50 mm ²	Top	Heat sink surface
T _{s5}	15	10 mm	Side 1	Insulation
T _{s6}	20	15 mm	Side 2	Insulation
T _{s7}	25	20 mm	Side 3	Insulation
T _{s8}	32	50×50 mm ²	Top	Insulation
T _{s9}	25	50×50 mm ²	Base	Insulation

(Downward)

Tracking mechanism

A tracking mechanism (Fig. 4.5) has been designed and fabricated to study the effect of inclination on the heat transfer performance of heat sink assembly. The tracking mechanism involving the heat sink is shown in Fig. 4.5. The base and support structure in the tracking mechanism is made of steel having four rubber mountings at the bottom. Shaft made of aluminum is provided at the top of the support structure with the help of two bearings to mount the heat sink. Bearings provide smooth rotation to the shaft. Angle indicator is attached to the support structure to calibrate the rotation of shaft in terms of inclination angles.

4.2.3 Preparation of PCM metallic foam composite and nano enhanced phase change material (NePCM)

PCM metallic foam composite

An open cell copper foam (Nanoshel LLC, USA) having pore size 10 PPI and 90% porosity is used in the present investigation. The microscopic picture of MF used in this investigation is presented in Fig. 4.6.

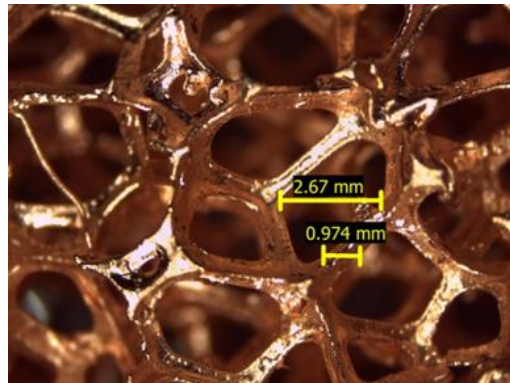


Fig. 4.6 Microscopic image of metallic foam (10 PPI)

The copper foam sample purchased from Nanoshel LLC, USA in the form of block and is cut into precise geometry with the help of sharp blade band saw within the tolerance limits of +0.1 mm. After the cutting of foam pieces into required geometry, the lateral surfaces are smoothed using a sander. The copper foam pieces are then cleaned with acetone, ethanol and water, and placed in vacuum oven for 72 h at 105°C for drying. Subsequently, the pieces are cooled down to ambient temperature before use. PCM is pre-melted for 24 h at 105°C, simultaneously; liquid PCM is dried and degassed. The MF-PCM composite is prepared by liquid infiltration process. In this process, the copper foam pieces are immersed in liquid PCM under a vacuum environment that ensures the removal of entrapped air bubbles from the liquid PCM. Later on, the PCM-copper foam composite is allowed to solidify till it attains the environmental temperature. The precise geometry of PCM and copper foam composite having same dimensions as copper foam pieces is obtained by

removing extra PCM surrounded on the copper foam pieces. Identical process was adopted by Fan and Jin [163] to obtain MF-PCM composite. Thermal paste (OT-201, OMEGATHERM, Omega India) having thermal conductivity of 2.30 W/m-K is employed to bond the foam to the base and fin surface. Thermal paste minimizes the thermal resistance between MF-fin as well as MF-heat sink base interfacial surfaces. Because of high cost associated with the brazing of MF with heat sinks, the foam is pressed forcibly between the fin gaps so that good contact can be ensured between all the surfaces. Similar procedure was reported by Baby and Balaji [136] and Bhattacharya et al. [154] in their experimental investigations. Fig. 4.7 shows the photographic view of four finned MF heat sink without PCM.

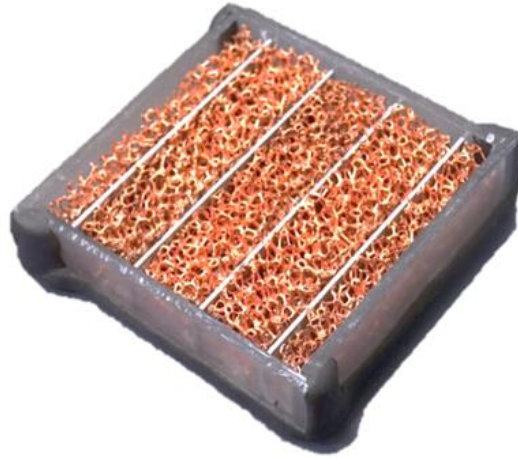


Fig. 4.7 Photograph of four finned MF heat sink without PCM

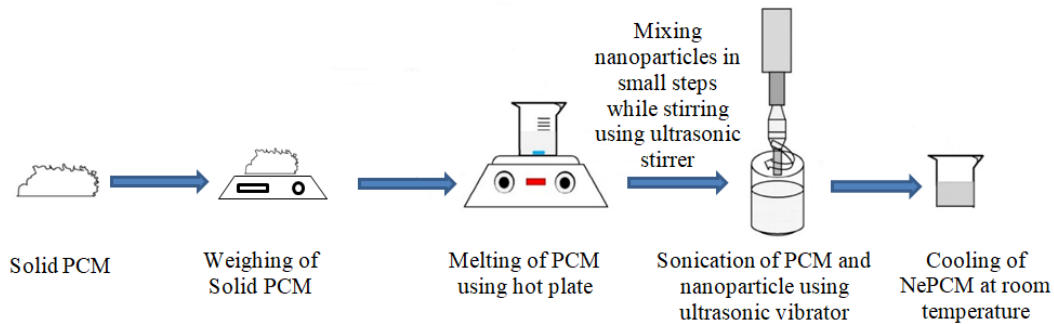


Fig. 4.8 Schematic diagram of the preparation of NePCM

Nano enhanced phase change material (NePCM)

Fig. 4.8 shows the test facility for the preparation of NePCM. Initially, the solid paraffin wax and Al_2O_3 nanoparticles are weighed in the required quantity using the electronic weighing balance (CX 265N, Citizen, India) with an accuracy of ± 0.1 mg. Later on, solid paraffin wax is melted using hot-plate (Sahil scientific, India) at 90°C and liquid PCM at 90°C is kept over the magnetic stirrer (REMI 2-MLH, Remi Elektrotechnik Limited, India). Magnetic stirrer consists of permanent magnet DC motor and stainless steel hot plate. DC motor maintains speed and hot plate maintains the temperature by supplying heat energy. Magnetic stirrer provides high accuracy of temperature control with embedded dual sensors. Temperature of the magnetic stirrer is maintained at 90°C throughout the operation that can be monitored on the display. Here, Al_2O_3 nanoparticles are added at regular intervals into the liquid PCM. Magnetic stirrer disperses the nanoparticle through the PCM by stirring the liquid PCM and nanoparticle mixture and the process continues for 2 h. Afterwards, ultrasonic vibrator (Rico scientific, USBT-12, India) is used to sonicate the mixture for 2 h at constant frequency. The ultrasonic vibrator operates at 220V/50Hz; the power and frequency is maintained at 200W and 50kHz, respectively. The unit consists of inbuilt heating arrangement and temperature controller that can maintain the constant temperature above the melting point temperature of PCM (i.e. 70°C) during sonication process. Temperature can be monitored regularly through the display. This process ensures uniform dispersal of nanoparticles in the PCM. After the sonication of PCM, the mixture is allowed to cool at room temperature. Similar procedure has been adopted by Sharma et al. [209] to prepare Palmitic acid- TiO_2 NePCM, and Tariq et al. [180] to prepare RT-44HC/GNPs in their experimental study.

The suspended nanoparticles in the PCM are found to be uniformly distributed which is confirmed by using Scanning Electron Microscopy (SEM) (FE-SEM, Supra55 Zeiss, Germany) and Transmission Electron Microscopy (TEM) (JEOL JEM 2100 PLUS, Japan). Results of SEM and TEM

are reported in Sec. 4.2.4. It has been observed that if the NePCM is kept in the liquid phase, the distribution of nanoparticle will be uniform within the PCM for significant durations (more than one day). Similar observation has been observed by Alimohammadi et al. [144] in their experimental investigation considering $Mn(NO_3)_2$ and Fe_3O_4 as PCM and nanoparticles, respectively. However, after the completion of melting experiments of NePCM in the heat sink that takes more than 2 h, mild sedimentation is observed in the bottom of the heat sink. Therefore, after each sets of experiment the NePCM mixture is re-sonicated [178].

4.2.4 Characterization and thermo-physical properties of PCM, NePCM and TCE

SEM/TEM analysis

Present study uses Aluminum-6063 to fabricate heat sink. Energy Dispersive X-ray Spectroscopy (EDX) analysis has been done using the Field-Emission Scanning Electron Microscope (FE-SEM, Supra55 Zeiss, Germany) to study the metallurgical composition of Aluminium-6063. Fig. 4.9 shows peak of the elements present in the material. It has been observed from the SEM analysis that the heat sink and TCE material used in this investigation is nearly pure aluminum [45].

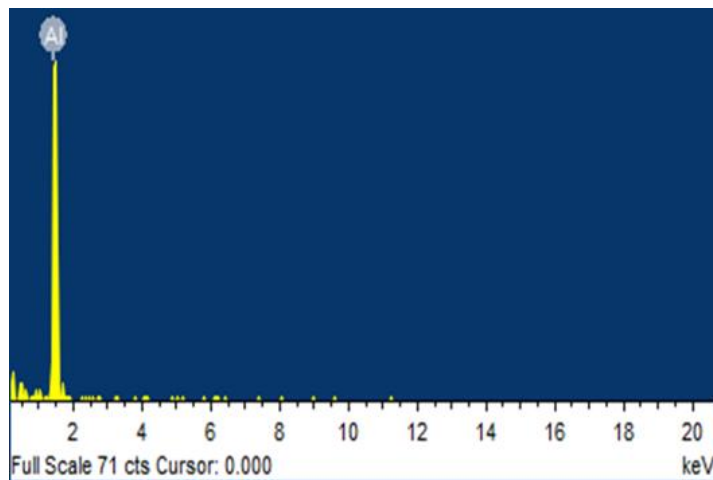
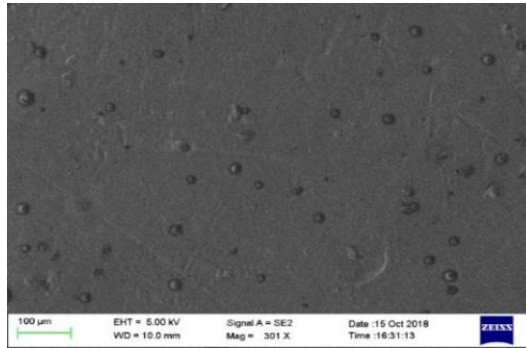
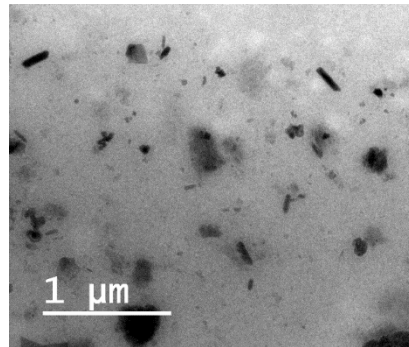


Fig. 4.9 Metallurgical composition of heat sink and TCE material

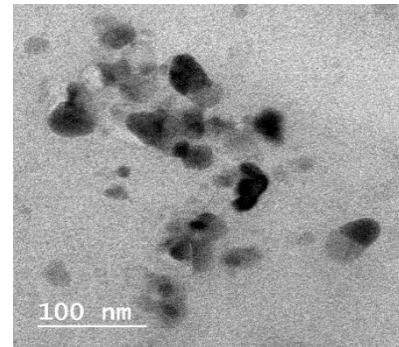
Scanning Electron Microscopy (SEM) (FE-SEM, Supra55 Zeiss, Germany) and Transmission Electron Microscopy (TEM) (JEOL JEM 2100 PLUS, Japan) are used to investigate the dispersal of nanoparticles in the PCM. Figs. 4.10(a) and 4.10(b-c) show the SEM and TEM analysis of NePCM composite, respectively. It can be seen from the figure that the nanoparticles are uniformly dispersed in the PCM.



(a)



(b)



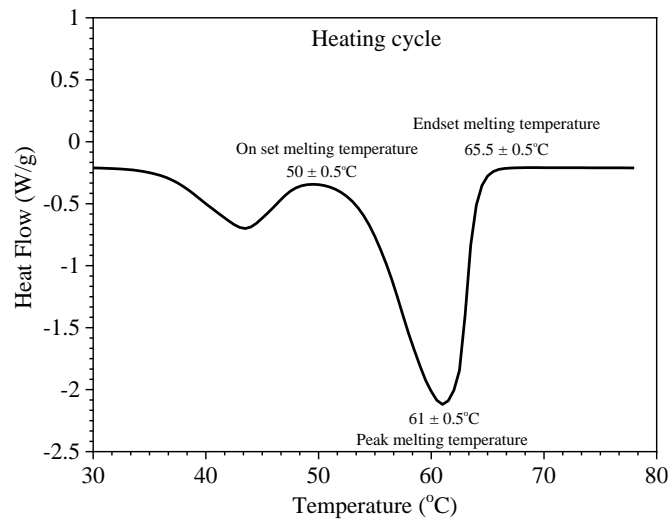
(c)

Fig. 4.10 (a) SEM image of NePCM, (b) TEM image of NePCM at 1 μm, and (c) TEM image of NePCM at 100 nm

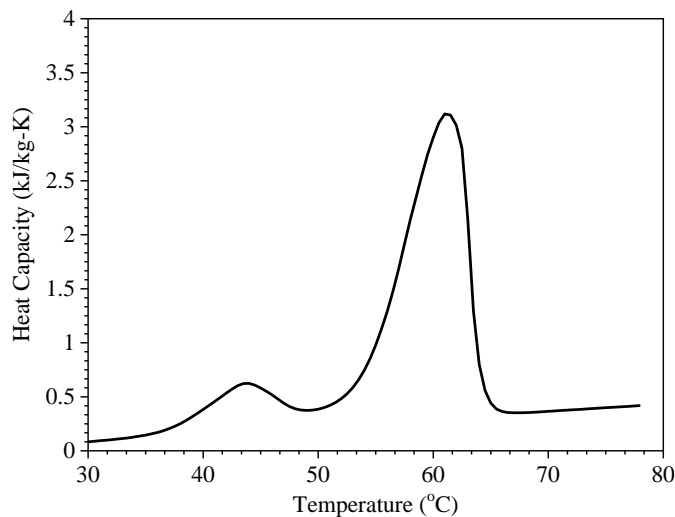
Measurement of thermo-physical properties of PCM

Differential Scanning Calorimeter (DSC) is used to determine the melting temperature and latent heat of the PCM. Fig. 4.11(a) shows the DSC heating curve of paraffin wax obtained by using DSC214 Polyma (Netzsch, Germany). The DSC thermal analysis is performed in the temperature range of 30-80°C with the heating rate of 20°C/min. Two peaks are obtained during the endothermic

melting of PCM. The solid-liquid phase change (i.e., melting) is identified by a primary peak that occurs at higher temperature of $\sim 61^{\circ}\text{C}$. While, the solid-solid phase change is presented by secondary peak that occurs at lower temperature of $\sim 40^{\circ}\text{C}$. It may be noted from the curve that the onset, peak point and end set of melting are found to be $50 \pm 0.5^{\circ}\text{C}$, $61 \pm 0.5^{\circ}\text{C}$, and $65.5 \pm 0.5^{\circ}\text{C}$, respectively. The melting of PCM occurs between these two temperature points. Also, the primary peak value obtained by DSC analysis agrees with the value specified by the supplier (Sigma Aldrich, USA).



(a)



(b)

Fig. 4.11 (a) Latent heat measurement, (b) Specific heat measurement curve of paraffin wax obtained using Differential Scanning Calorimeter

Specific heat capacity of paraffin wax is obtained by Differential Scanning Calorimetry (DSC214 Polyma, Netzch, Germany) and is shown in Fig. 4.11(b). The DSC thermal analysis is performed in the temperature range of 30 to 80°C with the heating rate of 20°C/min. The values of specific heat capacity in solid and liquid region are 2.13 kJ/kg-K (at 58°C) and 3.12 kJ/kg (at 62°C), respectively.

Here, the thermal conductivity of PCM in the solid phase is measured for a temperature range varying between 30-50°C with an interval of 5°C by utilizing TEMPOS thermal properties analyzer (TPA KS-3, Meter group, USA). It may be noted that thermal conductivity value measured for temperature below the melting point of PCM to avoid the possible natural convection effect in the mushy zone during melting. The thermal conductivity is found to be 0.2 W/m-K. The measurement is repeated five times to avoid any discrepancies in the result and the average value is presented here. The maximum deviation in the measurement of thermal conductivity is found to be $\pm 10\%$, respectively.

In order to measure the density of PCM, the solid paraffin wax is weighed in the required quantity using the electronic weighing balance (CX 265N, Citizen, India) with an accuracy of ± 0.1 mg. Later on, solid paraffin wax is melted using hot-plate (Sahil scientific, India) at 90°C and liquid PCM at 90°C is poured in the graduated cylinder. Subsequently, the cylinder is immersed in the constant temperature water bath (BTI35, Biotechnics, India). Readings of volume of PCM is recorded at various temperature values and are used to obtain the density of PCM. The maximum change in volume during solid-liquid phase change is found to be 20%. Similar procedure has been adopted by Shokouhmand and Kamkari [142] to obtain density of PCM in their experimental investigation. The measured thermo-physical properties of PCM are shown in Table 4.1.

Thermo-physical properties of NePCM

Fig. 4.12 shows the DSC heating curve of NePCM at different nanoparticle concentration obtained by using DSC214 Polyma (Netzch, Germany). Table 4.3

shows the melting temperature and latent heat of pure paraffin wax and NePCM composite at different mass fraction of nanoparticles.

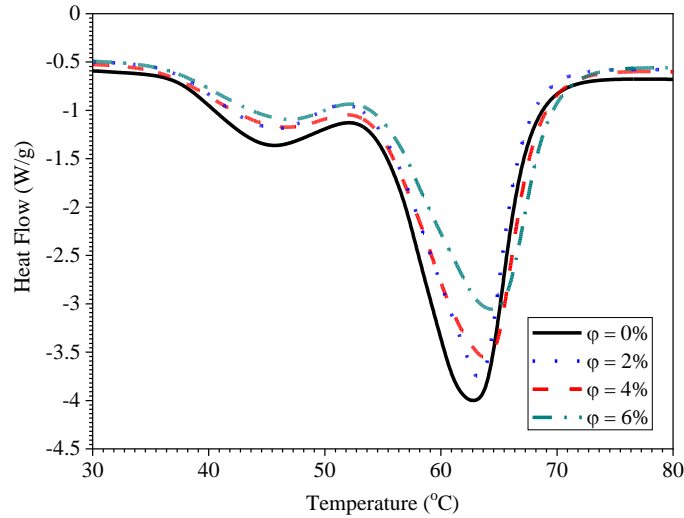


Fig. 4.12 Differential scanning calorimeter heating of PCM dispersed with various nanoparticle concentrations of Al_2O_3

Table 4.3 Melting temperature and latent heat variation of NePCMs

Sample	Melting temperature (°C)	Melting temperature variation (%)	Latent heat (kJ/kg)	Latent heat variation (%)
$\phi = 0\%$	62	0	143.8	0
$\phi = 2\%$	63.5	2.40	132.0	8.20
$\phi = 4\%$	64.5	4.03	121.6	15.43
$\phi = 6\%$	65	4.83	112.5	21.76

It may be noted from the table that the melting temperature of NePCM increases by 1.5, 2.5, and 3°C for nanoparticle mass fraction of 2, 4, and 6%, respectively compared to pure paraffin wax. The latent heat of NePCM is found to be lower than pure PCM. The reduction in the latent heat value is found to be 8.2, 15.43, and 21.76% for nanoparticle loadings of 2, 4, and 6%, respectively than pure

PCM. The changes in melting temperature and latent heat of NePCM are insignificant upto $\phi = 2\%$. However, with the increase in nanoparticle loading (4 and 6%) the change in latent heat of NePCM becomes significant. This is because of the substitution of PCM with nanoparticles that remains in the solid phase and absorb lower energy during the phase change compared to $\phi = 2\%$. Various researchers have reported similar results for different weight fractions of Al_2O_3 in paraffin wax [210, 211].

Nanoparticle weight fraction is described as the ratio of mass of Al_2O_3 particle to the mass of PCM.

$$\omega = \frac{m_N}{m_P} \quad (4.1)$$

The density, thermal conductivity, latent heat and specific heat capacity of NePCM can be estimated as a function of weight fraction of constituent [116, 212] as:

$$\rho_{NePCM} = \omega\rho_N + (1-\omega)\rho_P \quad (4.2)$$

$$k_{NePCM} = \omega k_N + (1-\omega)k_P \quad (4.3)$$

$$(\rho L)_{NePCM} = (1-\omega)(\rho L)_P \quad (4.4)$$

$$(\rho c_p)_{NePCM} = \omega(\rho c)_N + (1-\omega)(\rho c)_P \quad (4.5)$$

The variation of viscosity (μ) with addition of nanoparticles can be obtained from Eqs. (4.6-4.7) [213].

$$\mu_{NePCM} = 0.983e^{12.959\Phi} \mu_P \quad (4.6)$$

Where Φ represents the volume fraction of nanoparticles and can be obtained using the following expression.

$$\Phi = \frac{\frac{Wt_N}{\rho_N}}{\frac{Wt_N}{\rho_N} + \frac{Wt_P}{\rho_P}} \quad (4.7)$$

Where, Wt_N and Wt_{PCM} represent the weight of the nanoparticle and the weight of the PCM, respectively. Here, ρ_N and ρ_P represent the density of nanoparticle and PCM, respectively.

Table 4.4 shows the thermal conductivity, specific heat capacity and viscosity of NePCM at different nanoparticle concentrations. Table 4.4 shows that thermal conductivity and specific heat capacity increases and decreases, respectively with the inclusion of nanoparticles. This is because of lower specific heat capacity and higher thermal conductivity of Al_2O_3 nanoparticle compared to pure PCM. It can be seen from the Table 4.4 that percentage increase in viscosity is 4.4% upto mass fraction of 2%. However, the percentage increase in viscosity increases significantly with higher nanoparticle concentration (4% and 6%). Similar variation has been obtained by Ho and Gao [210].

Table 4.4 Specific heat capacity and thermal conductivity variation of NePCMs

Sample	Specific heat (kJ/kg-K)	Specific heat capacity variation (%)	Thermal conductivity (W/m-K)	Thermal conductivity variation (%)	Viscosity (kg/m-s)	Viscosity variation (%)
$\varphi = 0\%$	2.89	0	0.21	0	0.0235	0
$\varphi = 2\%$	2.71	4.50	4.565	20.73	0.0245	4.41
$\varphi = 4\%$	2.56	11.31	8.921	41.48	0.0261	11.12
$\varphi = 6\%$	2.42	16.02	13.277	62.223	0.0278	18.49

4.2.5 Experimental procedure, data reduction and comparison of results

Experimental procedure

Initially, small quantity of solid PCM is melted in a vacuum furnace and poured inside the heat sink enclosure and sufficient time is provided for solidification in each layer. The process is repeated for melting the entire PCM and poured inside the heat sink enclosure. This procedure ensures the absence of

any air pocket inside the PCM [138]. It may be noted that the constant mass of solid PCM is filled inside the heat sink enclosure for all the cases. All the tests are initiated at an ambient temperature of 30°C. Before start of the experiments, it was ensured that both the heat sink and PCM are maintained at temperature of 30°C. Later on, the heating system is turned on and the temperature readings are recorded by using data acquisition system (Agilent 34972A, USA) at the regular intervals of 10 s.

Heat flux is provided to the heat sink filled with PCM with the help of DC heater. Initially, the heat generated by the heater is absorbed by the PCM and the temperature of both PCM and heater increases till the PCM attains the melting point. During this stage, the supplied heat energy is absorbed in PCM and the temperature of PCM rises due to gain in sensible heat. After the PCM attains the melting temperature, it absorbs latent heat and the temperature of heater and PCM remains stable during that period. With the further supply of input heat energy, the liquid solid interface (melt front) moves from bottom to the top layer of PCM. As the time progresses, the complete melting of PCM take place and the temperature of electronic system tends to increase due to sensible heating of molten PCM. On the contrary, during cooling period the PCM tends to solidify as it losses heat energy. The insulation of one of the side wall is removed for 20 s for taking photographs of PCM at every 5 min during the melting of PCM. Readings and photographic images are taken for different heat sinks at various angles of inclination. Later on, the photographic images are used to calculate melt fraction of PCM at each time with the help of MATLAB image processing tool box (Matlab R2019, Mathworks, USA).

The melt fraction is calculated using the digital images captured from one side of the heatsink (front side). The recored images are initially cropped to the area of interest and subsequently the image contrast is enhanced to clearly visualize the interfaces. In such a case, the processed image enables to visualize the distinction between the liquid PCM, solid PCM, fin and air regions. Subsequently, the number of pixels of each region is calculated by defining a pixel intensity range for different regions in MATLAB. The melt fraction is calculated by the

adding the number of pixels of liquid PCM divided by the total number of pixel of solid and liquid PCM (Eq. 4.8).

$$\text{Melt fraction} = \frac{\text{Number of Pixels of liquid PCM}}{\text{Total number of pixels of solid and liquid PCM}} \quad (4.8)$$

Experimental uncertainty and losses

Pre calibrated Chromel-Alumel K-type thermocouples are used to record temperature at different positions of heat sink assembly. The thermocouples are calibrated for the temperature range of 0-100°C following the ASTM standards [214]. The calibration is performed using a constant temperature bath with standard mercury in glass thermometer (temperature range from 0°C to 200°C and 0.1°C resolution). In this process, one end of all the thermocouples are immersed in the water filled inside the constant temperature bath (BTI35, Biotechnics, India) and the other end is connected to the data acquisition system (34972A, Agilent Technologies, USA). The temperature data measured by thermocouples are processed and recorded by a data acquisition system connected to the computer. An immersion heater is kept inside the water bath to provide necessary heat input to the water and continuous stirring is carried out to maintain the uniform temperature in the water bath. Subsequently, the rise in temperature of water is measured by using the thermometer and the thermocouples at fixed time interval of 5 min. Electric power supply is switched off as soon as the water temperature reaches 100°C. Subsequently, the drop in the temperature of water is measured at regular intervals. The error in temperature measurement is calculated as $\pm 0.2^\circ\text{C}$.

A DC power supply (Aplab L3260, 0-32V/0-60A, India) is used to provide required electrical power to the plate heater. Input heat flux of 2.7 kW/m^2 is considered for the present analysis. Standard digital multi-meter (Mecco 206) is used to verify the readings of current and voltage measurements displayed by DC power source. The errors in the measurement of current and voltage are $\pm 0.1 \text{ A}$ and $\pm 0.1 \text{ V}$, respectively. Table 4.5 shows the uncertainty in measured and estimated parameters. Utilizing the individual uncertainties in each parameter, the

error analysis are made to estimate the errors associated in heat flux following the procedure suggested by Cole-man and Steele [103]. The uncertainty in measurement of heat flux is found as $\pm 6.02\%$ for heat flux value of 1.3 kW/m^2 . The details of calculation procedure for various heat flux values is elaborated in Appendix I.

Table 4.5 Uncertainty in measurement

Parameter	Error
Length (l)	0.02 mm
Width (w)	0.02 mm
Height (h)	0.02 mm
Temperature (T)	$\pm 0.2^\circ\text{C}$
Voltage (V)	$\pm 0.1 \text{ V}$
Current (I)	$\pm 0.1 \text{ A}$

The heat loss can be estimated by the Fourier's law for heat conduction as follows [216].

$$Q_{loss} = \frac{k_{ins} \Delta T}{\Delta x} \quad (4.9)$$

where Q_{loss} is the heat loss through the ceramic glass wool (insulation), k_{ins} is a thermal conductivity of insulation (0.12 W/m-K), ΔT is the temperature difference between the two surfaces of insulation, and Δx (0.025 m) is the thickness of the insulation layer. The temperature difference is calculated from the temperature data collected by using different thermocouples employed on the both the sides. The maximum loss of heat from all the surface of heat sink enclosure and the bottom of the heater is found to be 2.4% and 7.4% of the total power, respectively.

The insulation of one of the side wall is removed for 20 s for taking photographs of PCM at every 5 min to enable the melting front of PCM to be captured by a digital camera periodically. The process continues till the entire PCM is converted into liquid phase. The total time for which insulation removed

is about 2% of the total experiment time. The heat loss caused by the natural convection of plexiglas surfaces could be estimated by the following equations.

The average Nusselt number could be estimated by [217, 218]

$$Nu = 0.68 + \frac{0.67 Ra^{1/4}}{\left[1 + (0.492 / Pr)^{9/16}\right]^{4/9}} \quad (4.10)$$

The total heat loss during removal of the insulation could be estimated by the following equation [141, 142, 217]

$$Q_{loss} = \frac{Nu \times k}{L_c} A \Delta T \Delta t \quad (4.11)$$

Here, ΔT is the temperature difference between the insulation surface of the enclosure and the environment during the time interval (Δt). L_c is the characteristic length.

It may be noted that the heat loss energy during removal of insulation is found less than 2%.

Data reduction

Various parameters are used to explain the thermal performance of heat sinks. These includes volume fraction of PCM (ψ), enhancement ratio of the heat sink with TCE (ε), enhancement ratio of heat sink with MF composite (ϕ) and thermal conductance of PCM based heat sinks (G). The criteria for evaluation of various parameters are elaborated below.

The volume fraction of PCM (ψ) is described as the ratio of volume of PCM filled inside the heat sink to the difference between the total volume of heat sink and volume occupied by the fins [148] and can be expressed as:

$$\psi = \frac{V_P}{V_{HS} - V_{TCE}}$$

(4.12a)

The volume fraction of TCE (ζ) is described as the ratio of volume of TCE inside the heat sink to the total volume of heat sink [148] and can be expressed as:

$$\zeta = \frac{V_{TCE}}{V_{HS}} \quad (4.12b)$$

The enhancement ratio of heat sink with TCE (fins, metal foam, and nanoparticles) is described as ratio of time taken to attain a critical set point temperature (SPT) by the PCM based heat sink with TCE to PCM based heat sink without TCE [148, 149]. This can be expressed as:

$$\xi = \frac{t_{cr_{withTCE}}}{t_{cr_{withoutTCE}}} \quad (4.13)$$

In addition to this, the enhancement ratio of heat sink with MF (ϕ) is described as the time taken to attain a critical SPT by MF-PCM composite based heat sink to heat sink without MF-PCM composite and is expressed as:

$$\phi = \frac{t_{cr_{withMF-PCM}}}{t_{cr_{withoutMF-PCM}}} \quad (4.14)$$

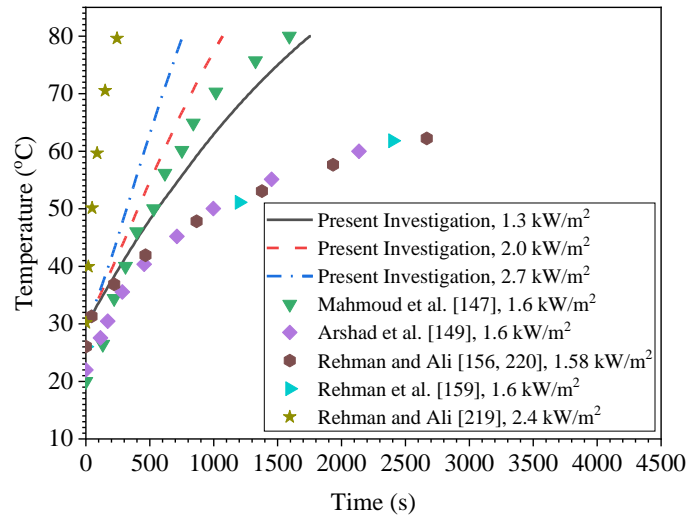
Thermal conductance (G) of PCM based heat sink is described as the amount of heat exchange from the heat sink surface [148, 155].

$$G = \frac{P_o}{T_{max} - T_{\infty}} \quad (4.15)$$

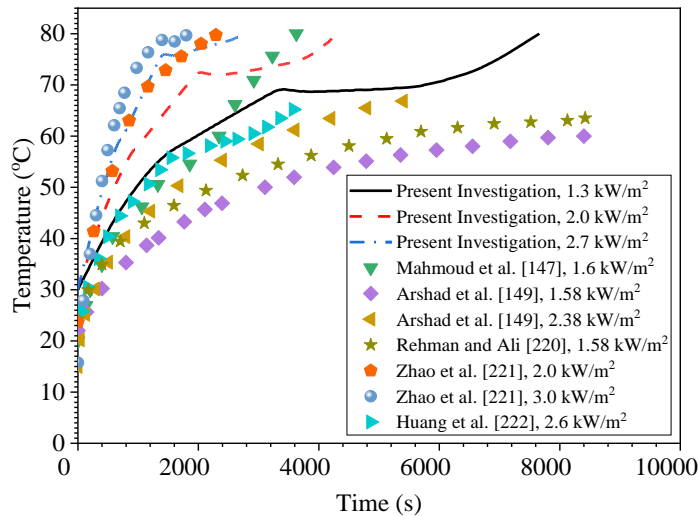
Comparison and repeatability of results

In order to validate present experimental results, the base temperature (T_b) of the heat sink obtained from the present experimental study are compared with the test data of Mahmoud et al. [147], Arshad et al. [149], Rehman and Ali [156, 159, 219] and Rehman et al. [220], Zhao et al. [221], and Huang et al. [222] (Figs. 4.13a-b). Most of the studies consider heat sink having dimension of $100 \times 100 \times 25 \text{ mm}^3$ [149, 156, 159, 219, 220, 222] and the heat flux values are varied

between 1.3-3.0 kW/m². Most of these studies consider paraffin wax with melting temperature range varying between (47-57°C) [159, 219], (56-58°C) [149, 156, 220] for the analysis. While studies also consider Rubitherm RT-42 with melting temperature of 42°C [147], Stearic acid with melting temperature of 68.77°C [221] and lauric acid with melting temperature varying between 42-44°C [222] for the analysis. The initial temperature of PCM was varied between 20-30°C in these studies [147, 149, 159, 156, 219-222].



(a)



(b)

Fig. 4.13 Comparison of temperature of heat sink base obtained from present results with the existing results for (a) without PCM, and (b) with PCM based heat sinks

In the present investigation, heat sink having dimensions of $100 \times 100 \times 22$ mm³ and paraffin wax (Sigma Aldrich, USA) having melting point of 58-62°C has been used. Comparison of present test results with available experimental results [147, 149, 156, 159, 219-222] for unfinned heat sink without PCM and with PCM are shown in Figs. 3.13(a) and 3.13(b), respectively. It can be seen from the figures that base temperature of heat sink obtained from the present study follow similar pattern as reported by various researchers [147, 149, 156, 159, 219-222]. However, the variation in the results obtained from the present experimental investigation with the existing test results may be due to the change in the heat sink design, the melting point temperature of PCM and starting temperature of PCM in the experimental investigation. Also, the results are checked for the repeatability and the error is found to be $\pm 1\%$ (Fig. 4.14).

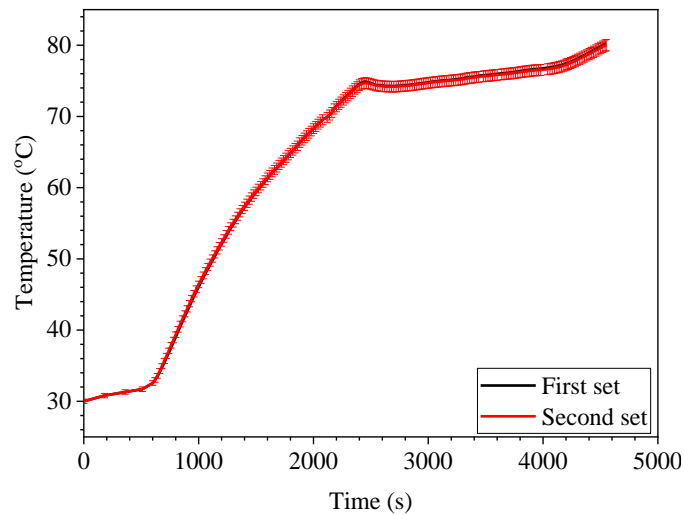


Fig. 4.14 Repeatability of readings of the base temperature of PCM based unfinned heat sink at 2.0 kW/m^2

4.3 Results and discussion

In the present investigation, tests are performed to investigate the combined effects of fin number, inclination angle and heat flux values on the thermal performance of PCM based heats sinks. In addition, the effect of various TCEs such as fins, metallic foam, nanoparticles and their combined effect on thermal

performance of heat sinks is investigated. Results obtained from various studies are elaborated below.

4.3.1 Effect of inclination angle on the performance of phase change material based finned heat sink configurations

In this section, a systematic study have been carried out to investigate the thermal performance of heat sinks incorporating the combined effects of fin number, inclination angle and heat flux values through experimental investigation. Four different heat sink configurations such as unfinned, one finned, two finned and three finned are analyzed in this study. Photographs of various heat sinks used in this study are presented in Fig. 4.15.

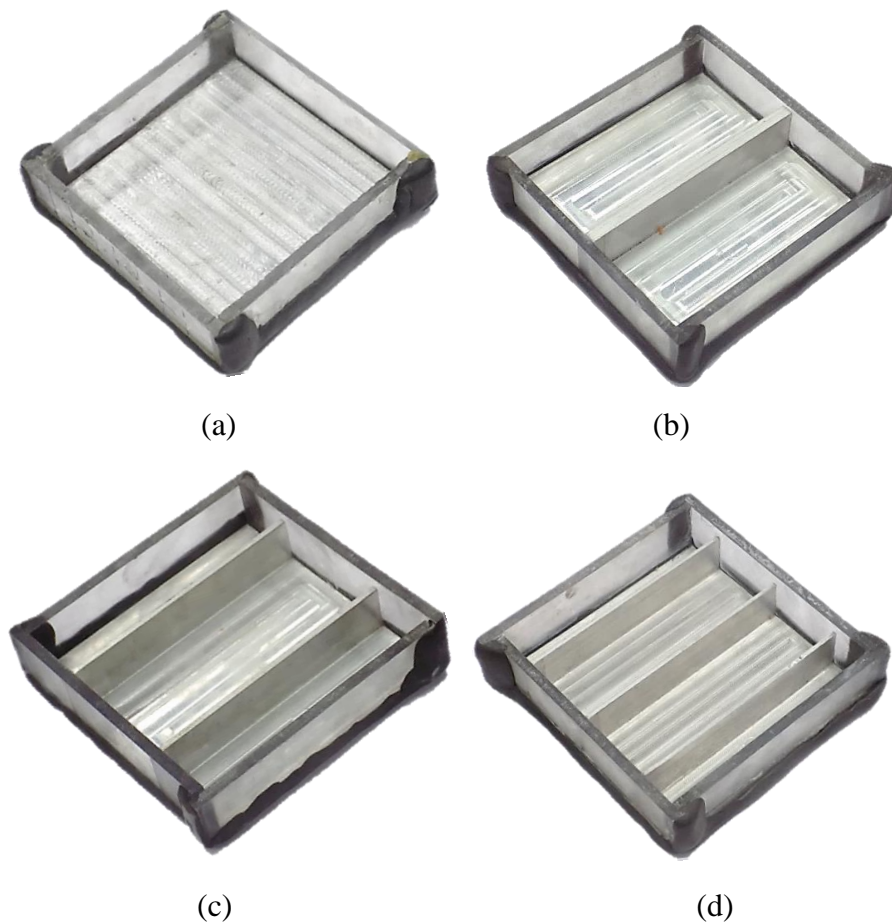


Fig. 4.15 Photographs of (a) unfinned (b) one finned, (c) two finned and (d) three finned heat sinks used in the present study

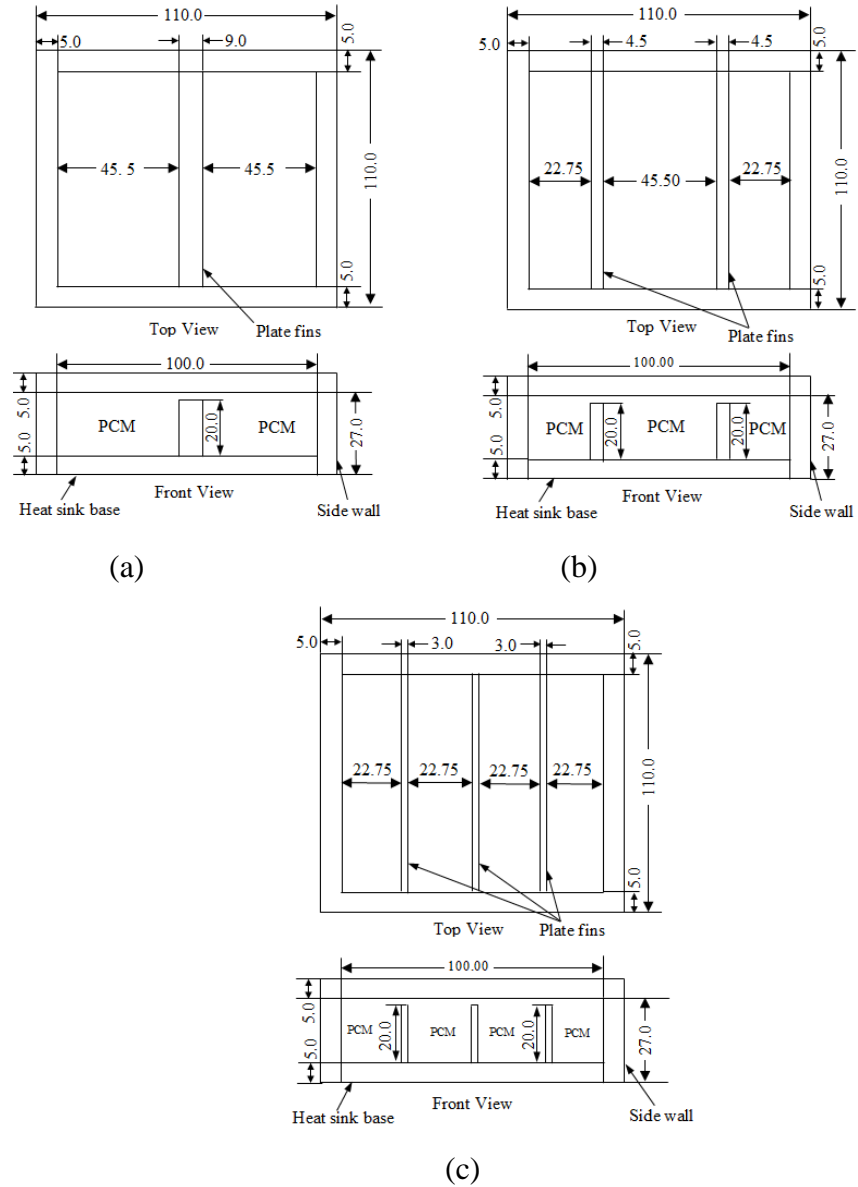


Fig. 4.16 Dimensions of (a) one finned, (b) two finned and (c) three finned heat sinks

Fig. 4.16 shows the plate fin heat sinks with different dimensions and Table 4.6 summarizes the dimensions of fins. The volume fraction of thermal conductivity enhancer (TCE); that is fin, inside the heat sink is kept constant for all the configurations. Constant mass (162 gm) of solid PCM or 180 cm³ of liquid PCM is filled inside the heat sink enclosure for all the cases. Tests are conducted at different inclination angles of heat sink 0° to 90° at the increment of 15°.

Initially, tests have been carried out for all three input heat flux values (1.3, 2.0 and 2.7 kW/m²) for seven inclination angles (0°, 15°, 30°, 45°, 60° and 75°, and 90°). It may be noted that similar pattern of results have been obtained at all three heat flux values for various inclination angles. Therefore, for the sake of brevity, the heat flux value of 2.0 kW/m² is used for 0°, 15°, 30°, 60° and 75°, and 90°. While, the heat flux values such as 1.3 and 2.7 kW/m² are considered for only three different angles of inclination (0°, 45° and 90°).

Table 4.6 Fin dimensions for different configuration of heat sinks

Heat sink Configurations	Total volume fraction of fins/TCE	Dimensions of each fin (mm³)
One finned heat sink		100 × 9.0 × 20
Two finned heat sink	9 %	100 × 4.5 × 20
Three finned heat sink		100 × 3.0 × 20

Effect of inclination angle on the heat sink base temperature

The distribution of base temperature for various heat sink assemblies such as unfinned, one finned, two finned and three finned heat sinks for varied range of inclination angle (0° to 90°) is shown in Figs. 4.17(a-d). In case of unfinned heat sink assembly, the base temperature increases sharply with time compared to other configurations. This configuration shortens the net usage time of electronic components and is undesirable. While, the usage time increases with the insertion of fins in the heat sink assembly. Figures show that inclination angle of heat sink significantly affects the thermal performance of unfinned, one finned and two finned heat sinks, mainly after 600 s. This occurs due to high latent heat storage capacity of PCM and mechanism of heat transfer inside the PCM. Initially, conduction heat transfer plays a prominent role during melting of PCM. As the time progresses, free convection pushes the liquid PCM near the heat sink towards up side due to density gradient. In such a case, the liquid fraction

increases inside the enclosure and free convection starts dominating the melting process. Consequently, the transfer of heat to the PCM increases and the rate of increase of base temperature decreases (Figs. 4.17(a-d)). With the increase in angle of inclination, the circulation because of convection gets weaker and results in higher base temperature.

The effect of inclination angle is found to be less significant in case of finned heat sinks compared to unfinned heat sink. Also, the effect of inclination on the thermal behavior decreases as the number of fins increases. This may be because the fins obstruct the natural convection.

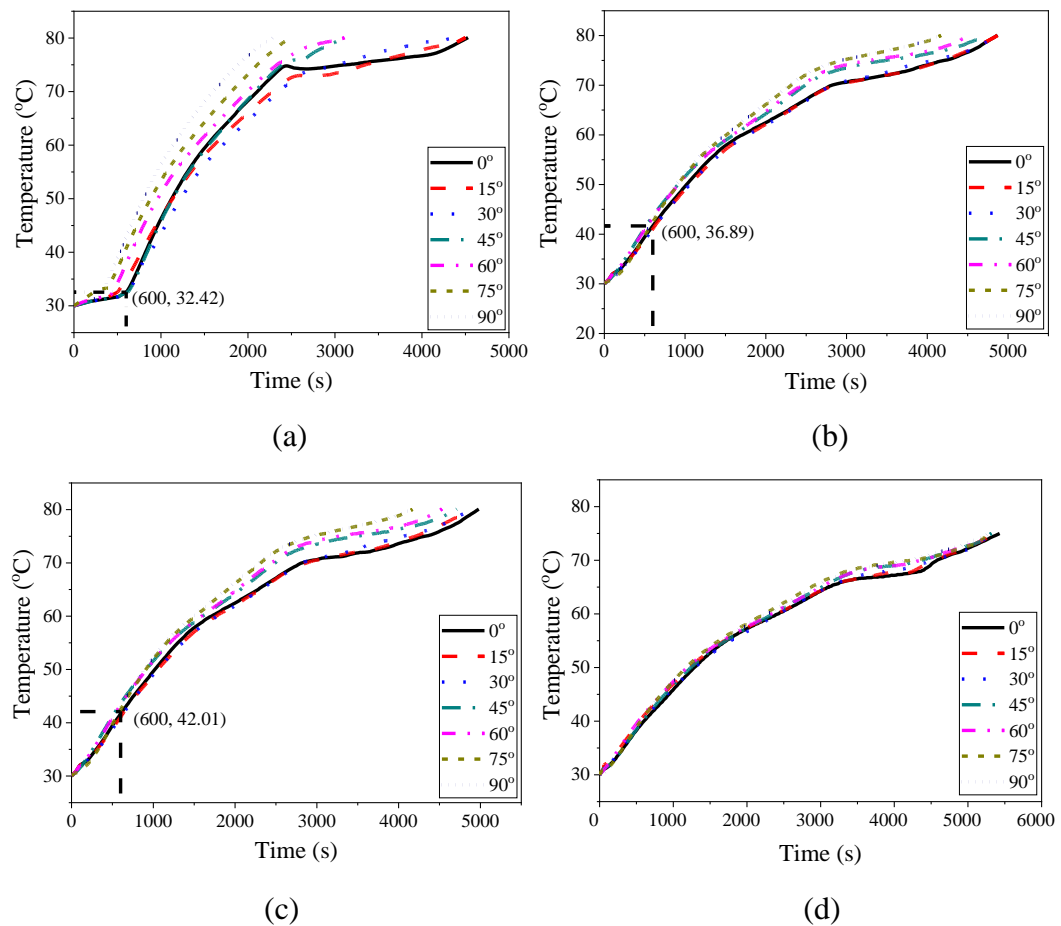


Fig. 4.17 Time histories of base temperature at different inclination angle of 0°, 15°, 30°, 45°, 60°, 75° and 90° for (a) unfinned, (b) one finned, (c) two finned, and (d) three finned PCM based heat sinks

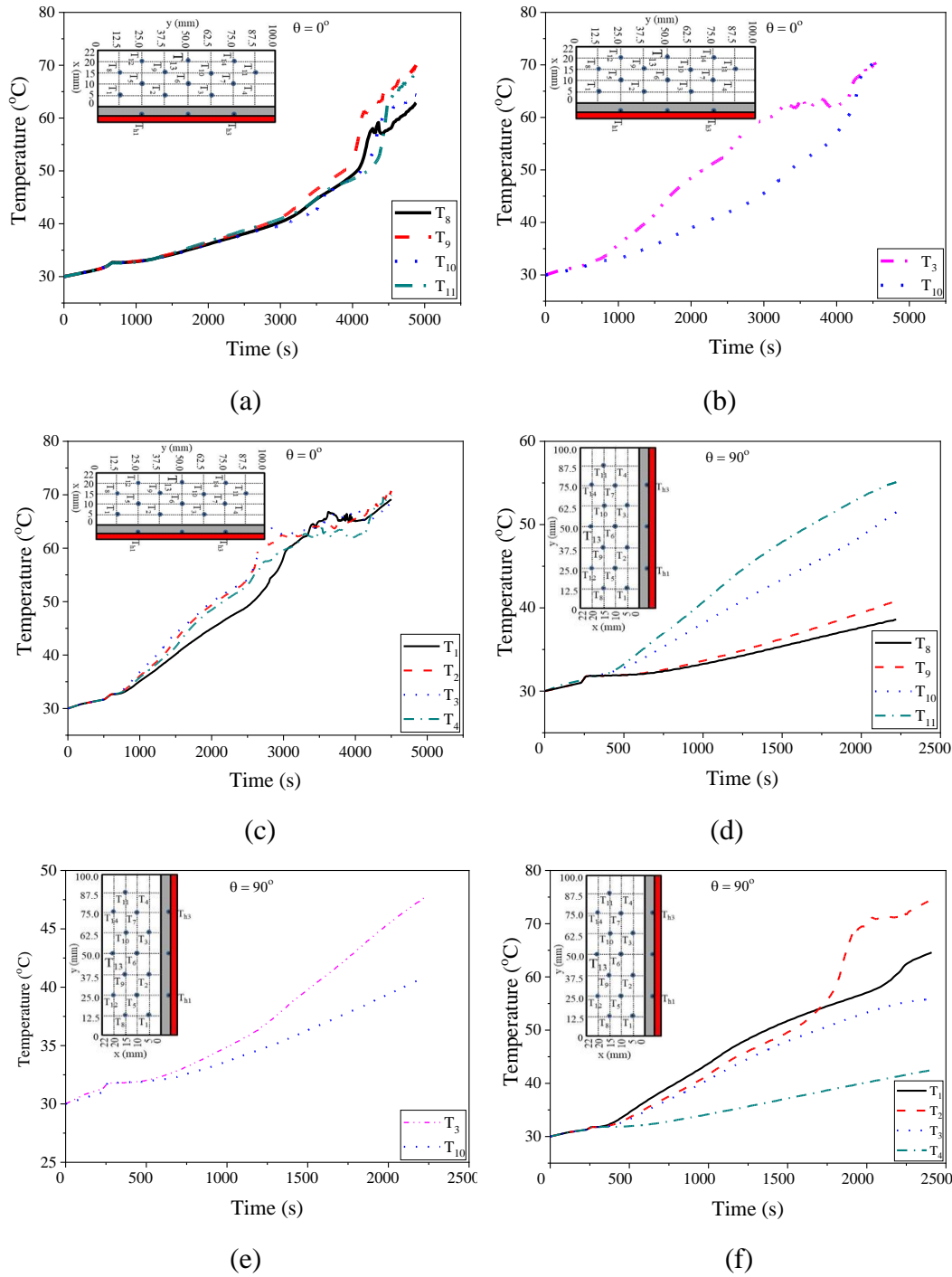


Fig. 4.18(a-f) Time history of temperature of PCM at different horizontal and vertical locations for unfinned PCM based heat sink

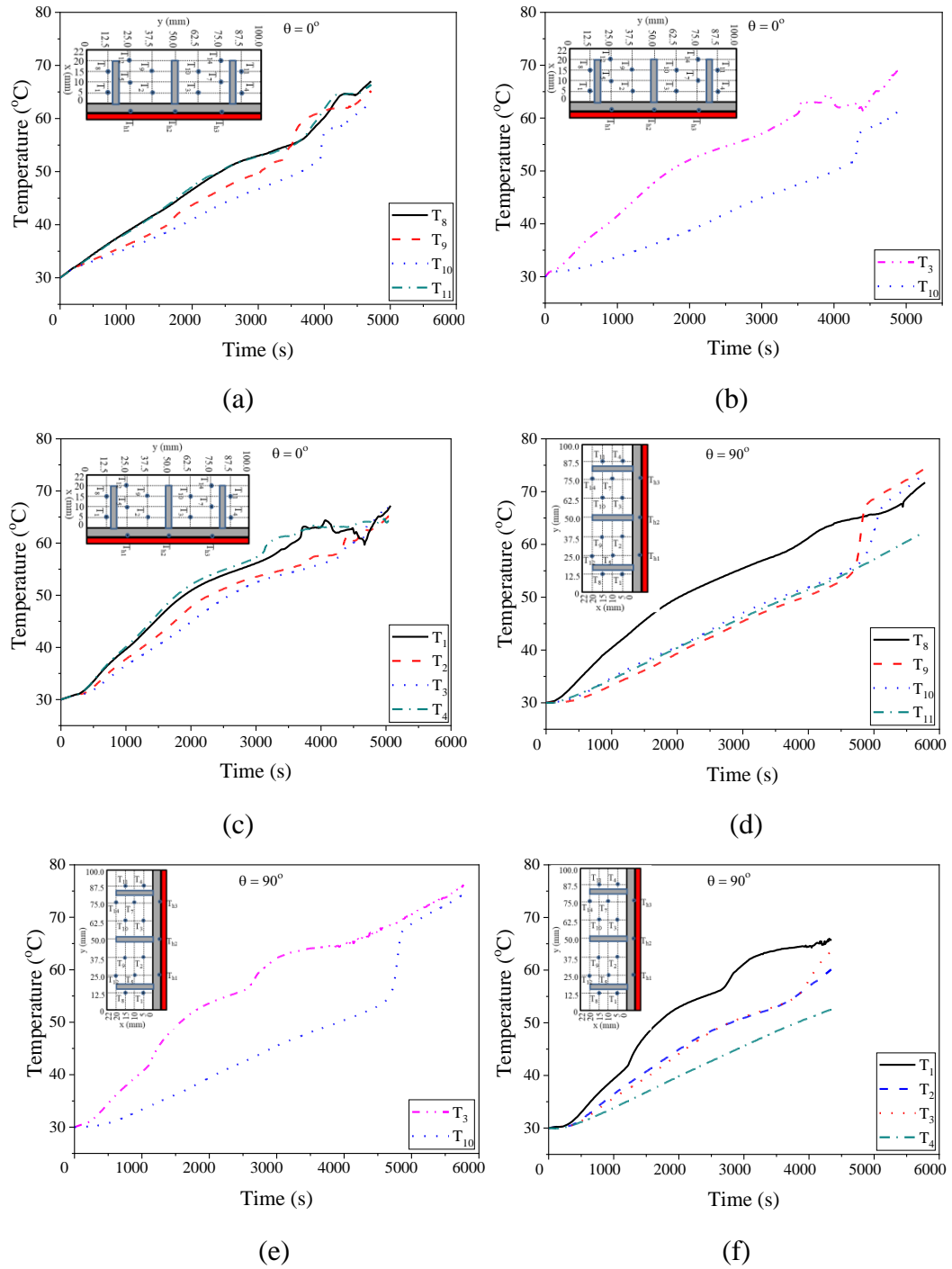


Fig. 4.19(a-f) Time history of temperature of PCM at different horizontal and vertical locations for three finned PCM based heat sink

The PCM temperature transients for $q'' = 2 \text{ kW/m}^2$ at different horizontal ($x = 5 \text{ mm}$ and 15 mm) and vertical ($y = 62.5 \text{ mm}$) planes for $\theta = 0^\circ$ and 90° for

unfinned heat sink are shown in Fig. 4.18. The angle of inclination significantly affects the distribution of temperature inside PCM for all the cases. It may be noted that for $\theta = 0^\circ$, the temperature distributions (T_1 and T_4 , T_2 and T_3 , T_8 and T_{11} , T_9 and T_{10}) in Y direction inside PCM are symmetric with respect to the center of heat sink. This may be because of the uniform PCM melting for $\theta = 0^\circ$.

The temperature transients of PCM inside the finned heat sink at different locations (T_1 , T_2 , T_3 and T_4) in the vertical plane ($x = 5$ mm), (T_8 , T_9 , T_{10} and T_{11}) in the vertical plane ($x = 15$ mm), and (T_3 and T_{10}) in the horizontal plane ($y = 62.5$ mm) of the PCM domain are shown in Fig. 4.19 for $\theta = 0^\circ$ and 90° at $q'' = 2$ kW/m². For the sake of brevity, temperature transients of PCM are shown only for three finned heat sinks. It is observed that the temperature in the upper half of the PCM domain are higher compared to lower half for $\theta = 90^\circ$. This may be due to buoyancy force; parallel to heater in this case, this pushes the PCM involving higher temperature towards the upper direction. It may be noted that the value of temperature of PCM at the selected locations decreases with the increase in number of fin. For the horizontal location, $\theta = 0^\circ$, the temperature variation at different locations (T_1 , T_2 , T_3 and T_4) and (T_8 , T_9 , T_{10} and T_{11}) exhibit similar trend.

Effect of inclination angle on solid-liquid interface shape

Figs. 4.20-4.23 show the movement of solid-liquid interface, captured by using digital camera (Sony RX10MII) for various configurations of heat sink at constant intervals of 5 min. The sequential photographs of melting operation are shown only for the inclination angle of 0° , 45° , and 90° at $q'' = 2.0$ kW/m² for the sake of brevity. In solid phase, paraffin wax exists in opaque white color, while it exists as transparent in liquid phase. Therefore, the black and white colors display the liquid and solid phases, respectively in all the photographs. The photographs are captured till all of the PCM is converted into liquid phase.

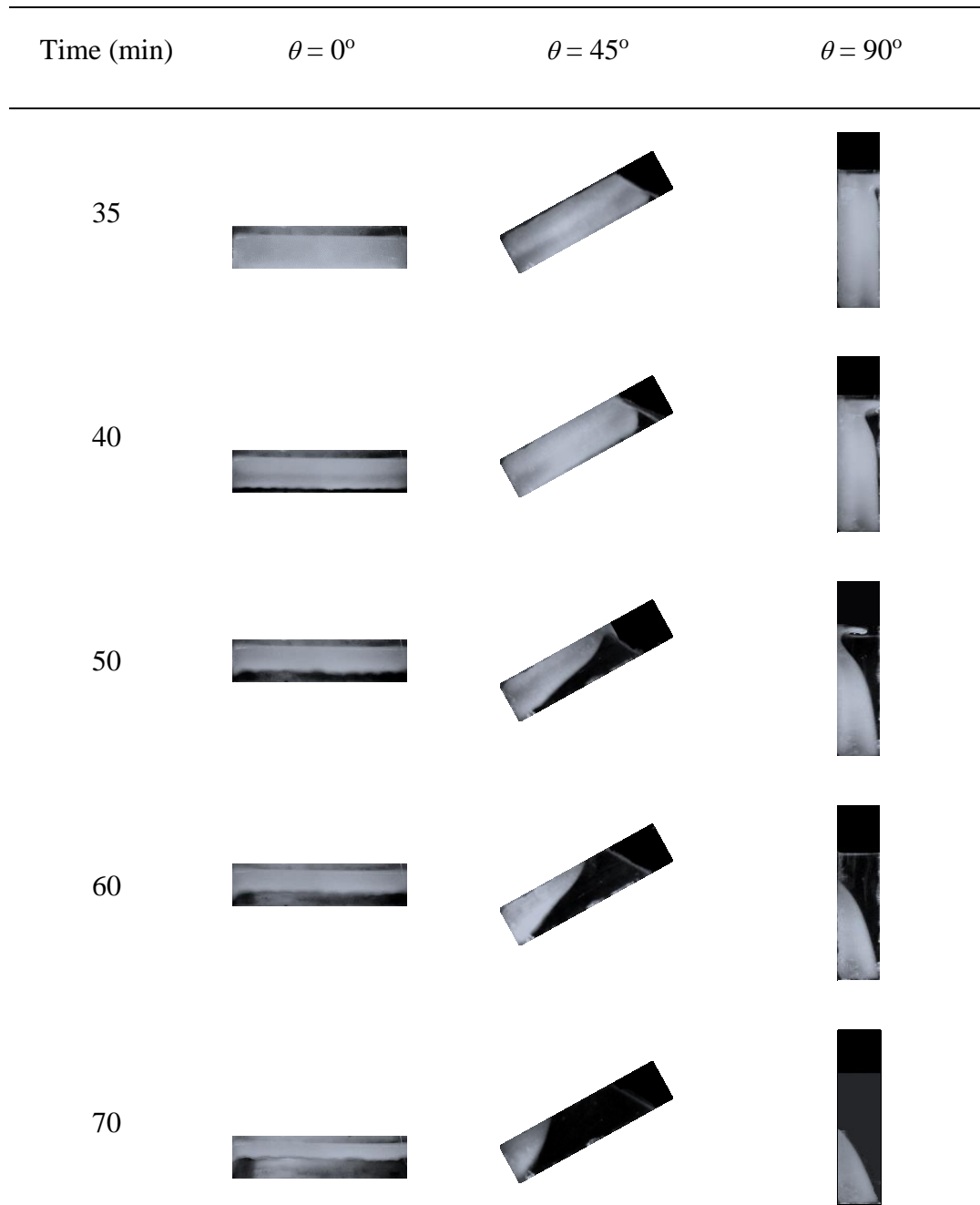


Fig. 4.20 Sequential photographs of solid-liquid interface progression at inclination angle of 0° , 45° and 90° for unfinned heat sink

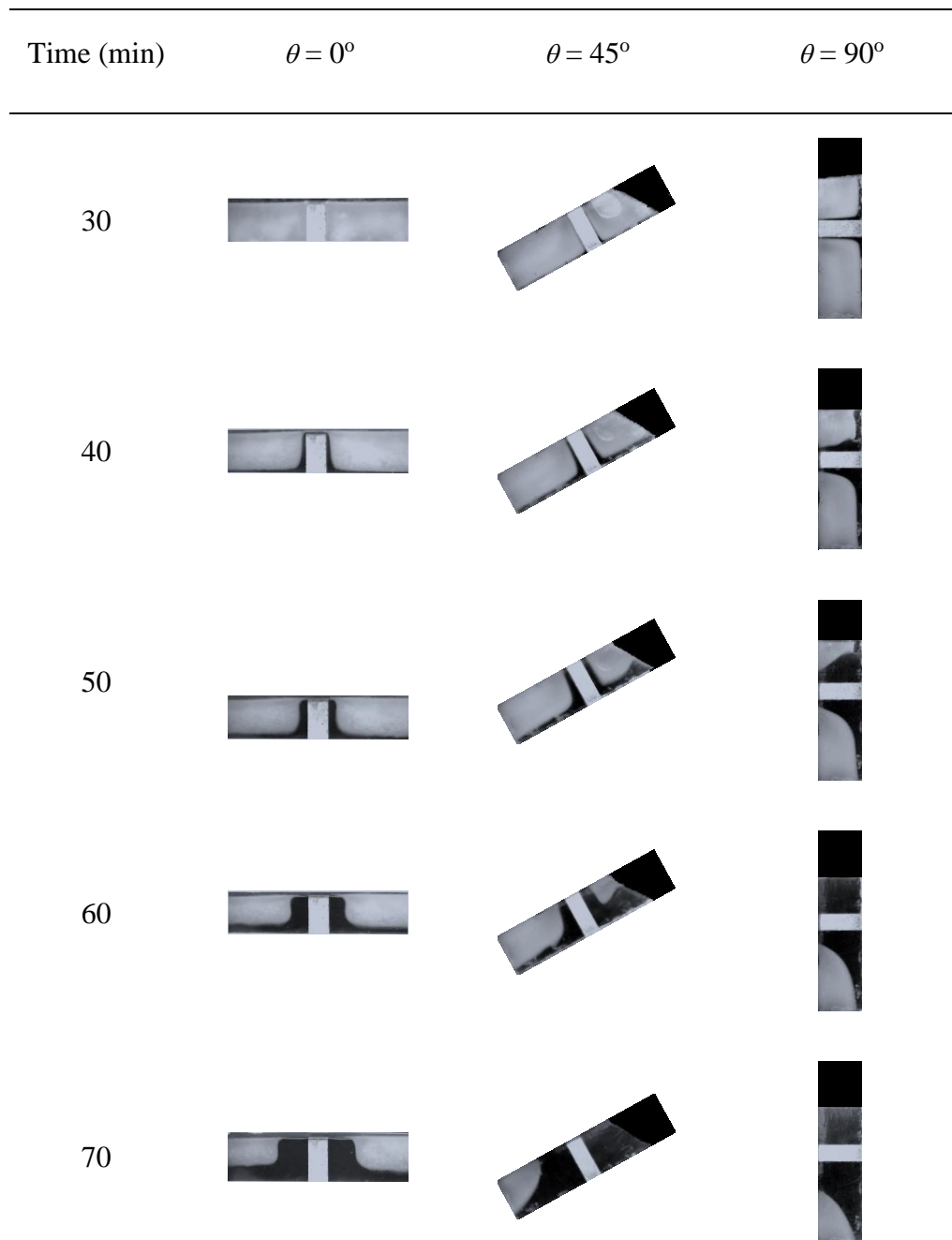


Fig. 4.21 Sequential photographs of solid-liquid interface progression at inclination angle of 0° , 45° and 90° for one finned heat sink

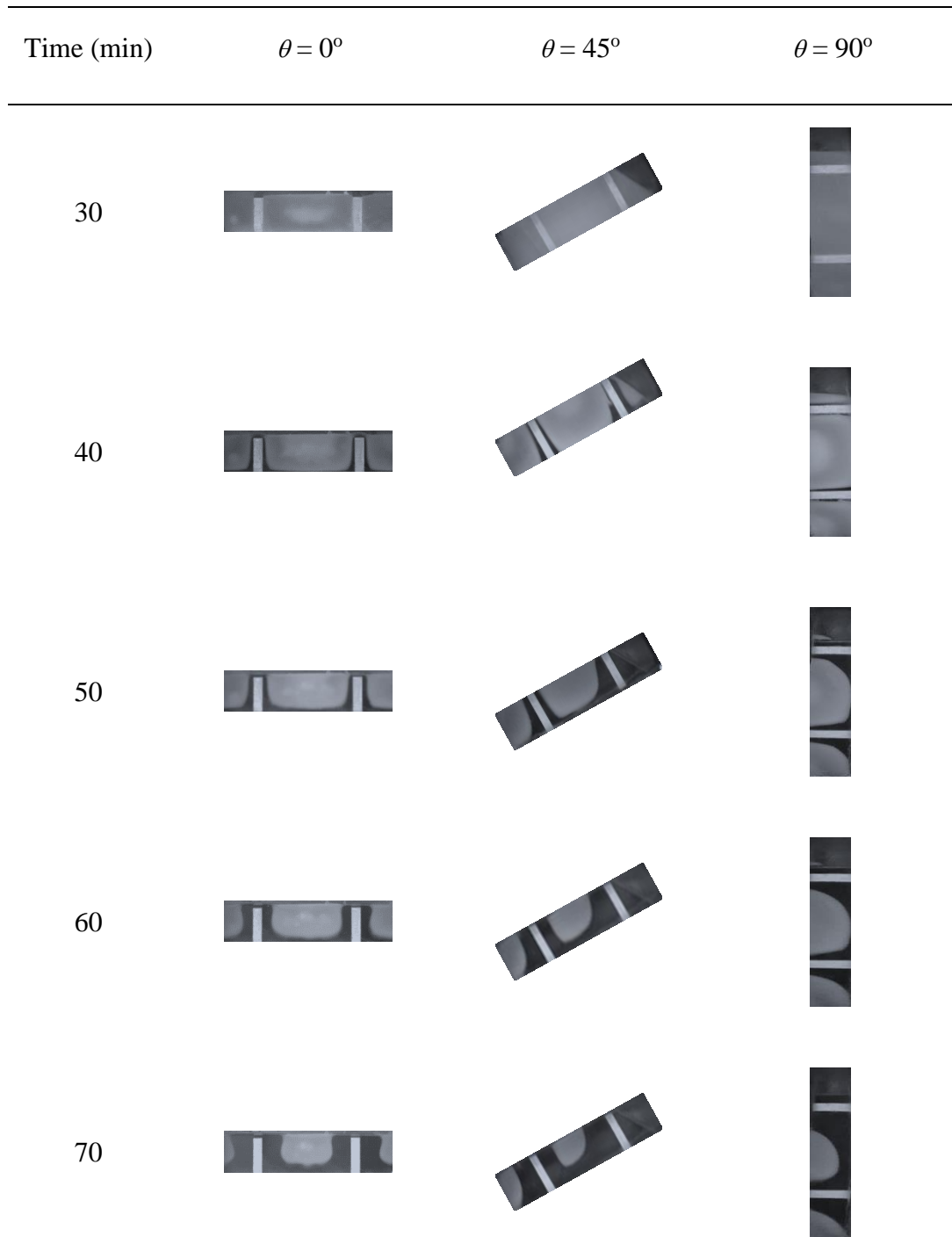


Fig. 4.22 Sequential photographs of solid-liquid interface progression at different inclination angle of 0° , 45° and 90° for two finned heat sink

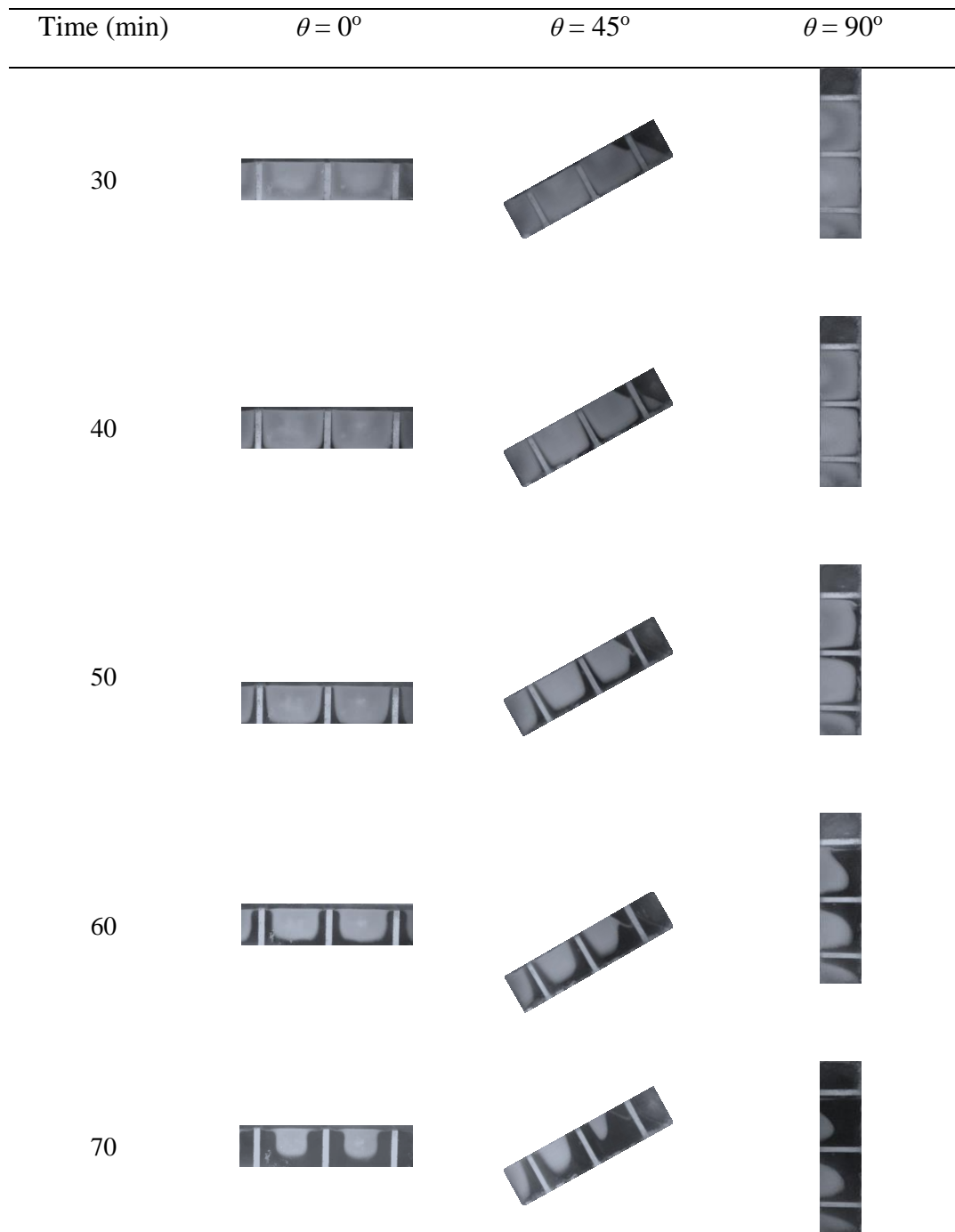


Fig. 4.23 Sequential photographs of solid-liquid interface progression at different inclination angle of 0° , 45° and 90° for three finned heat sink

Initially, the thickness of liquid layer of PCM increases at slow rate. It may be because conduction is the prominent mechanism for transfer of heat and viscous force is more dominant compared to buoyancy force. Hence, during the initial stage, solid-liquid interface remains parallel to the heated surface in case of unfinned heat sink (Fig. 4.20). However, after the progress of time, the thickness of liquid layer increases and the buoyancy force becomes more dominant compared to the viscous force, in such a case, a counter clockwise circulation current starts between cold and hot liquid PCM which promotes rate of melting of PCM and changes the solid-liquid interface profile.

Fig. 4.20 shows the photographic observation during melting of PCM inside unfinned heat sinks for various inclination angles ($\theta = 0^\circ, 45^\circ, \text{ and } 90^\circ$). For vertical orientation ($\theta = 90^\circ$), a concave curvature is obtained at interface of solid and liquid in the upper part of the heat sink and the interface tends to be linear in the lower part. This may be because of the fact the transfer of heat due to conduction is dominant in the lower part of the enclosure. Heat transfer rate is lower in this orientation and lot of PCM does not participate in the melting process. Similar phenomenon has been observed by Avci et al. [138] for vertical orientation of PCM based unfinned heat sink in their experimental investigation. However, as the angle of inclination decreases from 90° to 15° , the participation of circulating current increases towards the lower part of heat sink. In such a case the increase in buoyancy force helps the liquid PCM to erode the walls of solid PCM. This causes the non-uniformity in PCM melting and results in the concave shape. In case of $\theta = 0^\circ$, interface of solid and liquid is in linear shape during early melting stage because of dominance of conduction as the mechanism of heat transfer. With the progress of melting process, the influence of free convection increases and waviness is developed at the interface. It may be because of the formation of three dimensional Benard convection cells in the liquid PCM [141]. Avci et al. [138] observed similar patterns during the melting of PCMs inside the unfinned heat sinks at different inclination angles.

Fig. 4.21 shows the melting photographs of the PCM inside one finned heat sink for various angles of inclination ($\theta = 0^\circ, 45^\circ, \text{ and } 90^\circ$). The solid-liquid

interface remain parallel to the heat sink base for one finned heat sinks during early melting stage ($t = 30$ min). As explained earlier, this is due to the dominance of viscous force over buoyancy force. Here, conduction remains the prominent mode of transfer of heat. The thickness of liquid PCM is found to decrease along the fin length. It may be due to the gradient of temperature along the length of the fin which results in the higher melting rate at the base of the fin compared to the tip of the fin. With the progress of time, the thickness of liquid layer increases and curvature is obtained in the solid-liquid interface pattern. In such a case, the natural convection acts as the dominant role for the heat transfer. This implies that the buoyancy force overcomes the impedance of the viscous force. As the buoyancy force exerts in the vertical direction, the inclination of the heat sink causes a significant impact on the formation and propagation of buoyancy induced flow (Fig. 4.21).

For vertical orientation ($\theta = 90^\circ$), the melting rate above the fin (the upper part of the enclosure) increases significantly in comparison to the lower part of the enclosure with the progress of time. The transfer of heat at lower part of the heat sink is attributed to the continuous thermal boundary layer that starts from the bottom of the heated wall and ends at the fin tip. The liquid PCM tends to ascend in the lower part along the hot wall and flows towards left as it comes near to the fin and subsequently moves adjacent to the lower surface of the fin. It may be noted that some amount of liquid PCM cools down after coming in contact with the interface, while the remaining portion tends to flow to the upper part of the heat sink through the gap between the enclosure and fin. In the upper part of the enclosure, the heat is transferred from the hot wall to liquid layer due to natural convection and thermal plumes tend to originate from the top surface of the fin. This movement of liquid PCM and the vortex motion in the upper part of the heat sink promotes rapid propagation of the solid-liquid interface at the upper part of the enclosure and results in the concave interface pattern (Fig. 4.21, $\theta = 90^\circ$). This may be the one of the main reasons for enhancement in heat transfer in case of finned heat sink assembly. Also, the shape of interface at the bottom of the heat sink in one finned heat sinks is found to be similar to that of unfinned heat

sink. This may be due to the lesser space availability between the fin and solid PCM in the bottom part. Similar phenomenon and shapes have been observed by Yazici et al. [139], Kamkari et al. [141], and Kamkari and Groulx [143] in their numerical and experimental analysis.

With the change in the inclination angle from $\theta = 90^\circ$ to $\theta = 45^\circ$ for one finned heat sink (Fig. 4.21), the convection currents tend to widen in the lower part of the heat sink enclosure. The thickness of liquid layer increases in the lower part for $\theta = 45^\circ$ compared to vertical orientation ($t = 70$ min). It may be due to the separation of higher amount of warm liquid PCM, from the base of the fin, and subsequent contact with the solid PCM situated at both the sides of the fin. In such a case, two different circulating currents (upper and lower side of the fin) account for the enhancement in the melting rate in case of $\theta = 45^\circ$. Also, the shape of interface changes from concave ($\theta = 90^\circ$) to convex at $\theta = 45^\circ$. Kamkari et al. [141] and Avci et al. [138] reported similar observations for the generation of circulating currents and solid-liquid interface shapes in their investigation. For $\theta = 0^\circ$, the shape of interface always remain symmetric on both the sides of the fin. This is due to equal circulation of convective currents in the both halves of the heat sink. Waviness can be observed at the interface that may be because of the counter clock currents in the liquid PCM.

Figs. 4.22 and 4.23 show the melting of PCM inside the two and three finned heat sinks, respectively at different inclination angles ($\theta = 0^\circ, 45^\circ$ and 90°). Melting of PCM inside the two and three finned heat sink can be explained as mentioned earlier for the one finned heat sink. Also, it can be seen that concave and convex interface pattern obtained in case of one finned heat sink with the change in inclination is due to the circulating currents which alters the melting rate and indicates that the PCM melting depends on the circulating currents. The generation of circulating currents near fins in the liquid PCM increases with the increase in fin number. This increase in circulation currents result in the higher rate of melting of PCM. The convex and concave shape of the interface in case of

finned heat sinks exhibit the dependence of natural convection phenomena on the finned heat sink assembly.

Effect of inclination angle on heat sink performance

Heat transfer performance of heat sinks filled with PCM (unfinned, one finned, two finned, and three finned) and heat sink without PCM (unfinned) for numerous inclination angles are compared in terms of operating time to achieve a temperature of 75°C (Fig. 4.24).

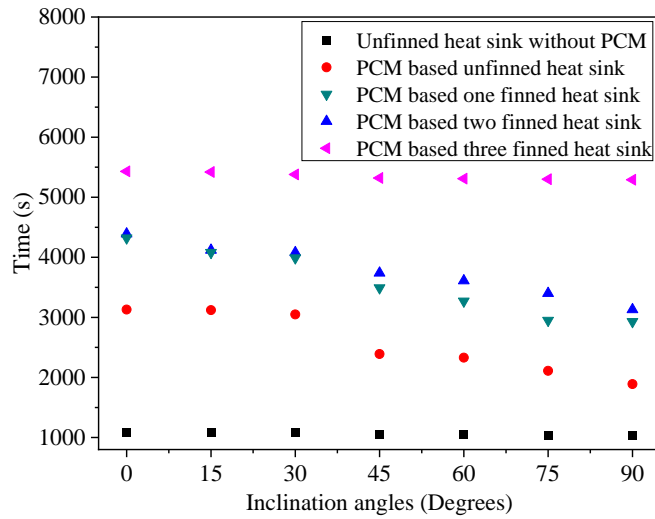


Fig. 4.24 Operating time at different inclination angle of 0°, 15°, 30°, 45°, 60°, 75°, and 90° for different configuration of PCM based heat sink

It is found that the operating time is relatively independent of the angle of inclination for the unfinned heat sink without PCM and three finned heat sink filled with PCM. Avci et al. [138] reported that the angle of inclination is insignificant in the heat transfer performance of unfinned heat sink without PCM. However, PCM based unfinned, one finned and two finned heat sinks show an increase in operating time with the decrease in inclination angle from 90° to 0°. The increase in operating time for PCM based unfinned, one finned and two finned heat sinks is found to be 66%, 45% and 43% for decrease in inclination angle from 90° to 0°. The increase in operating time is because of stronger influence of buoyancy force with the decrease in angle of inclination. Also, it is

observed that the operating time increases with the increase in the fin number. At $\theta = 0^\circ$, the enhancement in the operating time for three finned and two finned heat sinks compared to unfinned heat sink is found to be 74% and 38%, respectively.

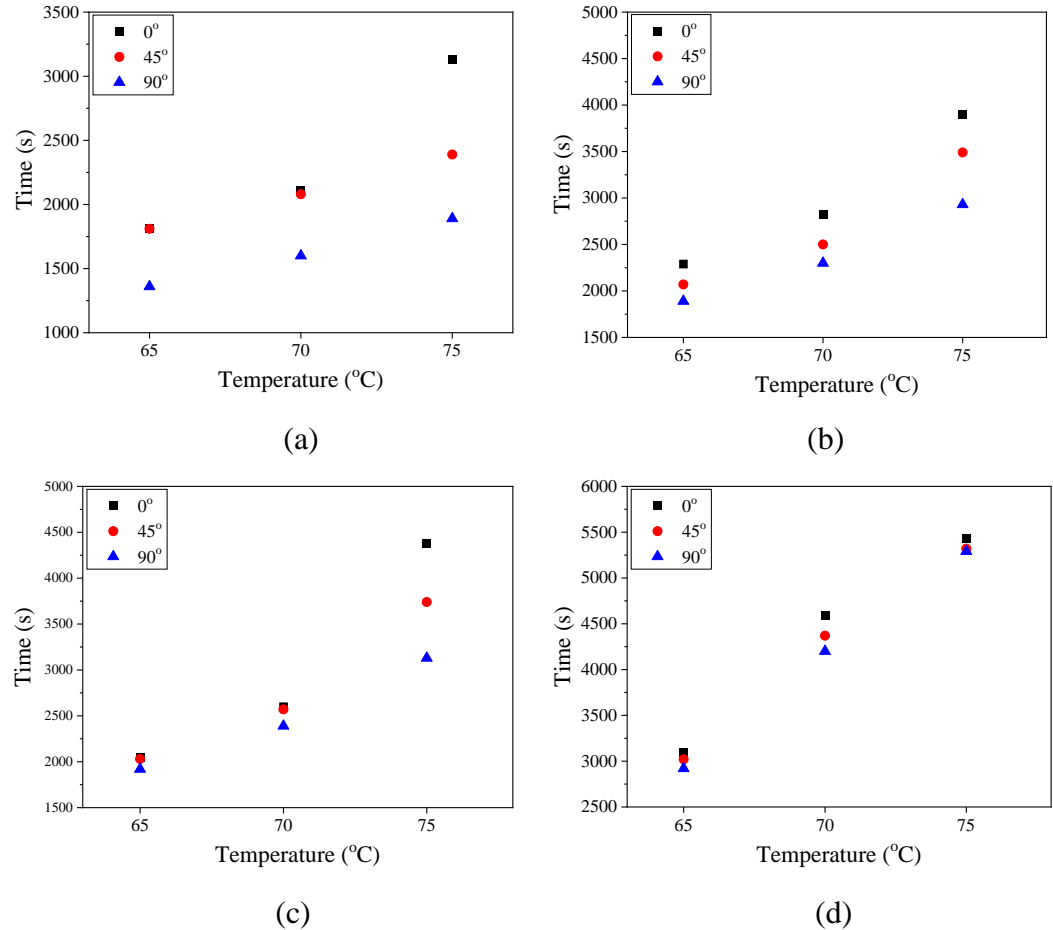


Fig. 4.25 Operating time at different inclination angle of 0° , 45° and 90° at different SPT of 65° , 70° , 75° for (a) unfinned, (b) one finned, (c) two finned and (d) three finned PCM based heat sinks

Fig. 4.25 shows the variation of operating time to attain different set point temperature (SPT) values (65°C , 70°C and 75°C) for different PCM based heat sink assemblies (unfinned, one finned, two finned and three finned) for various inclination angles (0° , 45° , and 90°) at $q'' = 2.0 \text{ kW/m}^2$. In most of the cases, heat sink assemblies exhibits higher value of operating time for $\theta = 0^\circ$ compared to $\theta = 45^\circ$, which is higher than the value obtained at $\theta = 90^\circ$. The change in operating time due to change in the inclination angle is found to be more significant for the

set point temperature of 75°C for all the heat sink assembly except the three finned heat sink assembly. For SPT = 65°C, the increase in operating time with the decrease in inclination angle from 90° to 0° is found to be 30%, 22% and 18% for unfinned, one finned, and two finned heat sinks, respectively. While, for SPT of 75°C, the increase in operating time is found to be 66%, 45% and 43% for unfinned, one finned, and two finned heat sinks, respectively. For a fixed inclination angle ($\theta = 0^\circ$), the maximum increase in operating time is found to be 53% with the increase in SPT from 65°C to 75°C.

Effect of heat flux on performance of heat sink

Enhancement in operating time to attain set point temperature (SPT) is expressed as enhancement ratio (ξ). It is defined as the ratio of time required to attain the SPT by different configurations of PCM based heat sinks to unfinned heat sink without PCM and expresses by Eq. (4.16).

$$\xi = \frac{t_{SPT_{withPCM}}}{t_{SPT_{withoutPCM}}} \quad (4.16)$$

Figs. 4.26(a-d) represent the variation in enhancement ratio with different inclination angles (0°, 45°, and 90°) and various heat flux values (1.3, 2.0, and 2.7 kW/m²) at critical SPT of 75°C for different configuration of heat sinks. Figures show that the enhancement ratio for $\theta = 0^\circ$ is found to be greater than that obtained for $\theta = 45^\circ$. Also, lower enhancement ratio is obtained at $\theta = 90^\circ$ compared to $\theta = 0^\circ$ and 45° in all the cases. This is due to the decrease in the convection currents with the increase in angle of inclination as explained in earlier section. Also, the enhancement ratio increases with the increase in fin number. This may be due to enhanced surface area with higher number of fins. The highest enhancement ratio in operating time of 4.7 is obtained at 2.7 kW/m² in case of three finned heat sinks.

Fig. 4.27 shows the melting time of PCM inside various configurations of heat sinks at different heat flux values (1.3, 2.0, and 2.7 kW/m²) at $\theta = 0^\circ$. The melting rate decreases with the increase in heat flux value. The decrease in melting time is found to be ~55% for all the cases with increase in heat flux value

from 1.3 to 2.7 kW/m². This may be due to the fact that circulation currents in the liquid PCM intensifies with the increase in the heat flux values. Identical observations were made by Kamkari et al. [144] in their study. In addition to this, time of melting decreases with the increase in fin number at constant value of heat flux. The maximum decrease in melting time is found to be ~16% with the increase in fin number from zero to three at 1.3 kW/m². In their study, Kamkari et al. [141] reported the decrease in time of melting with the increase in fin number for the given constant wall temperature.

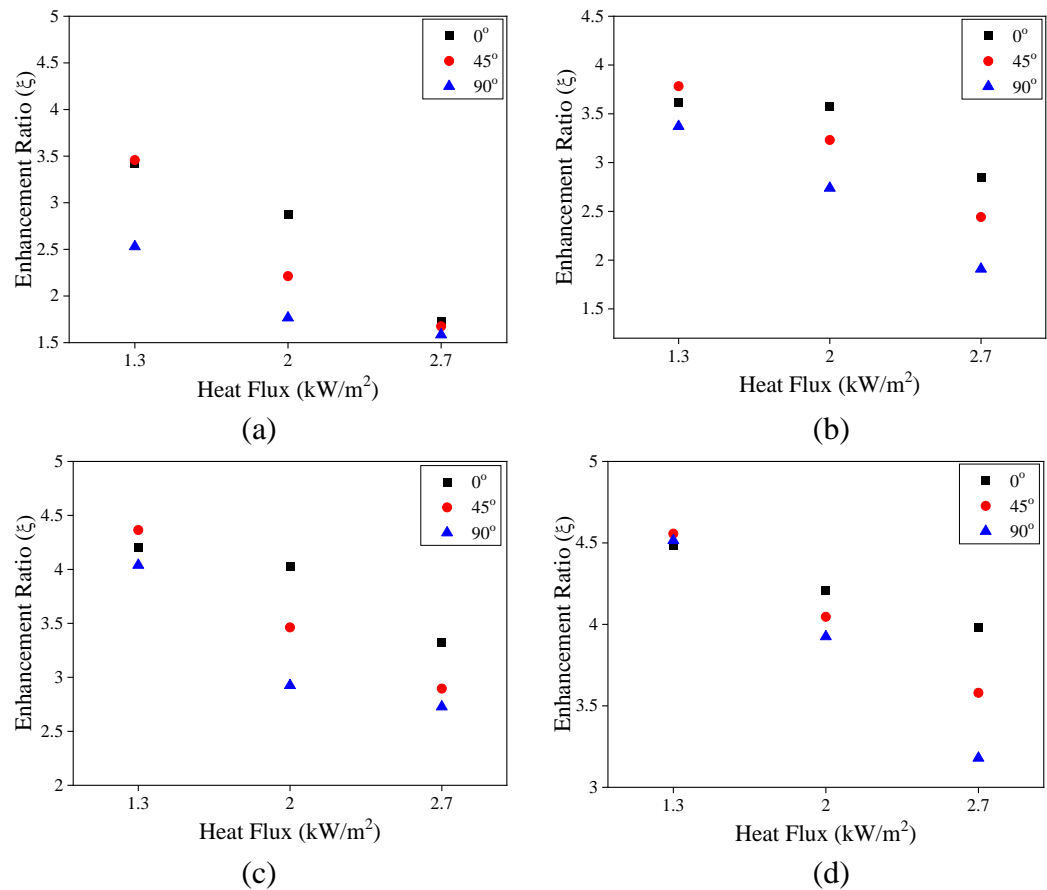


Fig. 4.26 Enhancement ratio at different inclination angle of 0°, 45° and 90° and different heat flux of 1.3, 2.0, and 2.7 kW/m² for (a) unfinned, (b) one finned, (c) two finned and (d) three finned PCM based heat sinks

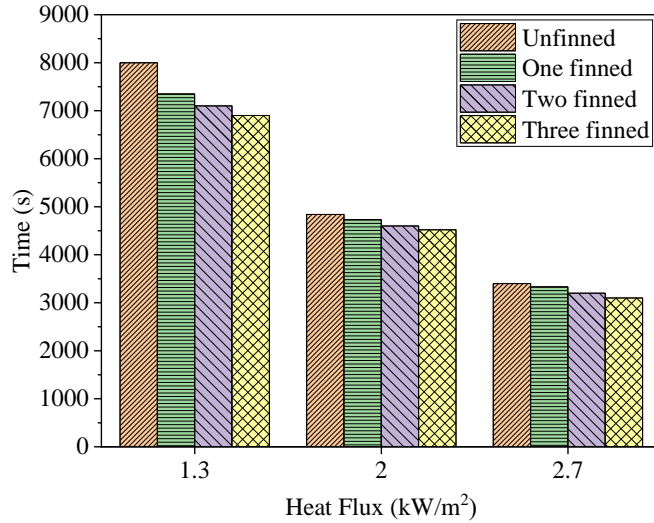


Fig. 4.27 Melting time at different heat flux of 1.3, 2.0, and 2.7 kW/m² for different configurations of heat sinks filled with PCM

Effect of angle of inclination on melting time and melt fraction

Figs. 4.28(a-d) show the variation of melt fraction with time for various inclination angles (0°, 45°, and 90°) for difference cases such as no fin, one fin, two fins and three fins heat sinks, respectively for $q'' = 2.0 \text{ kW/m}^2$. Initially, PCM absorbs sensible heat energy and remain in the solid phase. The value of melt fraction remains zero during this stage. The propagation of solid-liquid interface of PCM initiates after a time duration of 30 and 35 minutes for finned and unfinned heat sinks, respectively. It has been found that initially the melt fraction is higher for inclination angle of 45° followed by 0° and 90° for all the cases. With the progress of time, the melt fraction increases for inclination angle of 0° followed by 45° and 90° for all the configurations of the heat sinks. Figure shows that the melting rate of PCM increases with the decrease in inclination angle from 90° to 0°. Also, the melting rates are found to decrease with the progress of time for a given inclination angle. This transition is relatively sharp for inclination angle of 90°. The melt fraction of PCM follows the order of 0°, 45° and 90° to reach unity.

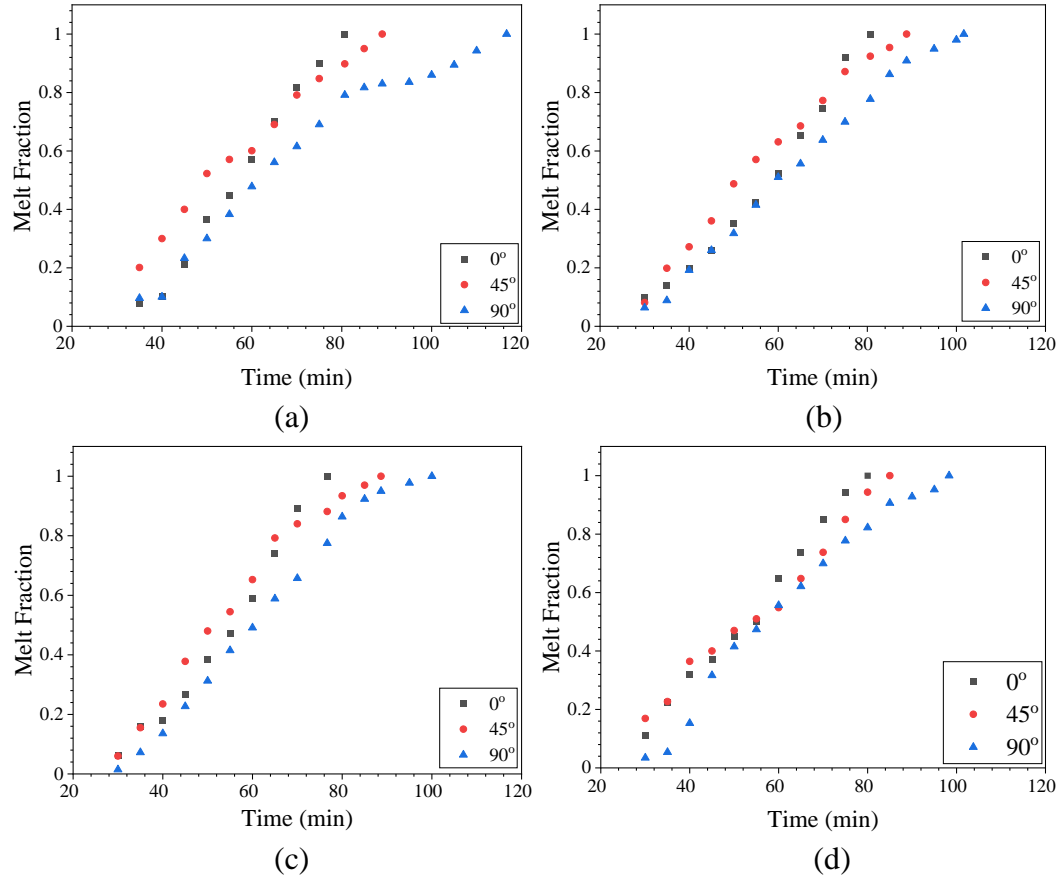


Fig. 4.28 Melt fraction of PCM at various inclination angles and different time duration for various heat sink configurations such as heat sinks (a) unfinned, (b) one finned, (c) two finned, and (d) three finned heat sinks

Melting time denotes the time when the melt fraction reaches unity. Melting time can be evaluated by calculating melt fraction. Melt fraction is defined as volume of liquid PCM at each time to the volume of initial solid PCM inside the heat sink. Fig. 4.29 shows the melting time for different configurations of heat sink such as no fin, one fin, two fins and three fins at various angle of inclination (0° , 15° , 30° , 45° , 60° , 75° , and 90°) for $q'' = 2.0 \text{ kW/m}^2$. The melting time is found to decrease by $\sim 44\%$ for unfinned heat sink and $\sim 30\%$ for finned heat sinks with the decrease in inclination angle from 90° to 0° . It may be due to the increase in circulation currents in the liquid PCM with the decrease in angle of inclination. Similar observation has been reported by Kamkari et al. [141] in their

experimental investigation. In addition, the decrease in melting time is found to be 14%, 17% and 19% for one finned, two finned and three finned heat sinks, respectively compared to unfinned heat sinks at $\theta = 90^\circ$. It can be noted that the difference in the percentage in melting time decreases with the increase in fin number. This can be explained by the hindrance to the flow of circulation currents in the presence of more number of fins [144].

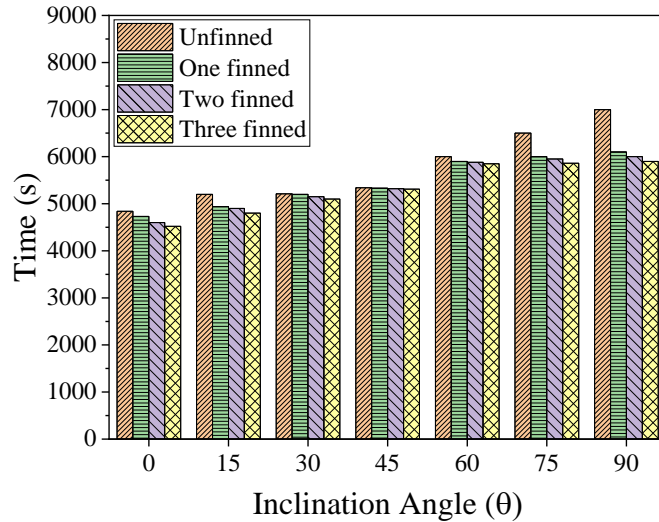


Fig. 4.29 Melting time at different inclination angle of 0° , 15° , 30° , 45° , 60° , 75° , and 90° for different configurations of PCM based heat sinks

4.3.2 Effect of metal foam and phase change material composite on the thermal performance of various finned and unfinned heat sink configurations

In this work, the thermal performance of various PCM based heat sinks such as unfinned with pure PCM, finned with pure PCM, unfinned with MF-PCM composite and finned with MF-PCM composite during melting process to stretch the operating time of the system for a given set point temperature is experimentally investigated. Photographs of various heat sinks used in the present investigation are shown in Fig. 4.30.



Fig. 4.30 Photographs of various heat sinks used in this investigation

Fig. 4.31 shows the plate fin heat sinks with different dimensions and Table 4.7 summarizes the dimensions of fins. Paraffin wax (Sigma Aldrich, USA) is used as PCM in the present investigation. The thermo-physical properties of PCM are shown in Table 4.1. Various parameters such as volume fraction of PCM,

effect of heat flux on the enhancement in operating time have been studied. Different volume fractions of PCM such as (i) $\psi = 0.00, 0.50, 0.86$, and 1.00 for unfinned and finned heat sink with pure PCM, (ii) $\psi = 0.90$ for unfinned heat sink with MF- PCM composite, and (iii) $\psi = 0.86$ for finned heat sink with MF- PCM composite are used in this study to investigate the effect of PCM volume fraction on different configurations of heat sink. Based on the literature, the heat flux values such as $1.3, 2.0$ and 2.7 kW/m^2 have been chosen in the present analysis.

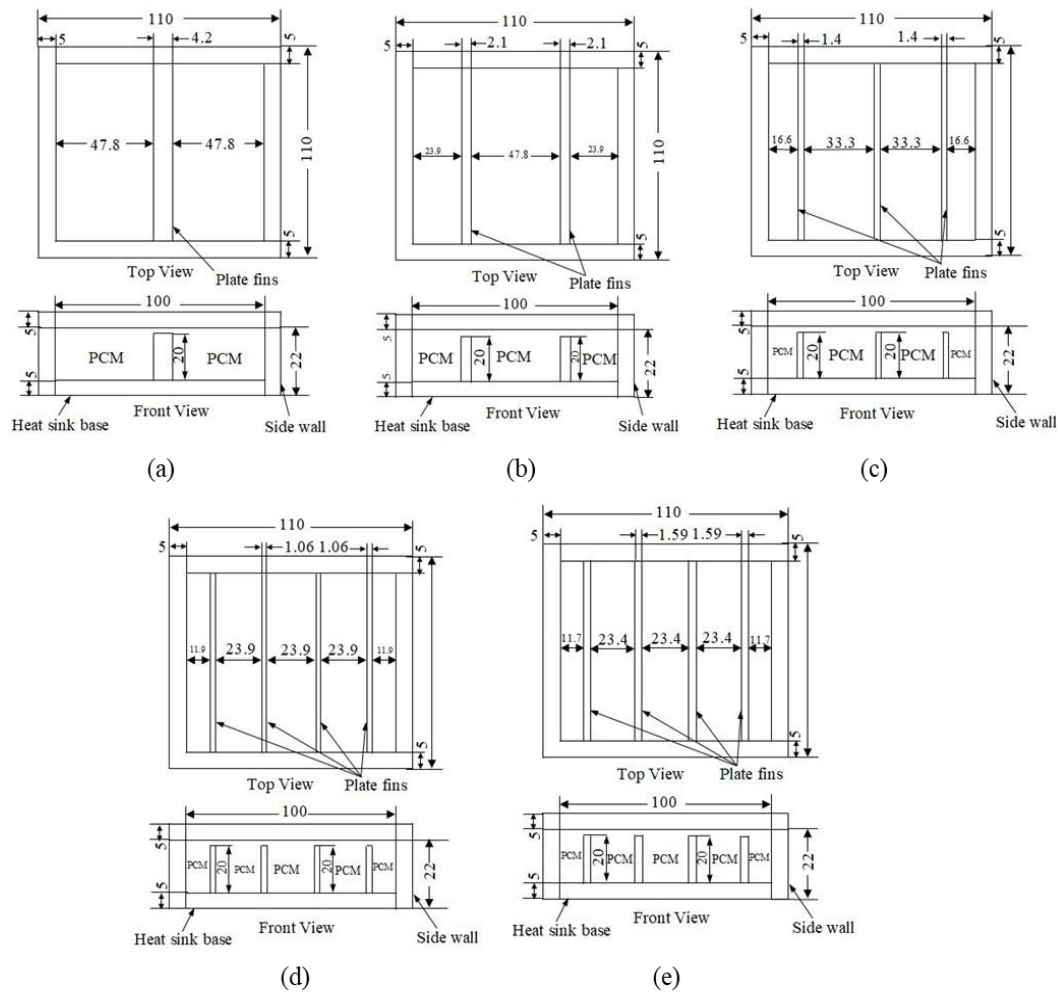


Fig. 4.31 Dimensions of various plate fin heat sinks: (a) one fin, (b) two fins, (c) three fins, (d) four fins (fin thickness 1.06 mm), and (e) four fins (fin thickness 1.59 mm)

Table 4.7 Fin dimensions for different configurations of heat sink

Heat sink configurations	Total volume fraction of TCE (%)	Volume fraction of fins (%)	Dimensions of fin (mm ³)
One fin			100 × 4.25 × 20
Two fin	13.825	4.25	100 × 2.12 × 20
Two fin			100 × 1.41 × 20
Four fin			100 × 1.06 × 20
Four fin	15.825	6.38	100 × 1.59 × 20

Baseline comparison

The comparison of heat sink base temperature (T_b) for the unfinned heat sink with PCM and without PCM at $q'' = 2.0 \text{ kW/m}^2$ is shown in Fig. 4.32. The average value of temperature recorded by thermocouples T_{h1} , T_{h2} , and T_{h3} is considered as T_b . The time taken to attain $T_b = 60^\circ\text{C}$ is found to be 920 s and 1130 s for heat sink without and with PCM, respectively. While, to reach a higher T_b of 70°C , it takes 1500 s and 1820 s for heat sink without and with PCM, respectively. The surface temperature is found to increase quickly for heat sink without PCM, which is not desirable and have adverse effect on the life of portable electronic components. The heat sink with PCM exhibits sharp rise in temperature for initial 520 s. This shows the sensible heating phase. The temperature rise takes place gradually during 520 s to 1750 s. The PCM starts to melt during this period and it is the latent heating stage. It may be noted that extending the latent heating period and maintaining a constant temperature during this phase is the key point for the thermal management. It can be noted that even in case of heat sink with PCM, the temperature rise takes place during latent heating period.

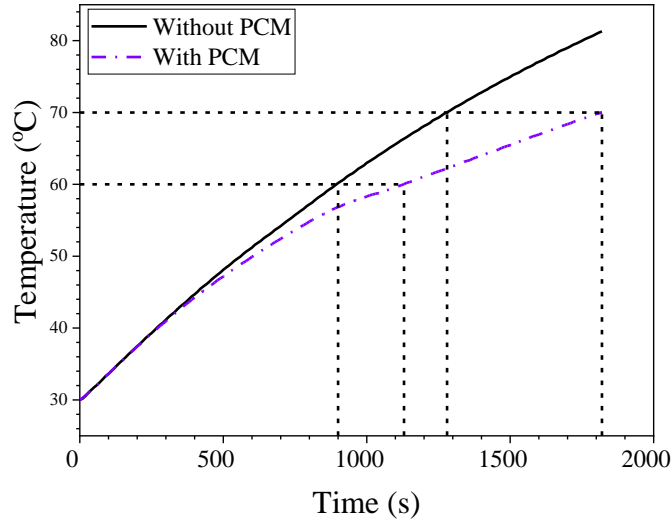


Fig. 4.32 Comparison of time-temperature distribution of base temperature for unfinned heat sink without and with PCM at 2.0 kW/m^2

Effect of PCM volume fraction, heat flux values, and heat sink configurations in lowering the base temperature

Figs. 4.33(a-e) compare the value of T_b for various configurations; namely, unfinned, one finned, two finned, three finned and four finned heat sinks for different PCM volume fractions ($\psi = 0, 0.50, 0.86, 1$) and MF-PCM composite at $q'' = 2.0 \text{ kW/m}^2$. The variation in temperature follows a similar trend for all the configuration of heat sink. T_b is found to increase rapidly for $\psi = 0$ in all the cases. It is because of the absence of PCM in heat sink. It is noticed that the combination of TCE and PCM provides better thermal performance. The extension of latent heat phase is significant for heat sinks with four fins compared to other configurations. Also, the heat sink with MF-PCM is found to exhibit better thermal performance compared to other configurations. Lower value of T_b is obtained in case of four finned heat sink at $q'' = 2.0 \text{ kW/m}^2$.

The variation of T_b for different heat sinks with various heat flux values ($q'' = 1.3, 2.0$ and 2.7 kW/m^2) for a given PCM volume fraction ($\psi = 0.86$) is shown in Fig. 4.34. The latent heating phase time duration is found to decrease with the rise in the input heat flux.

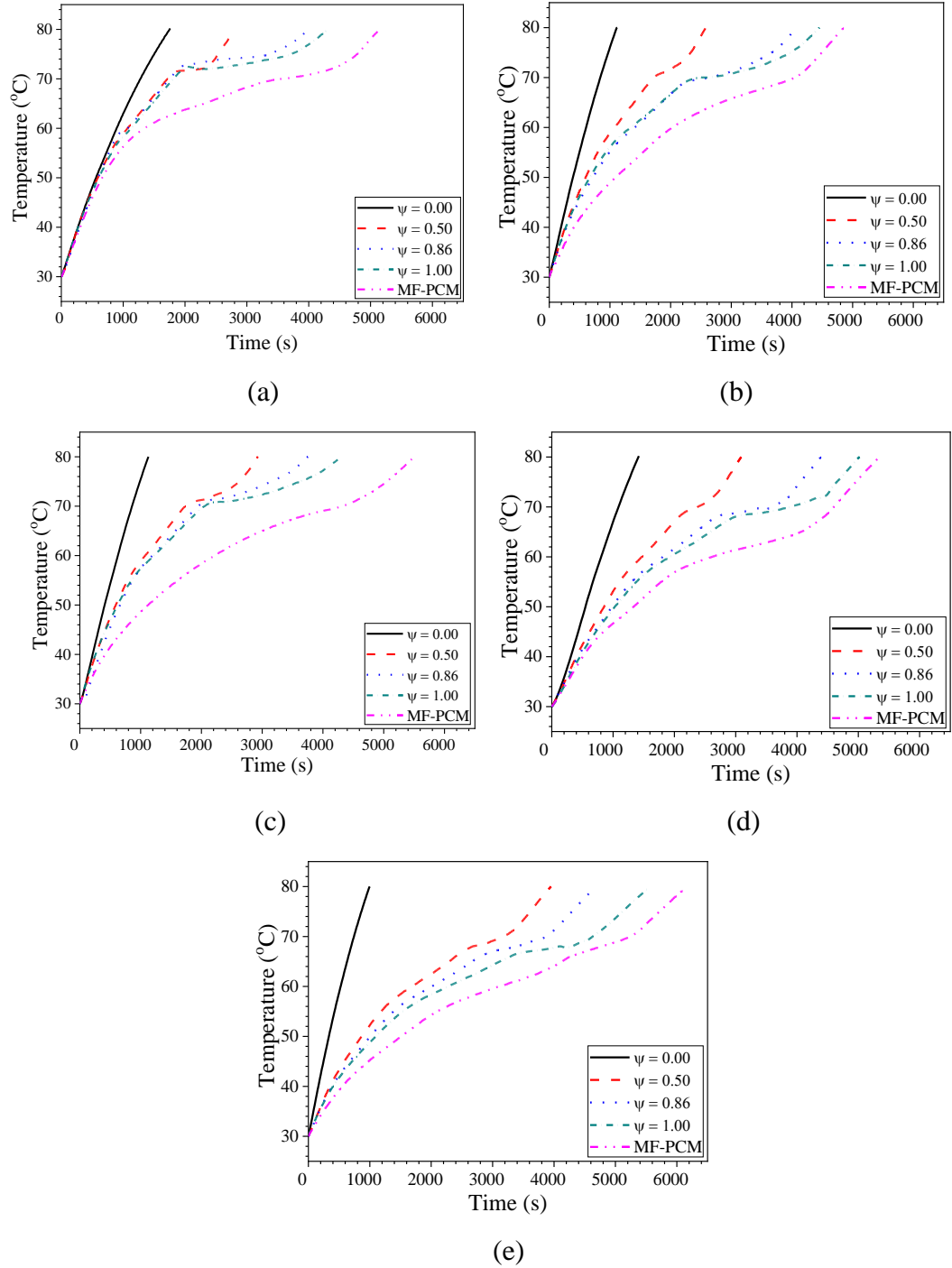


Fig. 4.33 Time-temperature distribution filled with different ψ at 2.0 kW/m^2 for different configuration of heat sinks: (a) unfinned, (b) one finned, (c) two finned, (d) three finned, (e) four finned heat sinks

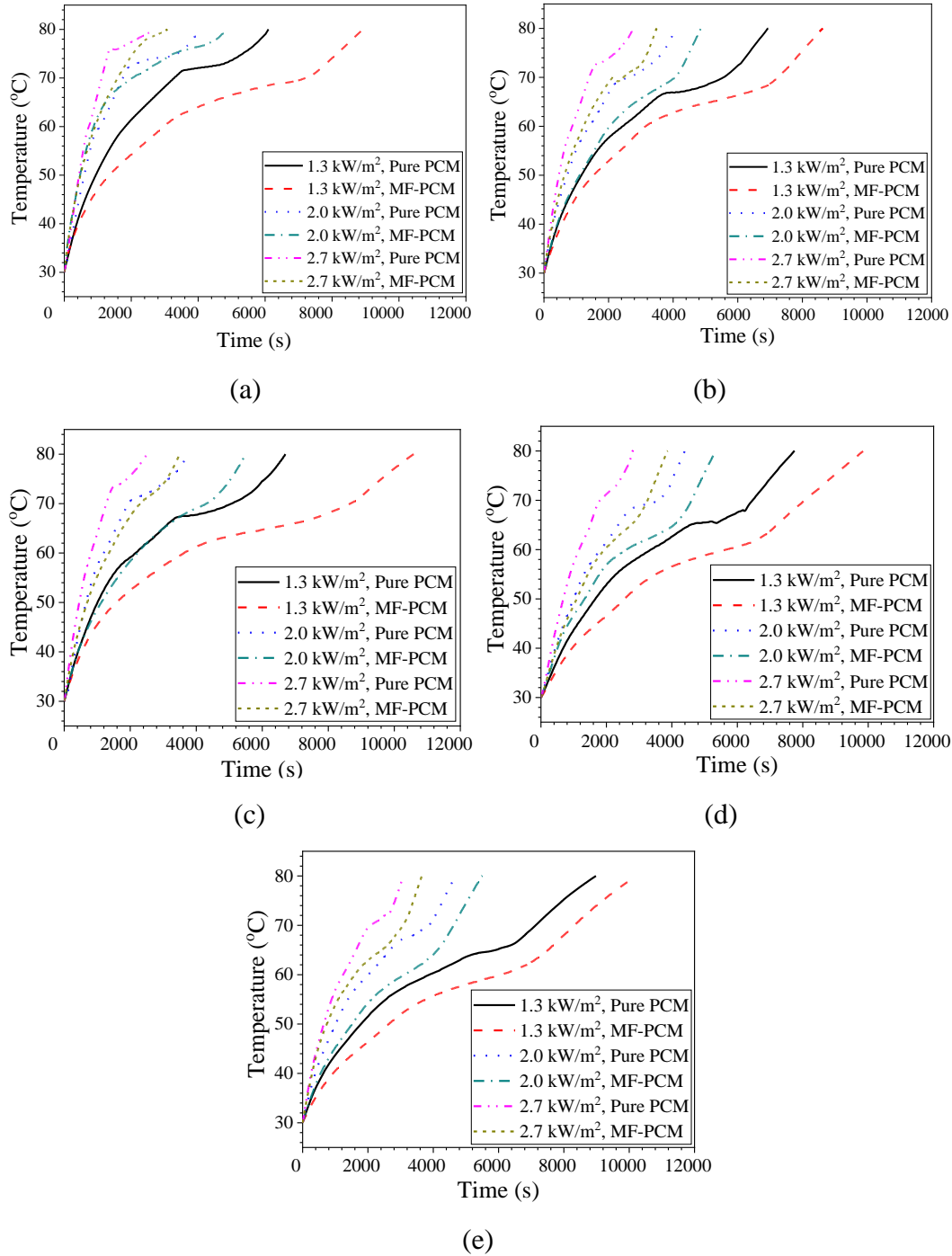


Fig. 4.34 Time-temperature distribution at different input heat flux for different heat sinks: (a) unfinned, (b) one finned, (c) two finned, (d) three finned, (e) four finned heat sinks

A closer look at four finned MF-PCM based heat sink revealed that for $q'' = 1.3$ kW/m², the latent heating phase is continuous even after 6000 s of heating and T_b is recorded as 59.8°C. On the contrary, for $q'' = 2.0$ kW/m², the latent heat phase ends at 4000 s. While, for $q'' = 2.7$ kW/m², the time duration for completion of latent heating phase is only 2970 s after that temperature increases rapidly. It is evident from the figures that PCM based heat sinks are less advantageous at lower heat flux. This may be due to non-utilization of entire latent heat of PCM at lower heat flux. However, for higher input heat flux values ($q'' = 2.0$ to 2.7 kW/m²), where majority of portable electronic devices operate, T_b for heat sink without PCM quickly reaches to uncomfortable zone.

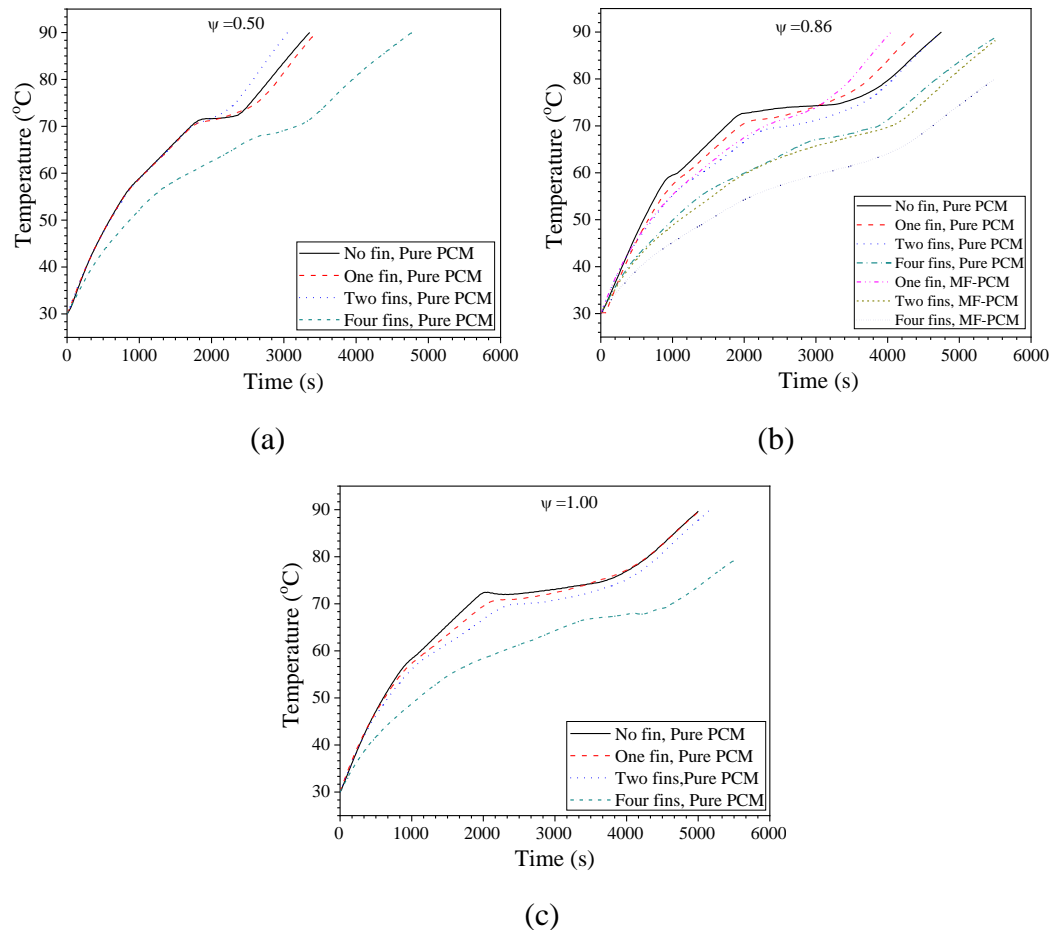


Fig. 4.35 Comparison of time-temperature distribution of different configurations of heat sinks at 2.0 kW/m² for (a) $\psi = 0.50$, (b) $\psi = 0.86$, (c) $\psi = 1.00$

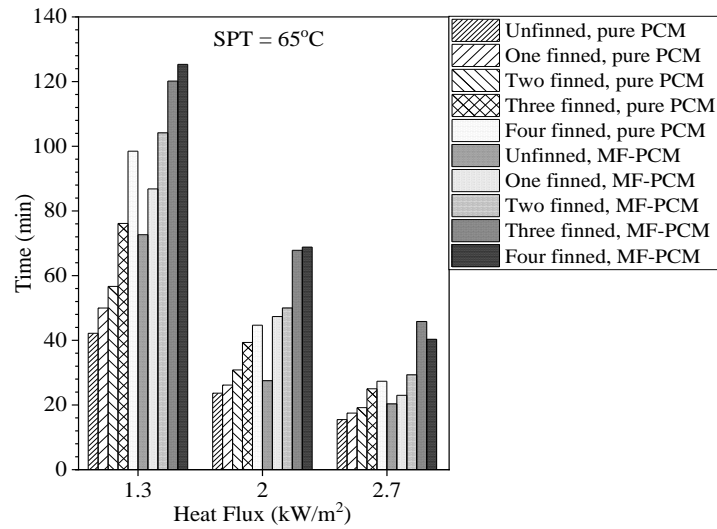
Fig. 4.35 depicts the comparison of T_b for different heat sink configurations with varied range of PCM volume fractions at $q'' = 2.0 \text{ kW/m}^2$. It may be seen from the figure that significant reduction in base temperature of heat sink is obtained with different ψ (0.5, 0.86 and 1). For $\psi = 0.86$, the time taken by different heat sinks such as unfinned with PCM, four finned with PCM, and four finned with MF-PCM composite to attain a set point temperature of 65°C is found to be 1420 s, 3120 s, and 4130 s, respectively. The entire melting process is categorized into three regions; namely, solid, partially molten and completely molten. Initially in solid region, the value of temperature of base of heat sink for all the cases increases rapidly due to pre-melting sensible heat storage. However in case of MF-PCM, base temperature of heat sink is lower compared to pure PCM cases. As the time progresses, base temperature of heat sink increases and arrives at the PCM melting temperature. Subsequently, the melting of PCM takes place. The phase change process is dominated by two factors; namely, free convection and heat conduction inside molten PCM. Conduction dominated heat transfer occurs in MF-PCM composite as the liquid PCM remains constrained in the MF pore, which suppresses the natural convection and increases the melting rate. This results in the lower value of T_b and therefore suitable for better thermal management of MF-PCM based heat sinks compared to other configurations.

It may also be noted that four finned heat sink maintains the value of T_b lower for extended duration compared to unfinned heat sink at 2.0 kW/m^2 , this is due to uniformity in PCM melting with the presence of TCE (fins). Also, aluminum (218 W/m-K) has higher thermal conductivity of about 20 times that of MF (10.1 W/m-K). Therefore, fins made of solid aluminum inserted between MF results in the increase in dissipation of heat by conduction. Also, greater heat transfer surface area is found to be in contact with MF in case of four finned MF-PCM (base and fins) compared to unfinned heat sink (only base).

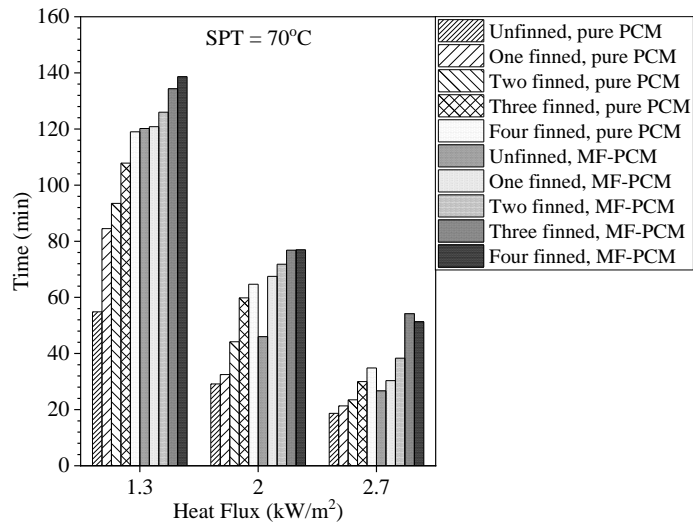
Enhancement in operation time for different critical SPTs

The thermal performance of various heat sink configurations at two different critical SPTs (65°C and 70°C) for varied range of heat flux values ($q'' = 1.3, 2.0$

and 2.7 kW/m^2) is studied. The critical SPT is the maximum operating temperature of electronic components above which the component may fail due to higher temperature. Figs. 4.36(a-b) show the time to attain SPT of 65°C and 70°C by various configurations of heat sinks for varied range of input heat flux values at $\psi = 0.86$.

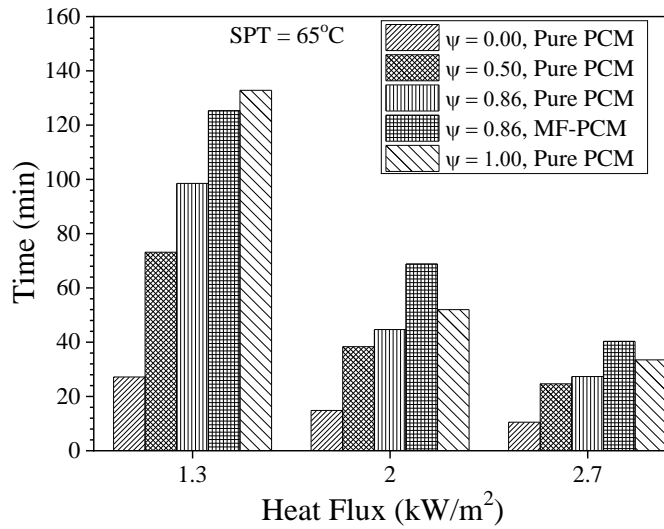


(a)

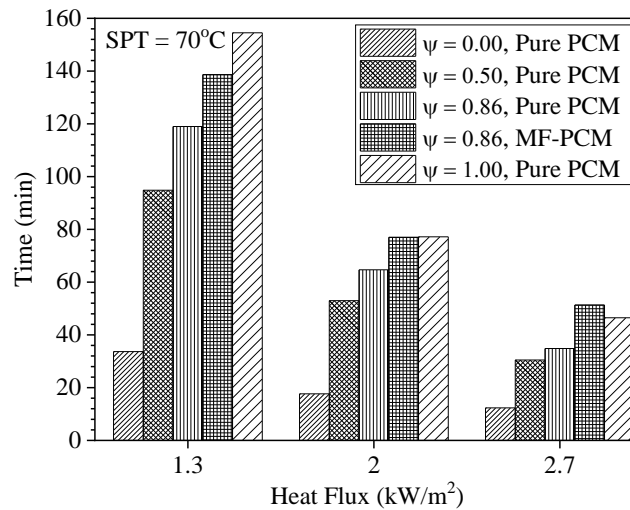


(b)

Fig. 4.36 Time to attain SPT at $q'' = 1.3, 2.0, \text{ and } 2.7 \text{ kW/m}^2$ for $\psi = 0.86$, (a) 65°C and (b) 70°C



(a)



(b)

Fig. 4.37 Time to attain SPT at $q'' = 1.3, 2.0,$ and 2.7 kW/m^2 for different values of ψ in four finned heat sink case, (a) 65°C and (b) 70°C

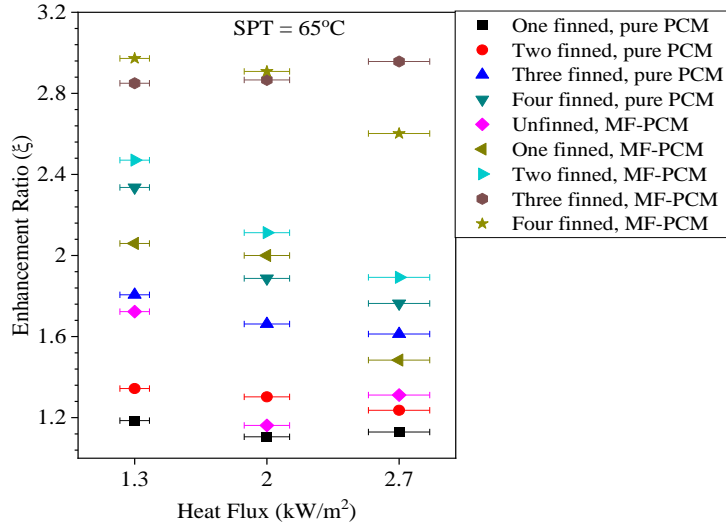
It is evident from the figures that operating time decreases with the rise in q'' for a fixed value of SPT. Four finned MF-PCM heat sink takes higher time compared to other configurations of heat sinks for $q'' = 1.3$ and 2.0 kW/m^2 . While, three finned MF-PCM heat sink takes higher time compared to other configurations of heat sinks for $q'' = 2.7 \text{ kW/m}^2$. The maximum value of enhancement in operating time for a given heat sink assembly depends on the

input heat flux values. The four finned MF-PCM takes maximum time of 125.33 and 138.67 minutes to attain the reach SPT of 65°C and 70°C, respectively at $q'' = 1.3 \text{ kW/m}^2$. For $q'' = 2.7 \text{ kW/m}^2$, three finned MF-PCM heat sink takes maximum time of 45.83 and 54.16 minutes to attain SPT of 65°C and 70°C, respectively.

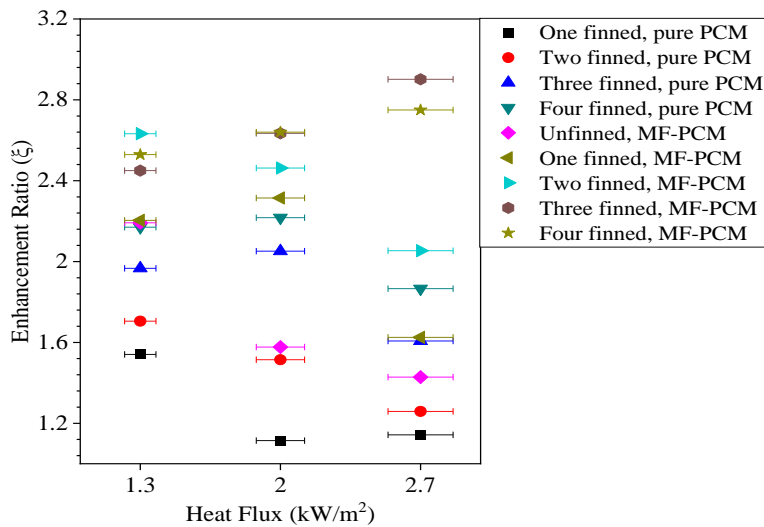
Thermal performance of four finned heat sink for different ψ to attain SPT of 65°C and 70°C is shown in Figs. 4.37(a-b). It may be noted that for $q'' = 2.0$ and 2.7 kW/m^2 , MF-PCM based heat sink takes longer time to attain the SPT value of 65°C and 70°C. While, for lower value of input heat flux ($q'' = 1.3 \text{ kW/m}^2$), four finned heat sink with pure PCM takes more time to attain the SPT value of 65°C and 70°C. It may be inferred that it is useful to use MF-PCM based heat sink for electronic components cooling at higher input heat flux (2.0 and 2.7 kW/m^2), which is a working range of most of the electronic components.

Enhancement ratio for different heat sink configuration and heat flux values

Enhancement in operating time to reach critical SPT is expressed as enhancement ratio and is defined by Eq. (4.13). Figs. 4.38(a-b) represent the enhancement ratio of various heat sink configurations to attain the critical SPT of 65°C and 70°C. The enhancement ratio for specific SPT is found to depend on the heat flux value. Four finned MF-PCM exhibits maximum value of enhancement ratio for $q'' = 1.3$ and 2.0 kW/m^2 to achieve SPT = 65°C. While, three finned MF-PCM shows the maximum value of enhancement ratio at $q'' = 2.7 \text{ kW/m}^2$. For SPT of 65°C, the enhancement ratio is more at $q'' = 1.3 \text{ kW/m}^2$. However, for SPT of 70°C, higher enhancement ratio is obtained at $q'' = 2.7 \text{ kW/m}^2$. This may be due to the different time spans of latent heating phase of PCM at different heat flux values. The highest enhancement ratio of ~ 2.97 is achieved for four finned MF-PCM heat sink and three finned MF-PCM heat sink at $q'' = 1.3$ and 2.7 kW/m^2 , respectively. The thermal performance is found to be better at lower value of SPT due to rapid increase in temperature in the post melting region. This phenomenon has been observed in earlier research studies as well [148].



(a)



(b)

Fig. 4.38 Enhancement ratio at $q'' = 1.3, 2.0,$ and 2.7 kW/m^2 and $\psi = 0.86$ for different SPT (a) 65°C and (b) 70°C

The influence of different values of SPT (65°C and 70°C) on enhancement ratio of MF-PCM composite heat sink (ϕ) for varied range of heat flux values at $\psi = 0.86$ is shown in Fig. 4.39. The enhancement ratios shown in Fig. 4.39 are estimated based on Eq. (4.14). It is observed that for $q'' = 1.3$ and 2.0 kW/m^2 , the

value of ϕ is highest at lower value of SPT. Also, ϕ decreases with the increase in value of SPT. While, for $q'' = 2.7 \text{ kW/m}^2$, ϕ is found to be higher for SPT of 70°C . At higher value of heat flux, the enhancement ratio is higher for higher value of SPT. This is due to the forward shifting in the latent heating phase at higher heat flux.

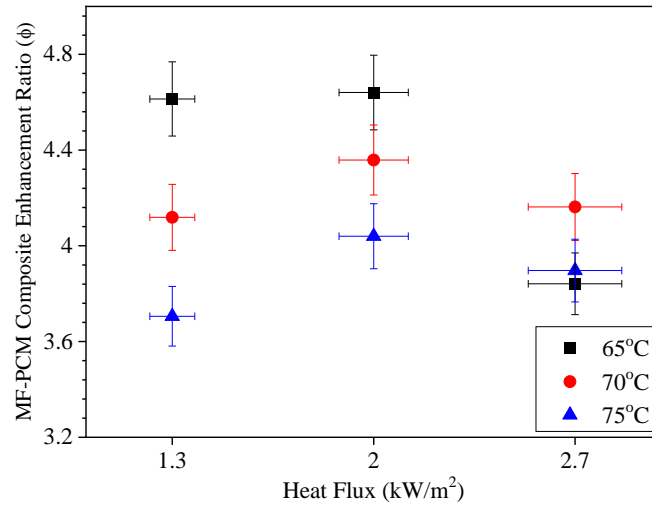


Fig. 4.39 MF-PCM composite enhancement ratio at $q'' = 1.3, 2.0, 2.7 \text{ kW/m}^2$ for four finned MF-PCM at $\psi = 0.86$

Comparison of thermal conductance

The thermal performance of a heat sink can be defined based on the thermal conductance (G). Here, G denotes the rate of heat transfer per unit temperature difference from the heat sink surface through the TCE/PCM and is expressed in Eq. (4.15). Fig. 4.40 depicts the thermal conductance values of different configurations of heat sink assemblies for varied range of input heat flux values. Four finned MF-PCM composite heat sink exhibits the best thermal conductance value compared to other configurations of heat sink for the $q'' = 1.3$ and 2.0 kW/m^2 . While, for $q'' = 2.7 \text{ kW/m}^2$, three finned heat sink provides higher thermal conductance compared to other configurations of heat sinks. Also, it is noticed that finned MF-PCM based heat sink assembly exhibits improved thermal performance in comparison to the heat sink with fin-PCM combination. The

overall highest thermal conductance value is obtained for three finned MF-PCM based heat sink at $q'' = 2.7 \text{ kW/m}^2$.

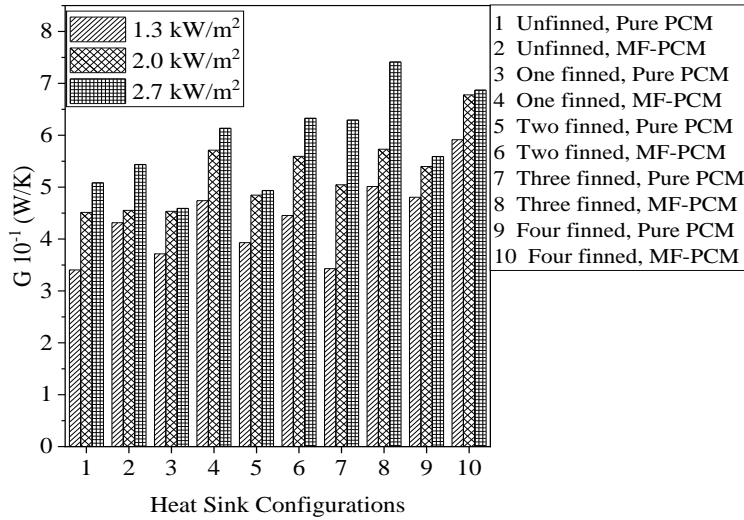
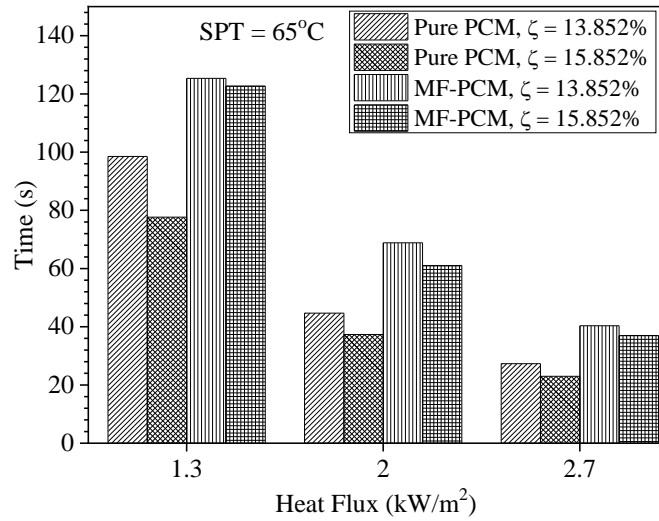


Fig. 4.40 Thermal conductance of various heat sink configurations for different heat flux values at $\psi = 0.86$

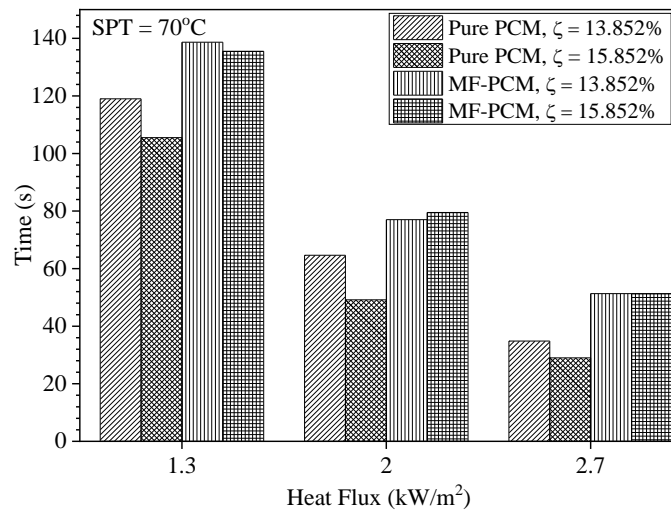
Effect of volume fraction of TCE on enhancement in operating time and enhancement ratio

Figs. 4.41(a-b) depict the operating time needed to attain different SPTs (65°C and 70°C) for the four finned heat sink assembly with various TCE volume fractions as well as varied range of TCE and q'' values. The operating time is found to decrease with the rise in input heat flux for a given SPT. At $q'' = 1.3 \text{ kW/m}^2$ and TCE volume fraction (ζ) of 13.825%, the time taken to attain SPT of 65°C is found to be 98.5 min and 125.33 min for four finned heat sink with PCM and four finned MF-PCM, respectively. While, for $q'' = 1.3 \text{ kW/m}^2$ and $\zeta = 15.825\%$, the time taken to attain SPT of 65°C is found to be 77.67 min and 122.67 min for four finned heat sink with PCM and four finned heat sink with MF-PCM, respectively. The time to attain SPT of 70°C for $q'' = 1.3 \text{ kW/m}^2$ and $\zeta = 15.825\%$ is found to be 119 min and 138.67 min for four finned heat sink with PCM and four finned heat sink with MF-PCM, respectively. While, At $q'' = 1.3 \text{ kW/m}^2$ and $\zeta = 15.825\%$, the time taken to attain SPT of 70°C is found to be

105.5 min and 135.33 min for four finned heat sink with PCM and four finned heat sink with MF-PCM, respectively. This may be due to slightly decrease in volume fraction of MF and PCM with the increase in the volume fraction of fins.

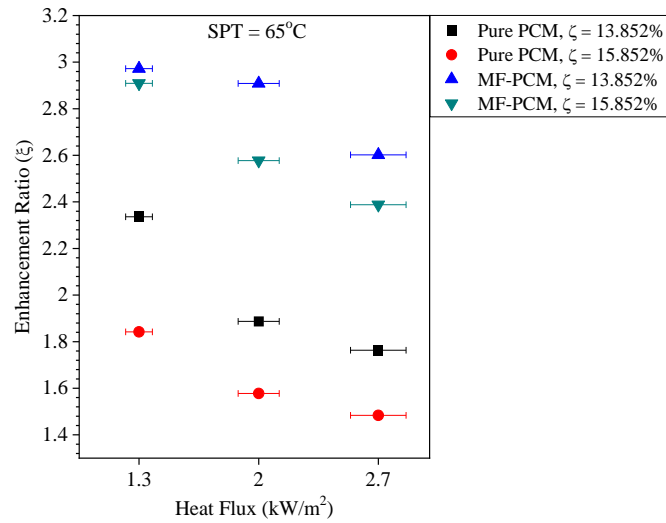


(a)

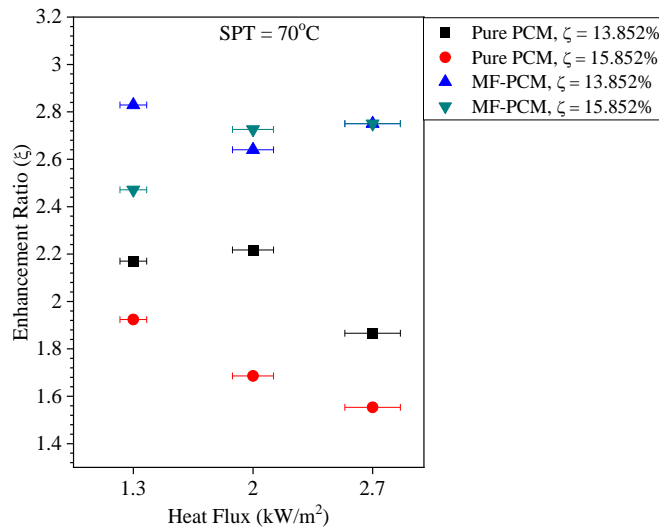


(b)

Fig. 4.41 Time to attain SPT at $q'' = 1.3, 2.0,$ and 2.7 kW/m^2 for different ζ in four finned heat sink case, (a) 65°C and (b) 70°C



(a)



(b)

Fig. 4.42 Enhancement ratio at different heat flux of 1.3, 2.0, and 2.7 kW/m² for different ζ and SPT of (a) 65°C and (b) 70°C

The enhancement ratios of two different heat sink assemblies such as four finned heat sink with PCM and four finned MF-PCM based heat sink for varied range of q'' are shown in Figs. 4.42(a-b). The results are shown for heat sink assemblies to achieve the SPT value of 65°C and 75°C. It may be noted that for SPT of 65°C, MF-PCM with $\zeta = 13.852\%$ shows better enhancement ratio compared to MF-PCM with $\zeta = 15.852\%$. While, PCM based heat sink

associated with $\zeta = 13.852\%$ exhibits better enhancement ratio compared to PCM based heat sink with $\zeta = 15.852\%$. At $q''=1.3 \text{ kW/m}^2$ and SPT of 70°C , MF-PCM with $\zeta = 13.852\%$ exhibits the best value of enhancement ratio compared to other fin configurations. While for $q'' = 2.0$ and 2.7 kW/m^2 , MF-PCM with $\zeta = 13.852\%$ shows same enhancement ratio as MF-PCM with $\zeta = 15.852\%$. While, PCM based heat sink associated with $\zeta = 13.852\%$ exhibits better enhancement ratio compared to PCM based heat sink with $\zeta = 15.852\%$ at all the heat flux values.

4.3.3 Analysis of thermal performance of nano enhanced phase change material (NePCM) based finned and unfinned heat sink configurations

Here, tests are conducted to investigate the effect of PCM and NePCM on the thermal performance of heat sinks without and with plate fins at constant heat flux condition. Aluminum and paraffin wax are considered as heat sink (HS) material and PCM, respectively. Aluminum oxide is chosen as nanoparticle material in this study. Three different heat sink configurations such as unfinned, one finned and three finned are analyzed in this study. The value of heat flux is maintained at 2.0 kW/m^2 for all the cases. Constant mass of PCM and constant volume fraction of fins (9%) are used in this study. Also, the NePCM based heat sinks are compared with the conventional pure PCM based heat sinks. Effect of nanoparticle concentration, heat sink configurations and set point temperatures on various parameters such as heat sink base temperature, operating time and enhancement ratio is studied. The results obtained from the studies are elaborated below.

Effect of nanoparticle concentration

Variation of T_b with time for different nanoparticle concentration ($\varphi = 0\%$, 2% , 4% , and 6%) are shown in Figs. 4.43(a-c). Results are shown for different configurations of heat sink assembly such as unfinned, one finned and three finned heat sink. Fig. 4.43(a) shows that adding small percentage of nanoparticles

($\varphi = 2\%$) in PCM based unfinned heat sink extends the operating time. This is because increase in nanoparticle concentration increases the thermal conductivity of the PCM based system and hence extract more heat from the base of the heat sink. The percentage increase in operating time of unfinned heat sink is found to be 25% with the addition of 2% nanoparticle in PCM compared to conventional pure PCM based unfinned heat sink. However, further increase in the nanoparticle concentration ($\varphi = 4\%$ and 6%) in the PCM does not significantly influence the operating time compared to conventional pure PCM ($\varphi = 0\%$) based unfinned heat sink. In addition, at higher nanoparticle concentration ($\varphi = 4\%$ and 6%), the operating time decreases in NePCM based unfinned heat sink compared to pure PCM based heat sink. Tariq et al. [180] employed different weight percentages (0.002, 0.005 and 0.008%) of graphite nanoparticles (GNPs) along with RT-44HC and RT-64HC in their study. For unfinned heat sink configuration, higher nanoparticle concentration in PCM does not significantly influence the operating time compared to pure PCM based heat sink. The viscosity is found to increase with the increase in nanoparticle concentration that reduces the convective circulation in the PCM and leads to the reduction in the heat transfer. Furthermore, the addition of nanoparticle decreases the amount of PCM in the system which reduces the latent heat capacity of the system.

The effect of nanoparticle concentration in PCM based heat sink varies with the number of fins inside the heat sink (Fig 4.43b-c). In case of one finned heat sink (Fig. 4.43b), lower concentration of nanoparticles ($\varphi = 2\%$) does not have significant effect on the operating time of PCM based heat sink. For addition of 2% nanoparticles in PCM in case of one finned heat sink, the operating time decreases slightly. The increase in thermal conductivity is less at lower nanoparticles concentration. Also, the addition of nanoparticle does not overcome the effect of increase in the viscosity. The operating time of one finned heat sink increases with the increase in the nanoparticle concentration ($\varphi = 4\%$) in the PCM. This may be because the effect of increase in thermal conductivity is significant due to the addition of 4% nanoparticle in one finned heat sink. The

percentage increase in operating time is found to be 28% with the addition of 4% nanoparticle in PCM based heat sink with one fin compared to conventional pure PCM based one finned heat sink. With further increase in the nanoparticle concentration the thermal conductivity of the system increases in one finned heat sink. While, it does not overcome the effect of increase in viscosity of the PCM and decrease in latent heat capacity of the PCM based heat sink. Bayat et al. [116] performed numerical investigation using Al_2O_3 and CuO nanoparticles and reported that performance of heat sink improves with addition of small percentage of nanoparticle concentration. However, the performance deteriorates at higher nanoparticle concentration.

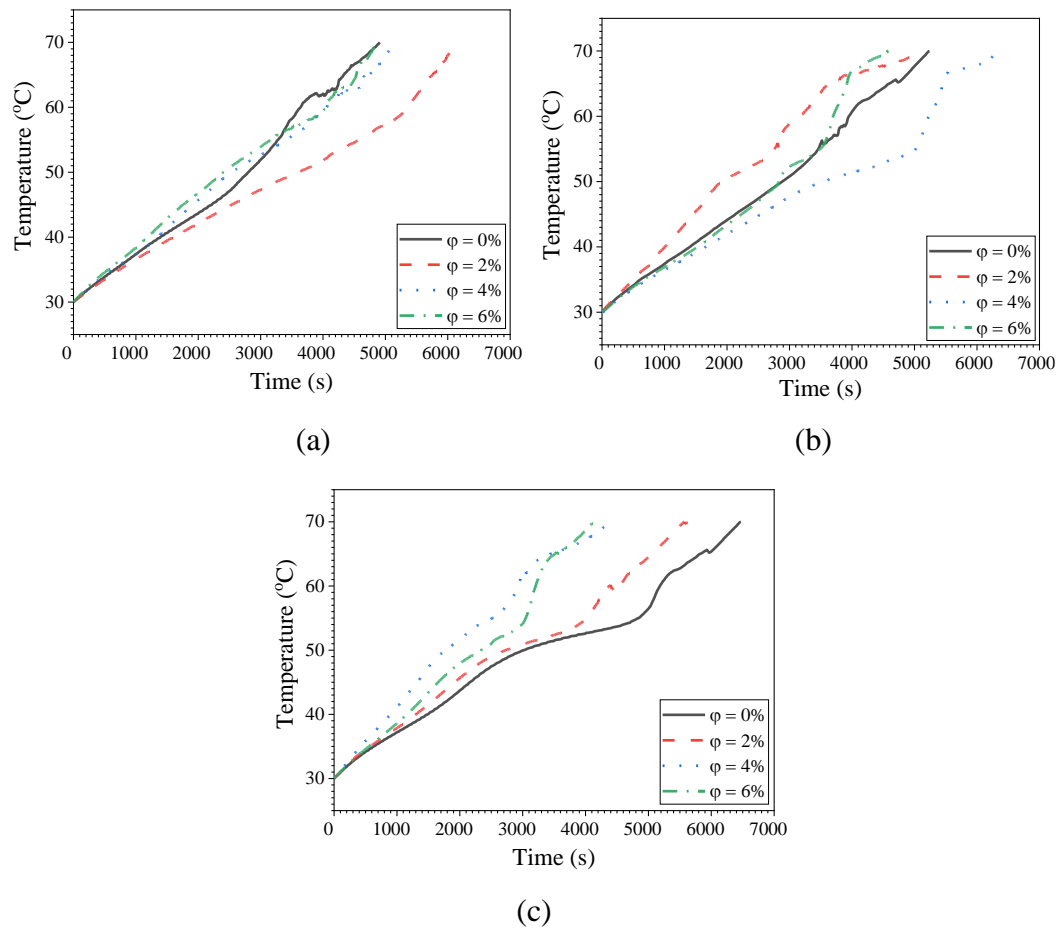


Fig. 4.43 Heat sink base temperature at various nanoparticle concentrations (0%, 2%, 4% and 6%) for different configuration of heat sinks (a) unfinned, (b) one finned, and (c) three finned heat sinks

Furthermore, different observation has been noted with the increase in number of fin from one to three. For three finned heat sink, the operating time is found to decrease with the addition of nanoparticles (Fig. 4.43c). The effect of increase in thermal conductivity is not significant due to the addition of nanoparticle in comparison to fins. Also, the addition of nanoparticle decreases latent heat capacity and increases the viscosity which in turn decreases the circulation of convection currents. Also, the addition of nanoparticles decreases the latent heat capacity of the system. In case of three finned heat sink, the maximum operating time is obtained for conventional pure PCM.

Effect of configuration of heat sink

Here, three different types of heat sink configurations such as unfinned, one finned and three finned heat sinks have been considered for the analysis. Various nanoparticles concentration ($\varphi = 0\%$, 2%, 4% and 6%) are used in the analysis, while the surface heat flux is maintained constant ($q'' = 2.0 \text{ kW/m}^2$) (Fig. 4.44a-d). Fig. 4.44(a) shows the variation of T_b for different configurations of heat sink for conventional pure PCM ($\varphi = 0\%$). It is observed that operating time of heat sink increases with fin numbers. This is due to the fact that increase in number of fins inside the heat sink increases the heat transfer from base to PCM. The highest operating time in case of pure PCM ($\varphi = 0\%$) is found to be 6470 s for three finned heat sink.

However, this trend changes for the nanoparticle concentration of 2% (Fig. 4.44b). In such a case, the heat sink with no fin exhibits the highest value of operating time. This may be due to the fact that enhancement in thermal conductivity of the PCM, due to the addition of nanoparticles, dominates the counter effect of increase in viscosity. While, in case of heat sink with fins the value of thermal conductivity is already high because of the fins. The nanoparticle addition increases the viscosity which reduces the convective currents in the finned heat sinks. The highest operating time at 2% nanoparticle concentration is found to be 6160 s for unfinned heat sink. With the further increase in nanoparticle concentration from 2% to 4%, the maximum operating time shifts

from unfinned heat sink to one finned heat sink (Fig. 4.44c). The maximum operating time in case of 4% nanoparticle concentration is found to be 6370 s for one finned heat sink assembly. Fig. 4.44d shows the base temperature of different configuration of heat sinks for nanoparticle concentration of 6%. The maximum operating time of 4880 s is obtained for unfinned heat sink.

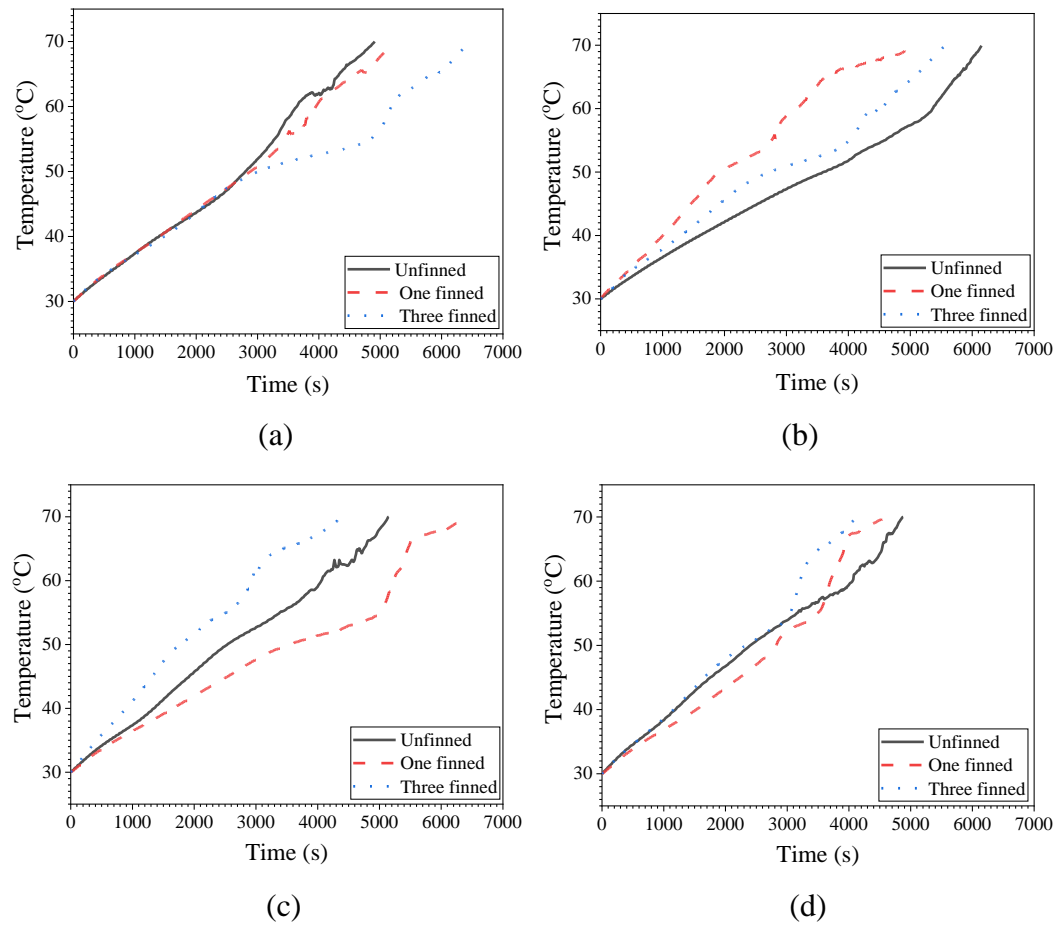


Fig. 4.44 Heat sink base temperature at different configuration of heat sinks (unfinned, one finned and three finned heat sinks) for various nanoparticle concentrations (a) 0%, (b) 2%, (c) 4%, and (d) 6%

It can be seen that the maximum operating time decreases with the addition of nanoparticle concentration. The maximum operating time is found to decrease by 24.5% with the increase in the nanoparticle concentration from 0% to 6%. The operating time decreases with the increase in nanoparticle concentration, which

may be due to the decrease in latent heat capacity of the PCM and also retardation of convection due to increase in viscosity of NePCM. It was argued that the operating time decreases with the addition of higher nanoparticle concentration in case of NePCM based finned [116] and unfinned [180] heat sinks.

Melt front propagation and melt fraction variation with time

The melt front propagation of PCM with and without finned heat sink at different time steps are shown in Fig. 4.45. This would help to understand the heat transfer mechanism during the phase change process in the heat sink. The propagation of melt front is recorded by using digital camera (Sony RX10 MII). The photographs are recorded, at every 20 minutes intervals, after 45 minutes from the initiation of the experiments till the completion of melting of entire PCM. Here, the photographs of melt front propagation are shown only for pure PCM for the sake of brevity. The photographs show the black and white colors that represent the liquid and solid phases of the PCM, respectively.

Time (min)	Unfinned	One finned	Three finned
45			
65			
85			
105			
115			

Fig. 4.45 Binary photographs of the melting front propagation of PCM in various configurations of heat sinks (unfinned, one finned and three finned)

Fig. 4.45 shows the binary image of melt front propagation in case of unfinned, one finned and three finned heat sinks. For PCM based unfinned heat sink, it can be seen that the melt front moves parallel to the hot surface which reveals that conduction is the dominant mode of transfer of heat within the thin liquid layer. With the progress of time, the influence of free convection increases and waviness is developed at the interface due to the generation of three-dimensional Benard convection cells in the liquid PCM [141].

In case of finned heat sinks, the heat transfer from the fin is directed by a continuous thermal boundary layer starting from the base and ending at the fin tip. As noticed in unfinned heat sink, conduction heat transfer remains the dominant mode of heat transfer for initial time duration. As the time progress, the interface of solid-liquid moves away from the fin and base surface. In such a case, free convection starts to dominate the heat transfer process. The PCM is heated from both the surfaces such as fin and base which in turn increases the thickness of PCM melt layer. Also, the thickness of liquid PCM is found to decrease along the fin length. It is observed that higher rate of melting takes place at the fin base compared to its tip. This may be because of the gradient of temperature along the fin length. Further, it may be noted that the interface shape remains symmetric to both the sides of the fin due to the equal convective currents on both the sides of the fins. It may be noted from the figure that melting rate increases with the increase in number of fins (zero to three fins) due to enhanced surface area. On comparing various heat sinks, it can be inferred that the rate of transfer of heat is more for three finned heat sink and also uniform melting is achieved with more number of fins. Kamkari et al. [141] reported similar observation in their experimental investigation during melting analysis of PCM.

Figs. 4.46(a-c) show the melt fraction variation with time for NePCM based heat sinks (unfinned, one finned and three finned) for different values of ϕ (0%, 2%, 4% and 6%). The melting starts early at lower nanoparticle concentration ($\phi = 2\%$) for unfinned heat sink due to increase in thermal conductivity of PCM (Fig. 4.46a). For unfinned heat sink, the melt fraction of PCM reaches to unity value at the same time for 2% and 4% nanoparticle concentrations followed by 6% and

0% nanoparticle concentrations. In case of one finned heat sink, the melt fraction of PCM follows the order of 4%, 2%, 6% and 0% to reach unity (Fig. 4.46b). While, in case of three finned heat sink, it follows the order of 4%, 6%, 2% and 0% to attain unity value of melt fraction (Fig. 4.46c). It is observed that nanoparticle concentration of 4% increases the melting rate of PCM in case of one finned and three finned heat sinks.

The total PCM melting time for unfinned, one finned and three finned heat sinks is shown in Fig. 4.47. In case of unfinned heat sink, the complete melting time of PCM decreases with the addition of nanoparticle (2% and 4%), however the melting time does not decrease with further addition of nanoparticle (6%).

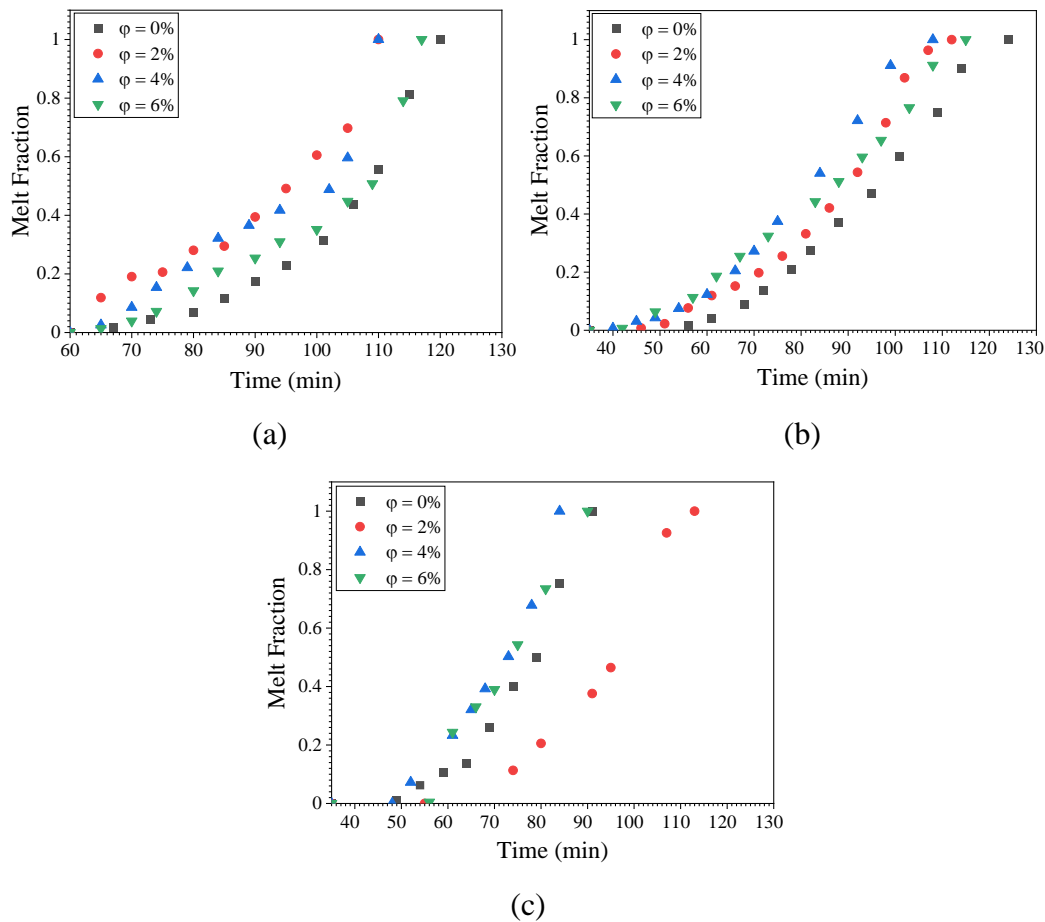


Fig. 4.46 Melt fraction of PCM at various nanoparticle concentration and different time duration for various heat sink configurations such as heat sinks (a) unfinned, (b) one finned, and (c) three finned heat sinks

Similar results are obtained with one finned and three finned heat sinks where the complete melting time decreases with the addition of nanoparticle (2% and 4%), however the melting time increases with the further addition of nanoparticles (6%). Present results are similar to the results obtained by Sahoo et al. [56] and Bayat et al. [116] obtained in their numerical investigation. The authors [56, 116] reported that melting time decreases with the addition of nanoparticles, however after certain limit further addition of nanoparticles do not have significant effect on the melting time of NePCM. Here, the maximum and minimum melting time is found to vary between 124-113 min, 112-91 min, 110-84 min and 117-90 min for nanoparticle concentration of 0%, 2%, 4% and 6%, respectively. Maximum melting time is observed for unfinned heat sink (4% and 6% nanoparticle concentrations) and one finned heat sink (0% and 2% nanoparticle concentration). However, the lowest melting time is heat sink is obtained for three finned heat sink for all the nanoparticle concentration. Because of nanoparticle addition, maximum reduction in melting time is found to be 9%, 13% and 26% for unfinned, one finned and three finned heat sinks, respectively. In order to achieve faster melting of PCM, one can add nanoparticles in the PCM.

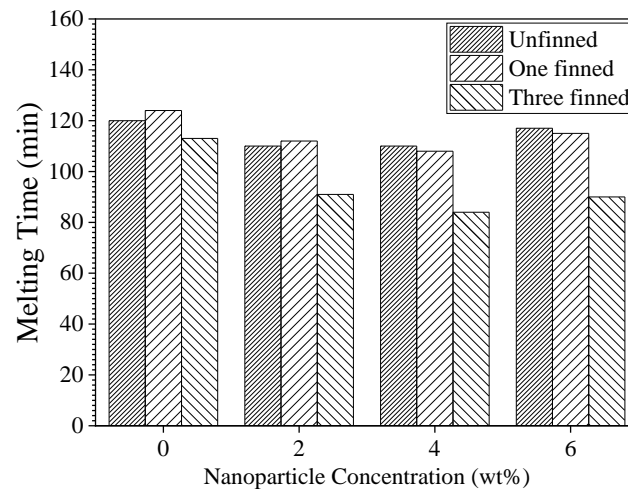


Fig. 4.47 Complete melting time of PCM at various nanoparticle concentration (0%, 2%, 4% and 6%) and heat sink configurations (unfinned, one finned and three finned)

Effect of nanoparticle concentration at different set point temperature (SPT)

Set point temperature (SPT) is defined as the maximum operating temperature of electronic devices upto which the electronic devices can work without failure, often termed as critical operating temperature. Stretching of the operating time to attain a given SPT is considered as the better performance in thermal management of the system. The effect of nanoparticle concentration to achieve the different value of SPTs (60°C, 65°C and 70°C) for different heat sink configurations (unfinned, one finned and three finned) are studied and are shown in Figs. 4.48(a-c).

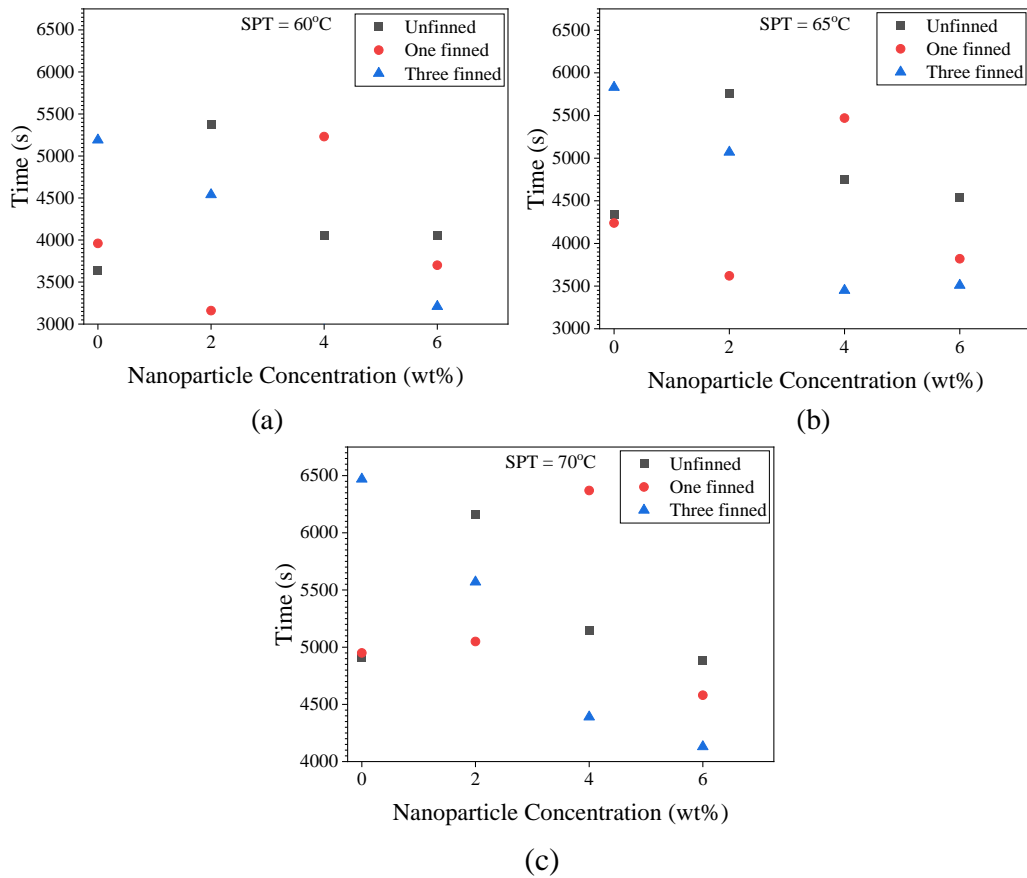


Fig. 4.48 Effect of nanoparticle concentration and different heat sink configurations at different set point temperature of (a) 60°C, (b) 65°C, and (c) 70°C

The unfinned heat sink is found to exhibit the highest value of operating time at 2% nanoparticle concentration for all the SPTs (60°C, 65°C and 70°C). The one

finned and three finned heat sinks exhibit maximum operating time with 4% and 0% nanoparticle concentrations, respectively for all the cases. The maximum operating time of 5370 s is obtained for unfinned heat sink at 2% nanoparticle concentration for SPT = 60°C. In case of pure PCM ($\varphi = 0\%$) based three finned heat sink, the maximum operating time is found to be 5830 s and 6470 s for SPT of 65°C and 70°C, respectively. It may be inferred from the figure that nanoparticles are not suitable option for thermal management of electronic devices at higher SPT as the nanoparticles tends to agglomerate at high temperature. Also, lower concentration of nanoparticle is useful to design systems that operate at SPT of 60°C. Similar results have been reported by Bayat et al. [116] in their numerical investigation. The nanoparticle concentration in NePCM is found to influence the operating time, while the magnitude of the impact depends on the value of SPT. Lower concentration of nanoparticle is found to be useful to enhance the operating time of NePCM based heat sinks [116].

Enhancement ratio for different nanoparticle concentration

Enhancement in operating time to reach the SPT is known as enhancement ratio. It is defined as the ratio of operating time to reach the SPT for Heat sink with nanoparticle embedded PCM to the operating time to reach the SPT for unfinned heat sink with pure PCM and is expressed by Eq. 4.13.

Fig. 4.49(a-c) shows the enhancement ratio at various nanoparticle concentrations ($\varphi = 0\%$, 2%, 4% and 6%) with different heat sink configurations (unfinned, one finned and three finned) for different SPTs (60°C, 65°C and 70°C). The enhancement ratio of heat sinks varies with the value of SPT and nanoparticle concentration. The unfinned heat sink is found to be exhibit highest enhancement at 2% nanoparticle concentration for all the SPTs (60°C, 65°C and 70°C). The one finned and three finned heat sinks show maximum enhancement ratio for 4% and 0% nanoparticle concentrations, respectively for all the cases. The maximum enhancement ratio of 1.48 is obtained for unfinned heat sink at 2% nanoparticle concentration for SPT = 60°C. The maximum enhancement ratio is found to be 1.35 and 1.32 for three finned heat sink with pure PCM ($\varphi = 0\%$) to achieve SPT

of 65°C and 70°C, respectively. Nanoparticle, may not be suitable option for thermal management of electronic devices at higher SPTs (65°C and 70°C), although useful with lower concentration for SPT of 60°C.

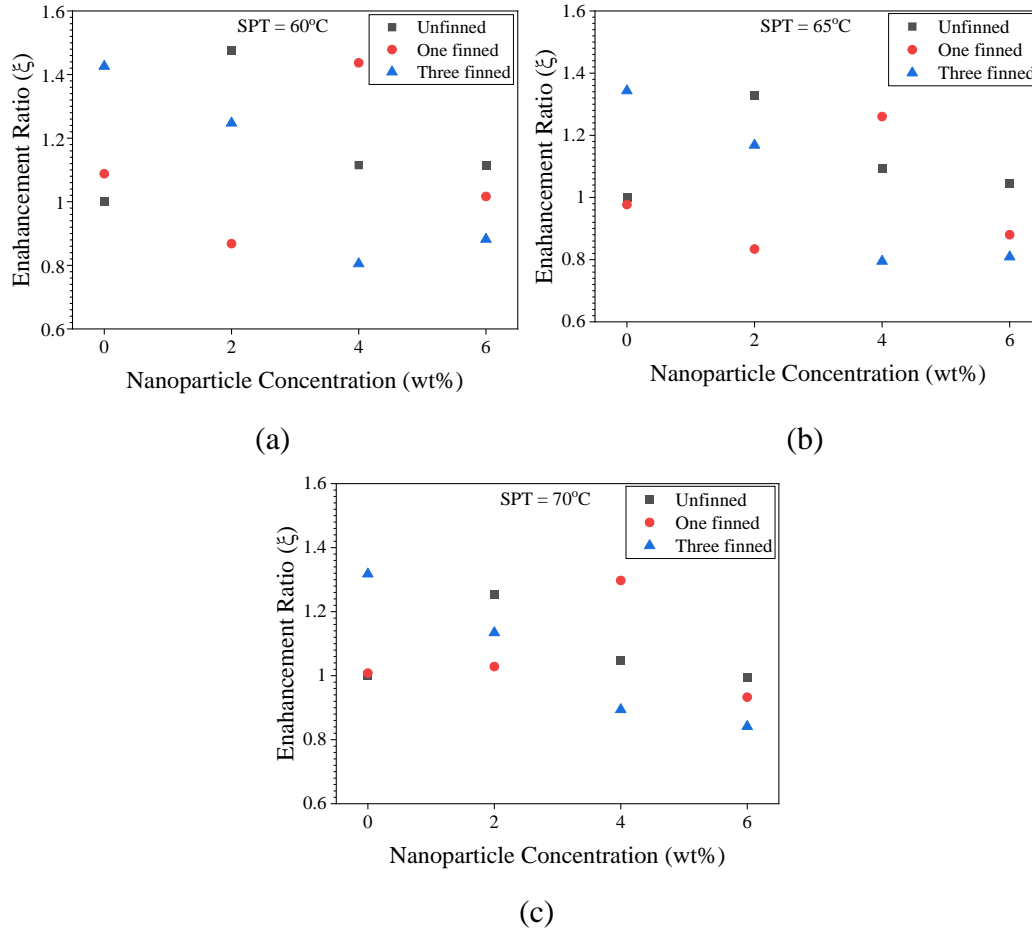


Fig. 4.49 Enhancement ratio at various nanoparticle concentration and heat sink configurations for different set point temperature of (a) 60°C, (b) 65°C, and (c) 70°C

4.4 Concluding Remarks

The thermal performance of various heat sink configurations are studied through experimental investigation. In all the cases, aluminum and paraffin wax with melting temperature range 58-62°C are considered as heat sink material and PCM, respectively. These studies mainly consider the effect of inclination angles,

different heat flux values, fin numbers, metal foam and nanoparticle concentration on the thermal performance.

In the first problem, tests are performed to investigate the thermal performance of phase change material (PCM) based heat sinks without and with plate fins for various inclination angles (0° to 90°) and different heat flux values (1.3 - 2.7 kW/m²). The solid-liquid interface position is studied through photographic observation. The operating time, does not depend significantly on the angle of inclination for the unfinned heat sink without PCM and three finned heat sink filled with PCM, while, increases with decrease in inclination angle from 90° to 0° for PCM based unfinned, one finned and two finned heat sinks. The melting time decreases with the reduction in inclination angle from 90° to 0° for unfinned heat sink and finned heat sinks.

In the second problem, experiments are conducted to analyze the thermal performance of various heat sink configurations such as unfinned with pure PCM, finned with pure PCM, unfinned with metallic foam (MF)-PCM composite and finned with MF-PCM composite for different heat flux values and PCM volume fraction. The unfinned heat sink without and with PCM is used for baseline comparison. The effect of various parameters such as PCM volume fraction, heat sink type and heat flux on the stretching of operating time to achieve a set point temperature (SPT) is studied. The enhancement in operating time is found to vary with the SPT and heat flux values. MF-PCM based heat sinks are more advantageous for higher value of input heat flux (2.0 and 2.7 kW/m²). The highest enhancement ratio for four finned MF-PCM heat sink and three finned MF-PCM heat sink for 1.3 and 2.7 kW/m², respectively.

In the next problem, the thermal performance of various PCM based heat sink configurations (unfinned, one finned and three finned) with different nanoparticle concentration is studied through experimental investigation. Aluminum oxide is chosen as nanoparticle material in this study. The highest value of operating time is obtained with pure PCM based three finned heat sink assembly. Maximum reduction in melting time is observed in NePCM based three finned heat sinks compared to other configurations. Results indicate that NePCM

with lower value of nanoparticle concentration is useful for the heat sinks with SPT value of 60°C.

The experimental study demonstrates the thermal performance of PCM based heat sink configurations for different design conditions involving angle of inclination, heat flux values, fin numbers, metal foam and nanoparticle concentration. These experimental results will be useful for the design of heat sinks for thermal management applications.

Chapter 5

Summary and conclusions

Present dissertation reports the theoretical and experimental investigations pertaining to the heat transfer characteristics of phase change materials (PCMs) during melting/solidification. The objective of the present study is to analyze the thermal performance of PCM based systems for various applications including thermal management of electronic components and thermal energy storage systems.

Initially, analytical models have been proposed to analyze melting and solidification of PCM in annular and rectangular geometries. A variety of boundary conditions involving constant heat flux, adiabatic condition and convective condition are used for the analysis. In this study, heat balance integral method (HBIM) has been used to solve the conduction equation with the associated boundary conditions. Closed form expressions have been obtained for the temperature distribution for all the cases. Efforts have been made to propose correlations to predict melting and solidification time as a function of aspect ratio and end wall boundary conditions for all the cases. Also, unconstrained and constrained melting behavior of PCM in the spherical capsule is analyzed through CFD numerical technique by using Ansys Fluent. Numerous models involving symmetric/axisymmetric formulations with varying density, constant density and Boussinesq approximation have been simulated to analyze the melting behavior. The results obtained from numerical simulation such as melting pattern and melt fraction of PCM are found to be in good agreement with the available test data.

Furthermore, a test facility involving various modules such as DC power supply, data acquisition system, thermocouples, computer and PCM based heat sink assembly has been developed to analyze the heat transfer performance of PCM based heat sinks for thermal management of electronic devices. Tests have been carried out to investigate the effect of various parameters such as fin

number, inclination angle and heat flux values on the thermal performance. The solid-liquid interface position and the melt fraction are analyzed for different angle of inclination and heat sink configurations through photographic observation. In addition, tests are performed to study the thermal performance of PCM based heat sinks with the combination of different TCEs such as fins, MF, nanoparticles and combination of these TCEs. The significant findings obtained from the present studies are elaborated below:

5.1 Theoretical investigation on melting and solidification of phase change material inside the thermal energy storage system

Here, analytical models have been proposed to analyze melting and solidification of PCM in annular and rectangular geometries. A variety of boundary conditions involving constant heat flux, adiabatic condition and convective condition are used for the analysis. Efforts have been made to propose correlations to predict melting and solidification time as a function of aspect ratio and end wall boundary conditions for all the cases.

5.1.1 Melting and solidification analysis of phase change material inside annular thermal energy storage system

A one-dimensional conduction heat transfer model has been proposed to study the melting and solidification of phase change material (PCM) inside an annulus. Here, the phase change process is divided into two main sub-processes such as melting and solidification sub-process. Subsequently, each sub-process is analyzed for various temporal regimes. The temporal regimes include completely solid, partially molten and completely molten for melting sub-process and in reverse order for solidification sub-process. Later on, the solution for temperature distribution for each temporal regime is obtained either by employing variational formulation or using a method of quasi-steady state. The solution of each temporal regime is coupled to provide the solution for temperature distribution for

the sub-process. The significant outcomes obtained from the present analysis are elaborated below.

- In all the cases, closed form expressions are obtained for temperature distribution as a function of various modelling parameters such as boundary heat flux, heat transfer coefficient, thermo-physical properties of PCM, and physical dimension of thermal storage unit.
- Present model exhibits good agreement with the existing test data during melting and solidification of PCM.
- The heat transfer coefficient has no significant effect on the melting of PCM. However, heat transfer coefficient plays a crucial role for controlling the solidification time of PCM, and significant role to analyze the transient interface position and frozen fraction during solidification of PCM.
- Decreasing the radius ratio of annulus from $\eta = 0.5$ to $\eta = 0.33$ increases the melt duration from 1238 s to 3046 s. This indicates that melt duration can be increased by increasing the thickness of PCM in annular geometry.
- Presence of a high-conductivity material has a significant effect on PCM temperature. It is observed that for any thermal storage unit there exists a particular percentage of TCE-PCM distribution through which maximum melt duration can be achieved.

5.1.2 Melting and solidification analysis of phase change material inside rectangular thermal energy storage system involving fins

The melting and solidification processes of phase change material (PCM) are analyzed in a two-dimensional finite storage system with plate fins. Solutions are obtained for various boundary conditions, namely, constant heat flux, constant temperature and convective air environment at the end walls by employing heat balance integral method (HBIM). The model predicts the solid-liquid interface, temperature distribution and melt/solid fraction. Melting/solidification time has been reported for various aspect ratios (σ) and different end wall conditions. Correlations have been proposed to predict the melting time as a function of

various parameters. The conclusions drawn from the present study are elaborated below.

Melting analysis

- Closed form expressions are obtained for various parameters such as temperature distribution, solid-liquid interface and melt fraction.
- Good agreement have been obtained between the present predictions and existing numerical and analytical solutions.
- The melting time is found to reduce by decreasing the aspect ratio from 2 to 0.5 by 49%, 53% and 50% for constant heat flux, constant temperature and constant air environment at the end walls.
- Also, the melting time decreases with the increase in the value of imposed parameters at the end walls, that is, melting time reduces by,
 - (a) 74% by increasing the heat flux from 500 W/m² to 2000 W/m²,
 - (b) 52% by increasing the temperature from 48°C to 68°C, and
 - (c) 76% by increasing the ambient temperature from 38°C to 58°C at 55 W/m²-K
- Correlations have been proposed for the melting time as a function of end wall conditions and aspect ratio. The proposed correlation is able to predict the melting time for a range of $0.125 \leq \sigma \leq 8$ within an error band of $\pm 10\%$ for 99% of the test data.

$$t_m = \begin{cases} 48142.267(\sigma)^{0.7016} (q_w'')^{-0.5563} & \text{Constant heat flux} \\ 24187182.9219(\sigma)^{0.9998} (T_w)^{-2.5424} & \text{Constant temperature} \\ 1993.4784(\sigma)^{0.4577} (h)^{-0.9685} (T_\infty)^{-2.6537} (T_m)^{3.9814} & \text{Convective air} \end{cases}$$

Solidification analysis

- Closed form expressions are obtained for various parameters such as temperature distribution, solid-liquid interface and solid fraction.
- Present predictions agree well with the results obtained by employing separation of variable and finite difference methods.

- The solidification time is found to reduce by 93% and 99% by reducing the aspect ratio from 8 to 0.125 for constant heat flux boundary condition and reducing the aspect ratio from 5 to 0.2 for constant wall temperature boundary condition, respectively.
- For the same aspect ratio, the solidification time is found to be more for salt hydrate compared to paraffin. By reducing the aspect ratio from $\sigma = 0.2$ to $\sigma = 5$, the solidification time was found to reduce by 50% and 73% for paraffin and salt hydrate, respectively. The solidification time was found to decrease by 88% for paraffin by reducing the aspect ratio from 8 to 0.125 for constant convective air boundary condition.
- Correlations for the solidification time have been proposed as a function of end wall conditions and aspect ratio. The proposed correlation is able to predict the melting time for a range of $0.125 \leq \sigma \leq 8$ within an error band of $\pm 10\%$ for 99% of the test data.

$$t_s = \begin{cases} 125077.867(\sigma)^{0.6768} (q_w'')^{-0.5976} & \text{Constant heat flux} \\ 329.3757(\sigma)^{1.0021} (T_w)^{1.0512} & \text{Constant temperature} \\ 125077.867(\sigma)^{0.5014} (h)^{-0.5814} (T_m - T_\infty)^{-1.0002} & \text{Convective air} \end{cases}$$

The present analytical model can contribute to better understanding of melting and solidification of PCM in a finite storage with internal fins. The present study reports the effect of various geometrical and thermal boundary conditions on melting and solidification time. The present analytical model can be useful in optimum design of PCM based thermal energy storage system with internal fins.

5.2 Unconstrained and constrained melting behavior of phase change material inside the spherical capsule through numerical investigation

Computational fluid dynamics (CFD) simulations have been performed to analyze the unconstrained and constrained melting of PCM inside the spherical capsule by using Ansys Fluent. Numerous models involving

symmetric/axisymmetric formulations with varying density, constant density and Boussinesq approximation have been considered to analyze the melting behavior. Volume of fluid model and solidification and melting model are used to simulate the melting of PCM. Efforts have been made to investigate the effect of various modeling parameters on melt fraction and temperature distribution of PCM.

5.2.1 Unconstrained melting analysis of phase change material in a spherical capsule

The unconstrained melting behavior of phase change material (PCM) in the spherical capsule is analyzed through CFD numerical technique with Ansys Fluent 19.2 software. Transient two-dimensional axisymmetric and symmetric melting models are simulated for different cases such as linear density variation in mushy and liquid regions, linear density variation in mushy region but constant density in liquid and solid regions, Boussinesq approximation in mushy region but constant density in liquid and solid regions. Melting pattern and melt fraction of PCM for different cases are compared with the existing test data for different time instant. The main results of the study are summarized as follows.

- Difference between melting time of PCM in spherical capsule obtained through experimental investigation and present model is found to be 12.5% and 20% for axisymmetric and symmetric cases, respectively.
- Axisymmetric melting exhibit close agreement with experimental results compared to symmetric melting of PCM.
- Melting pattern, rate and time obtained numerically using Boussinesq approximation do not agree well with experimental observation.
- Axisymmetric melting with constant density in liquid region (case II) underestimates the interface rise of PCM during melting process as well as heat storage capacity of the PCM in the capsule.

Results of this study shows that axisymmetric modelling with varying density in liquid phase (case I) more closely simulate the unconstrained melting of PCM in a spherical capsule compared to the other cases.

5.2.2 Constrained melting analysis of phase change material in a spherical capsule

The constrained melting of phase change material (PCM) inside the spherical capsule is studied through numerical investigation. Computations are performed for different cases such as axisymmetric modeling with Boussinesq approximation, axisymmetric modeling with constant density, symmetric modeling with Boussinesq approximation and symmetric modeling with constant density of PCM. Melting patterns and melt fractions obtained from present simulations are compared with the test data. The conclusions drawn from the study are summarized here.

- Axisymmetric and symmetric modelling with constant density (Cases II and IV) do not agree well with the visualized melt contours. However, the model with Boussinesq approximation (cases I and III) agrees well with the existing experimentally obtained melt contours.
- Axisymmetric melting with Boussinesq approximation (case I) underestimates the melt fraction, while the symmetric melting with Boussinesq approximations (case III) overestimates the melt fraction.
- Deviation of results obtained between axisymmetric and symmetric modeling with Boussinesq approximation is found to be approximately 14%.
- Waviness pattern obtained with symmetric modelling more closely resembles with the experimentally obtained melting pattern compared to axisymmetric modeling.

5.3 Experimental investigation of phase change materials inside the heat sink for thermal management applications

Here, a systematic study have been carried out to analyze the thermal performance of heat sinks with the combined effects of fin number, inclination angle and heat flux values through experimental investigation. The thermal performance of various heat sink configurations such as pure PCM without fin,

PCM with fin, PCM with MF matrix and PCM with MF matrix and fin systems during melting process is studied through experimental investigation. In addition, the combined effect of fins (0, 1, and 3 fins) and nanoparticles (2, 4, and 6 wt%) with PCM based heat sink for thermal management application have been analyzed. The operating time to stretch a critical set point temperature is studied for various heat sink configurations and design parameters.

5.3.1 Effect of inclination angle on the performance of phase change material based finned heat sink configurations

In the present work, tests are performed to investigate the thermal performance of phase change material (PCM) based heat sinks without and with plate fins (1, 2 and 3) for various inclination angles (0° to 90°) and different heat flux values (1.3 - 2.7 kW/m^2). The solid-liquid interface position is studied through photographic observation. The conclusions obtained from the experimental study are elaborated below.

- Inclination angle of heat sink significantly affects the thermal performance of the unfinned heat sinks. Effect of inclination angle on thermal performance is found to be less significant in case of one and two finned heat sinks, especially three finned heat sink assembly.
- With the decrease in inclination angle from 90° to 0° , the operating time is found to increase by 66%, 45% and 43% for PCM based unfinned, one finned and two finned heat sinks, respectively at $\text{SPT} = 75^\circ\text{C}$.
- Enhancement ratio increases with the increase in number of fins. The highest enhancement ratio in operating time is found to be 4.7 for PCM based three finned heat sink assembly at $q'' = 2.7$ kW/m^2 .
- Operating time increases with the increase in fin number. Compared to unfinned heat sink, the enhancement in the operating time for three finned and two finned heat sinks is found to be 74% and 38%, respectively at $\theta = 0^\circ$.

- With the reduction in inclination angle from 90° to 0° , the melting time is found to decrease by ~44% and ~30% for unfinned heat sink and finned heat sinks, respectively.

Based on the observations, it is found that the phase change materials should be incorporated in finned heat sinks. Also, heat sink with the higher number of fins (three finned heat sink in the present study) need to be incorporated in order to minimize the effect of inclination on thermal performance during thermal management of electronic devices.

5.3.2 Effect of metal foam and phase change material composite on the thermal performance of various finned and unfinned heat sink configurations

Experiments are conducted to analyze the thermal performance of various heat sink configurations such as unfinned with pure PCM, finned with pure PCM, unfinned with metallic foam (MF)-PCM composite and finned with MF-PCM composite for different heat flux values (1.3 , 2.0 and 2.7 kW/m^2) and PCM volume fraction (0 , 0.50 , 0.86 , and 1). The unfinned heat sink configurations without and with PCM are used for baseline comparison. The effect of various parameters such as PCM volume fraction, heat sink type and heat flux on the stretching of operating time to achieve a set point temperature (SPT) is studied. The conclusions obtained from this experimental study are elaborated below.

- Inclusion of PCM inside heat sink increases the maximum operating time required to reach critical SPT in comparison to heat sink without PCM.
- Lower base temperature and better thermal management capability are obtained in case of MF-PCM composite based heat sinks compared to pure PCM based heat sinks.
- MF-PCM heat sinks are more advantageous for higher input heat flux values (2.0 and 2.7 kW/m^2) due to utilization of entire latent heat of PCM. Also, at higher heat flux, MF-PCM takes longer time to reach SPT compared to pure PCM based heat sinks.

- The highest operating time and enhancement ratio of heat sinks vary with the variation in the heat flux value. Highest operating time and enhancement ratio is obtained for four finned MF-PCM heat sink compared to other configurations of heat sink for $q'' = 1.3$ and 2.0 kW/m^2 . While, for $q'' = 2.7 \text{ kW/m}^2$, three finned heat MF-PCM based heat sink shows better performance.
- Enhancement in operating time is found to vary with the value of SPT and heat flux values. At SPT= 65°C , enhancement is higher at lower value of heat flux ($q'' = 1.3 \text{ kW/m}^2$). However, at SPT= 70°C , greater enhancement is obtained at 2.7 kW/m^2 .
- The highest enhancement ratio of ~ 2.97 is achieved for four finned MF-PCM based heat sink and three finned MF-PCM based heat sink at $q'' = 1.3$ and 2.7 kW/m^2 , respectively. Also, three finned heat sink provide higher heat transfer rate and highest thermal conductance at $q'' = 2.7 \text{ kW/m}^2$.

5.3.3 Analysis of thermal performance of nano enhanced phase change material (NePCM) based finned and unfinned heat sink configurations

Here, tests are conducted to analyze the combined effect of nanoparticle concentration and number of fins in PCM based heat sinks for thermal management of electronic devices. The thermal performance of various PCM based heat sink configurations (unfinned, one finned and three finned) with different nanoparticle concentration (0, 2, 4 and 6 wt%) for $q'' = 2.0 \text{ kW/m}^2$ is studied through experimental investigation. Aluminum and paraffin wax are considered as heat sink material and PCM, respectively. Aluminum oxide is considered as nanoparticle material in this study. The evolution and propagation of melt front inside the heat sink is studied through photographic observation. The conclusions obtained from the present study are elaborated here.

- Latent heat of NePCM decreases with increase in the nanoparticle concentration; maximum decrease is found to be 21.76% for NePCM ($\varphi = 6\%$) compared to pure PCM.
- Operating time increases by 25% and 28% with the lower nanoparticle concentration ($\varphi = 2\%$) in PCM based unfinned and one finned heat sinks, respectively. However, the operating time decreases with the further increase in the nanoparticle concentration (4% and 6%).
- Operating time of three finned heat sink involving NePCM (2%, 4% and 6% nanoparticle concentration) is found to be lower compared to pure PCM based three finned heat sink.
- The highest operating time of 6470 s is obtained for pure PCM ($\varphi = 0\%$) based three finned heat sink.
- Maximum reduction in melting time is found to be 9%, 13% and 26% for NePCM based unfinned, one finned and three finned heat sinks, respectively.
- For higher value of SPT ($SPT > 60^\circ\text{C}$), NePCM based heat sink may not be a suitable option for thermal management of electronic devices. However, for lower value of SPT ($SPT < 60^\circ\text{C}$), NePCM based heat sink is useful for thermal management application.

It is inferred from the study that NePCM based heat sinks with higher nanoparticles concentration are not suitable option for thermal management of electronic devices at higher SPT. Also, lower concentration of nanoparticle is useful to design heat sink systems that operate at SPT of 60°C .

5.4 Recommendations for further investigation

Phase change materials (PCMs) are widely used for different thermal energy storage and thermal management applications because of the constant temperature solid-liquid phase transition. However, the dissipation of heat from the components is limited because of the poor conductivity of PCMs. Also, lower value of thermal conductivity of PCM results in slower melting and solidification

rates, which leads to the decrease in heat storage efficiency of the system. In view of this, high thermal conductivity materials namely, metallic fins, metallic foams (MFs), and nanoparticles are embedded in the phase change material (PCM) system. The present dissertation proposed theoretical models for melting and solidification phenomena of PCM in two different cases such as annular TES and rectangular TES with plate fin. Also, tests have been performed to investigate the thermal performance of different heat sink configurations. Combined effects of fin number, inclination angle and heat flux values on the thermal performance of PCM based heats sinks are analyzed. In addition, the effect of various TCEs such as fins, metal foam, nanoparticles and their combined effect on thermal performance of heat sinks is investigated. The research work carried out in this dissertation may provide useful information for further investigation in this area. In view of this certain important directions for the future investigation are elaborated below.

- Efforts should be made to develop theoretical models to obtain temperature distribution, solid-liquid interface position, and thermal performance of cascaded PCM based TES systems.
- Theoretical models need to be developed to analyze the effect of air void and shrinkage/expansion for various boundary conditions on the heat transfer performance of PCM based systems.
- Efforts need to be made to study heat transfer analysis of melting and solidification of encapsulated PCM in novel shape capsules such as elliptical and torus shapes using computational analysis and could be extended further by conducting experiments.
- Tests should be carried out to investigate the effect of novel light weight thermal conductivity enhancers on PCM based thermal energy storage and thermal management systems.
- Efforts need to be made to analyze the effect of hybrid nanoparticles, and combination of fins, metal foams and hybrid nanoparticles on thermal performance through experimental investigation.

References

- [1] The U.S. Energy Information Administration (EIA), *International Energy Outlook 2019 (IEO2019)*, assessed on February 28, 2021, <https://www.eia.gov/todayinenergy/detail.php?id=41433>
- [2] J. Yoon, “Flexible Solar Cells Made of Nanowires/Microwires”, *Semiconductor Nanomaterials for Flexible Technologies, Micro and Nano Technologies*, Elsevier, 159–196, 2010.
- [3] R. Jacob, and F. Bruno, “Review on shell materials used in the encapsulation of phase change materials for high temperature thermal energy storage” *Renew Sustain Energy Reviews* 48, 79-87, 2015.
- [4] L. Fan, Z. Zhu, S. Xiao, M. Liu, H. Lu, Y. Zeng, Z. Yu, and K. Cen, “An experimental and numerical investigation of constrained melting heat transfer of a phase change material in a circumferentially finned spherical capsule for thermal energy storage” *Appl Therm Engg* 100, 1063–1075, 2016.
- [5] E.M. Alawadhi, and C.H. Amon, “Performance analysis of an enhanced PCM thermal control unit”, *Proceed. of the seventh intersociety conference on thermal and thermomechanical phenomena in electronic systems*, IThERM2000(Cat No00CH37069), 283-289, 2000.
- [6] S. Sahoo, M. Das, and P. Rath, “Application of TCE-PCM based heat sinks for cooling of electronic components: A review” *Renew Sustainable Energy Rev* 59, 550-582, 2016.
- [7] R. Grimes, E. Walsh, and P. Walsh, “Active cooling of a mobile phone handset” *Appl Therm Engg* 30(16), 2363-2369, 2010.
- [8] Y. Peles, A.K. Ar, C. Mishra, C.J. Kuo, and B. Schneider, “Forced convective heat transfer across a pin fin micro heat sink” *Int J Heat Mass Transf* 48(17), 3615–3627, 2005.
- [9] K.C. Ng, C.R. Yap, and M.A. Chan, “A universal performance chart for CPU cooling devices” *Heat Transf Engg* 29(7),651–656, 2008.
- [10] E. Walsh, P. Walsh, R. Grimes, and V. Egan, “Thermal management of

- low profile electronic equipment using radial fans and heat sinks” *J Heat Transf* 130(12), 125001, 2008.
- [11] M. Malik, I. Dincer, and M.A. Rosen, “Review on use of phase change materials in battery thermal management for electric and hybrid electric vehicles” *Int J Energy Research* 40, 1011-1031, 2016.
- [12] Y.Y. Ganatra, “Passive thermal management using phase change materials”, Master’s thesis, Purdue University, 2016.
- [13] A.O. Ercan, “Storage of thermal energy. Energy Storage Systems”, Eolss Publishers, 2006.
- [14] G.A. Lane, “Solar heat storage- latent heat materials,” vol. I. Boca Raton, FL: CRC Press Inc. 1983.
- [15] A. Sharma, V.V. Tyagi, C.R. Chen, and D. Buddhi, “Review on thermal energy storage with phase change materials and applications” *Renew Sustain Energy Reviews* 13, 318–345, 2009.
- [16] F. Talati, A.H. Mosaffa, and M.A. Rosen, “Analytical approximation for solidification process in PCM storage with internal fins: imposed heat flux” *Heat Mass Transf* 47, 369-376, 2011.
- [17] P. Lamberg, and K. Siren, “Approximate analytical model for solidification in a finite PCM storage with internal fins” *Appl Mathematical Modelling* 27, 491-513, 2003.
- [18] A. Abhat, “Low temperature latent heat storage: heat storage materials” *Solar Energy* 30(4), 313-332, 1983.
- [19] B. Zalba, J.M. Marin, L.F. Cabeza, and H. Mehling, “Review on thermal energy storage with phase change materials, heat transfer analysis and applications” *Appl Therm Engg* 23(3), 251-283, 2003.
- [20] S.D. Sharma, H. Kitano, and K. Sagara, “Phase change materials for low temperature solar thermal applications” *Res Rep Fac Eng Mie Univ* 29(1), 31-67, 2004.
- [21] G.A. Lane, S. Aboul-Enein, and N. A. Malatidis, “Heat of fusion systems for solar energy storage” *Proceed. workshop on solar energy storage*

subsystems for the heating and cooling of buildings 1975.

- [22] C. Herrick, and D. Golibersuch, “Qualitative behavior of a new latent heat storage device for solar heating/cooling systems” *General Electric Company Corporate Research and Development*, 1977
- [23] R.M.R. Saeed, "Advancement in thermal energy storage using phase change materials" Doctoral Dissertations 2687, 2018. https://scholarsmine.mst.edu/doctoral_dissertations/2687
- [24] A. George, “Hand book of thermal design” In: C. Guyer, editor. *Phase change thermal storage materials*. McGraw Hill Book Co., chapter 1, 1989.
- [25] S.D. Sharma, and K. Sangara, “Latent heat storage materials and systems: a review” *Int. J. Green energy* 2(1), 1-56, 2005.
- [26] M. Kenisarin, and K. Mahkamov, “Solar energy storage using phase change materials” *Renew sustain energy reviews* 11(9), 1913-1965, 2007.
- [27] K. Jaewan, O. Jinwoo, and L. Hoseong, “Review on battery thermal management system for electric vehicles” *Appl Thermal Engg* 149, 192–212, 2019.
- [28] M.M. Islam, A.K. Pandey, M. Hasanuzzaman, and N.A. Rahim, “Recent progresses and achievements in photovoltaic-phase change material technology: a review with special treatment on photovoltaic thermal-phase change material systems” *Energy Convers Management* 126, 177–204, 2016.
- [29] A. Waqas, J. Ji, L. Xu, M. Ali, Zeashan, and J. Alvi, “Thermal and electrical management of photovoltaic panels using phase change materials - a review”, *Renew Sustain Energy Reviews* 92, 254–271, 2018.
- [30] M.M.A. Khan, R. Saidur, and F.A. Al-Sulaiman, “A review for phase change materials (PCMs) in solar absorption refrigeration systems” *Renew Sustain Energy Reviews* 76, 105–137, 2017.
- [31] K. Kant, A. Shukla, A. Sharma, A. Kumar, and A. Jain, “Thermal energy storage based solar drying systems: A review” *Innovative Food Science*

- Emerging Techno* 34, 86–99, 2016.
- [32] A. Shukla, K. Kant, and A. Sharma, “Solar still with latent heat energy storage: a review” *Innovative Food Science Emerging Techno* 41, 34–46, 2017.
- [33] M.H. Abokersh, M. Osman, O. El-Baz, M. El-Morsi, and O. Sharaf, “Review of the phase change material (PCM) usage for solar domestic water heating systems (SDWHS)” *Int J Energy Res* 42, 329–357, 2018.
- [34] S.Y. Kee, Y. Munusamy, and K.S. Ong, “Review of solar water heaters incorporating solid-liquid organic phase change materials as thermal storage” *Appl Therm Engg* 131, 455–471, 2018.
- [35] X. Ben Xu, L. Peiwen, and C. Chan, “Application of phase change materials for thermal energy storage in concentrated solar thermal power plants: a review to recent developments” *Appl Energy* 160, 286–307, 2015.
- [36] H. Panchal, J. Patel, and S. Chaudhary, “A comprehensive review of solar cooker with sensible and latent heat storage materials” *Int J Ambient Energy* 40(3), 329-334, 2017.
- [37] A. Gutierrez, L. Miró, A. Gil, J. Rodríguez-Aseguinolaza, C. Barreneche, N. Calvet, X. Py, A.I. Fernández, M. Grágeda, S. Ushak, and L.F. Cabeza, “Advances in the valorization of waste and by-product materials as thermal energy storage (TES) materials” *Renew Sustain Energy Reviews* 59, 763–783, 2016.
- [38] T.J. Lu, “Thermal management of high power electronics with phase change cooling” *Int J Heat Mass Transf* 34, 2245–2256, 2000.
- [39] A.G. Evans, M.Y. He, and M. Hutchinson, “Temperature distribution in advanced power electronics and effect of phase change materials on temperature suppression during power pulses” *J Electronic Package* 123 211–217, 2001.
- [40] X. Duan, and G.F. Naterer, “Heat transfer in phase change materials for thermal management of electric vehicle battery modules” *Int J Heat Mass*

- Transf* 53(23-24), 5176–5182, 2010.
- [41] D.C. Price, “A review of selected thermal management solutions electronics for military system” *IEEE Trans Component Pack Tech* 26, 26-39, 2003.
- [42] R. Kumar, M.K. Misra, R. Kumar, D. Gupta, P.K. Sharma, B.B. Tak, and S.R. Meena, “Phase change materials: Technology status and potential defence application” *Defence Sci J* 61 (2011) 576–582.
- [43] D.V. Hale, M.J. Hoover, and M.J. O’Neill, “Phase Change Materials Handbook Report No. HREC-5183-2 LMSC-HREC D225138 NASA” *Marshal Space Flight Centre, Alabama*, 1971.
- [44] A.J. Fosset, M.T. Maguire, A.A. Kudirka, F.E. Mills, and D.A. Brown, “Avionics passive cooling with microencapsulated phase change materials” *ASME J Electronics Package* 120, 238–242, 1998.
- [45] R. Baby, and C. Balaji, “Experimental investigations on phase change material based finned heat sinks for electronic equipment cooling” *Int J Heat Mass Transf* 55, 1642–1649, 2012.
- [46] N. Sharifi, T.L. Bergman, and A. Faghri, “Enhancement of PCM melting in enclosures with horizontally-finned internal surfaces” *Int J Heat Mass Transf* 54, 4182-4192, 2011.
- [47] K.A.R. Ismail, and F.A.M. Lino, “Fins and turbulence promoters for heat transfer enhancement in latent heat storage systems” *Exp Therm Fluid Sci* 35, 1010–1018, 2011.
- [48] R. Baby, and C. Balaji, “Thermal optimization of PCM based pin fin heat sinks: an experimental study” *Appl Therm Engg* 54, 65-77, 2013.
- [49] R. Akhilesh, A. Narasimhan, and C. Balaji, “Method to improve geometry for heat transfer enhancement in PCM composite heat sinks” *Int J Heat Mass Transf* 48, 2759–2770, 2005.
- [50] C.Y. Zhao, W. Lu, and Y. Tian, “Heat transfer enhancement for thermal energy storage using metal foams embedded within phase change materials (PCMs)” *Solar Energy* 84, 1402-1412, 2010.

- [51] Z. Chen, D. Gao, and J. Shi, Experimental and numerical study on melting of phase change materials in metal foams at pore scale, *Int J Heat Mass Transf* 72, 646–655, 2014.
- [52] J. Wang, H. Xie, Z. Xin, Y. Li, and L. Chen, “Enhancing thermal conductivity of palmitic acid based phase change materials with carbon nanotubes as fillers” *Solar Energy* 84, 339-344, 2010.
- [53] K. Tumuluri, J.L. Alvarado, H. Taherian, and C. Marsh, “Thermal performance of a novel heat transfer fluid containing multiwalled carbon nanotubes and microencapsulated phase change materials” *Int J Heat Mass Transf* 54, 5554–5567, 2011.
- [54] C.Y. Zhao, and Z.G. Wu, “Heat transfer enhancement of high temperature thermal energy storage using metal foams and expanded graphite” *Solar Energy Mater Solar Cells* 95, 636–643, 2011.
- [55] E. Assis, L. Katsman, G. Ziskind, and R. Letan, “Numerical and experimental study of melting in a spherical shell”, *Int J Heat Mass Transf* 50, 1790-1804, 2007.
- [56] S.K. Sahoo, M.K. Das, and P. Rath, “Numerical study of cyclic melting and solidification of nano enhanced phase change material based heat sink in thermal management of electronic components” *ASME 2016 5th Int Conf Micro/Nanoscale Heat Mass Transf (MNHMT2016)*, Biopolis, Singapore, January 4-6, 2016.
- [57] R.K. Sharma, P. Ganesan, J.N. Sahu, H.S.C. Metselaar, and T.M.I. Mahila, “Numerical study for enhancement of solidification of phase change materials using trapezoidal cavity” *Powder Tech* 268, 38-47, 2014.
- [58] S.S. Sebti, M. Mastiani, H. Mirzaei, A. Dadvand, S. Kashani, and S.A. Hosseini, “Numerical study of the melting of nano-enhanced phase change material in a square cavity” *J. Zhejiang University-Science A (Applied Physics and Engineering)* 14(5), 307-316, 2013.
- [59] L. Fan, and J.M. Khodadadi, “A theoretical and experimental

- investigation of unidirectional freezing of nanoparticle-enhanced phase change materials” *J Heat Transf* 134, 1-9, 2012.
- [60] M. Nabil, and J.M. Khodadadi, “Experimental determination of temperature-dependent thermal conductivity of solid eicosane-based nanostructure-enhanced phase change materials” *Int J Heat Mass Transf* 67, 301-310, 2013.
- [61] K. Chintakrinda, R.D. Weinstein, and A.S. Fleischer, “A direct comparison of three different material enhancement methods on transient thermal response of paraffin phase change material exposed to high heat fluxes” *Int J Thermal Sci* 50, 1639-1647, 2011.
- [62] Y. Lin, Y. Jia, G.P. Alva, and G. Fang, “Review on thermal conductivity enhancement, thermal properties and applications of phase change materials in thermal energy storage” *Renew Sustain Energy Reviews* 82(3), 2730-2742, 2018.
- [63] Z.A. Qureshi, H.M. Ali, and S. Khushnood, “Recent advances on thermal conductivity enhancement of phase change materials for energy storage system: A review” *Int J Heat Mass Transf* 127, 838-856, 2018.
- [64] S. Wu, T. Yan, Z. Kuai, and W. Pan, “Thermal conductivity enhancement on phase change materials for thermal energy storage: A review” *Energy Storage Materials* 25, 251-295, 2020.
- [65] L. Fan, and J.M. Khodadadi, “Thermal conductivity enhancement of phase change materials for thermal energy storage: a review” *Renew Sustain Energy Reviews* 15(1), 24-46, 2011.
- [66] N.I. Ibrahim, F.A. Al-Sulaiman, S. Rahman, B.S. Yilbas, and A.Z. Sahin, “Heat transfer enhancement of phase change materials for thermal energy storage applications: a critical review” *Renew Sustain Energy Reviews*, 74 26-50, 2017.
- [67] A.H. Mosaffa, F. Talati, M.A. Rosen, and H.B. Tabrizi, “Approximate analytical model for PCM solidification in a rectangular finned container with convective cooling boundaries” *Int comm Heat Mass Transf* 39,

- 318-324, 2012.
- [68] H. Carslaw, and J. Jaeger, "Conduction of heat in solids" 2nd edn. *Oxford University Press*, New York, 1959.
- [69] M.N. Ozisik, "Heat Conduction" 2nd edn. *John Wiley and Sons*, New York, 1993.
- [70] V. Alexiades, and A.D. Solomon, "Mathematical Modelling of Melting and Freezing Processes" *Hemisphere Publishing Corporation*, Washington DC, 1993.
- [71] A.D. Solomon, D.G. Wilson, and V. Alexiades, "The quasistationary approximation for the Stefan problem with the convective boundary condition", *Int J Mathematics and Mathematical Sci* 7, 549-563, 1993.
- [72] S. Chakraborty, and P. Dutta, "Analytical solution for heat transfer during cyclic melting and freezing of phase change material used in electronic of electrical packaging" *J Electronic Packaging*, 125, 126-133, 2003.
- [73] A. Laouadi, and M. Lacroix, "Thermal performance of a heat energy storage ventilated panel for electronic load management" *Int J Heat Mass Transf* 42, 275-286, 1999.
- [74] Q. Xia, Y. Chen, C. Yang, T. Zhang, and Y. Zang, "A new model of phase change process for thermal energy Storage" *Int J Energy Res*, 42, 3877-3887, 2018.
- [75] S.K. Saha, and P. Dutta, "Performance analysis of heat sinks with phase change materials subjected to transient and cyclic heating" *Heat Transf Engg*, 36(16), 1349-1359, 2015.
- [76] L.M. Jiji, and S. Gaye, "Analysis of solidification and melting of PCM with energy generation" *Appl Therm Engg* 26, 568-575, 2006.
- [77] S. Kalaiselvam, M. Veerappan, A.A. Aaron, and S. Iniyar, "Experimental and analytical investigation of solidification and melting characteristics of PCMs inside cylindrical encapsulation" *Int J Thermal Sci*, 47, 858-874, 2008.
- [78] S. Kalaiselvam, R. Parameshwaran, and S. Harikrishnan, "Analytical and

- experimental investigations of nano particles embedded phase change materials for cooling applications in modern buildings” *Renew Energy* 39, 375-387, 2012.
- [79] M. Safdari, S. Sadeghzadeh, and R. Ahmadi, “A semi-analytical solution for time-varying latent heat thermal energy storage problems” *Int J Energy Res* 2019, doi: 10.1002/er.5078.
- [80] L. Khatra, and H.E. Qarnia, “Semianalytical solution for PCM solidification during the discharging of a planar thermal energy accumulator” *Int J Energy Res* 2019, doi: 10.1002/er.4737.
- [81] Z. Zhang, Z. Wang, and X. He, “Analytical solution of the melting process of phase-change materials in thermal energy storage system” *Energy Sources, Part A: Recovery, Utilization, and Environmental Effects* 2020, doi: 10.1080/15567036.2020.1779413
- [82] N.K. Bansal, and D. Buddhi, “An analytical study of a latent heat storage system in a cylinder” *Energy Convers Management* 33, 235-242, 1992.
- [83] D. Janghel, S.K. Saha, and S. Karagadde, “Effect of shrinkage void on thermal performance of pure and binary phase change materials based thermal energy storage system: a semi-analytical approach” *Appl Therm Engg* 167, 114706, 2020.
- [84] E.B.S. Mettawee, and G.M.R. Assassa, “Thermal conductivity enhancement in a latent heat storage system” *Solar Energy*, 81, 839-845, 2007.
- [85] A. Siahpush, J. O’Brien, and J. Crepeau, “Phase change heat transfer enhancement using copper porous foam” *ASME transactions heat transf*, 130, 1614-1616, 2008.
- [86] M. Lacroix, “Study of heat transfer behavior of a latent heat thermal energy storage unit with a finned tube” *Heat Mass Transf* 36, 2083-2092, 1993.
- [87] P. Lamberg, and K. Siren, “Analytical model for melting in a semi-infinite PCM storage with an internal fin” *Heat Mass Transf* 39, 167-176,

2003

- [88] P. Lamberg, “Approximate analytical model for two phase solidification problem in a finned phase-change material storage” *Applied Energy*, 77, 131-152, 2004.
- [89] T. Bauer, “Approximate analytical solutions for the solidification of PCMs in fin geometries using effective thermophysical properties” *Int J Heat Mass Transf* 54, 4923-4930, 2011.
- [90] M. Taghilou, and F. Talati, “Analytical and numerical analysis of PCM solidification inside a rectangular finned container with time-dependent boundary condition” *Int Journal Thermal Sci* 133, 69–81, 2018.
- [91] A.H. Mosaffa, F. Talati, H.B. Tabrizi, and M.A. Rosen, “Analytical modelling of PCM solidification in a shell and tube finned thermal storage for air conditioning systems” *Energy Buildings* 49, 356-361, 2012.
- [92] V.R. Voller, “Fast implicit finite-difference method for analysis of phase change problems” *Numerical Heat Transf, Part B: Fundamentals*, 17, 155-169, 1990.
- [93] B. Zivkovich, and I. Fujii, “An analysis of isothermal phase change of phase change material within rectangular and cylindrical containers” *Solar Energy*, 70, 51-61, 2001.
- [94] W. Saman F. Bruno, and E. Halawa, “Thermal performance of PCM thermal storage unit for a roof integrated solar heating system” *Solar Energy* 78, 341-349, 2005.
- [95] M. Esen, “Thermal performance of solar aided latent heat store used for space heating by heat pump” *Solar Energy* 69, 15-25, 2000.
- [96] W.D. Bennon, and F.P. Incropera, “A continuum model for momentum, heat and species transport in binary solid-liquid phase change systems-I. Model formulation” *Int J Heat Mass Transf* 30, 2161-2170, 1987.
- [97] M.A. Hassab, M.M. Sorour, M.K. Mansour, and M.M. Zaytoun, “Effect of volume expansion on the melting process’s thermal behavior” *Appl*

- Therm Engg* 115, 350–362, 2017.
- [98] X. Wang, A.S. Mujumdar, and C. Yap, “Effect of orientation for phase change material (PCM)-based heat sinks for transient thermal management of electric components” *Int Comm Heat Mass Transf* 34, 801-808, 2007.
- [99] H. Zennouhi, W. Benomar, T. Kousksou, A.A. Msaad, A. Allouhi, M. Mahdaoui, and T.E. Rhafiki, “Effect of inclination angle on the melting process of phase change material” *Case Studies Thermal Engg.* 9, 47–54, 2017.
- [100] M. Costa, D. Buddhi, and A. Oliva, “Numerical simulation of latent heat thermal energy storage system with enhanced heat conduction” *Energy Convers Management* 39, 319-330, 1998.
- [101] P. Lamberg, R. Lehtiniemi, and A.M. Henell, “Numerical and Experimental investigation of melting and freezing processes in phase change material storage” *Int J Thermal Sci* 43, 277-287, 2004.
- [102] R.D.C. Oliveski, F. Becker, L.A.O. Rocha, C. Biserni, and G.E.S. Eberhardt, “Design of fin structures for phase change material (PCM) melting process in rectangular cavities” *J Energy Storage* 35, 102337, 2021.
- [103] M.R. Hajmohammadi, S. Poozesh, and R. Hosseini, “Radiation effect on constructal design analysis of a TeY-shaped assembly of fins” *J Therm Sci Technol* 7, 677-692, 2012.
- [104] S.K. Saha, K. Srinivasan, and P. Dutta, “Studies on optimum distribution of fins in heat sinks filled with phase change materials” *J Heat Transfer* 130(3), 034505, 2008.
- [105] S.K. Saha, and P. Dutta, “Heat transfer correlations for PCM-based heat sinks with plate fins” *Appl Therm Engg* 30(16), 2485–2491, 2010.
- [106] R. Pakrouh, M.J. Hosseini, A.A. Ranjbar, and R. Bahrampoury, “A numerical method for PCM-based pin fin heat sinks optimization” *Energy Convers Management* 103, 542–552, 2015.

- [107] R. Baby, and C. Balaji, “A neural network-based optimization of thermal performance of phase change material-based finned heat sinks—an experimental study” *Exp Heat Transf* 54(1), 65–77, 2013.
- [108] N. Yusup, A.M. Zain, and S.Z.M. Hashim, “Evolutionary techniques in optimizing machining parameters: review and recent applications (2007–2011)” *Expert Syst Applications* 39(10), 9909-9927, 2013.
- [109] J. Fukai, M. Kanou, Y. Kodama, and O. Miyatake, “Thermal conductivity enhancement of energy storage media using carbon fibers” *Energy Convers Management* 41, 1543-1556, 2000.
- [110] K. Lafdi, and O. Mesalhy, “Merits of Employing Foam Encapsulated Phase Change Materials for Pulsed Power Electronics Cooling Application” *J Electronic Pack* 130(2), 1-8. 2008.
- [111] F. Zhu, C. Zhang, and X. Gong, “Numerical analysis and comparison of the thermal performance enhancement methods for metal foam/phase change material composite” *Appl Therm. Engg* 109, 373–383, 2016.
- [112] A. Chamkha, A. Veismoradi, M. Ghalambaz, and P. Talebizadehsardari, “Phase change heat transfer in an L-shape heat sink occupied with paraffin copper metal foam” *Appl Therm Engg* 177, 115493, 2020.
- [113] A. Veismoradi, A. Modir, M. Ghalambaz, and A. Chamkha, “A phase change/metal foam heat sink for thermal management of battery packs” *Int J Therm Sci* 157, 106514, 2020.
- [114] R.Y. Farsani, A. Raisi, A.A.Nadooshan, and S. Vanapalli, “Does nanoparticles dispersed in a phase change material improve melting characteristics?” *Int Comm Heat Mass Transf* 89, 219–229, 2017.
- [115] N.S. Bondareva, B. Buonomo, O. Manca, and M.A. Sheremet, “Heat transfer inside cooling system based on phase change material with alumina nanoparticles” *Appl Therm Engg* 144, 972–981, 2018.
- [116] M. Bayat, M.R. Faridzadeh, and D. Toghraie, “Investigation of finned heat sink performance with nano enhanced phase change material (NePCM)” *Therm Sci Engg Progress* 5, 50-59, 2018.

- [117] M. Ghalambaz, A.J. Chamkha, and D. Wen, “Natural convective flow and heat transfer of Nano-Encapsulated Phase Change Materials (NEPCMs) in a cavity” *Int J Heat Mass Transf* 138, 738-749, 2019.
- [118] H. Babazadeh, M.A. Sheremet, H.A. Mohammed, M.R. Hajizadeh, and Z. Li, “Inclusion of nanoparticles in PCM for heat release unit” *J Molecular Liquids* 313, 113544, 2020.
- [119] H. Faraji, M. Faraji, and M.E. Alami, “Numerical Survey of the Melting Driven Natural Convection Using Generation Heat Source: Application to the Passive Cooling of Electronics Using Nano-Enhanced Phase Change Material” *J Thermal Science Engg Applications* 12, 021005-1/021005-17, 2020.
- [120] N.H. Boukani, A. Dadvand, and A.J. Chamkha, “Melting of a Nano-enhanced phase change material (NePCM) in partially-filled horizontal elliptical capsules with different aspect ratios” *Int J Mech Sci* 149, 164-177, 2018.
- [121] J.M. Khodadadi, and Y. Zhang, “Effects of buoyancy-driven convection on melting within spherical containers” *Int J Heat Mass Transf* 44, 1605-1618, 2001.
- [122] F.L. Tan, S.F. Hosseinizadeh, J.M. Khodadadi, and L. Fan, “Experimental and computational study of constrained melting of phase change materials (PCM) inside a spherical capsule” *Int J Heat Mass Transf* 52, 3464-3472, 2009.
- [123] M. Bechiri, K. Mansouri, and S. Saleem, “Study of heat sink effects during melting of constrained phase change material inside a spherical enclosure” *J. Energy Storage*, 27 , 101151, 2020.
- [124] W. Li, S. Li, S. Guan, Y. Wang, X. Zhang, and X. Liu, “Numerical study on melt fraction during melting of phase change material inside a sphere” *Int J Hydrogen Energy* 42, 18232-18239, 2017.
- [125] H. Sattari, A. Mohebbi, M.M. Afsahi, and A.A. Yancheshme, “CFD simulation of melting process of phase change materials (PCMs) in a

- spherical capsule” *Int J Refrig* 73, 209-218, 2017.
- [126] S.K. Roy, and S. Sengupta, “The melting process within spherical enclosures” *J Heat Transf* 109, 460-462, 1987.
- [127] P.A. Bahrami, and T.G. Wang, “Analysis of gravity and conduction-driven melting in a sphere” *J Heat Transf* 109, 806-809, 1987.
- [128] S.K. Roy, and S. Sengupta, “Melting of a free solid in a spherical enclosure: effects of subcooling” *J Sol Energy Engg* 111, 32-36, 1989.
- [129] S.F. Hosseinizadeh, A.A.R. Darzi, F.L. Tan, and J.M. Khodadadi, “Unconstrained melting inside a sphere” *Int J Therm Sci* 63, 55-64, 2013.
- [130] A.R. Archibold, M.M. Rahman, D.Y. Goswami, and E.K. Stefanakos, “Analysis of heat transfer and fluid flow during melting inside a spherical container for thermal energy storage” *Appl Therm Engg* 64, 396-407, 2014.
- [131] A.R. Archibold, J. Gonzalez-Aguilar, M.M. Rahman, D.Y. Goswami, M. Romero, and E.K. Stefanakos, “The melting process of storage materials with relatively high phase change temperatures in partially filled spherical shells” *Appl Energy* 116, 243-252, 2014.
- [132] A.F. Elmozughi, L. Solomon, A. Oztekin, and S. Neti, “Encapsulated phase change material for high temperature thermal energy storage–heat transfer analysis” *Int J Heat Mass Transf* 78, 1135-1144, 2014.
- [133] J.F.R. Junior, R.D.C. Oliveski, L.A.O. Rocha, and C. Biserni, “Numerical investigation on phase change material (PCM): The melting process of erythritol in spheres under different thermal conditions” *Int J Mech Sci* 148, 20-30, 2018.
- [134] R. Kandasamy, X.C. Wang, and A.S. Mujumdar, “Application of phase change materials in thermal management of electronics” *Appl Therm Engg* 27, 2822–2832, 2007.
- [135] S.C. Fok, W. Shen, and F.L.Tan, “Cooling of portable hand-held electronic devices using phase change materials in finned heat sinks” *Int J Thermal Sci* 49(1),109-117, 2010.

- [136] R. Baby, and C. Balaji, “Experimental investigations on thermal performance enhancement and effect of orientation on porous matrix filled PCM based heat sink” *Int Comm Heat Mass Transf* 46, 27-30, 2013.
- [137] J. Lu, L. Fan, Y. Zeng, Y. Xiao, X. Xu, and Z. Yu, “Effect of the inclination angle on the transient performance of a phase change material-based heat sink under pulsed heat loads” *J Zhejiang Univ-Sci A (Appl Phys Engg)* 15(10), 789-797, 2014.
- [138] M. Avci, and M.Y. Yazici, “An experimental study on effect of inclination angle on the performance of a PCM-based flat-type heat sink” *Appl Therm Engg* 131, 806–814, 2018.
- [139] M.Y. Yazici, M. Avci, and O. Aydin, “Combined effects of inclination angle and fin number on thermal performance of a PCM-based heat sink” *Appl Therm Engg* 159, 113956, 2019.
- [140] D. Pal, and Y.K. Joshi, “Melting in a side heated tall enclosure by a uniformly dissipating heat source” *Int J Heat Mass Transf* 44, 375-387, 2001.
- [141] B. Kamkari, H. Shokouhmand, and F. Bruno, “Experimental investigation of the effect of inclination angle on convection-driven melting of phase change material in a rectangular enclosure” *Int J Heat Mass Transf* 72 186–200, 2014.
- [142] H. Shokouhmand, and B. Kamkari, “Experimental investigation on melting heat transfer characteristic of lauric acid in a rectangular thermal storage unit” *Exp Therm Fluid Sci* 50, 201-212, 2013.
- [143] B. Kamkari, and D. Groulx, “Experimental investigation of melting behaviour of phase change material in finned rectangular enclosures under different inclination angles” *Exp Therm Fluid Sci* 97, 94-108, 2018.
- [144] B. Kamkari, and H. Shokouhmand, “Experimental investigation of phase change material melting in rectangular enclosures with horizontal partial

- fins” *Int J Heat Mass Transf* 78, 839-851, 2014.
- [145] R. Baby, and C. Balaji, “Thermal management of electronics using phase change material based pin fin heat sinks” *6th European Thermal Sciences Conference: J. Phys. 2012*, IOP Publishing, 2012.
- [146] S.F. Hosseinizadeh, F.L. Tan, and S. Moosania, “Experimental and numerical studies on performance of PCM-based heat sink with different configurations of internal fins” *Appl Therm Engg* 31, 3827-3838, 2011.
- [147] S. Mahmoud, A. Tang, C. Toh, R. AL-Dadah, and S.L. Soo, “Experimental investigation of inserts configurations and PCM type on the thermal performance of PCM based heat sinks” *Appl Energy* 112, 1349-1356, 2013.
- [148] H.M. Ali, and A. Arshad, “Experimental investigation of n-eicosane based circular pin-fin heat sinks for passive cooling of electronic devices” *Int J Heat Mass Transf* 112, 649-661, 2017.
- [149] A. Arshad, H.M. Ali, M. Ali, and S. Manzoor, “Thermal performance of phase change material (PCM) based pin-finned heat sinks for electronics devices: Effect of pin thickness and PCM volume fraction” *Appl Therm Engg* 112, 143-155, 2017.
- [150] K.Y. Leong, S.P. Chew, B.A. Gurunathan, K.Z.K. Ahmad, and H.C. Ong, “An experimental approach to investigate thermal performance of paraffin wax and 1-hexadecanol based heat sinks for cooling of electronic system” *Int Comm Heat Mass Transf* 109, 104365, 2019.
- [151] R. Velraj, R.V. Seeniraj, B. Hafner, C. Faber, and K. Schwarzer, “Experimental analysis and numerical modelling of inward solidification on a finned vertical tube for latent heat storage unit” *Solar Energy* 60, 281-290, 1997.
- [152] C. Liu, and D. Groulx, “Experimental study of phase change heat transfer inside a horizontal cylindrical latent heat energy storage system” *Int J Therm Sci* 82, 100-110, 2014.
- [153] M. Rahimi, A.A. Ranjbar, D.D. Ganji, K. Sedighi, and M.J. Hosseini,

- “Experimental investigation of phase change inside a finned-tube heat exchanger” *J of Engg* 11, 641954, 2014.
- [154] A. Bhattacharya, and R.L. Mahajan, “Finned Metal Foam Heat Sinks for Electronics Cooling in Forced Convection” *J Electronic Pack* 124, 155-163, 2002.
- [155] S. Gharbi, S. Harmand, and S.B. Jabrallah “Experimental comparison between different configurations of PCM based heat sinks for cooling electronic components” *Appl Therm Engg* 87, 454-462, 2015.
- [156] Tauseef-ur-Rehman, and H.M. Ali, “Experimental study on the thermal behavior of RT-35HC paraffin within copper and Iron-Nickel open cell foams: Energy storage for thermal management of electronics” *Int J Heat Mass Transf* 146, 118852, 2020.
- [157] G.R. Jackson, and T.S. Fisher, “Response of porous foams filled with phase change material under transient heating conditions” *45th AIAA Thermophysics Conference*, Dallas, TX, 2015.
- [158] X. Xiao, P. Zhang, and M. Li, “Preparation and thermal characterization of paraffin/metal foam composite phase change material” *Appl Energy* 112, 1357-1366, 2013.
- [159] Tauseef-ur-Rehman, and H.M. Ali, “Thermal performance analysis of metallic foam-based heat sinks embedded with RT-54HC paraffin: an experimental investigation for electronic cooling” *J Therm. Analysis Calorimetry* 140 979-990, 2020.
- [160] P. Zhang, Z.N. Meng, H. Zhu, Y.L. Wang, and S.P. Peng, “Melting heat transfer characteristics of a composite phase change material fabricated by paraffin and metal foam” *Appl Energy* 185, 1971-1983, 2017.
- [161] H. Wang, F. Wang, Z. Li, Y. Tang, B. Yu, and W. Yuan, “Experimental investigation on the thermal performance of a heat sink filled with porous metal fiber sintered felt/paraffin composite phase change material” *Appl Energy* 176, 221-232, 2016.
- [162] H. Zheng, C. Wang, Q. Liu, Z. Tian, and X. Fan, “Thermal performance

- of copper foam/paraffin composite phase change material” *Energy Convers Management* 157, 372-381, 2018.
- [163] L.W. Fan, and H.Q. Jin, “Local thermal non equilibrium during melting of a paraffin filled in an open-cell copper foam: a visualized study at pore-scale” *J Heat Transf* 139, 034505-1/034505-6, 2017.
- [164] Y. Yao, H. Wu H, Z. Liu, and Z. Gao, “Pore-scale visualization and measurement of paraffin melting in high porosity open-cell copper foam” *Int J Therm Sci* 123, 73-85, 2018.
- [165] Y. Yao, and H. Wu, “Thermal transport process of metal foam/paraffin composite (MFPC) with solid-liquid phase change: An experimental study” *Appl Therm Engg* 179, 115668, 2020.
- [166] S.S. Sebti, M. Mastiani, H. Mirzaei, A. Dadvand, S. Kashani, and S.A. Hosseini, “Numerical study of the melting of nano-enhanced phase change material in a square cavity” *J Zhejiang University-Science A (Applied Physics Engg)* 14(5), 307-316, 2013.
- [167] L. Fan, and J.M. Khodadadi, “A theoretical and experimental investigation of unidirectional freezing of nanoparticle-enhanced phase change materials” *J Heat Transf* 134, 1-9, 2012.
- [168] M. Nabil, and J.M. Khodadadi, “Experimental determination of temperature-dependent thermal conductivity of solid eicosane-based nanostructure-enhanced phase change materials” *Int J Heat Mass Transf* 67, 301-310, 2013.
- [169] K. Chintakrinda, R.D. Weinstein, and A.S. Fleischer, “A direct comparison of three different material enhancement methods on transient thermal response of paraffin phase change material exposed to high heat fluxes” *Int J Thermal Sci* 50, 1639-1647, 2011.
- [170] K.Y. Leong, M.R.A. Rahman, and B.A. Gurunathan, “Nano-enhanced phase change materials: A review of thermo-physical properties, applications and challenges” *J Energy Storage* 21, 18-31, 2019.
- [171] S.L. Tariq, H.M. Ali, M.A. Akram, M.M. Janjua, and M.

- Ahmadlouydarab, “Nanoparticles enhanced phase change materials (NePCMs) - a recent review” *Appl Therm Engg* 176, 115305, 2020.
- [172] S. Nizetic, M. Jurcevic, M. Arıcı, A.V. Arasu, and G. Xie, “Nano-enhanced phase change materials and fluids in energy applications: A review” *Renew Sustainable Energy Rev* 129, 109931, 2020.
- [173] M.S. Kamel, F. Lezsovits, and A.K. Hussein, “Experimental studies of flow boiling heat transfer by using nanofluids: a critical recent review” *J Thermal Analysis Calorimetry* 138, 4019-4043, 2019.
- [174] Z. Ma, W. Lin, and M.I. Sohel, “Nano-enhanced phase change materials for improved building performance” *Renew Sustainable Energy Rev* 58 1256-1268, 2016.
- [175] T. Xiong, L. Zheng, and K.W. Shah, “Nano-enhanced phase change materials (NePCMs): A review of numerical simulations” *Appl Therm Engg* 178 115492, 2020.
- [176] R.Y. Farsani, A. Raisi, A.A.Nadooshan, and S. Vanapalli, “Does nanoparticles dispersed in a phase change material improve melting characteristics?” *Int Comm Heat Mass Transf* 89, 219-229, 2017.
- [177] S. Sharma, L. Micheli, W. Chang, A.A. Tahir, K.S. Reddy, and T.K. Mallick, “Nano-enhanced Phase Change Material for thermal management of BICPV” *Appl Energy* 208, 719-733, 2017.
- [178] M. Alimohammadi, Y. Aghli, E.S. Alavi, M. Sardarabadi, and M. Passandideh-Fard, “Experimental investigation of the effects of using nano/phase change materials (NPCM) as coolant of electronic chipsets, under free and forced convection” *Appl Therm Engg* 111, 271–279, 2017.
- [179] M. Joseph, and V. Sajith, “Graphene enhanced paraffin nanocomposite based hybrid cooling system for thermal management of electronics” *Appl Therm Engg* 163, 114342, 2019.
- [180] S.L. Tariq, H.M. Ali, M.A. Akram, and M.M. Janjua, “Experimental investigation on graphene based nanoparticles enhanced phase change materials (GbNePCMs) for thermal management of electronic

- Equipment” *J Energy Storage* 30, 101497, 2020.
- [181] Q. Ren, P. Guo, and J. Zhu, “Thermal management of electronic devices using pin-fin based cascade microencapsulated PCM/expanded graphite composite” *Int J Heat Mass Transf* 149, 119199, 2020.
- [182] I. Zarma, M. Emam, S. Ookawara, and M. Ahmed, “Thermal management of concentrator photovoltaic systems using nano-enhanced phase change materials-based heat sink” *Int J Energy Res* 1-21, 2020, doi: 10.1002/er.5504.
- [183] V. Pethurajan, and S. Sivan, “Fabrication, characterisation and heat transfer study on microencapsulation of nano-enhanced phase change material” *Chem Engg Processing - Process Intensification* 133, 12-23, 2018.
- [184] D. Huu-Quan, M. Sheremet, M.S. Kamel, and M. Zadi, “Investigation of thermal-hydro dynamical behavior on nano-encapsulated PCM suspension: Effect of fin position, fractioning and aspect ratio” *Chem Engg Processing - Process Intensification* 157, 108122, 2020.
- [185] M. Ghalambaz, A.J. Chamkha, and D. Wen, “Natural convective flow and heat transfer of nano-encapsulated phase change materials (NEPCMs) in a cavity” *Int J Heat Mass Transf* 138, 738-749, 2019.
- [186] H. Babazadeh, M.A. Sheremet, H.A. Mohammed, M.R. Hajizadeh, and Z. Li, “Inclusion of nanoparticles in PCM for heat release unit” *J Molecular Liquids* 313, 113544, 2020.
- [187] J. Krishna, P.S. Kishore, and A.B. Solomon, “Heat pipe with nano enhanced-PCM for electronic cooling application” *Exp Therm Fluid Sci* 81, 84-92, 2017.
- [188] M. Sivashankar, C. Selvam, S. Manikandan, and S. Harish, “Performance improvement in concentrated photovoltaics using nanoenhanced phase change material with graphene nanoplatelets” *Energy* 208, 118408, 2020.
- [189] M. Kazemi, A. Kianifar, and H. Niazmand, “Nanoparticle loading effect on the performance of the paraffin thermal energy storage material for

- building applications” *J Therm Analysis Calorimetry* 139, 3769-3775, 2020.
- [190] F. Bahiraei, A. Fartaj, and G. Nazri, “Experimental and numerical investigation on the performance of carbon-based nanoenhanced phase change materials for thermal management applications” *Energy Convers Management* 153 115-128, 2017.
- [191] A. Arshad, M. Jabbal, and Y. Yan, “Preparation and characteristics evaluation of mono and hybrid nanoenhanced phase change materials (NePCMs) for thermal management of microelectronics” *Energy Convers Management* 205, 112444, 2020.
- [192] V. S. Apraci, “Conduction Heat Transfer” *Addison-Wesley*, Reading, MA, 1996.
- [193] Z. Liu, X. Sun, and C. Ma, “Experimental investigations on the characteristics of melting process of stearic acid in an annulus and its thermal conductivity enhancement by fins” *Energy Convers Management* 46, 959-969, 2005.
- [194] Z. Liu, X. Sun, and C. Ma, “Experimental investigations on the characteristics of solidification process of stearic acid in an annulus and its thermal conductivity enhancement” *Energy Convers Management* 46, 971-984, 2005.
- [195] M.Y. Ramandi, I. Dincer, and G.F. Naterer, “Heat transfer and thermal management of electric vehicle batteries with phase change materials” *Heat Mass Transf* 47, 777-788, 2011.
- [196] G.H. Kim, J. Gonder, J. Lustbader, and A. Pesaran, “Thermal management of batteries in advanced vehicles using phase-change materials” *23rd Int Electric Vehicles Symposium and Exposition*, Anaheim, California, 2007.
- [197] P.J. Shamberger, “Cooling capacity figure of merit for phase change materials” *J Heat Transf* 138, 024502-1/024502-8, 2016.
- [198] F.P. Incropera, and D.P. DeWitt, “Fundamentals of heat and mass

- transfer” *3rd edn*, John Wiley and Sons, New York, 1990.
- [199] R. Marshall, “Experimental determination of heat transfer coefficient in a thermal storage containing a phase change material - the rectangular cavity” *Int Conf on Future Energy Concept*, 216-220, 1979.
- [200] Marshall, R. (1978) Natural convection effects in rectangular enclosures containing phase change material, Thermal heat transfer in solar energy systems, Kreith F; Boehm R; Mitchell J; Bannerot R. ASME pp. 61–69
- [201] J. Eftekhari, A. Haji-Sheikh, and D. Lou, “Heat transfer enhancement in a paraffin wax thermal energy storage system” *J Solar Energy Engg* 106, 299-306, 1984.
- [202] R. Henze, and J. Humphrey, “Enhanced heat conduction in phase change thermal energy storage devices” *Int J Heat Mass Transf* 24, 459-474, 1981.
- [203] V.R. Voller, and C. Prakash, “A fixed grid numerical modelling methodology for convection-diffusion mushy region phase-change problems” *Int J Heat Mass Transf* 30(8), 1709-1719, 1987.
- [204] A.D. Brent, V.R. Voller, and K.T.J. Reid, “Enthalpy-porosity technique for modelling convection-diffusion phase change: application to the melting of pure metal” *Num Heat Transf A Appl* 13(3), 297-318, 1988.
- [205] F.L. Tan, “Constrained and unconstrained melting inside a sphere” *Int Comm Heat Mass Transf* 35, 466-475, 2008.
- [206] S.V. Patankar, “Numerical heat transfer and fluid flow” Washington DC, USA: Hemisphere, 1980.
- [207] Ansys Fluent Theory Guide, SAS, IP, INC, 2015.
- [208] Y. Ganatra, J. Ruiz, J.A. Howarter, and A. Marconnet, “Experimental investigation of Phase Change Materials for thermal management of handheld devices” *Int J Therm Sci* 129, 358-364, 2018.
- [209] R.K. Sharma, P. Ganesan, V.V. Tyagi, H.S.C. Metselaar, and S.C. Sandaran, Thermal properties and heat storage analysis of palmitic acid-TiO₂ composite as nano-enhanced organic phase change material

- (NEOPCM), *Appl Therm Engg* 99, 1254-1262, 2016.
- [210] C.J. Ho, and J.Y. Gao, "Preparation and thermophysical properties of nanoparticle-inparaffin emulsion as phase change material" *Int Comm Heat Mass Transf* 36, 467-470, 2009.
- [211] J. Wang, H. Xie, Y. Li, and Z. Xin, "PW based phase change nanocomposites containing- Al_2O_3 " *J Therm Analysis Calorimetry* 102, 709-713, 2010.
- [212] L.C. Chow, and J.K. Zhong, "Thermal conductivity enhancement for phase change storage media" *Int Comm Heat Mass Transf* 23, 91-100, 1996.
- [213] N.S. Bondareva, B. Buonomo, O. Manca, and M.A. Sheremet, "Heat transfer performance of the finned nano-enhanced phase change material system under the inclination influence" *Int J Heat Mass Transf* 135, 1063-1072, 2019.
- [214] G.W. Burns, M.G. Scroger, G.F. Strouse, M.C. Croarkin, and W.F. Guthrie, "Temperature electromotive force reference functions and tables for the letter-designated thermocouple types based on the ITS-90" *NASA STI/Recon Technical Report N*, 1993.
- [215] H.W. Coleman, and W.G. Steele, "Experimental and uncertainty analysis for engineers" New York: Wiley, 1989.
- [216] N.S. Effendi, and K.J. Kim, "Orientation effects on natural convective performance of hybrid fin heat sinks" *Appl Therm Engg* 123, 527-536, 2017.
- [217] J. Duan, and F. Li, "Transient heat transfer analysis of phase change material melting in metal foam by experimental study and artificial neural network" *J Energy Storage* 33, 102160, 2021.
- [218] S.W. Churchill, and H.H.S. Chu, "Correlating equations for laminar and turbulent free convection from a vertical plate" *Int J Heat Mass Transf* 18(11), 1323-1329, 1975.
- [219] Tauseef-ur-Rehman, and H.M. Ali, "Experimental investigation on

- paraffin wax integrated with copper foam based heat sinks for electronic components thermal cooling” *Int Comm Heat Mass Transf* 98, 155-162, 2018.
- [220] Tauseef-ur-Rehman, H.M. Ali, A. Saieed, W. Pao, and M. Ali, “Copper foam/PCMs based heat sinks: An experimental study for electronic cooling systems” *Int J Heat Mass Transf* 127, 381-393, 2018.
- [221] L. Zhao, Y. Xing, and X. Liu, “Experimental investigation on the thermal management performance of heat sink using low melting point alloy as phase change material” *Renewable Energy* 146, 1578-1587, 2020.
- [222] Y. Huang, Q. Sun, F. Yao, and C. Zhang, “Experimental study on the thermal performance of a finned metal foam heat sink with phase change material” *Heat Transf Engg*, 2020, doi:10.1080/01457632.2020.1716482.

Appendix I

Uncertainty analysis

The test facility developed for the present experimental investigation consists of various subsystems such as PCM based heat sink assembly, scheme for power supply, the instrumentation scheme, and the solid-liquid interface tracking system. The present experimental study involves the measurement of various parameters namely, length, width, and thickness of the heat sink, temperature of heat sink and PCM, and supply voltage and current. The deviation in measured quantities initiates error in test results. Hence, in the present experimental investigation, the calibrated instruments are used to minimize errors in measurements.

An error analysis is made to estimate the errors associated in various parameters following the procedure suggested by Cole-man and Steele [I.1] and elaborated below.

If R is a dependent variable and is a function of n independent variables, it can be expressed as:

$$R = f(v_1, v_2, v_3, \dots \dots v_n) \quad (\text{I.1})$$

Let the uncertainties associated with independent variables be $e_1, e_2, e_3, \dots \dots e_n$ and resulting uncertainty (e) can be expressed as:

$$e = \left[\left\{ \left(\frac{\partial R}{\partial v_1} e_1 \right)^2 + \left(\frac{\partial R}{\partial v_2} e_2 \right)^2 + \left(\frac{\partial R}{\partial v_3} e_3 \right)^2 + \dots \dots \dots \left(\frac{\partial R}{\partial v_n} e_n \right)^2 \right\} \right]^{1/2} \quad (\text{I.2})$$

Error in basic quantity

In the present experimental investigation, a DC power supply (Aplab L3260, 0-32V/0-60A, India) is used to provide required electrical power to the plate heater. Standard digital multi-meter (Mecco 206) is used to verify the readings of current and voltage measurements displayed by DC power source. A vernier

caliper is used to measure dimensions of the test section and K-type thermocouples are used to measure the temperature of the test section.

The voltage and current readings recorded displayed by DC power source are used to estimate the input heat flux (q'') to the heat sink assembly by using the following equation.

$$q'' = \frac{V \times I}{l \times w} \quad (I.3)$$

Where, V is the voltage supplied by DC power source in volts, I is the current supplied by DC power source in amps, l is the length heater, and w is the width of heater. The length and width of the heater is considered as 100 mm in this study.

Table I.1 Error associated with measurement of various parameters

Parameter	Error
Length (l)	0.02 mm
Width (w)	0.02 mm
Height (h)	0.02 mm
Temperature (T)	$\pm 0.2^\circ\text{C}$
Voltage (V)	± 0.1 V
Current (I)	± 0.1 A
Angle (θ)	1°

The individual uncertainties involved in various measuring parameters such as V , I , l , w , h and T are shown in Table I.1. The uncertainty in the estimated result for heat flux (q'') is given below. The uncertainty in heat flux is calculated as below.

$$q'' = f(V, I, l, w) \quad (I.4)$$

The errors involved in V , I , l , and w are e_v , e_i , e_l , e_w respectively. The uncertainty ($e_{q''}$) supplied heat flux is calculated by using Eq. (I.2) as:

$$\frac{e_{q''}}{q''} = \frac{1}{q''} \left[\left\{ \left(\frac{\partial q''}{\partial V} e_v \right)^2 + \left(\frac{\partial q''}{\partial I} e_I \right)^2 + \left(\frac{\partial q''}{\partial l} e_l \right)^2 + \left(\frac{\partial q''}{\partial w} e_w \right)^2 \right\} \right]^{1/2} \quad (\text{I.5})$$

$$\frac{e_{q''}}{q''} = \left[\left\{ \left(\frac{e_v}{V} \right)^2 + \left(\frac{e_I}{I} \right)^2 + \left(\frac{e_l}{l} \right)^2 + \left(\frac{e_w}{w} \right)^2 \right\} \right]^{1/2} \quad (\text{I.6})$$

(a) *Uncertainty in supplied heat flux* $q'' = 1.3 \text{ kW/m}^2$

Here, $V = 7.7 \text{ V}$, $I = 1.7 \text{ A}$, the Eq. (I.6) can be written as:

$$\frac{e_{q''}}{q''} = \left[\left\{ \left(\frac{0.1}{7.7} \right)^2 + \left(\frac{0.1}{1.7} \right)^2 + \left(\frac{0.02}{100} \right)^2 + \left(\frac{0.02}{100} \right)^2 \right\} \right]^{1/2} \quad (\text{I.7})$$

$$\frac{e_{q''}}{q''} = \left[\left\{ \left(\frac{0.1}{7.7} \right)^2 + \left(\frac{0.1}{1.7} \right)^2 + \left(\frac{0.02}{100} \right)^2 + \left(\frac{0.02}{100} \right)^2 \right\} \right]^{1/2} \quad (\text{I.8})$$

$$\frac{e_{q''}}{q''} = 0.0602 \quad (\text{I.9})$$

$$e_{q''}\% = 6.02\% \quad (\text{I.10})$$

(b) *Uncertainty in supplied heat flux* $q'' = 2.0 \text{ kW/m}^2$

Here, $V = 9.6 \text{ V}$, $I = 2.1 \text{ A}$, the Eq. (I.6) can be written as:

$$\frac{e_{q''}}{q''} = \left[\left\{ \left(\frac{0.1}{9.6} \right)^2 + \left(\frac{0.1}{2.1} \right)^2 + \left(\frac{0.02}{100} \right)^2 + \left(\frac{0.02}{100} \right)^2 \right\} \right]^{1/2} \quad (\text{I.11})$$

$$\frac{e_{q''}}{q''} = \left[\left\{ \left(\frac{0.1}{9.6} \right)^2 + \left(\frac{0.1}{2.1} \right)^2 + \left(\frac{0.02}{100} \right)^2 + \left(\frac{0.02}{100} \right)^2 \right\} \right]^{1/2} \quad (\text{I.12})$$

$$\frac{e_{q''}}{q''} = 0.0487 \quad (\text{I.13})$$

$$e_q \% = 4.87\% \quad (\text{I.14})$$

(c) *Uncertainty in supplied heat flux* $q'' = 2.7 \text{ kW/m}^2$

Here, $V = 10.5 \text{ V}$, $I = 2.6 \text{ A}$, the Eq. (I.5) can be written as:

$$\frac{e_{q''}}{q''} = \left[\left\{ \left(\frac{0.1}{10.5} \right)^2 + \left(\frac{0.1}{2.6} \right)^2 + \left(\frac{0.02}{100} \right)^2 + \left(\frac{0.02}{100} \right)^2 \right\} \right]^{1/2} \quad (\text{I.15})$$

$$\frac{e_{q''}}{q''} = \left[\left\{ \left(\frac{0.1}{10.5} \right)^2 + \left(\frac{0.1}{2.6} \right)^2 + \left(\frac{0.02}{100} \right)^2 + \left(\frac{0.02}{100} \right)^2 \right\} \right]^{1/2} \quad (\text{I.16})$$

$$\frac{e_{q''}}{q''} = 0.0396 \quad (\text{I.17})$$

$$e_q \% = 3.96\% \quad (\text{I.18})$$

The error in supplied heat flux of 1.3 kW/m^2 , 2.0 kW/m^2 , and 2.7 kW/m^2 is found to be 6.02%, 4.87% and 3.96%, respectively (as shown in Eq. I.10, I.14, and I.18)

Additional Reference

[I.1] H.W. Coleman, and W.G. Steele, *Experimental and uncertainty analysis for engineers*, New York: Wiley, 1989.

Appendix II

Specifications of equipment

Items	Details	Pictorial View
CNC milling	<p>Make: EMCO MAIER G.M.B.H. AUSTRIA;</p> <p>Model: EMCOMILL E 350;</p> <p>Specifications: Controller: Sinumerik 828D from Siemens;</p> <p>X-axis travel: 150 - 300 mm; Y-axis travel: 150 - 300 mm; Z-axis travel: 150 - 300 mm</p>	 <p>A photograph of a red and white EMCO MILL E350 CNC milling machine. The machine has a large, curved protective enclosure. The control panel on the right side features a digital display and a keypad. The text 'EMCO MILL' and 'E350' are prominently displayed on the machine's body.</p>
Data Acquisition System	<p>Make: Agilent;</p> <p>Model: 34972-A;</p> <p>Maximum up to 60 channels</p>	 <p>A photograph of the Agilent 34972-A Data Acquisition System. It is a compact, rack-mountable device with a front panel featuring a digital display showing 'MUX' and 'OFF', and several control buttons and indicators.</p>
Differential Scanning calorimeter	<p>Make: Netzch;</p> <p>Model: DSC214 Polyma</p>	 <p>A photograph of the Netzch DSC 214 Polyma Differential Scanning Calorimeter. The device is white with a black control panel on the front. A sample pan is visible on top of the instrument.</p>

<p>DC Power source</p>	<p>Make: Aplab; Model: L3260; Operating voltage: 0-32V; Operating current: 0-60A</p>	
<p>Heater</p>	<p>Make: Sunrise Product: Maximum heat flux: 15.0 kW/m²</p>	
<p>Microscope</p>	<p>Make: Dewinter; Model: DMI Prime; Mechanical stage: 210mm X 140mm</p>	

<p>Scanning Electron Microscope (SEM)</p>	<p>Make: Carl ZEISS; Model: Supra 55 Resolution: 1.0 nm @ 15 kV, 1.7 nm @ 1 kV, 4.0 nm @ 0.1 kV; Operating voltage range: 0.02-30 kV</p>	
<p>Vacuum Oven</p>	<p>Make: MLE make; Model: RS44; Control Logic : PID; Power supply : 90~270 VAC, 50/60 Hz.</p>	

LIST OF PUBLICATIONS

(A) Publications from PhD thesis work:

A1. In Refereed Journals (Accepted/Published)

1. **R. Kothari**, S. K. Sahu, S. I. Kundalwal, and S. Sahoo, Experimental investigation of the effect of inclination angle on the performance of phase change material based finned heat sink, *Journal of Energy Storage* 37 (2021) 102462. (IF = 6.58) <https://doi.org/10.1016/j.est.2021.102462>
2. **R. Kothari**, S. K. Sahu, and S. I. Kundalwal, Investigation on thermal characteristics of nano enhanced phase change material based finned and unfinned heat sinks for thermal management system, *Chemical Engineering Processing and Process Intensification*, 162 (2021) 108328. (IF = 4.23) <https://doi.org/10.1016/j.cep.2021.108328>
3. **R. Kothari**, S. K. Sahu, S. I. Kundalwal, and P. Mahalkar, Thermal performance of phase change material–based heat sink for passive cooling of electronic components: An experimental study, *International Journal of Energy Research*, 45 (2021) 5939-5963. (IF = 5.16) <https://doi.org/10.1002/er.6215>
4. **R. Kothari**, S. Das, S. K. Sahu, and S. I. Kundalwal, Analysis of solidification in a finite PCM storage with internal fins by employing heat balance integral method, *International Journal of Energy Research*, 43 (2019) 6366-6368. (IF = 5.16) <https://doi.org/10.1002/er.4363>
5. **R. Kothari**, S. K. Sahu, and S. I. Kundalwal, Comprehensive analysis of melting and solidification of a phase change material in an annulus, *Heat and Mass Transfer*, 55(3) (2019) 769-790. (IF =2.43) <https://doi.org/10.1007/s00231-018-2453-9>

A2. In Refereed Journals (To be submitted)

1. **R. Kothari**, S. K. Sahu, and S. I. Kundalwal, Comprehensive analysis of melting of phase change material in a finite PCM storage with internal fins.

2. **R. Kothari**, S. T. Revankar, S. K. Sahu, and S. I. Kundalwal, Unconstrained melting of PCM inside the spherical capsule: a numerical study.
3. **R. Kothari**, S. T. Revankar, S. K. Sahu, and S. I. Kundalwal, Computational study of constrained melting of PCM inside the spherical capsule.

A3. In Referred Conferences

1. **R. Kothari**, S. Malviya, S. K. Singh, S. K. Sahu, and S. I. Kundalwal, Thermal management of electric vehicle battery modules with phase change materials”, *Proceedings of 24th National and 2nd International ISHMT-ASTFE Heat and Mass Transfer Conference (IHMTTC2017-15-0805)*, BITS Hyderabad, Telangana, India, Dec 27-31, 2017.
2. **R. Kothari**, S. Das, S. K. Sahu, and S. I. Kundalwal, Approximate analytical model for solidification process in a rectangular phase change material storage with internal fins, *Proceedings of 6th International Conference on Advances in Energy Research (Paper72)*, IIT Bombay, Mumbai, India, December 12-14, 2017.
3. **R. Kothari**, P. Mahalkar, S. K. Sahu, and S. I. Kundalwal, Experimental investigations on thermal performance of PCM based heat sink for passive cooling of electronic components, *Proceedings of the ASME 2018 16th International Conference on Nanochannels, Microchannels, and Minichannels (ICNMM2018-7732)*, Dubrovnik, Croatia, June 10-13, 2018. *(Recipient of SERB Travel Grant)* <https://doi.org/10.1115/ICNMM2018-7732>
4. **R. Kothari**, S. P. Sahoo, S. K. Sahu, and S. I. Kundalwal, Experimental investigation on effect of inclination angle on the performance of phase change material based heat sinks, *Proceedings of the 7th International and 45th National Conference on Fluid Mechanics and Fluid Power (FMFP2018-268)*, IIT Bombay, Mumbai, India, December 10-12, 2018.
5. **R. Kothari**, D. V. Vaidya, V. Shelke, S. K. Sahu, and S. I. Kundalwal, Experimental investigation of thermal performance of nano-enhanced phase change materials for thermal management of electronic components, *ASME*

2019 power conference (POWER2019-1883), Salt Lake City, Utah, USA, June 14-18, 2019. (*Winner of Qualified Student Award by ASME*)
<https://doi.org/10.1115/POWER2019-1883>

6. **R. Kothari**, A. Kumar, P. K. Singh, S. K. Sahu, and S. I. Kundalwal, Analytical Model for Melting Process in a Rectangular Phase Change Material Storage with Internal Fins, *Proceedings of the 25th National and 3rd International ISHMT-ASTFE Heat and Mass Transfer Conference (IHMTTC-2019-203)*, IIT Roorkee, Roorkee, India, December 28-31, 2019.
7. **R. Kothari**, S. Revankar, S. K. Sahu, and S. I. Kundalwal, A comparative study of constrained and unconstrained melting inside a sphere, *Proceedings of the 2020 28th Conference on Nuclear Engineering Joint with the ASME 2020 Power Conference (ICONE28-POWER2020-6524)*, Anaheim, California, USA, August 2-6, 2020. (*Winner of Qualified Student Award by ASME and Best Presentation Award in Asia Region*)
<https://doi.org/10.1115/ICONE2020-16056>

A4. Book Chapters

1. **R. Kothari**, S. Das, S. K. Sahu, and S. I. Kundalwal, Approximate Analytical Model for Solidification Process in a Rectangular Phase-Change Material Storage with Internal Fins, *Advances in Energy Research*, In: Suneet Singh and Venkatasailanathan Ramadesigan (Eds.), *Advances in Energy Research*, Vol. 1. Springer Proceedings in Energy. Springer, Singapore, 2020.
https://doi.org/10.1007/978-981-15-2666-4_22

(B) Other publications during PhD:

B1. In Refereed Journals (Accepted)

1. **R. Kothari**, S. I. Kundalwal, S. K. Sahu, and M.C. Ray. Modeling of hybrid nanocomposites for next generation polymeric composites, *Polymer Composites*, 39(12) (2018) 4243-4274. (*IF = 3.17*)
<https://doi.org/10.1002/pc.24483>

2. **R. Kothari**, S. K. Sahu, and S. I. Kundalwal. Transversely isotropic thermal properties of carbon nanotubes containing vacancies, *Acta Mechanica*, 229(7) (2018) 2787-2800. (IF = 2.69) <https://doi.org/10.1007/s00707-018-2145-z>
3. A. Kumar, **R. Kothari**, S. K. Sahu, and S. I. Kundalwal, Selection of phase change material for thermal management of electronic devices using multi-attribute decision making technique, *International Journal of Energy Research*, 45 (2021) 2023–2042. (IF = 5.16) <https://doi.org/10.1002/er.5896>
4. A. Kumar, **R. Kothari**, S. K. Sahu, S. I. Kundalwal, and M.P. Paulraj, Numerical simulation of cross plate fin heat sink filled with PCM for cooling application of portable electronic devices, *International Journal of Energy Research*, (2021). (IF = 5.16) <https://doi.org/10.1002/er.6404>
5. A. Kumar, **R. Kothari**, S. K. Sahu, and S. I. Kundalwal, Thermal performance of heat sink using nano-enhanced phase change material (NePCM) for cooling of electronic components, *Microelectronics Reliability*, 121 (2021) 114144. (IF = 1.58) <https://doi.org/10.1016/j.microrel.2021.114144>
6. J. Sutradhar, **R. Kothari**, and S. K. Sahu, Solidification and melting model of phase change material with volumetric shrinkage/expansion void in an annulus, *Applied Thermal Engineering*, 195 (2021) 117202. (IF = 5.29) <https://doi.org/10.1016/j.applthermaleng.2021.117202>

B2. In Refereed Journals (Under Revision)

1. J. Sutradhar, R. Kothari, S. K. Sahu, Melting and solidification analysis of phase change material-metal foam composite with expansion/shrinkage void in rectangular system, *Journal of Energy Storage*, EST-D-21-01239. (IF = 6.58)
2. A. Kumar, R. Kothari, S. K. Sahu, and S. I. Kundalwal, A comparative study and optimization of phase change material based heat sinks for thermal management of electronic components, *Journal of Energy Storage*, EST-D-21-01674. (IF = 6.58)

3. V. Saxena, R. Kothari, A. Kumar, S. K. Sahu, S. I. Kundalwal, A theoretical models for the effective thermal conductivity of open-cell coated metal foams saturated with PCM/Fluid, *Journal of Energy Storage*, EST-D-21-02424. (I.F. = 6.58)
4. A. Kumar, R. Kothari, V. Saxena, S. K. Sahu, S. I. Kundalwal, Experimental investigation on paraffin wax based heat sinks with cross plate fin arrangement for cooling of electronic components, *Journal of Thermal Analysis and Calorimetry*, JTAC-D-21-01341. (I.F. = 4.62)

B3. In Refereed Conferences

1. V. Saxena, **R. Kothari**, S. K. Sahu, and S. I. Kundalwal, Modelling the Effective Thermal Conductivity of Externally Coated Open-Cell Metal Foam Saturated with Phase Change Material: An Analytical Approach, *Proceedings of the 26th National and 4th International Heat and Mass Transfer Conference (IHMT-ASTFE 2021-511)*, Virtual Conference, Indian Institute of Technology Madras, India, December 17-20, 2021.
2. A. Sharma, **R. Kothari**, V. Saxena, and S. K. Sahu, Effect of fin location on constrained melting heat transfer of phase change material in a spherical capsule: A numerical study, *Proceedings of the 26th National and 4th International Heat and Mass Transfer Conference (IHMT-ASTFE 2021-458)*, Virtual Conference, Indian Institute of Technology Madras, India, December 17-20, 2021.
3. A. Kumar, A. K. Singh, A. A Chitre, **R. Kothari**, V. Saxena, S. K. Sahu, and S. I. Kundalwal, Thermal performance of PCM based heat sink with solid and hollow fins for thermal management of electronics, *Proceedings of the 26th National and 4th International Heat and Mass Transfer Conference (IHMT-ASTFE 2021-345)*, Virtual Conference, Indian Institute of Technology Madras, India, December 17-20, 2021
4. A. Kumar, A. Chitre, A. Singh, **R. Kothari**, V. Saxena, S. K. Sahu and S. I. Kundalwal, Thermal performance investigation of phase change material based heat sinks with hollow fins for cooling of electronic devices,

- Proceedings of International Conference on Latest Trends in Civil, Mechanical and Electrical Engineering (Ltcmee2021-34)*, virtual conference, April 12-13, 2021. (Submitted)
5. V. Saxena, **R. Kothari**, A. Kumar, S. K. Sahu, and S. I. Kundalwal, Theoretical Modeling for the effective thermal conductivity of open-cell metal foams infiltrated with phase change material, *Proceedings of 15th International Conference on Heat Transfer, Fluid Mechanics and Thermodynamic (ATE-HEFAT2021)*, virtual conference, July 25-28, 2021. (Submitted)
 6. J. Sutradhar, **R. Kothari**, V. Saxena, and S. K. Sahu, Investigation of melting of pure phase change material and nanoenhanced phase change material considering volumetric expansion: An analytical approach, *Proceedings of 15th International Conference on Heat Transfer, Fluid Mechanics and Thermodynamic (ATE-HEFAT2021)*, virtual conference, July 25-28, 2021. (Submitted)
 7. A. Kumar, **R. Kothari**, S. K. Sahu, S. I. Kundalwal, and A. Sharma, Investigation of phase change material integrated with high thermal conductive carbon foam inside heat sinks for thermal management of electronic components, *Proceedings of the ASME 2021 Power Conference (POWER2021-65569)*, Anaheim, CA, USA, July 18-22, 2021. (Accepted, **Winner of Qualified Student Award by ASME**)
 8. A. Sharma, **R. Kothari**, A. Kumar, and S. K. Sahu, Effect of fin orientation on PCM melting in a spherical enclosure for latent heat storage, *Proceedings of the ASME 2021 Power Conference (POWER2021-10495)*, Anaheim, CA, USA, July 18-22, 2021. (Accepted)
 9. J. Sutradhar, **R. Kothari**, A. Kumar, and S. K. Sahu, Study of solidification process of PCM with shrinkage void effect in an annulus, *Proceedings of the 8th International and 47th National Conference on Fluid Mechanics and Fluid Power (FMFP2020-164)*, IIT Guwahati, Guwahati-781039, Assam, India, December 09-11, 2020.

10. A. Kumar, **R. Kothari**, P. K. Singh, R. Vaidya, S. K. Sahu, and S. I. Kundalwal, Thermal performance Enhancement of PCM Based Cross Plate Finned Heat Sink for Electronic Cooling, *Proceedings of the 8th International and 47th National Conference on Fluid Mechanics and Fluid Power (FMFP2020-95)*, IIT Guwahati, Guwahati-781039, Assam, India, December 09-11, 2020.
11. P. K. Singh, **R. Kothari**, S. K. Sahu, and P. K. Upadhyay, Experimental and Numerical Investigation of Thermal Performance of Synthetic Jet Impingement, *Proceedings of the 2020 28th Conference on Nuclear Engineering Joint With the ASME 2020 Power Conference (ICONE28-POWER2020-16775)*, Anaheim, California, USA, August 2-6, 2020. <https://doi.org/10.1115/ICONE2020-16775>
12. A. Kumar, **R. Kothari**, P. K. Singh., M. P. Paulraj, S. K. Sahu, and S. I. Kundalwal, Numerical simulation of PCM based heat sink with plate fins for thermal management of electronic components, *Proceedings of the International Conference on Innovations in Thermo-Fluid Engineering and Sciences (ICITFES2020-13724)*, NIT Rourkela, India, February 10-12, 2020.
13. P. K. Singh, **R. Kothari**, P. K. Upadhyay, and S. K. Sahu, Heat transfer characteristics of hot surface by synthetic jet impingement, *Proceedings of the 7th International and 45th National Conference on Fluid Mechanics and Fluid Power (FMFP2018-466)*, IIT Bombay, Mumbai, India, December 10-12, 2018.
14. A. Kumar, **R. Kothari**, S. K. Sahu, and S. I. Kundalwal, Effect of CuO nanoparticle in PCM integrated heat sink for thermal management of electronic component: an experimental study, *Proceedings of the 25th National and 3rd International ISHMT-ASTFE Heat and Mass Transfer Conference (IHMTTC2019-PCM-056)*, IIT Roorkee, Roorkee, India, December 28-31, 2019.

B4. Book Chapters

1. A. Kumar, **R. Kothari**, P. K. Singh., M. P. Paulraj, S. K. Sahu, and S. I. Kundalwal, Numerical simulation of PCM based heat sink with plate fins for thermal management of electronic components, In: F. Cavas-Martinez, F. Chaari, F. Gherardini, M. Haddar, V. Ivanov, Y.W. Kwon, J. Trojanowska (Eds.), *Lecture Series in Mechanical Engineering, 2021*.
https://doi.org/10.1007/978-981-33-4165-4_20

B5. Poster Presentation at National and International Symposium

1. A. Kumar, **R. Kothari**, S. K. Sahu, and S. I. Kundalwal, Development of light weight heat sink integrated with phase change material (PCM) for cooling application, Second *International Meeting on Clean Energy Material Innovation challenge (IC6)*, New Delhi, February 2019.
2. A. Kumar, **R. Kothari**, S. K. Sahu, and S. I. Kundalwal, Development of light weight heat sink integrated with phase change material (PCM) for cooling application, *Industry academia conclave on energy storage*, MNIT Jaipur, November 30, 2019.

ROHIT KOTHARI

ADDRESS 69/2, Sutar Ka Was, Ratlam-457001, Madhya Pradesh, India
Mobile: +91 7828766646
Email: rohitkothari2892@gmail.com
phd1601103003@iiti.ac.in

 https://www.researchgate.net/profile/Rohit_Kothari4/contributions

 <https://www.linkedin.com/in/rohit-kothari-67378561/>

 <https://orcid.org/0000-0002-7678-6690>

EDUCATION

- Indian Institute of Technology Indore** **Indore, India**
• *Ph.D.* 2016-2021
Mechanical Engineering
Advisor: Dr. S. K. Sahu and Dr. S. I. Kundalwal
- National Institute of Technology Patna** **Patna, India**
• *Master of Technology* (CGPA 9.68/10) 2014- 2016
Mechanical Engineering (Specialization: Thermal turbo Machines)
Advisor: Prof. Om Prakash
- Ujjain Engineering College (Govt.)** **Ujjain, India**
• *Bachelor of Engineering* (80.94%, Hons) 2009- 2013
Mechanical Engineering

Ph.D. OBJECTIVES

- Development of theoretical models to analyze melting and solidification of PCM in annular and rectangular geometries during melting and solidification process for host of boundary conditions.
- Understanding the phenomena of unconstrained and constrained melting behavior of phase change material (PCM) in the spherical capsule through CFD numerical technique.
- Design and fabricate a test facility involving various modules such as: test section, the scheme for orientation of the test specimen, the instrumentation scheme: temperature measurement.
- Investigate the thermal performance of heat sinks incorporating the combined effects of fin number, inclination angle and heat flux values.
- Study the thermal performance of PCM based heat sinks with combination of different TCEs such as fins and MF, and fins and nanoparticles.

CURRENT TEACHING ASSISTANCE EXPERIENCE

- Engineering Graphics (IC153: autumn 2016; tutorial)
- Machine Drawing (ME257: autumn 2017; tutorial)
- Fluid Mechanics and Machinery Lab (ME254: spring 2017, spring 2018; practical)
- Fluid Mechanics and Machinery (ME203 and ME204: spring 2017, spring 2018, autumn 2018; tutorial)

PAPER PRESENTED IN CONFERENCES

- *24th National and 2nd International ISHMT-ASTFE Heat and Mass Transfer Conference (IHMTTC2017-15-0805)*, BITS Hyderabad, Telangana, India, Dec 27-31, 2017.
- *6th International Conference on Advances in Energy Research (Paper72)*, IIT Bombay, Mumbai, India, December 12-14, 2017.
- *16th International Conference on Nanochannels, Microchannels, and Minichannels (ICNMM2018-7732)*, Dubrovnik, Croatia, June 10-13, 2018.
- *7th International and 45th National Conference on Fluid Mechanics and Fluid Power (FMFP2018-268)*, IIT Bombay, Mumbai, India, December 10-12, 2018.
- *ASME 2019 power conference (POWER2019-1883)*, Salt Lake City, Utah, USA, June 14-18, 2019.
- *25th National and 3rd International ISHMT-ASTFE Heat and Mass Transfer Conference (IHMTTC-2019-203)*, IIT Roorkee, Roorkee, India, December 28-31, 2019.
- *28th Conference on Nuclear Engineering Joint with the ASME 2020 Power Conference (ICONE28-POWER2020-6524)*, virtual online, USA, August 2-6, 2020.

HONORS AND AWARDS/FELLOWSHIPS

- Research article selected as **Qualified Student Award Winner and Best Presentation in Asia Region** in the 28th Conference on Nuclear Engineering Joint with the ASME 2020 Power Conference (ICONE28-POWER2020), virtual online, USA, August 2-6, 2020.
- Research article selected as **Qualified Student Award Winner** of the student paper competition in the ASME Power and Nuclear forum conference (ASME POWER2019), Salt lake city, Utah, USA, 2019.
- Recipient of prestigious **SERB Overseas Visiting Doctoral Fellowship (SERB-OVDF)** to work as visiting research scholar at **Purdue University**, USA under the supervision of **Prof. Shripad Revankar** for one year.

- Recipient of the prestigious **SERB-DST International Travel Fund [ITS/2018/001298]** for attending the International conference on Nanochannels, Microchannels and Minichannels (ICNMM2018).
- Recipient of the prestigious **DST INSPIRE Fellowship Award [IF170534]**.
- Recipient of the **Presidents Gold Medal Award and Institute Gold Medal Award** for the overall topper of the postgraduate program and Branch topper in Mechanical Engineering for the session 2014-2016 at National Institute of Technology Patna, India.
- Qualified GATE 2015 with 710 GATE score and all India rank of 2408.
- Completed Bachelor of Engineering Degree with **Honors** in 2013.
- Vice President of Mechanical Engineering Society at UEC, Ujjain.
- Coordinator of human values in technical education conducted by SSUN, New Delhi.

COMPUTER SKILLS

Application Softwares:

CAD Packages	AutoCAD, ProE, SolidWorks
Analysis Packages	ANSYS, MATLAB, LAMMPS, Material Studio, NanoEngineer-1, PACKMOL, Visual Molecular Dynamics, Origin Pro, DataFit

Programming Languages: Basic level in C, C++

MISCELLENEOUS ACTIVITES

Reviewer: Journal of the Taiwan Institute of Chemical Engineers, Elsevier

PERSONAL DETAILS

Date of Birth	May 20, 1992 (Madhya Pradesh, India)
Nationality	Indian
Sex	Male
Religion	Jainism
Marital Status	Unmarried
Phone	+91-7828766646
Permanent Address	69/2, Sutaro ka Was, Ratlam-452001 (MP), India
Languages known	Hindi, English